Acoustical Physics, Vol. 48, No. 6, 2002, pp. 643–655. Translated from Akusticheskiĭ Zhurnal, Vol. 48, No. 6, 2002, pp. 725–740.

Solitons and Nonlinear Periodic Strain Waves in Rods, Plates, and Shells (A Review)

V. I. Erofeev and N. V. Klyueva

Blagonravov Institute of Mechanical Engineering, Nizhni Novgorod Branch, Russian Academy of Sciences, ul. Belinskogo 85, Nizhni Novgorod, 603024 Russia

e-mail: wvs@dynamo.nnov.ru

Received March 27, 2002

Abstract—The most significant results of theoretical and experimental studies of solitons and nonlinear periodic strain waves in rods, plates, and shells are reviewed. The review covers the period 1970–2000. © *2002 MAIK "Nauka/Interperiodica".*

INTRODUCTION

From the wave theory, it is well known that the whole variety of wave processes in one-dimensional systems is determined by the relation between nonlinearity, dispersion, and dissipation. In two- and three-dimensional systems, the diffraction phenomenon also comes into play. In the case when the nonlinear, dispersion, and diffraction factors compensate each other and the dissipation is small, solitary nonlinear stationary waves (solitons) can be formed in the system, these waves propagating with a constant speed without changing their form. According to the definition given in the encyclopedia [99], "A soliton is a structurally stable solitary wave in a nonlinear dispersive system. Solitons behave like particles; i.e., on interacting with each other and with some other disturbances, solitons do not collapse but move away retaining their structure." The term "soliton" was introduced by N. Zabuski and M. Kruskal in 1965. This type of waves was noticed by J. Scott Russell when observing waves in channels as early as in 1834. A soliton solution for long waves on a liquid surface was obtained for the first time by Boussinesque (1872). Korteweg and de Vries derived the equation named after them and determined a solution in the form of periodic (cnoidal) waves in 1895.

Interest in solitons grew continuously after the discovery of the method of the inverse scattering problem by C. Gardner, J. Greene, M. Kruskal, and R. Miura [108] in 1967 and a series of completely integrable equations (see monographs [1, 11, 12, 16, 21, 39, 49, 57, 58, 62, 95, 96]). Soon after the discovery of the method of the inverse scattering problem, P. Lax in 1968 performed a study that revealed the algebraic mechanism forming the basis of this method [112]. V.E. Zakharov and A.B. Shabat [42] developed a general scheme that provided an opportunity to integrate some physically interesting equations like the Boussinesque's equation (connected with the Lax operator of the third order) and the Kadomtsev–Petviashvili equation using the inverse scattering problem. The method of the inverse problem was developed substantially in works by V.E. Zakharov and A.B. Shabat [41–43], V.E. Zakharov and A.V. Mikhailov [40], and also by M. Ablowitz, D. Kaup, A. Newell, and H. Segur [103] and V.E. Zakharov and S.V. Manakov [38]. Solutions to nonlinear equations that were of no lesser interest than the Korteweg–de Vries equation were determined using this method.

As interest in solitons grew, interest in nonlinear waves in rods, as one of the objects most suitable for experimental investigation and at the same time used widely in technology, arose [2, 3, 15, 72].

A rod is commonly understood as a deformable solid with its two dimensions being small in comparison with the third one and with a finite rigidity in tension, torsion, and bending. Normal modes excited in rods are divided into three types: longitudinal, torsional, and flexural modes. In the linear approximation, different types of waves propagating in straight rods do not interact.

LONGITUDINAL WAVES IN RODS

The classical model by D. Bernoulli (the technological theory) presumes that, in describing the longitudinal vibrations of a rod, it is possible to ignore the potential energy of shear strain and the kinetic energy of the transverse motion of the rod particles. According to this theory, linear waves in rods propagate with the velocity $c_0 = \sqrt{E/\rho}$ (where E is the Young's modulus and ρ is the density of the material), which does not depend on frequency. Therefore, the adopted assumptions do not allow us to describe the geometric dispersion of longitudinal waves that is observed experimentally.

The mathematical models proposed by J. Rayleigh and A. Love, R. Bishop, R. Mindlin, and J. Hermann (the refined theories) [3] eliminate this disadvantage.

1063-7710/02/4806-0643$22.00

Considering one-dimensional models, the Mindlin–Hermann model describes the dispersion of longitudinal waves in a wide frequency band most accurately.

Accounting for the nonlinearity of the relation between strains and displacement gradients (geometric nonlinearity) and strain and stress (physical nonlinearity) leads to a nonlinear generalization of the aforementioned mathematical models.

Under certain conditions, the Korteweg–de Vries equation is suitable for the description of nonlinear longitudinal waves in rods:

$$v_t + 6vv_x + v_{xxx} = 0, \quad (1)$$

where $v = u_x$, u is the longitudinal displacement of the particles of the median line, x is the dimensionless coordinate, and t is the dimensionless time. (Here and below, the subscript letter denotes the differentiation with respect to the corresponding independent variable.) This was first demonstrated by G.A. Nariboli [114]. Later, the dissipation effects were taken into account, and the generalized Burgers–Korteweg–de Vries equation, which describes the influence of dispersion and dissipation on the waves of small but finite amplitude in viscoelastic rods and plates, was derived by G.A. Nariboli and A. Sedov [115]:

$$v_t + \frac{n}{2}\frac{v}{t} + \alpha vv_x - \beta v_{xx} - \gamma v_{xxx} = 0, \quad (2)$$

where α, β, and γ are the parameters describing the effects of nonlinearity, dissipation, and dispersion; n = 0, 1, and 2 for plane, cylindrical, and spherical waves, respectively. The case of a spherical wave was presented only for generality, and it is not considered in this paper. The Korteweg–de Vries equation was obtained in [114, 115] by the perturbation method in several small parameters from an exact set of equations of the theory of elasticity that describes nonlinear waves in a circular rod.

The ideas of the perturbation method are also used in a book by Yu.K. Engelbrecht and U.K. Nigul [102] proceeding from complex equations of motion to simple ones (in particular, the Korteweg–de Vries equation); specifically, the authors use the ideas of the ray method. For example, in the model of a viscoelastic rod, the transfer equation of the first order has the form of the Burgers–Korteweg–de Vries equation.

L.A. Ostrovskiĭ and A.M. Sutin [76, 77] considered the propagation of longitudinal waves in a homogeneous rod made from a nonlinearly elastic material with the internal energy being a function of the invariants of the strain tensor with an accuracy up to the cubic term inclusive. They demonstrate that the evolution of the longitudinal component of the displacement vector is described by the equation (the nonlinear generalization of the Rayleigh–Love model or the nonlinear Boussinesque equation)

$$u_{tt} - u_{xx} - u_xu_{xx} - u_{xxtt} = 0. \quad (3)$$

The simplification method developed by one of the authors for sets of equations with small nonlinearity and dispersion was applied to this equation [75]. In the case of small nonlinearity and dispersion, this equation is reduced to the Korteweg–de Vries equation.

I.A. Molotkov and S.A. Vakulenko [69, 14] considered a rod with a density and a Young's modulus changing slowly along the median line. The perturbed Korteweg–de Vries equation for the longitudinal velocity of rod particles was solved using the perturbation method. Expressions for the amplitude and velocity of a perturbed soliton were obtained. The solution is the soliton kernel localized in a small spatial region with the soliton tail of an almost constant value following it.

An approximate solution to the perturbed Korteweg–de Vries equation was determined more rigorously using the asymptotic method of operation [110] by A.M. Samsonov and E.V. Sokurinskaya [85, 87, 90, 122]. They studied the wave propagation in rods with continuously varying elastic properties: rods with varying cross section, Young's modulus, Poisson's ratio, and nonlinear parameter were considered, and asymptotic and numerical solutions to the problem of evolution of solitons in these rods were determined. A satisfactory coincidence of numerical and asymptotic solutions was obtained. More exact expressions for the amplitude and velocity of a soliton than those by Molotkov and Vakulenko were derived. Interesting behavior of the solution is observed at certain relations between the nonlinear parameter β and the Young's modulus E, namely: at β^2E^3 = const, the amplitude and energy of a soliton do not change. At β^4E^3 = const, the amplitude of a soliton changes but the plateau after the soliton is not formed. It was noticed that, when the material hardens (E increases), the soliton loses mass and energy, and when the material softens (E decreases), the amplitude and energy can increase infinitely, which may lead to irreversible deformations.

V.I. Erofeev and A.I. Potapov [36] proposed a technique for reducing the three-dimensional equations of the nonlinear theory of elasticity to the approximate equations of the theory of rods, which was based on the approximation of motion in the rod cross section and the application of the Hamilton–Ostrogradski variation principle. The nonlinear equations generalizing the Bishop and Mindlin–Hermann models were obtained. The first of these equations has the form

$$u_{tt} - c_0^2\left(1 - \frac{6\sigma}{E}u_x\right)u_{xx} - \nu^2 r_p(u_{tt} - c_\tau^2 u_{xx})_{xx} = 0, \quad (4)$$

where $\alpha = \frac{E}{2} + \frac{\nu_1}{6}(1 - 6\nu) + \nu_2(1 - 2\nu) + \frac{4}{3}\nu_3$ is the coefficient characterizing the geometric and physical nonlinearities of the rod, $c_\tau = \sqrt{\mu/\rho}$ is the propagation velocity of an elastic shear wave in the material, μ is the shear modulus, ν is the Poisson's ratio, and r_p is the polar radius of inertia of the rod cross section.

A.M. Samsonov and E.V. Sokurinskiĭ [84, 86, 89, 91, 92, 121] investigated rigorously Eq. (4) rewritten using the displacement gradients

$$v_{tt} - v_{xx} = \varepsilon(6v^2 + v_{tt} - bv_{xx})_{xx}, \qquad (5)$$

where $b = (2(1+\nu))^{-1} < 1$ and $\varepsilon < 1$ is the small parameter of the problem. The authors called Eq. (5) "an equation with two dispersions." The allowable values of velocities, i.e., the values at which the propagation of a solitary wave is possible, lie within the intervals $(0, c_\tau)$ and (c_0, ∞), and, therefore, Eq. (5) allows "subsonic" solitons as solutions apart from the solutions of the type of "supersonic" strain solitons, the existence of which (but with different parameters) follows from the analysis of the solutions to the Korteweg–de Vries equation. The condition of balance between nonlinearity and dispersion that provides the existence of a localized quasistationary solution to Eq. (5) differs fundamentally from the analogous condition for the Korteweg–de Vries and Boussinesque equations, because it connects all the parameters of the solution rather than only the amplitude and width of a pulse. This can be explained by the different dispersion properties of these equations and, in particular, by the fact that the dispersion terms in the equation can even compensate each other at the velocity close to the velocity of a shear wave, after which the balance of nonlinearity and dispersion becomes violated. Several conservation laws are determined for Eq. (5). According to [121], the reduction of Eq. (5) to the Korteweg–de Vries equation considerably narrows the class of the solutions and provides rough estimates for soliton parameters, which makes their experimental detection in rods more difficult.

The major part of the paper by G.V. Dreiden, Yu.I. Ostrovskiĭ, A.M. Samsonov, I.V. Semenova, and E.V. Sokurinskaya [17] is devoted to the experimental investigation of the formation and propagation of solitary waves in rods. According to them, as a result of the excitation of a compression pulse with pressure amplitude P_0 and length $\tau_0 = \dfrac{\lambda_0}{c}$ at the end of a rod of radius R, a localized plane wave with strain amplitude A, width λ, and velocity V can be formed at distance λ from the end of the rod:

$$l \approx (RV/4)(E/|\beta A|)^{3/2}, \quad |A| \approx P_0/E,$$

$$\lambda \approx RV(2 + 6(E-\mu)/|\beta A|)^{1/2},$$

$$V \approx c_0(1 + A\beta/3E)^{1/2},$$

where

$$\beta = 3E + 2A(1-2\nu^3) + 6B(1-2\nu+2\nu^2-4\nu^3) + 2C(1-2\nu)^3 = 3E + 2l(1-2\nu)^3 + 4m(1-2\nu)(1+\nu)^2 + 6n\nu^2$$

is the parameter of the material nonlinearity that depends on the elastic moduli of the second (E and ν) and third orders (A, B, and C are the Landau moduli and l, m, and n are the Murnaghan moduli).

Specific examples of calculating the parameters of solitary waves at a preset radius of the rod and a preset pressure of the initial pulse are given. Apparently, the authors were the first to generate a nonlinear solitary wave (soliton) of longitudinal strain in a solid waveguide (a polystyrene rod) from a primary shock wave and to detect it.

The same authors in [19] somewhat modified their experimental technique to increase the possibility of detecting the waves of interest in comparison with [17]. This provided an opportunity to observe not only the generation of a solitary wave but also its propagation at large distances and, therefore, to demonstrate experimentally that the wave really retains its form and the ratio of the amplitude to the wavelength, which allows one to call it a longitudinal strain soliton.

The paper [20] considers the problem on the soliton reflection from the end of a waveguide. Two cases of boundary conditions are examined for the "equation with two dispersions" that correspond to two types of fixation: free and fixed ends of a rod. Trying a solution in the form

$$u_0 = u_{01}(\xi, \tau) + u_{02}(\eta, \tau),$$

where $\xi = x + t$, $\eta = x - t$, and $\tau = \varepsilon t$, the authors arrive at two Korteweg–de Vries equations for u_{01} and u_{02},

$$2u_{1,\xi\eta} = 2u_{01,\xi\tau} - 2u_{02,\eta\tau} + \frac{\beta}{2E}((u_{01}^2)_{\xi\xi} + 2u_{01,\xi}u_{02,\eta} + (u_{02}^2)_{\eta\eta}) + \frac{\nu^2}{2}(u_{01,4\xi} + u_{02,4\eta}).$$

It is demonstrated that a solitary wave is reflected from the fixed end without changing its sign and shape, whereas it cannot be reflected from the free end and must vanish. The papers [20, 124] give the results of physical experiments on the reflection of a compression soliton from the end of a polystyrene waveguide. In the case of reflection of a solitary wave from a free end, a considerable reduction of the wave amplitude is observed, which, according to the authors, indicates the impossibility of the existence of a solitary tension wave in polystyrene. To obtain the conditions of fixation, the waveguide was glued to a massive brass plate. Experiments demonstrated that the soliton amplitude almost did not change after its reflection from the fixed end.

A.V. Porubov and A.M. Samsonov in [78] refined the hypotheses underlying the theory of propagation of a longitudinal strain wave in a nonlinearly elastic rod of a cylindrical shape, this hypothesis being based on nonlinear Eq. (5). The following relations for the axial u

and radial w components of the displacement vector along the x and r axes, respectively, were adopted:

$$u = U(x,t) + r^2V(x,t), \quad w = -r\nu U_x + r^3W(x,t),$$

where U, V, and W are the functions to be determined. At $V = W = 0$, these expressions are the record of the hypothesis of Love's plane sections, which was used to derive the equation with two dispersions. The form of the functions V and W is obtained from the condition of the zero values of the components of the Piola–Kirchhof tensor, $P_{rr}|_{r=a} = 0$ and $P_{rz}|_{r=a} = 0$, at the free surface of the rod:

$$V = \frac{1}{2}\nu U_{xx}, \quad W = -\frac{\nu^2}{2(3-2\nu)}U_{xxx}.$$

A refined "equation with two dispersions" for the longitudinal strain component $v = u_x$ is obtained:

$$U_{tt} - c_0^2 U_{xx} = \frac{1}{2}\left(\frac{\beta}{\rho}U^2 + \nu R^2(\nu-1)U_{tt} + \nu R^2 c_0^2 U_{xx}\right)_{xx}, \quad (6)$$

where β is the parameter of nonlinearity of the material, which depends on the elastic moduli of the second (E and ν) and third (l, m, and n) orders, and ν is the Poisson's ratio. The tangential stress component at the lateral surface of a rod is obtained within the framework of the refined theory: $\sigma_{rx} < 3.95R^3\mu\nu^2A/(3-2\nu)\lambda^3$; i.e., the value of the maximal stress σ_{rx} at the boundary decreases by a factor of $\frac{E}{|\beta A|}$ in comparison with its maximal value in the theory given in [84]. The refined model given by Eq. (6) differs little in the coefficient values from those obtained earlier, but this refinement can be of some importance for the estimation of the experimental parameters in the case of the observation of strain solitons in a nonlinearly elastic rod.

It is necessary to note that, apart from the general theory of perturbations for partial solutions of nonlinear equations [110, 128], which was used in [14, 69, 85, 87, 90, 92, 122], there exists the theory of perturbations for solitons that was developed using the method of the inverse scattering problem (here, we should note first of all the papers by V.I. Karpman and E.M. Maslov [50, 51] and also the paper by D. Kaup and A. Newell [109]). These methods provide an opportunity to derive the perturbed equations describing the evolution of the scattering data using the perturbation theory for a corresponding linear problem of scattering.

M.P. Soerensen, P.L. Christiansen, P.S. Lomdahl, and O. Scovgaard [126, 127] demonstrated that taking into account the terms of the fourth order in the expansion of the elastic energy density with respect to the invariants of the strain tensor and in the case of the nonlinear relation between the radial displacement u_{rad} and the longitudinal strain

$$u_{rad} = -\nu_1 r u_x - \nu_2 r u_x^2 - \nu_3 r u_x^3$$

(ν_1, ν_2, and ν_3 are the Poisson's ratios of the first, second, and third orders), the propagation of longitudinal nonlinear solitary waves is described by the modified refined Boussinesque equation

$$v_{tt} - v_{xx} \pm \frac{1}{3}(v^3)_{xx} + v_{xxtt} = 0 \quad (7)$$

and, with allowance for the terms of only the third order, by the refined Boussinesque equation

$$v_{tt} - v_{xx} + \frac{1}{2}(v^2)_{xx} + v_{xxtt} = 0. \quad (8)$$

The authors determined solutions of the solitary wave type to these equations [solutions in the form of an antisoliton and a breather exist also in the case of Eq. (7)]. In the numerical investigation of collisions of such solutions, their almost elastic behavior was discovered; i.e., the waves almost retained their shape and velocity but an additional radiation appeared. Collisions of a soliton and an antisoliton, joint propagation of a soliton and an antisoliton moving close to each other and with the same velocity in a breather-like state, and the collision of breathers for Eq. (7) were studied. It was demonstrated that, in the case of a quadratic nonlinearity, antisolitons either collapse or lead to singular solutions. The reflection and splitting of solitary waves in a rod with a varying cross section (the cross section varies continuously and in a jump), the reflection of solitary waves from a massive end, and also the explosion and collapse of an antisoliton in the case of the modified Boussinesque equation were studied numerically in [127]. The equations considered are almost integrable, and their solutions of the solitary wave type are not solitons in the strict sense. However, the solutions in the form of solitary waves with small amplitudes reveal the soliton behavior due to the fact that these equations can be reduced to completely integrable ones (the Korteweg–de Vries equation and the modified Korteweg–de Vries equation) in the case of small amplitudes.

P.A. Clarcson, R.J. LeVeque, and R. Saxton [106] obtained an equation for longitudinal waves in rods made from nonlinear incompressible or almost incompressible materials:

$$v_{tt} - v_{xx} \pm \frac{1}{p}(v^p)_{xx} + v_{xxtt} = 0, \quad (9)$$

where $p = 3$ or 5, depending on the parameters of the material. It was noted that even values of p are of interest when the rod material is known to be dynamically unstable globally. The authors called the last equation the Pochhammer–Cree equation. A collision of two solitary waves that represent the solutions to the nonlinear Pochhammer–Cree equation was studied numerically

for the case when these waves have the same parameters and move towards each other. It is necessary to note that the applicability of the models of a nonlinear incompressible material (the models by Mooney, Mooney–Rivlin, and others) seems to be rather limited. It is believed that these models can be used for rubberlike materials and polyvinylidene chloride.

A.I. Potapov and N.P. Semerikova [80] considered nonlinear longitudinal waves in a rod by taking into account the interaction of strain and temperature fields. The set of equations for the nonlinear dynamic problem of thermoelasticity has the form

$$\begin{aligned} u_{tt} - (1 + 6u_x)u_{xx} - \varepsilon(u_{tt} - bu_{xx})_{xx} &= -\alpha_T(T - T_0)_x, \\ T_t - \chi T_{xx} + \alpha(T - T_0) &= -\alpha_T u_{xt}, \end{aligned} \tag{10}$$

where T and T_0 are the dimensionless values of the current and ambient temperatures; $\varepsilon < 1$ is the small parameter; α_T, α, and χ are the dimensionless coefficients of thermal expansion and heat exchange and the thermal diffusivity, respectively; and $b = (2(1 + \nu))^{-1} < 1$. If we differentiate the first equation of the set with respect to x and write it as an equation in the longitudinal strain $v = u_x$, it will differ from Eq. (5) only by the presence of the term describing the thermal expansion. Based on the analysis of Eqs. (10), it was demonstrated that convective heat transfer leads to the dissipation of the longitudinal wave energy, which is typical of the model of a viscoelastic material with an aftereffect and a relaxation. An equation for the amplitude variation of a traveling wave was obtained, and the attenuation laws for quasi-harmonic and cnoidal waves and solitons were determined.

I.V. Miloserdova and A.I. Potapov studied nonlinear longitudinal waves in a rod of finite length with rigidly fixed ends [66]. The boundary problem was solved for the same equation as in [77]. An approximation (which is often called a single-wave approximation) was used that considers two stationary waves moving towards each other with the effect of nonlinearity taken into account in two stages. At first, the interaction of contradirectional waves is not taken into account and only the effects of nonlinearity and dispersion for one wave are considered. The solutions to the equation of single-wave approximation are expressed in terms of elliptical functions. It is presumed that contradirectional waves do not interact in the first approximation in a system with a quadratic nonlinearity. The soliton solutions obtained in [77] cannot exist in this case.

Despite the developed analytical theory that provides a fundamental possibility to determine nonstationary solutions to completely integrable equations with the help of the method of the inverse scattering problem, the problem of numerical algorithms for the Korteweg–de Vries equation and other completely integrable equations seems important, because, in the case of arbitrary initial data, it is hardly possible to obtain a solution in a closed form using analytical techniques. Such predictor–corrector schemes as the Lax, Lax–Wendrof, and McCormack schemes are used for numerical investigation of the Korteweg–de Vries and Boussinesque–Korteweg–de Vries equations. These difference schemes distort the monotonic solutions because of the frequency dispersion. However, they may be used in solving the Korteweg–de Vries and Boussinesque–Korteweg–de Vries equations if the step in the spatial coordinate is selected in such way that the numerical dispersion is considerably smaller than the physical one. Three-level explicit schemes that are quite simple and convenient for realization are also used. Semispectral and spectral techniques are used as well to solve the Korteweg–de Vries and Boussinesque–Korteweg–de Vries equations. In the spectral method, the desired solution is expanded into a harmonic series. The substitution of this series into the initial equation produces an infinite set of equations for harmonic amplitudes. The maximal wave number with a fitted value is introduced to make the set finite. These techniques can provide a good accuracy, but they are much more complicated than finite-difference methods and inefficient from the point of view of computer time. A review of numerical techniques with a detailed description of physical models, algorithms, and calculation results is given by Yu.A. Berezin [7], along with a large number of references on numerical simulation. There are papers where numerical investigations of the Korteweg–de Vries and Boussinesque–Korteweg–de Vries equations are the basic means for studying nonlinear wave processes in rods. However, the effects noted in these papers are not characteristic (i.e., inherent in rods only). A paper by A. Nakamura [113] is an example of this. This paper studies the soliton propagation in a thin rod made of fused quartz.

A paper by A.M. Samsonov, G.V. Dreiden, A.V. Porubov, and I.V. Semenova [125] analyzes theoretically the evolution of a solitary wave of longitudinal strain and presents experimental data on a nonlinearly elastic cone like rod. A soliton focusing in a rod with a decreasing cross section, which is observed experimentally, is predicted. An asymmetric deformation of a soliton in the process of focusing is observed. An approach to the determination of analytical relations between longitudinal and shear nonlinear strains is developed in the paper, and an asymptotic solution exactly satisfying the boundary conditions at the lateral surface of a rod is determined. An exact expression for the soliton amplitude depending on the change of the radius of the rod cross section is obtained. It is demonstrated that an allowable interval of soliton velocities exists and depends on the elastic properties of the rod. It is shown experimentally that an elastic strain soliton is not absorbed even at distances greater than the typical length of linear damping of a wave in polystyrene.

Papers [88, 117] treat the propagation of nonlinear longitudinal solitary strain waves in a cylindrical rod that is in contact with an external elastic and viscous (antiviscous) medium. A.M. Samsonov and E.V. Sokurinskaya [88] use the refined Winkler–Pasternak model

as the model of an elastic medium. According to this model, the effect of the surrounding medium can be presented as the result of the work of elastic springs for compression and shear, and in [117] the response to shear is assumed to be zero. A nonlinear equation for longitudinal strain waves is derived. In the case of an elastic medium, this equation coincides with the already known "equation with two dispersions" but with the increased linear "rod-type" and decreased shear velocities. In the case of a viscous (active) medium, the term v_{txx} appears in the equation. Unlike the case of a free rod, the external medium can change the type of the strain soliton. An approach to possible experimental determination of the Murnaghan elastic moduli of the third order is proposed.

V.I. Erofeev, N.V. Klyueva, and N.P. Semerikova [32, 33] examined the nonlinear mathematical model describing longitudinal vibrations of a rod taking into account shear strains and transverse motions of particles of the median line (the nonlinear generalization of the Mindlin–Hermann model). Specific features of the propagation of stationary strain waves, i.e., periodic waves and solitons, were studied. The interdependences of the basic parameters of such waves (the wave amplitude, the wavelength, the propagation velocity, and the coefficient of nonlinear distortion of the wave form) were obtained. It is demonstrated that the anomalous behavior of solitons (the wave amplitude decreases with increasing velocity) can also be observed together with their classical behavior (a wave with a large amplitude has a smaller width and propagates with greater velocity).

S.A. Rybak and Yu.I. Skrynnikov [83] demonstrated that the propagation of nonlinear waves of longitudinal strain in a rod with a constant curvature can be described by the Klein–Gordon equation of the form

$$v_{tt} - c_0^2 v_{xx} + \frac{c_0^2}{R^2} v = \frac{\alpha}{2\rho}(v^2)_{xx}, \qquad (11)$$

where R is the curvature radius. Transverse motions, which are connected with longitudinal ones in curvilinear rods already in the linear approximation, are ignored. A solution in the form of a solitary stationary wave is obtained. The soliton of Eq. (11) has a parabolic profile in the vicinity of the peak, and its tails decreasing at infinity have the same structure as the tails of the Korteweg–de Vries soliton. The soliton width is $\Delta \sim \sqrt{A}$ (where A is the amplitude). The influence of dissipation on the properties of the solitons described by Eq. (11) was analyzed by Yu.I. Skrynnikov [92].

N.N. Myagkov [70] studied the propagation of longitudinal elastic-plastic waves in a rod. The rod was in the state called strain softening (a decrease in stress at an increase in strain). Such behavior precedes fracture for a wide class of materials (metals, concrete, geomaterials, etc.). A model, where the yield function depends not only on stress and strain but also on the strain gradient of the second order, is examined:

$$\frac{\partial \varepsilon}{\partial t} = \frac{\partial V}{\partial x}, \quad \frac{\partial V}{\partial t} = \frac{d\sigma_s(\varepsilon)}{d\varepsilon}\frac{\partial \varepsilon}{\partial x} - \delta^2 \frac{\partial^3 \varepsilon}{\partial x^3}, \qquad (12)$$

where ε is the total strain, V is the velocity, and $\sigma_s(\varepsilon)$ is the stress–strain diagram of the material (it is assumed to be quadratic). The quantity δ is a small dimensionless parameter whose introduction provides an opportunity to regularize the model, since attempts to describe the softening by using models that are insensitive to the strain rate lead to the loss of hyperbolicity of the set of equations and to an incorrect statement of the Cauchy problem. Exact solutions to the set obtained from Eq. (12) for the strain increments (ε') are constructed with the help of the Hirota transformation. Such solutions are nonstationary solitary waves, the evolution of which describes the process of strain localization in a softening rod, which originates from a smooth initial perturbation and ends in collapse.

In many cases, rods operate within the limits of linear-elastic behavior of a material, and only the boundary fixations are nonlinear (e.g., the presence of gaps or arresters in detail joints). I.V. Miloserdova, A.A. Novikov, and A.I. Potapov [65, 67, 68] demonstrated that nonlinear stationary strain waves with a wide frequency spectrum and properties similar to the properties of waves in rods with distributed elastic nonlinearity can exist in such systems in the presence of internal resonances.

V.V. Kazhaev [45, 46] presented the results of analog and numerical simulation of nonstationary wave processes that occur in rods with nonlinear-elastic fixation and include the effects of the decay of the initial perturbation into solitons, the exchange interaction between solitons, and the phenomenon of recovery.

FLEXURAL WAVES IN RODS

Unlike longitudinal waves, flexural waves in a rod have a strong dispersion. According to the Bernoulli–Euler model (the technological theory), the frequency of a harmonic wave is proportional to the square of the wave number. Therefore, the dispersion has an anomalous character. The group velocity is two times greater than the phase velocity at any frequency.

The propagation of flexural waves in a nonlinearly elastic rod is described by the equation (the geometric nonlinearity is taken into account)

$$w_{tt} + w_{xxxx} = \frac{1}{2}(w_x^3)_x. \qquad (13)$$

Here, the dimensionless variables $x' = x/r_y$, $t' = c_0 t/r_y$, and $w' = w/r_y$ are introduced, where r_y is the axial radius of inertia of the cross section. The primes in Eq. (13) are omitted.

V.I. Erofeev [25] analyzed the nonlinear stationary waves of envelopes, which arise in the process of propagation of quasi-harmonic flexural waves in a rod. A transition from Eq. (13) to two coupled nonlinear Schrödinger equations is performed using the method of coupled normal modes [74]. One of these equations has the form

$$i\frac{\partial U}{\partial t} - \frac{\partial^2 U}{\partial x^2} + \frac{1}{2}(U - U^*)|U - U^*|^2 = 0, \qquad (14)$$

and the second one is a complex conjugate of Eq. (14) (U^* is the complex conjugate of U). The functions U and U^* are connected with the transverse displacement w by the relations

$$\frac{\partial w}{\partial t} = -\frac{\partial}{\partial x}(U + U^*), \quad \frac{\partial w}{\partial x} = i(U^* - U).$$

The amplitude variation of a quasi-harmonic wave $U = Ae^{i(\omega t - kx + \psi)}$ + c.c. is described by the equation of an anharmonic oscillator

$$\frac{d^2 A}{d\xi^2} + \frac{V^2}{4}A - \frac{3}{2}A^3 - d^2 A^{-3} = 0.$$

It is stated that the equation has a soliton solution at $|d| = V/18\sqrt{3}$, where V is the velocity of a stationary wave. All parameters of the soliton can be expressed through the strain wave amplitude at the rod boundary (a_0). The soliton velocity is proportional to the first power of a_0, $V = 3\sqrt[4]{3}\,a_0$, and its amplitude is proportional to the square of this quantity, $A_0 = \frac{3\sqrt{3}}{2}a_0^2$. The soliton width is determined by the expression $\Delta = 2/3\sqrt[4]{3}\,a_0$.

V.I. Erofeev [23] investigated nonlinear flexural oscillations of a rod when the points of its median line perform motions in two mutually perpendicular planes. Helicons in an infinite rod (in particular, the solitons of helicon envelopes) and circularly polarized vibrations of a finite-length rod were studied.

A model of flexural vibrations of a physically nonlinear rod is proposed in a book by G. Kauderer [52]:

$$w_{tt} + \alpha w_{xxxx} = -\alpha^2\lambda[w_{xxxx}(w_{xx})^2 + 2(w_{xxx})^2 w_{xx}], \qquad (15)$$

where $w(x, t)$ is the deflection of the point x of the rod axis at the moment t, and α and λ are some constants containing geometric and elastic characteristics of the rod. Stationary wave solutions to this equation were investigated by A.A. Berezovskiĭ and Yu.V. Zhernovoĭ [8].

A.K. Abramian, D.A. Indejtsev, and S.A. Vakulenko [104] considered the propagation of a soliton in a nonlinear rod being in contact with an ideal compressible liquid. The soliton propagating along a rod contacting a liquid was interpreted as a "moving inclusion." Analytical solutions for solitary waves were determined. Two cases were examined: when the soliton velocity was greater than the velocity of acoustic waves in the liquid and when the soliton velocity was smaller than the sound velocity in the liquid. In the first case, the liquid cannot be involved in the soliton motion and large resistance forces arise. A soliton loses its velocity rather fast in this case. In the second case, a soliton moving along a beam causes the liquid to move as well, while the motion of the liquid has little effect on the soliton motion.

V.I. Erofeev, V.V. Kazhaev, and N.P. Semerikova [27, 28, 107] studied the specific features of nonlinear flexural wave propagation in Timoshenko's rod. The equations describing the dynamics of such a rod with allowance for the geometric and physical nonlinearities were obtained in [24]:

$$\begin{aligned}
&\rho F w_{tt} - \aleph\mu F(w_{xx} - \varphi_x) = [2\alpha_2 J_2 w_x \varphi_x^2 + 4\alpha_3 F w_x^3 \\
&+ 2\alpha_4 F\varphi^2 w_x + \alpha_5 J_2 \varphi w_x^2 + 3\alpha_6 F\varphi w_x^2 + \alpha_6 F\varphi^3]_x, \\
&\rho J_2 \varphi_{tt} - E J_2 \varphi_{xx} + \aleph\mu F(\varphi - w_x) = [4\alpha_1 J_1 \varphi_x^3 \\
&+ 2\alpha_2 J_2 \varphi_x(\varphi^2 + w_x^3) + 2\alpha_5 J_2 \varphi\varphi_x w_x]_x - 2\alpha_2 J_2 \varphi\varphi_x^2 \\
&- 2\alpha_4 F\varphi w_x^2 - 2\alpha_3 F\varphi^3 - \alpha_5 J_2 w_x \varphi_x^2 - \alpha_6 F w_x^3 - 3\alpha_6 F\varphi^2 w_x,
\end{aligned} \qquad (16)$$

where $w(x, t)$ is the transverse displacement, $\varphi(x, t)$ is the rotation angle of the cross section, ρ is the volume density of the material, $J_1 = \iint_F z^4 dF$ and $J_2 = \iint_F z^2 dF$ are the axial moments of inertia, $\aleph$ is Timoshenko's coefficient, and α_j ($j = \overline{1–6}$) are the coefficients characterizing the geometric and physical nonlinearities of the medium. On the assumption of smallness of the rotation angles of the cross sections for long-wave processes, Eqs. (16) are reduced to a single equation. In the case of stationary waves, it takes the form of the Duffing equation. Conditions for the appearance of the modulation instability of quasi-harmonic waves that leads to their self-modulation and formation of stationary waves of envelopes were analyzed in [27]. Timoshenko's model is not unambiguous in comparison with the Bernoulli–Euler model of flexural vibrations, where flexural waves are always stable. Quasi-harmonic flexural waves may be both stable and unstable, depending on the frequency and the corresponding dispersion branch of the elastic properties of the material. A diagram showing the regions of stability and instability on the dispersion curves is presented. Unlike [27], the main attention in [28] is given to the case when flexural waves have a high intensity and lie within the region of weak dispersion. It is demonstrated that qualitatively different wave patterns can be observed, depending on the value of the velocity. The expressions connecting the basic parameters of stationary waves (periodic waves and solitons) are determined: the wave ampli-

tude, the wavelength, the propagation velocity, and the coefficient of nonlinear distortions of the wave form. It is shown that the anomalous behavior of solitons can be observed in certain velocity ranges.

V.V. Kazhaev, A.I. Potapova, and N.P. Semerikova [47, 48] studied localized flexural stationary waves in a thin stretched rod:

$$w_{tt} - c_1^2(1 + \alpha w_x)w_{xx} - r_y(1 - \nu)(w_{tt} - c_2^2 w_{xx})_{xx} = 0, \quad (17)$$

where $c_1 = 2\varepsilon_0(\lambda + \mu)/\rho$ is the velocity of transverse waves in the rod, $c_2 = \left\{\frac{E}{2} + \varepsilon_0[3(\lambda + 2\mu) - (5\lambda + \mu)\nu]\right\}/(1 - \nu)$ is a quantity that has the dimension of velocity, λ and μ are the scale factors, ε_0 is the initial strain, and $\alpha = 3\varepsilon_0^{-1}$ is the coefficient of nonlinearity. Analytical and numerical investigations of this equation were conducted. An implicit three-level difference scheme with the approximation order $O(\tau^2, h^2)$ was used for numerical simulation. It is necessary to note that, at $C = \frac{c_2}{c_1} > 1$, the equation has an anomalous (positive) dispersion that gives rise to new nonlinear effects. Two regions of restricted solutions with qualitatively different behavior exist for stationary waves in the amplitude–velocity plane at $C > 1$. The solutions from the region of strongly nonlinear waves, nonexistent at amplitudes smaller than a certain critical value, were studied. Such waves are described by the expression

$$U(x, t) = \pm A\Delta \arctan\left[\sinh\left(\frac{x - Vt}{\Delta}\right)\right], \quad w_x = U(x, t),$$

and (as follows from the results of numerical investigation) in many cases behave like solitons but have some properties that differ from those of classical solitons. For example, in the case of collisions of contradirectional waves, the latter split producing secondary particle-like waves and a wave packet, if their amplitudes exceed a certain threshold value.

An experimental observation of the splitting of pulses with different polarity in the case of such collisions is described in a paper by A.I. Potapov and A.I. Vesnitsky [119].

The inclusion of the geometric nonlinearity leads not only to self-action of flexural waves but also to the interaction of flexural and longitudinal waves.

The resonance interactions of quasi-harmonic longitudinal and flexural waves in straight rods and circular resonators with the resulting formation of nonlinear waves of envelopes were studied in [26, 34, 56, 111].

Longitudinal-flexural waves in an elastic infinite rod were studied by A.A. Berezovskiĭ and Yu.V. Zhernovoĭ [9]. Periodic cnoidal wave solutions for the inflection $w(x, t) = w(kx - \omega t)$ and the longitudinal motion were determined in an explicit form using elliptical Jacobians. The corresponding dispersion relations connecting the wave number k, the frequency ω, and the amplitude parameter A were obtained.

A group of problems that stand somewhat apart deals with "forced nonlinear stationary waves," i.e., waves excited by loads moving along nonlinearly elastic guides. Some of these problems were examined in the dissertation by V.A. Bychenkov [13] and a paper by A.V. Metrikin [63].

TORSIONAL WAVES IN RODS

Torsional waves can also propagate in rods in addition to longitudinal and flexural waves. A special feature of torsional waves is the absence of dispersion of the zero mode; i.e., the phase and group velocities of this mode are equal to $c_\tau = \sqrt{\mu/\rho}$. This fact is the reason for the lesser interest expressed in nonlinear torsional waves.

I.V. Miloserdova derived an equation with cubic nonlinearity for nonlinear torsional waves in rods by taking into account warping effects:

$$\theta_{tt} - (1 + (\theta_x)^2)\theta_{xx} - (\theta_{tt} - C^2\theta_{xx})_{xx} = 0, \quad (18)$$

which is a generalization of the known nonlinear wave equations [64]. Here, θ is the dimensionless torsion angle. Equation (18) is also applicable to the case of nonlinear flexural waves in rods. Above, we already discussed the analytical and numerical investigation of this equation in [47, 48].

V.I. Erofeev, N.V. Klyueva, S.A. Monichev, and N.P. Semerikova [29–31] studied the influence of different moduli of the material and warping on the propagation of nonlinear torsional waves in a rod. A difference in the moduli due to the presence of material damage leads to the dominance of the square nonlinearity instead of the cubic one (the existence of a square nonlinearity for shear and torsional waves is forbidden by the classical theory of elasticity). The combined effect of cubic nonlinearity and dispersion caused by warping leads to the formation of solitons and stationary periodic waves. The interdependences of the basic wave parameters (the velocity, the amplitude, and the width for a soliton or the frequency for a periodic wave) and the material damage were determined. It was demonstrated that these dependences can serve as the basis for the development of an acoustic technique for testing the state of materials and structures.

WAVES IN PLATES

The propagation of solitary plane longitudinal waves in plates is described by the same equations as those used for describing similar processes in rods. Naturally, the coefficients of these equations are different [77, 115].

A.V. Martynov [61] studied longitudinal vibrations of a plate and demonstrated that, in the case of the propagation of a plane wave, the initial equations can be reduced to the sine-Gordon equation, which has solutions in the form of solitons.

One-dimensional quasi-harmonic flexural waves in a nonlinearly-elastic plate placed on a linearly elastic base were studied by D.Kh. Topchyan [97]. It was demonstrated that, for $kh < 0.3$ (where k is the wave number and h is the plate thickness), the stability of wave packets is observed, while for $kh > 0.3$, the modulation instability leading to the formation of stationary waves of envelopes takes place.

A.G. Bagdoev and L.A. Movsisyan [4–6] examined modulated waves in plates in the presence of geometric and physical nonlinearities. In this case, the physical nonlinearity is quadratic and (or) cubic. In the case of a quadratic nonlinearity, the instability of modulation is always present independently of the sign of the coefficient. The conditions when the cubic nonlinearity can lead to stability are determined.

L.A. Shenyavskiĭ determined two types of exact wave solutions to the following nonlinear equations for longitudinal-flexural vibrations of a plate [101]:

$$u_{tt} - c_0^2(u_{xx} + w_x w_{xx}) = 0,$$
$$w_{tt} + c_0^2\left[\frac{h^2}{12}w_{xxxx} - (w_x u_x)_x\right] = 0, \quad c_0^2 = \frac{E}{\rho(1-\nu^2)}. \tag{19}$$

These equations were obtained from the theory of thin flat shells with an infinite curvature radius. The solutions describing coupled longitudinal-flexural waves in Eqs. (19) at the propagation velocity $c > c_0$ have the form

$$w(\xi) = h\sqrt{\frac{a}{3}}\ln\frac{\mathrm{dn}(4\mathbf{K}\upsilon\xi) - k\,\mathrm{cn}(4\mathbf{K}\upsilon\xi)}{\sqrt{1-k^2}},$$

$$u(\xi) = \frac{2h^2\mathbf{K}\upsilon}{3c}\mathrm{zn}(4\mathbf{K}\upsilon\xi),$$

$$\upsilon = \frac{\sqrt{3}c^2}{2hc_0}\frac{1}{\sqrt{\mathbf{K}(\vartheta)\mathbf{E}(\vartheta)}}, \quad \vartheta = \frac{2\sqrt{\kappa}}{1+\kappa}$$

and at $c < c_0$,

$$w(\xi) = h\sqrt{\frac{-a}{3}}\arcsin[\kappa\,\mathrm{sn}(4\mathbf{K}\upsilon\xi)],$$

$$u(\xi) = \frac{2h^2\mathbf{K}\upsilon}{3c}\mathrm{zn}(4\mathbf{K}\upsilon\xi),$$

$$\upsilon = \frac{\sqrt{3}c^2}{2hc_0}\{\mathbf{K}(\kappa)[2\mathbf{E}(\kappa) - \mathbf{K}(\kappa)]\}^{-\frac{1}{2}},$$

where h is the plate thickness; zn is the zeta function; sn, cn, and dn are the elliptical Jacobians; κ is the modulus of the elliptical function; **K** and **E** are the complete elliptical integrals of the first and second kinds, respectively; and $\xi = t - x/c$. Coupled longitudinal-flexural waves are completely determined by two parameters, e.g., by the propagation velocity c and the modulus κ. The frequency of oscillations of the longitudinal component u is twice the frequency of oscillations of the flexural component w. At $c > c_0$, nonlinear coupled longitudinal-flexural waves degenerate into a purely longitudinal wave. The dependences of the propagation velocities of longitudinal-flexural waves on frequency for different amplitude values of the flexural components were calculated.

An important difference in the problem statement for nonlinear waves in plates is the question of the stability of plane waves with respect to transverse perturbations. It is not evident that the soliton existing in a rod will exist in a plate. The problem is that, in two-dimensional systems, transverse perturbations can destroy an unstable solitary wave. A paper by O.I. Bogoyavlenskiĭ [10] may be an example. This paper studied the interaction of long waves propagating along one coordinate axis together with the simple Riemann waves propagating in the transverse direction. It was demonstrated that, in the case of such an interaction, the soliton solutions turn over. V.E. Zakharov, E.A. Kuznetsov, and A.M. Rubenchik [129] demonstrated for the Kadomtsev–Petviashvili equation that solitary and periodic stationary waves in a medium with negative dispersion are stable with respect to transverse perturbations. The situation with waves with positive dispersion is entirely different. Here, a one-dimensional soliton is unstable with respect to transverse perturbations.

The presence of one more spatial variable makes plane waves no more characteristic of plates and shells. Even if, at the initial moments, the wave front in an infinite plate is close to a straight line, it becomes distorted with time because of the diffraction divergence. The competition of nonlinearity, dispersion, and diffraction gives rise to new effects, such as self-focusing.

A.I. Potapov and I.N. Soldatov [82] derived two-dimensional equations for longitudinal vibrations of a plate taking into account the geometric and physical nonlinearities. The propagation of a weakly divergent beam of nonlinear longitudinal waves in a plate was investigated, and it was demonstrated that, in this case, the longitudinal strain component satisfies the Kadomtsev–Petviashvili equation

$$\frac{\partial}{\partial\xi}(\psi_x + \alpha\psi\psi_\xi - b\psi_{\xi\xi\xi}) = -\gamma\psi_{\eta\eta}, \tag{20}$$

and two-dimensional solitons can propagate in plates. (Here, $\psi = u_{0\xi}$ is the longitudinal strain component.) It was noted that the influence of the boundary conditions (i.e., the fact that the beam propagates in a plate and not in an infinite medium) manifests itself in the values of the nonlinearity coefficients and in the diffraction

divergence in addition to the fact that a dispersion term is present in the equation.

Equations for waves of nonlinear longitudinal strain in plates made of incompressible Mooney's material and compressible Murnaghan's material are given in a paper by E.V. Sokurinskaya [94]. It was demonstrated that, using the function of strain $f = u_x$ (u is the displacement along the direction of wave propagation in the median plane of the plate), these equations can be reduced to the form

$$f_{\theta\theta} + a f^2 + 12bf = 0, \tag{21}$$

where $\theta = x \pm ky \pm Vt$, V, k = const, $a = \dfrac{72(k^2+1)}{(k^2+1)-4V^2}$, and $b = \dfrac{4(y^2-(k^2+1))}{\varepsilon(k^2+1)[(k^2+1)-4V^2]}$. The expressions for the coefficients a and b are given here for Mooney's material, while their form for Murnaghan's material is somewhat different. The last equation is reduced through a change of variables to the well-known Weierstrass equation, which can be solved in elliptical functions. The Weierstrass equation investigated explicitly in [84, 88] has a solution in the form of localized shocks and cnoidal and solitary waves. It is asserted that, unlike the description of two-dimensional nonlinear strain waves with the help of the Kadomtsev–Petviashvili equation in [84], which permits only compression solitons, the description of strain waves in a plate with the help of the Weierstrass equation is more general, because the last equation has a wider class of solutions including, in particular, the localized waves of not only compression but also tension.

Yu.S. Kivshar' and E.S. Syrkin [53] considered shear solitons in an elastic plate, and a nonlinear parabolic equation (the nonlinear Schrödinger equation) describing the dynamics of shear wave envelopes was derived. It was demonstrated that "light" or "dark" shear solitons with the parameters connected with the linear modes of an elastic plate can propagate in it, depending on its nonlinear properties. Shear solitons in an elastic plate were observed experimentally by M. Planat and M. Hoummady [116].

The results of the experiments on the excitation of a localized nonlinear wave of longitudinal strain that can propagate retaining its form in an elastic polystyrene plate are given in a paper by G.V. Dreiden, A.V. Porubov, A.M. Samsonov, and I.V. Semenova [19]. A setup analogous to that used in the experiments on the soliton excitation in rods served to generate a solitary wave [17, 19]. The amplitude of the longitudinal strain soliton was found to be 2.45 times smaller than in the case of a rod under the same excitation conditions. The soliton itself was a sufficiently long wave of a trough-shaped longitudinal compression, behind which no tension waves of any significant amplitude were observed.

WAVES IN SHELLS

The conditions for the appearance of a modulation instability of quasi-harmonic flexural waves in nonlinearly elastic cylindrical shells were studied in the papers by A.G. Bagdoev and L.A. Movsisyan [4, 5] already cited above.

The first experimental observation of the soliton of a flexural wave envelope in a thin metallic cylindrical shell was described by I. Rudnick, J. Wu, J. Wheatley, and S. Putterman [120].

M.D. Martynenko, Nguyen Dang Bik, and Fam Shi Vinh [59, 60] analyzed the existence conditions for solitons in nonlinearly elastic bodies and considered the problems of the propagation of elastic waves in moving cylindrical shells with allowance for the nonlinear effects caused by the influence of inertial forces.

The nonlinear resonance interactions of quasi-harmonic waves of various types in a thin-walled cylindrical shell were studied in the papers by D.A. Kovrigin [54, 55]:

(a) the parametric interaction of an axisymmetric wave with flexural waves propagating together in the longitudinal direction or in opposite circular directions;

(b) the cross-interaction of axisymmetric and non-axisymmetric waves that leads to the formation of a stationary wave;

(c) the self-modulation of an axisymmetric wave in the longitudinal direction.

It was demonstrated that three-frequency solitons of envelopes that represent modulated waves propagating in the longitudinal direction can be formed in both a straight rod and a shell.

The reduction of the equations of shell (and also rod and plate) dynamics to nonlinear evolutionary equations was performed in the dissertation by Yu.A. Chovnyuk [100].

Many problems of nonlinear wave dynamics of cylindrical shells are discussed in the papers by A.I. Zemlyanukhin and L.I. Mogilevich that were combined to form a mongraph [44]. The problems considered there include

(a) the derivation of the evolutionary equations simulating the propagation of longitudinal, shear, and flexural waves in nonlinearly elastic, nonlinearly viscoelastic, homogeneous, and inhomogeneous cylindrical shells;

(b) the determination of the classes of exact soliton and shock-wave solutions;

(c) the determination of the conditions at which the models are connected with the integrable technique of the inverse scattering problem;

(d) the theoretical-group analysis of nonlinear equations in partial derivatives and the mechanical interpretation of the invariant solutions.

CONCLUSION

In this review, attention was concentrated on the problems of propagation of strain solitons in the elastic elements of structures when the presence of dispersion was associated with the finiteness of the dimensions of the objects under consideration in the direction transverse to the direction of wave propagation, i.e., with the waveguide properties of the tested objects.

Another factor giving rise to a dispersion is the effect of the microscopic structure of materials. The analysis shows that the dispersion caused by the microstructure of a material and manifesting itself at much higher frequencies than waveguide dispersion can lead to the formation of strain solitons in the material in the presence of nonlinearity.

Various problems of nonlinear wave dynamics of solid media with a microscopic structure are discussed in the books by K.A. Naugol'nykh and L.A. Ostrovskiĭ [71], V.N. Nikolaevskiĭ [73], and V.I. Erofeev [22].

ACKNOWLEDGMENTS

This work was supported by the Russian Foundation for Basic Research, project no. 00-02-17337.

REFERENCES

1. M. Ablowitz and H. Segur, *Solitons and the Inverse Scattering Transform* (SIAM, Philadelphia, PA., 1981; Mir, Moscow, 1987).
2. *Aviation Acoustics*, Ed. by A. G. Munin (Mashinostroenie, Moscow, 1986), Vols. 1, 2.
3. I. I. Artobolevskiĭ, Yu. I. Bobrovnitskiĭ, and M. D. Genkin, *Introduction to Acoustic Dynamics of Engines* (Nauka, Moscow, 1979).
4. A. G. Bagdoev and L. A. Movsisyan, Izv. Akad. Nauk SSSR, Mekh. Tverd. Tela, No. 4 (1981).
5. A. G. Bagdoev and L. A. Movsisyan, in *Proceedings of XXII All-Union Conference on the Theory of Shells and Plates* (Akad. Nauk Arm. SSR, Erevan, 1980).
6. A. G. Bagdoev and L. A. Movsisyan, in *Problems of the Interaction Dynamics of Deformed Media* (Akad. Nauk Arm. SSR, Erevan, 1990), pp. 50–52.
7. Yu. A. Berezin, *Modeling of Nonlinear Wave Processes* (Nauka, Novosibirsk, 1982).
8. A. A. Berezovskiĭ and Yu. V. Zhernovoĭ, *Ukr. Mat. Zh.* **33** (4), 493 (1981).
9. A. A. Berezovskiĭ and Yu. V. Zhernovoĭ, Mat. Fiz. (Kiev), No. 30, 41 (1981).
10. O. I. Bogoyavlenskiĭ, *Overturning Solitons* (Nauka, Moscow, 1991).
11. *Solitons*, Ed. by R. K. Bullough and P. J. Caudrey (Springer, Berlin, 1980; Mir, Moscow, 1983).
12. P. Bhatnagar, *Nonlinear Waves in One-Dimensional Dispersive Systems* (Clarendon, Oxford, 1979; Mir, Moscow, 1981).
13. V. A. Bychenkov, Candidate's Dissertation in Physics and Mathematics (Gor'ki State Univ., Gor'ki, 1988).
14. S. A. Vakulenko, I. A. Molotkov, L. A. Ostrovskiĭ, and A. M. Sutin, in *Proceedings of VIII All-Union Symposium on Wave Diffraction and Propagation* (Inst. of Radio Engineering and Electronics, USSR Acad. Sci., Moscow, 1981), Vol. 2, p. 107.
15. *Vibrations in Engineering*, Ed. by V. V. Bolotin (Mashinostroenie, Moscow, 1978), Vol. 1.
16. R. K. Dodd, J. C. Eilbeck, J. Gibbon, and H. C. Morris, *Solitons and Nonlinear Wave Equations* (Academic, New York, 1982; Mir, Moscow, 1988).
17. G. V. Dreĭden, Yu. I. Ostrovskiĭ, A. M. Samsonov, *et al.*, Zh. Tekh. Fiz. **58** (10), 2040 (1988) [Sov. Phys. Tech. Phys. **33**, 1237 (1988)].
18. G. V. Dreĭden, Yu. I. Ostrovskiĭ, A. M. Samsonov, *et al.*, Pis'ma Zh. Tekh. Fiz. **21** (11), 42 (1995) [Tech. Phys. Lett. **21**, 415 (1995)].
19. G. V. Dreĭden, A. V. Porubov, A. M. Samsonov, and I. V. Semenova, Pis'ma Zh. Tekh. Fiz. **22** (21), 61 (1996) [Tech. Phys. Lett. **22**, 891 (1996)].
20. G. V. Dreĭden, A. V. Porubov, A. M. Samsonov, and I. V. Semenova, Zh. Tekh. Fiz. **71** (5), 1 (2001) [Tech. Phys. **46**, 505 (2001)].
21. B. A. Dubrovin, V. B. Matveev, and S. P. Novikov, Usp. Mat. Nauk **31** (1), 55 (1976).
22. V. I. Erofeev, *Wave Processes in Solids with Microstructure* (Mosk. Gos. Univ., Moscow, 1999).
23. V. I. Erofeev, Prikl. Mekh. **27** (9), 100 (1991).
24. V. I. Erofeev, in *Applied Problems of System Dynamics* (Gor'ki Gos. Univ., Gor'ki, 1983), No. 6, pp. 90–107.
25. V. I. Erofeev, Akust. Zh. **38**, 172 (1992) [Sov. Phys. Acoust. **38**, 89 (1992)].
26. V. I. Erofeev, V. V. Kazhaev, and A. I. Potapov, in *Waves and Diffraction* (Inst. Radiotekh. Élektron. Akad. Nauk SSSR, Moscow, 1981), Vol. 2, pp. 82–85.
27. V. I. Erofeev, V. V. Kazhaev, and N. P. Semerikova, in *Testing of Materials and Structures* (Intelservis, Nizhni Novgorod, 1996), pp. 180–187.
28. V. I. Erofeev, V. V. Kazhaev, and N. P. Semerikova, in *Applied Mechanics and Mechanical Engineering Technologies* (Intelservis, Nizhni Novgorod, 1997), No. 3, pp. 56–66.
29. V. I. Erofeev, N. V. Klyueva, S. A. Monichev, and N. P. Semerikova, in *Testing of Materials and Structures* (Intelservis, Nizhni Novgorod, 2000), No. 2, pp. 117–136.
30. V. I. Erofeyev and S. A. Monichev, J. Mech. Behav. Mater. **11** (1–3), 31 (2000).
31. V. I. Erofeev and N. V. Klyueva, Izv. Ross. Akad. Nauk, Mekh. Tverd. Tela (in press).
32. V. I. Erofeev, N. V. Klyueva, and N. P. Semerikova, Izv. Vyssh. Uchebn. Zaved., Prikl. Nelin. Din. **7** (4), 35 (1999).
33. V. I. Erofeev, N. V. Klyueva, and N. P. Semerikova, in *Applied Mechanics and Mechanical Engineering Technologies* (Intelservis, Nizhni Novgorod, 1998), No. 1(4), pp. 85–95.
34. V. I. Erofeev and A. I. Potapov, in *Dynamics of Systems* (Gor'ki Gos. Univ., Gor'ki, 1985), pp. 75–84.
35. V. I. Erofeev, A. I. Potapov, and I. N. Soldatov, Available from VINITI (Gor'ki Gos. Univ., Gor'ki, 1986), No. 5440-B 86.

36. V. I. Erofeev and A. I. Potapov, *Aerohydromechanics and the Theory of Elasticity* (Dnepropetr. Gos. Univ., Dnepropetrovsk, 1984), No. 32, pp. 78–82.
37. V. E. Zakharov, Zh. Éksp. Teor. Fiz. **65** (1), 219 (1973) [Sov. Phys. JETP **38**, 108 (1974)].
38. V. E. Zakharov and S. V. Manakov, Zh. Éksp. Teor. Fiz. **69** (5), 1654 (1975) [Sov. Phys. JETP **42**, 842 (1975)].
39. V. E. Zakharov, S. V. Manakov, S. P. Novikov, and L. P. Pitaevskiĭ, *Theory of Solitons: The Inverse Scattering Method* (Nauka, Moscow, 1980; Consultants Bureau, New York, 1984).
40. V. E. Zakharov and A. V. Mikhaĭlov, Zh. Éksp. Teor. Fiz. **74**, 1953 (1978) [Sov. Phys. JETP (1978)].
41. V. E. Zakharov and A. B. Shabat, Funkts. Anal. **13** (3), 13 (1979).
42. V. E. Zakharov and A. B. Shabat, Funkts. Anal. **8** (3), 43 (1974).
43. V. E. Zakharov and A. B. Shabat, Zh. Éksp. Teor. Fiz. **61** (1), 118 (1971) [Sov. Phys. JETP **34**, 62 (1971)].
44. A. I. Zemlyanukhin and L. I. Mogilevich, *Nonlinear Waves in Cylindrical Shells* (Saratov, 1999).
45. V. V. Kazhaev, Candidate's Dissertation in Physics and Mathematics (Nf IMASh RAN, Nizhni Novgorod, 1998).
46. V. V. Kazhaev, Izv. Vyssh. Uchebn. Zaved. Sev.-Kavk. Reg., Estest. Nauki, Special Issue: Mat. Model., 95 (2001).
47. V. V. Kazhaev, A. I. Potapov, and N. P. Semerikova, in *Wave Problems of Mechanics* (Nf IMASh RAN, Nizhni Novgorod, 1991), pp. 123–129.
48. V. V. Kazhaev, A. I. Potapov, and N. P. Semerikova, Izv. Vyssh. Uchebn. Zaved. Radiofiz. **38** (1–2), 100 (1995).
49. F. Calogero and A. Degasperis, *Spectral Transform and Solitons: Tools to Solve and Investigate Nonlinear Evolution Equations* (North-Holland, Amsterdam, 1982; Mir, Moscow, 1985).
50. V. I. Karpman, Zh. Éksp. Teor. Fiz. **77** (1), 114 (1979) [Sov. Phys. JETP **50**, 58 (1979)].
51. V. I. Karpman and E. M. Maslov, Zh. Éksp. Teor. Fiz. **75** (2), 504 (1978) [Sov. Phys. JETP **48**, 252 (1978)].
52. H. Kauderer, *Nichtlineare Mechanik* (Springer, Berlin, 1958; Inostrannaya Literatura, Moscow, 1961).
53. Yu. S. Kivshar' and E. S. Syrkin, Akust. Zh. **37**, 104 (1991) [Sov. Phys. Acoust. **37**, 53 (1991)].
54. D. A. Kovrigin, Preprint, Gf IMASh AN SSSR (Gor'ki, 1990).
55. D. A. Kovrigin, Candidate's Dissertation in Physics and Mathematics (Nf IMASh RAN, Nizhni Novgorod, 1992).
56. D. A. Kovrigin and A. I. Potapov, Dokl. Akad. Nauk SSSR **305** (4), 803 (1989) [Sov. Phys. Dokl. **34**, 330 (1989)].
57. G. L. Lamb, Jr., *Elements of Soliton Theory* (Wiley, New York, 1980; Mir, Moscow, 1983).
58. G. L. Lamb, *Elements of Soliton Theory* (Mir, Moscow, 1984) (Russian Translation).
59. M. D. Martynenko, Nguen Dang Bik, and Fam shi Vin, Dokl. Akad. Nauk BSSR **35** (4) (1991).
60. M. D. Martynenko and Nguen Dang Bik, Differ. Uravn. **26** (12) (1990).
61. A. V. Martynov, in *Selected Problems of Algebra, Geometry, and Discrete Mathematics* (Mosk. Gos. Univ., Moscow, 1992).
62. V. A. Marchenko, *Nonlinear Equations and Operator Algebra* (Naukova Dumka, Kiev, 1986).
63. A. V. Metrikin, Akust. Zh. **40**, 647 (1994) [Acoust. Phys. **40**, 573 (1994)].
64. I. V. Miloserdova, Available from VINITI (Gor'ki, 1983), No. 1796.
65. I. V. Miloserdova, A. A. Novikov, and A. I. Potapov, in *Waves and Diffraction* (IRÉ AN SSSR, Moscow, 1981), Vol. 2, pp. 118–121.
66. I. V. Miloserdova and A. I. Potapov, Akust. Zh. **29**, 515 (1983) [Sov. Phys. Acoust. **29**, 306 (1983)].
67. I. V. Miloserdova and A. I. Potapov, Izv. Akad. Nauk SSSR, Mekh. Tverd. Tela, No. 6, 178 (1980).
68. I. V. Miloserdova and A. I. Potapov, in *Dynamics of Systems* (Gor'ki Gos. Univ., Gor'ki, 1987), pp. 172–182.
69. I. A. Molotkov and S. A. Vakulenko, in *Interference Waves in Layered Media* (Nauka, Leningrad, 1980), pp. 64–73.
70. N. N. Myagkov, Mekh. Kompoz. Mater. Konstr. **5** (3), 28 (1999).
71. K. A. Naugol'nykh and L. A. Ostrovskiĭ, *Nonlinear Wave Processes in Acoustics* (Nauka, Moscow, 1990).
72. A. S. Nikiforov and S. V. Budrin, *Propagation and Absorption of Acoustic Vibration in Ships* (Sudostroenie, Leningrad, 1968).
73. V. N. Nikolaevskiĭ, *Fluid Mechanics and Fluid Dynamics* (Nedra, Moscow, 1996).
74. A. A. Novikov, Izv. Vyssh. Uchebn. Zaved., Radiofiz. **19** (2), 321 (1976).
75. L. A. Ostrovskiĭ and E. N. Pelinovskiĭ, Prikl. Mat. Mekh. **38** (1), 121 (1974).
76. L. A. Ostrovskiĭ and A. M. Sutin, Preprint No. 71, NIRFI (Radiophysical Research Inst., Gor'ki State Univ., 1975).
77. L. A. Ostrovskiĭ and A. M. Sutin, Prikl. Mat. Mekh. **41** (3), 531 (1977).
78. A. V. Porubov and A. M. Samsonov, Pis'ma Zh. Tekh. Fiz. **19** (12), 26 (1993) [Tech. Phys. Lett. **19**, 748 (1993)].
79. A. V. Porubov, in *Abstracts of Papers of 8th All-Russia Congress on Theoretical and Applied Mechanics* (Perm, 2001), p. 496.
80. A. I. Potapov and N. P. Semerikova, Prikl. Mekh. Tekh. Fiz., No. 1, 57 (1988).
81. A. I. Potapov and I. N. Soldatov, Prikl. Mekh. Tekh. Fiz., No. 1, 144 (1986).
82. A. I. Potapov and I. N. Soldatov, Akust. Zh. **30**, 819 (1984) [Sov. Phys. Acoust. **30**, 486 (1984)].
83. S. A. Rybak and Yu. I. Skrynnikov, Akust. Zh. **36**, 730 (1990) [Sov. Phys. Acoust. **36**, 410 (1990)].
84. A. M. Samsonov, Dokl. Akad. Nauk SSSR **299**, 1083 (1988) [Sov. Phys. Dokl. **33**, 298 (1988)].
85. A. M. Samsonov, in *Proceedings of II International Workshop on Problems of Nonlinear and Turbulent Processes in Physics* (Naukova Dumka, Kiev, 1985), Part 1, p. 219.

86. A. M. Samsonov, Preprint No. 1259 (Physicotechnical Inst., USSR Academy of Sciences, 1988).
87. A. M. Samsonov, Dokl. Akad. Nauk SSSR **277** (2), 332 (1984) [Sov. Phys. Dokl. **29**, 586 (1984)].
88. A. M. Samsonov and E. V. Sokurinskaya, Preprint No. 1293 (Physicotechnical Inst., USSR Academy of Sciences, 1988).
89. A. M. Samsonov and E. V. Sokurinskaya, Zh. Tekh. Fiz. **58** (8), 1632 (1988) [Sov. Phys. Tech. Phys. **33**, 989 (1988)].
90. A. M. Samsonov and E. V. Sokurinskaya, Preprint No. 983 (Physicotechnical Inst., USSR Academy of Sciences, 1985).
91. A. M. Samsonov and E. V. Sokurinskaya, in *Theory of Wave Propagation in Elastic and Elastoplastic Media* (IGD SO AN SSSR, Novosibirsk, 1987), pp. 28–32.
92. A. M. Samsonov and E. V. Sokurinskaya, Prikl. Mat. Mekh. **51** (3), 483 (1987).
93. Yu. I. Skrynnikov, Akust. Zh. **44**, 712 (1998) [Acoust. Phys. **44**, 620 (1998)].
94. E. V. Sokurinskaya, Pis'ma Zh. Tekh. Fiz. **20** (3), 36 (1994) [Tech. Phys. Lett. **20**, 105 (1994)].
95. *Solitons in Action*, Ed. by K. Lonngren and A. Scott (Academic, New York, 1978; Mir, Moscow, 1981).
96. L. A. Takhtadzhyan and L. D. Faddeev, *Hamiltonian Methods in the Theory of Solitons* (Nauka, Moscow, 1986; Springer, Berlin, 1987).
97. D. Kh. Topchyan, in *Problems of Interaction Dynamics of Deformed Media* (Akad. Nauk Arm. SSR, Erevan, 1987), pp. 270–274.
98. G. B. Whitham, *Linear and Nonlinear Waves* (Wiley, New York, 1974; Mir, Moscow, 1977).
99. *Physical Encyclopedia*, Ed. by A. M. Prokhorov (Sovetskaya Éntsiklopediya, Moscow, 1988–1998).
100. Yu. V. Chovnyuk, Candidate's Dissertation in Physics and Mathematics (KISI, Kiev, 1988).
101. L. A. Shenyavskiĭ, Prikl. Mat. Mekh. **43** (6), 1089 (1979).
102. Yu. K. Éngel'brekht and U. K. Nigul, *Nonlinear Strain Waves* (Nauka, Moscow, 1981).
103. M. J. Ablowitz, D. J. Kaup, A. C. Newell, and H. Segur, Phys. Rev. Lett. **31**, 125 (1973).
104. A. K. Abramian, D. A. Indejtsev, and S. A. Vakulenko, Flow Turbul. Combust., No. 61, 1 (1999).
105. J. Bejda, Arch. Mech. Stosow **29** (3), 477 (1977).
106. P. A. Clarcson, R. J. LeVeque, and R. Saxton, Stud. Appl. Math. **75** (2), 95 (1986).
107. V. I. Erofeyev and N. P. Semerikova, in *Proceedings of International Seminar on Wave Mechanical Systems* (Technologija, Kaunas, 1996), pp. 12–15.
108. C. S. Gardner, J. M. Greene, M. D. Kruskal, and R. M. Miura, Phys. Rev. Lett. **19**, 1095 (1967).
109. D. J. Kaup and A. C. Newell, Proc. R. Soc. London, Ser. A **361**, 413 (1978).
110. J. Kodama and M. Ablowitz, Stud. Appl. Math. **64**, 225 (1981).
111. D. A. Kovriguine and A. I. Potapov, Eur. J. Mech. A/Solids **15**, 1049 (1996).
112. P. D. Lax, Commun. Pure Appl. Math. **21**, 159 (1969).
113. A. Nakamura, in *Proceedings of XI International Symposium on Nonlinear Acoustics* (Novosibirsk, 1987), Part 1, p. 378.
114. G. A. Nariboli, J. Math. Phys. Sci. **4**, 64 (1970).
115. G. A. Nariboli and A. Sedov, J. Math. Anal. Appl. **32** (3), 661 (1970).
116. M. Planat and M. Hoummady, Appl. Phys. Lett. **55** (2), 103 (1989).
117. A. V. Porubov, A. M. Samsonov, M. G. Velarde, and A. V. Bukhanovsky, Phys. Rev. E **58** (3), 3854 (1998).
118. A. V. Porubov and M. G. Velarde, Wave Motion **31** (3), 197 (2000).
119. A. I. Potapov and A. I. Vesnitsky, Wave Motion **19**, 29 (1994).
120. I. Rudnick, J. Wu, J. Wheatley, and S. Putterman, in *Proceedings of XI International Symposium on Nonlinear Acoustics* (Novosibirsk, 1987), Part 2, p. 208.
121. A. M. Samsonov, in *Proceedings of International Conference on Plasma Physics* (Naukova Dumka, Kiev, 1987), Vol. 4, p. 88.
122. A. M. Samsonov, in *Nonlinear and Turbulent Processes in Physics*, Ed. by R. Z. Sagdeev (Gordon and Beach, New York, 1984), Vol. 2, pp. 1029–1035.
123. A. M. Samsonov, Appl. Anal. **57**, 85 (1995).
124. A. M. Samsonov, *Strain Solitons in Solids and How to Construct Them* (Chapman and Hall/CRC, London, 2001).
125. A. M. Samsonov, G. V. Dreiden, I. V. Porubov, and I. V. Semenova, Phys. Rev. B **57**, 5778 (1998).
126. M. P. Soerensen, P. L. Christiansen, and P. S. Lomdahl, J. Acoust. Soc. Am. **76**, 871 (1984).
127. M. P. Soerensen, P. L. Christiansen, P. S. Lomdahl, and O. Scovgaard, J. Acoust. Soc. Am. **81**, 1718 (1987).
128. T. Taniuti and C. C. Wei, J. Phys. Soc. Jpn. **24**, 941 (1968).
129. V. E. Zakharov, E. A. Kuznetsov, and A. M. Rubenchik, Preprint No. 199 (Inst. of Automation and Electrometry, USSR Academy of Sciences, 1983).

Translated by M. Lyamshev

Acoustical Physics, Vol. 48, No. 6, 2002, pp. 656–664. Translated from Akusticheskiĭ Zhurnal, Vol. 48, No. 6, 2002, pp. 741–750.

The Effect of the Subsurface Channel on the Insonification Rate of a Shadow Zone in a Deep Ocean

K. V. Avilov, A. V. Mikryukov, and O. E. Popov

Andreev Acoustics Institute, Russian Academy of Sciences, ul. Shvernika 4, Moscow, 117036 Russia

e-mail: po5791@aport.ru

Received December 3, 2001

Abstract—On the basis of the experimental data obtained in the tropical zone of the Indian Ocean with the use of explosive sources, the characteristics of signals that penetrate the shadow zone as a result of leakage from the subsurface channel are studied. The propagation velocity of these signals, the transformation of their spectrum due to the frequency-dependent transmission loss, the maximum of the correlation function, and the optimal frequency of the shadow zone insonification by these signals are determined. On the basis of computer modeling with a code realizing the wide-angle parabolic approximation, the effects of individual parameters of the medium on the energy leakage from the subsurface channel are estimated. The numerical results are reliably confirmed by the experimental data. © *2002 MAIK "Nauka/Interperiodica"*.

The solution of the problems of applied acoustics requires knowledge of the characteristics of both the total sound field and its individual components. In particular, this statement extends to sound signals that are weak against the background of the oceanic ambient noise. To such signals, we can assign those recorded in the geometric shadow zone of the deep ocean after their penetration there by the water paths (i.e., without bottom or surface reflections). In addition to the diffraction-caused penetration of sound through the boundary of the shadow zone [1], the appearance of water-path signals in the shadow zone can be caused by energy leakage from the subsurface channel [2] and by the reflection (or scattering) of sound from fine-structure inhomogeneities of the water medium [3]. Sound can also penetrate into the shadow zone through microchannels in the sound velocity profile [4].

In spite of the low energy content of these signals, it was found that the energy leakage from the subsurface channel at frequencies lower than the critical frequency is substantial, and a receiver placed in a shadow zone is reliably insonified at low frequencies [5]. It is also known that the acoustic energy that penetrates the second shadow zone due to the reflection by fine-structure inhomogeneities of the water medium can in some frequency range be comparable with the energy of the bottom-reflected signals [6]. In this connection, it is of interest to estimate the possibility of using the measured characteristics of these signals for both enhancing the efficiency of detection systems and obtaining the information on the medium.

The analysis of our experimental results obtained in various regions of the ocean showed that the use of high-power wide-band sources of the explosive type allows one to detect the aforementioned signals and to study their characteristics in detail. Below, we dwell on the results of the experiment carried out in the Indian Ocean (along 6° S), where the signals penetrating through the boundary of the geometric shadow zone were found to be most pronounced in the experimental records.

The experiment was carried out along a 50-km track at an ocean depth of 5000 m. The receiving ship with hydrophones lowered to depths of 350 and 3000 m was adrift at the initial point of the track. The transmitting ship was initially in the proximity of the receiving ship and began its motion dropping charges of a weight of 2.88 kg. The charges were exploded at depths of 195 m at spatial intervals of about 1.0 km. The state of the sea surface was estimated as Beaufort 3.

The results of the hydrological survey at the initial point of the track showed that a mixed water layer with the sound velocity at the sea surface $c_0 = 1541.1$ m/s and the weak positive gradient $g_1 = 0.010$ s^{-1} was observed within the depths from zero to 30 m. Below, a water layer with a steep negative gradient $g_2 = 0.616$ s^{-1} was located.

The sound propagation conditions were such that the lower hydrophone (3000 m) was located in the insonified zone, whereas the upper hydrophone (350 m), beginning from the first several kilometers, was located in the region where water-path rays do not penetrate (the so-called geometric shadow zone).

The shadow zone boundary (in the geometric acoustics approximation) is unambiguously determined only

1063-7710/02/4806-0656$22.00 © 2002 MAIK "Nauka/Interperiodica"

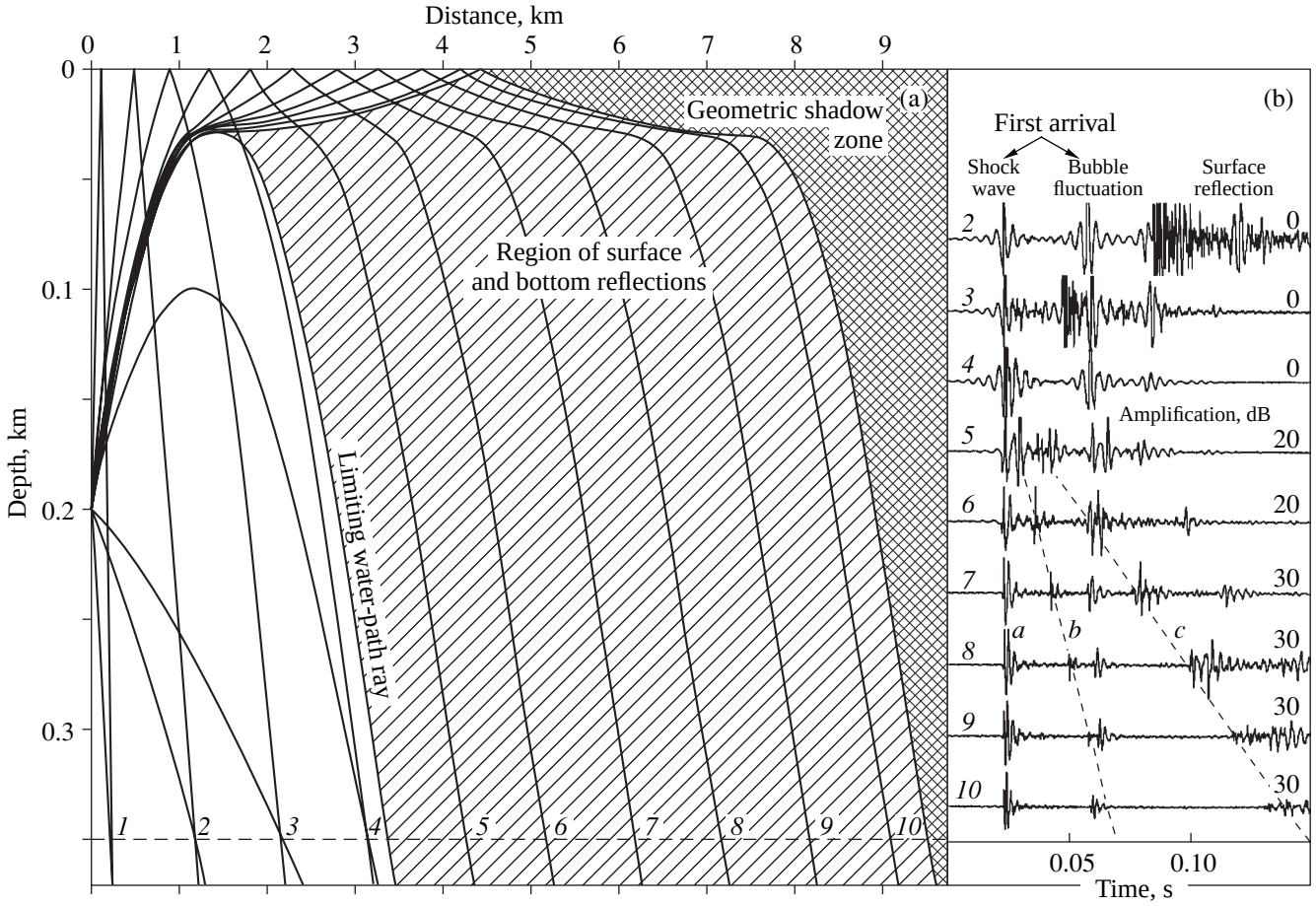

Fig. 1. (a) Ray pattern in the presence of the subsurface channel and the location of the transmitting ship at the instants of charge explosions *1–10*. (b) Records of the initial segments of the signals from explosions *2–10* recorded by the upper hydrophone. Records *5–10* exhibit the signal arrivals (*a*) from the subsurface channel; (*b*) due to the diffraction-caused sound penetration through the boundary of the shadow zone; and (*c*) due to the reflection from fine-structure inhomogeneities of the water medium.

in the case of the sound velocity profile with a negative gradient that begins directly from the ocean surface. It is described by the trajectory of the limiting water-path ray, i.e., the ray that has the upper turning point at the ocean surface. Given the subsurface channel in the ocean, the limiting water-path ray will have a turning point near the lower boundary of the channel, where it is split into two rays. One of them refracts downward, whereas the other penetrates the channel under the zero grazing angle. Strictly speaking, in this case, the boundary of the shadow zone is interpreted as the trajectory of this ray (Fig. 1a). At a small positive gradient in the subsurface layer, the distance travelled by this ray in the channel can be rather long (up to 7 km in the Indian Ocean). Thus, the interval of distances between the trajectory of the limiting water-path ray and the new boundary of the shadow zone will be additionally insonified by rays that are singly reflected from the surface. The amplitude of signals propagating along these rays must be very small due to the expansion of the ray tube, and their propagation times are very close to the propagation times of signals observed in the experiment. As a result, in the above-mentioned interval of distances, we obtain a ray pattern that, at first glance, is very close to the actual field observed in the ocean.

Nevertheless, a more detailed analysis of experimental data brings up the question of the validity of using the ray approximation for studying the real physical picture. This is caused by several facts. The first of them is the considerable discrepancy between the experimental data and the calculations by the ray theory in estimating the spectrum of signals recorded outside the reliably insonified region bounded by the trajectory of the limiting water-path ray.

Figure 1b shows the records of the initial segments (without bottom reflections) of signals from explosions *2–10* recorded by the upper hydrophone (z = 350 m). The first three signals (*2–4*) are direct and surface reflected signals recorded in the insonified zone. Their propagation paths in the ray approximation, including the signals from the first explosion, are shown in Fig. 1a. For the signal from explosion *5* (r = 4.2 km), the receiver is in the region where signals, in the ray approximation, cannot penetrate by the water paths,

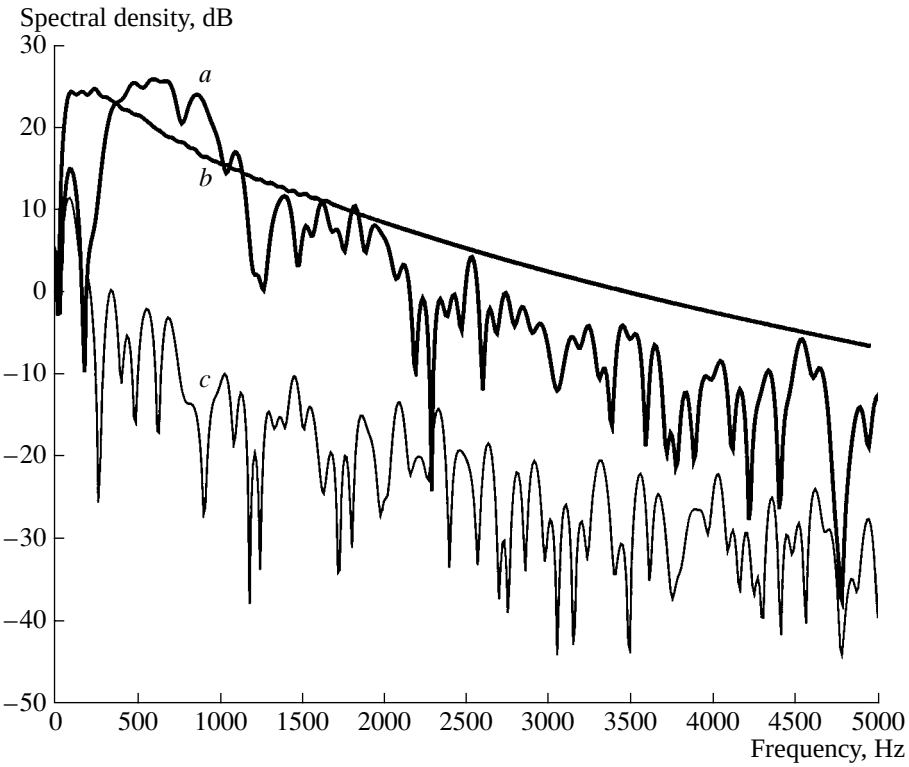

Fig. 2. Comparison of shock-wave spectra for (*a*) the signal from the subsurface channel (r = 8.15 km, z = 350 m) and (*b*) the water-path signal (r = 8.25 km, z = 3000 m); (*c*) the noise spectrum in the shadow zone.

and it begins to detect only low-energy signals (bottom reflections, as before, are not considered). As the distance increases, it becomes apparent that the signal recorded is not a single one but represents a superposition of signals of various nature and with individual characteristics: spectrum, propagation velocity, decay factor, etc. We identified these signals as those caused by (a) the presence of the subsurface channel, (b) the diffraction penetration of sound from the insonified zone, and (c) the reflection from fine-structure inhomogeneities of the water medium. In this paper, we mainly consider the signals from the subsurface channel.

Figure 2a shows the shock wave spectra of the signal under study, and Fig. 2b, the levels of ambient noise recorded by the upper hydrophone at a distance of 8.15 km from the source (explosion *9*) and their comparison with the spectrum of the shock wave of the water-path signal recorded by the lower hydrophone (3000 m) at a distance of 8.25 km. The difference (compensated in Fig. 2) in the spectrum levels of the signals presented in Figs. 2a and 2b exceeds 22 dB at a frequency of 500 Hz. The comparison of the spectra of the two signals reveals the lack of low frequencies in the spectrum of the signal from the subsurface channel. The maximum observed in the spectrum of this signal in a frequency range of 500–700 Hz corresponds to the frequency range corresponding to the maximal energy leakage from the subsurface channel at the given distance. As the distance increases, this maximum is shifted to the region of higher frequencies due to the frequency-dependent leakage of the energy from the channel. The disappearance of the low-frequency signals from the spectrum in Fig. 2a cannot be explained in the framework of the ray acoustics but is reliably illustrated by calculations with the wave theory [7] as the result of the waveguide propagation in the subsurface water layer.

In addition, computations with the wave theory (Fig. 3) and the experimental data (Fig. 4) testify that the sound propagation in a subsurface channel and the energy leakage from it into the underlying deep-water sound channel are observed up to distances that are much greater than classical geometric acoustics can explain. In order to make this theory consistent with the observed experimental data, one needs to introduce a rough boundary of the subsurface channel into the waveguide model. This boundary causes sound scattering, and the latter leads to the trapping of rays by the channel. At the same time, as follows from the curves in Fig. 3, similar calculations by the wave theory for a plane-layered model of the subsurface channel point to a satisfactory agreement with the propagation distances observed in the experiments.

In this experiment, the signals from the subsurface channel were observed with confidence up to distances above 20 km (Fig. 4) and the signals reflected by fine-structure inhomogeneities, up to the far boundary of the

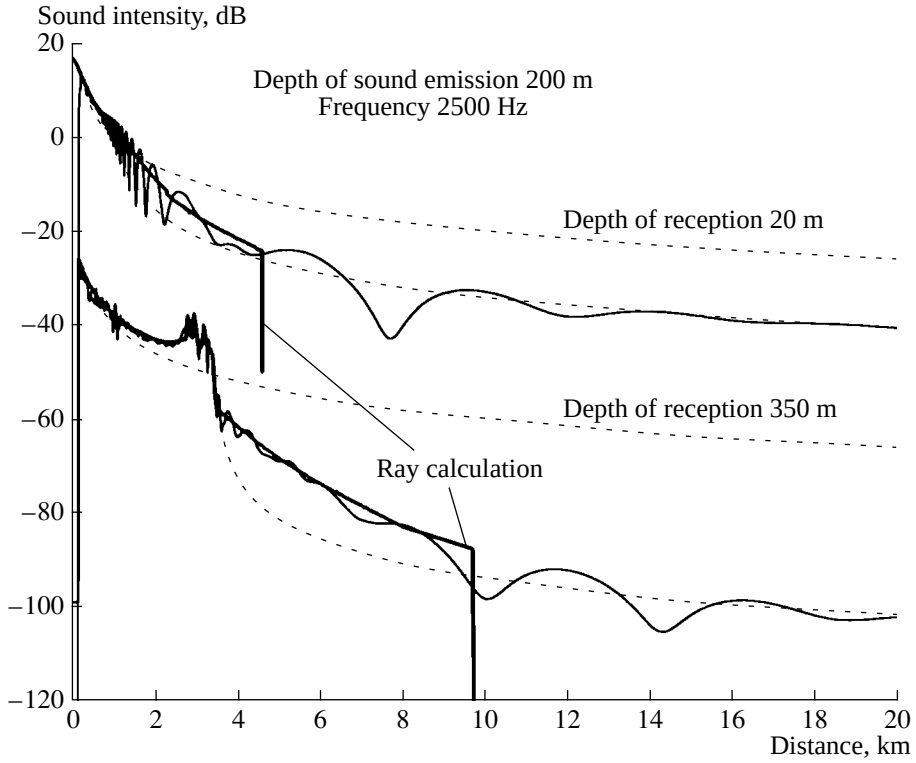

Fig. 3. Comparison of the sound intensity decay laws calculated by the ray and wave methods for the upper ocean layer (z_0 = 200 m, z = 20 and 350 m). The curves for z =350 m are shifted downward by 40 dB. The dashed curves show the spherical decay laws beginning at a distance of 1 km and at the boundary of the shadow zone for a given depth of reception, respectively.

shadow zone. The temporal characteristics of impulse signals calculated for the distances of interest to us confirmed the existence of two first families of signals caused by the presence of the subsurface channel and the diffraction penetration of sound from the insonified zone. This calculation was performed with the Avilov code [7] for a range-independent sound velocity profile obtained in the course of the experiment. The introduction of a disturbing layer of several tens of meters in thickness into the sound velocity profile at a certain depth leads to the appearance of signals from the third family. All three families of signals are noticeably ahead of the bottom-reflected signal arrival.

The fact that the highest velocity signal (a) observed in the experiment is caused by the existence of the subsurface channel is reliably confirmed by the calculations of the characteristics of the impulse signals. The calculated propagation velocity of the signal that first arrives at the point of reception is very close to the sound velocity in the subsurface channel (1537.8 m/s). Besides, the arrival angle of this signal at the reception depth in the shadow zone does not depend on distance (Fig. 5) and equals the arrival angle of the limiting water-path ray at this depth. Calculations show that the change of the sound velocity gradient in the subsurface channel causes only insignificant changes in the amplitude of the signal of interest. In this case, the arrival angle and the velocity of its propagation remain invariable. In particular, as the gradient decreases or even takes small negative values, the signal in the shadow zone continues to be observed, although its intensity noticeably decreases. This suggests that the necessary condition for the appearance of a given signal in the shadow zone is the presence of a jump in the values of the sound velocity gradient, namely, a virtual boundary in the upper part of the water layer, rather than the existence of the subsurface channel itself.

The analysis of spectrograms of both calculated and recorded signals, in full agreement with literature data [8, 9], points to an almost complete absence of dispersion of the group velocities within the whole frequency range under study (500–5000 Hz). This fact explains the high cross-correlation of the signals of interest. The correlation function maximum remains almost constant (0.50–0.55) in a band of 200–900 Hz and at a level of 0.75–0.80 in a narrower band of 600–700 Hz, as the distance varies from 7 to 15 km. Note that, for single-reflected bottom signals received from the same distances, the maximum of the cross-correlation function in the same frequency band is only 0.12 and 0.18, respectively.

However, our computations show that, for such a small thickness of the channel (30 m) and a weak positive gradient (0.010 s^{-1}) of the sound velocity in it, there exist no normal waves propagating with group velocities close to the sound velocity in the subsurface chan-

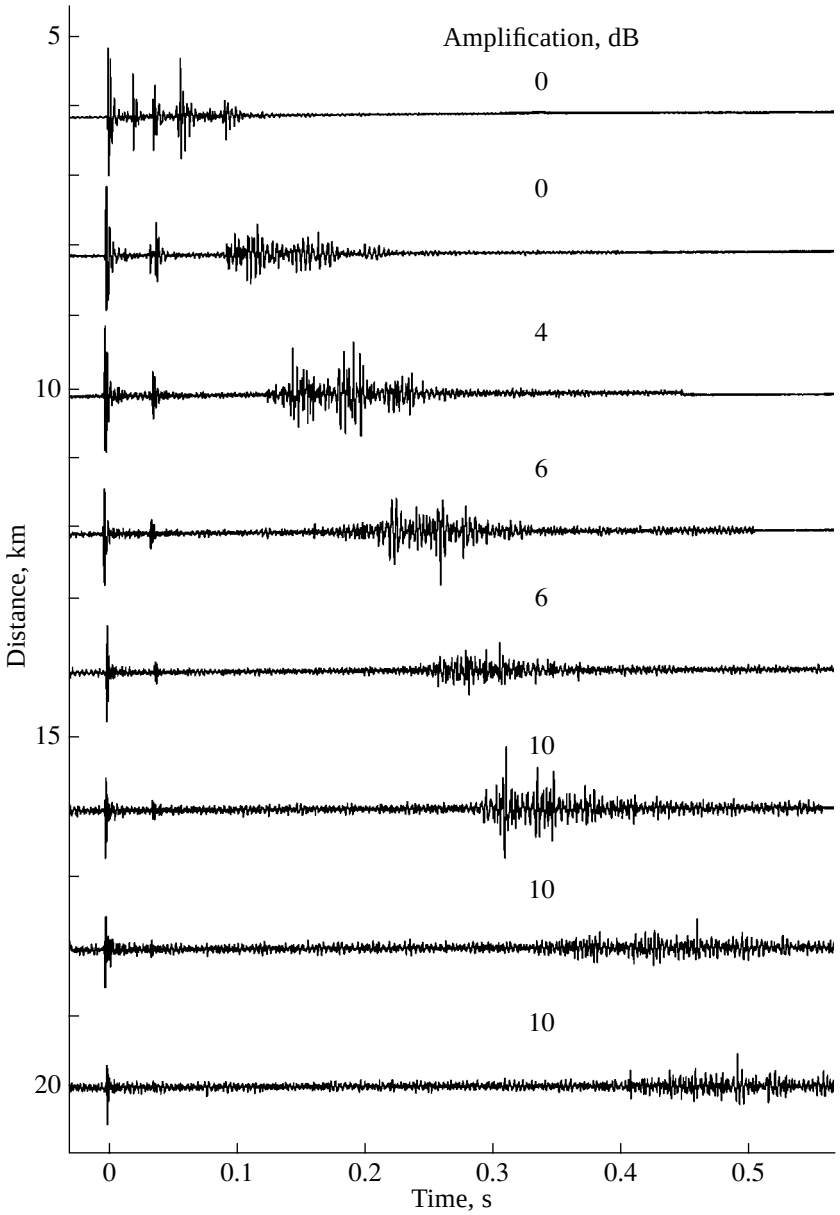

Fig. 4. Records of the initial segments of signals (without bottom reflections) recorded by the upper hydrophone. The instant of the signal arrival from the subsurface channel is taken as zero time.

nel [8] at frequencies below the critical frequency of the channel (about 1450 Hz). The propagation of low-frequency signals in the shadow zone with a velocity close to that in the subsurface channel can best be illustrated using the geometric diffraction theory. According to this theory, the boundary diffraction ray must propagate along the aforementioned virtual boundary in the upper oceanic layer. At every point of the boundary, this ray is split, emitting one more ray that leaves the boundary in the direction tangential to it [10]. This ray repeats, continuously shifting in the horizontal plane, the trajectory of the limiting water-path ray. This shows, first, that the arrival angles of the considered signals at the depth of reception are invariable as the distance varies and, second, their propagation velocity is frequency-independent, as for a lateral wave. Further, the ray leaving the boundary behaves in full accordance with the laws of ray acoustics. This allows us to experimentally observe the signals from the subsurface channel at all depths of reception, in particular, at a reception depth of 3000 m.

The above-noted analogy with the lateral wave allows us to use a mathematical method developed in geophysics for the determination of the propagation velocity of the signals observed in the experiment. The signal travel times to a given point of reception were calculated in two steps. First, the arrival time t_r of the first bottom signal was calculated at the distance r. Second, the time delay Δt of the bottom signal arrival at a

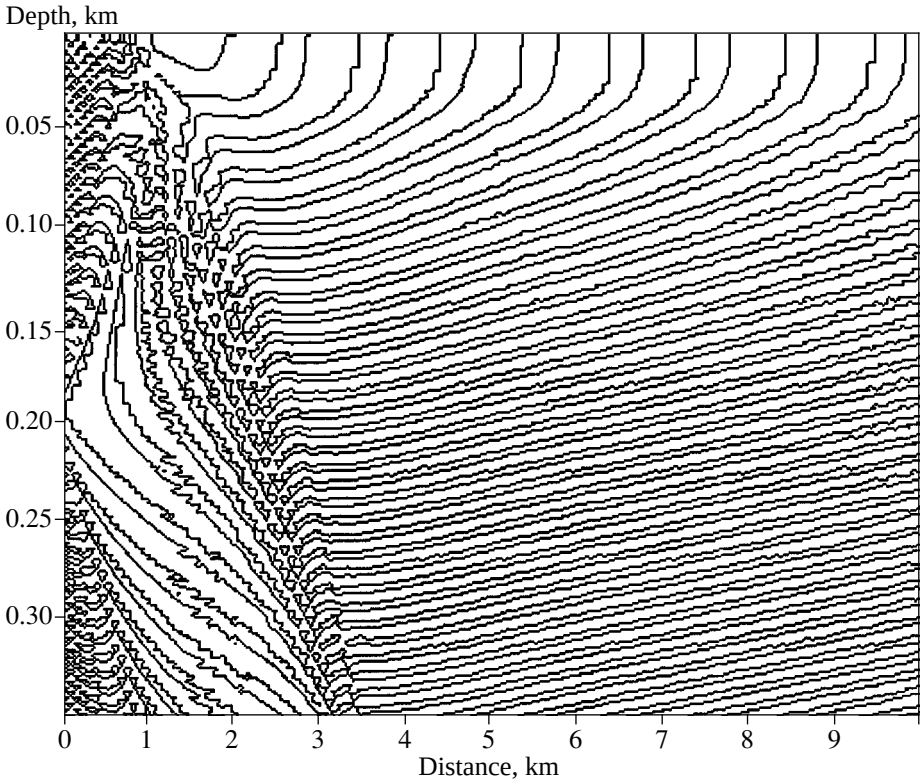

Fig. 5. Position of the wave fronts in the upper 350-m water layer. The frequency is 1000 Hz.

given point of reception with respect to the main pulse was estimated from experimental records. In this case, the arrival time t of a signal from the subsurface channel is determined as

$$t = (t_r - \Delta t) = t_0 + (r - r_0)/c,$$

where r_0 is the horizontal source–receiver distance travelled by the limiting water-path ray, t_0 is the travel time along this ray, and c is the unknown propagation velocity of our pulse. The values of the function $t(r)$ obtained in such a way were approximated by the method of least squares for distances from 6 to 24 km. They correspond to the propagation velocity 1538.9 m/s of the experimental pulse, which is very close to the above-calculated value 1537.8 m/s and the sound velocity 1541.4 m/s at the lower boundary of the subsurface channel.

It is easy to show (this is evident from the physical point of view, as well) that the attenuation of signals with their penetration and further propagating in the first shadow zone of the deep ocean are fully determined by the losses in the subsurface channel itself. Figure 6 shows the laws of the sound intensity decay with distance in the subsurface channel calculated at a depth of 20 m (z_0 = 200 m) for a number of frequencies. For a frequency of 100 Hz, the sound field at this depth is entirely determined by the diffraction penetration of sound through the boundary of the shadow zone. However, above 200 Hz, the total sound field begins to exceed the pure diffraction field, although the transmission loss in the channel is very high due to the energy leakage from it. The loss decreases gradually as the frequency increases. For frequencies above the critical frequency of the channel (~1450 Hz), the intensity decay with distance (beginning from the boundary of the shadow zone) follows the spherical law. A further increase in frequency leaves the average level of the field invariable (in the framework of the plane-parallel boundaries) but leads to the formation of a distinct interference pattern due to the excitation of the trapped modes of ever increasing numbers. The result of this is that the energy leakage from the channel with increasing distance will have an oscillating character rather than a continuous one, as at lower frequencies. This phenomenon can be seen in the experimental curves beginning from a frequency of 1000 Hz.

The comparison of the field levels at depths of 20 and 350 m (in the subsurface channel and in the shadow zone, respectively) should be carried out beginning from 500 Hz because of the difference in the rate of the diffraction field decay. According to the results of the computation of the vertical run of the field performed at a distance of 12 km from the source, the field levels in the channel and in the shadow zone are almost the same at a given frequency (Fig. 7). As frequency increases, the trapped energy level continues to increase. As a consequence, the field level in the shadow zone also increases up to certain frequencies, although the rate of

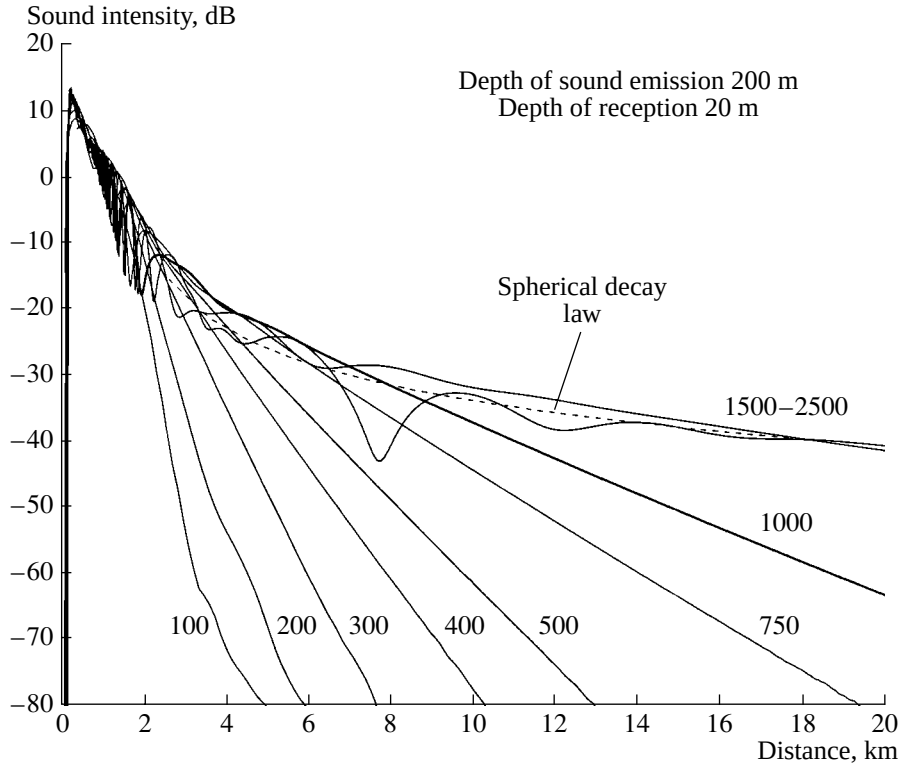

Fig. 6. Computed sound intensity decay laws in the subsurface channel for a frequency range of 100 to 2500 Hz.

this increase continuously decreases with growing frequency. In the end, at a frequency of 1450 Hz, which is the critical frequency of the channel, the increase in the field level terminates at both depths. In the upper water layer, the sound propagation becomes completely of a waveguide character. Now, the field levels in the shadow zone will almost completely be determined by the exponential tails of the normal waves trapped by the channel at a frequency higher than the critical one. The decay rate of these waves with depth grows as the frequency increases. This leads to a decrease in the field level in the shadow zone at a given depth as the frequency increases further. Thus, there exists an optimal frequency of the shadow zone insonification, which corresponds to the critical frequency of the subsurface channel.

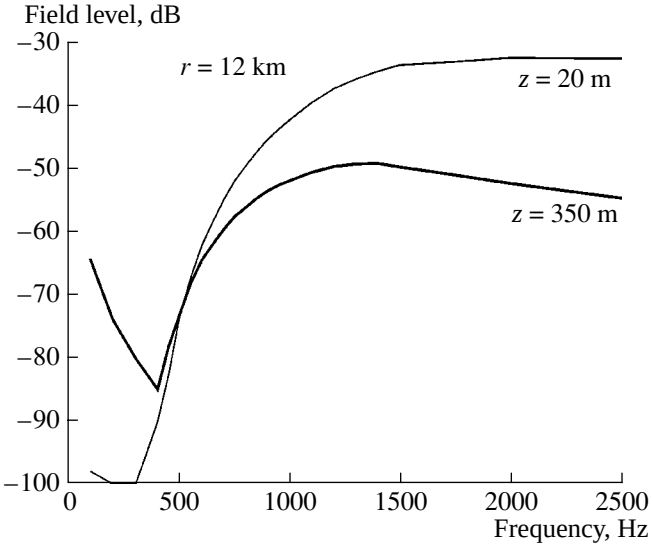

Fig. 7. Frequency dependence of the field level in the subsurface channel (z = 20 m) and in the shadow zone (z = 350 m). Depth of emission 200 m.

The sound propagation in the isovelocity subsurface water layer overlying a liquid halfspace with a negative sound velocity gradient was considered in [11]. It was shown that, in the isovelocity water layer, the sound intensity follows the spherical decay law with distance, with additional field attenuation caused by the energy leakage from the layer into the lower halfspace. The magnitude of these losses is inversely proportional to the channel thickness, the frequency to the power –2/3, and the negative sound velocity gradient in the lower halfspace to the power –1/3. In general, the dependence of the losses on the parameters of the medium agrees reasonably with our computations. It is worth noting that, for real sound velocity profiles in the ocean, the main role in the change of loss levels is played by the magnitude of the sound velocity gradient just below the channel boundary (g_2). The variation of the gradient (g_1) in the subsurface channel from zero to its typical values of 0.017–0.018 s^{-1} affects the transmission losses practi-

cally in the same way as the change of g_2 (according to the law close to the power –1/3).

Figure 8 shows the frequency dependence of the transmission loss, which was computed for different values of the thickness h of the subsurface channel and $g_1 = 0.018$ s^{-1} and of $g_2 = 0.616$ s^{-1}. For a frequency of 500 Hz, the possible dispersion of the transmission loss varies from 0.001 to 0.018 s^{-1} for g_1 and from 0.230 to 1.600 s^{-1} for g_2. Here, the circles show the experimental data obtained for several central frequencies in the 100-Hz band. The inset in Fig. 8 shows the experimental data for the entire range of frequencies.

In spite of the large volume of computer modeling, we could not obtain a universal analytical dependence of the transmission loss on the medium parameters and the frequency. The dependence obtained is an almost straight sloping line at low frequencies, which smoothly passes into a curve of the parabolic type as the frequency approaches the critical frequency of the subsurface channel. As follows from these curves, the main parameter of the medium determining the magnitude of the losses is the thickness of the subsurface channel. The effect of obviously overstated (in our computer modeling) variations of the values of the sound velocity gradients on each side of the lower boundary of the channel on the loss values can be compensated by a very small change of the channel thickness. The latter can be caused, for example, by passing internal waves. Thus, for real estimates of both the transmission loss in the subsurface channel and the energy leakage from the channel into the shadow zone, one should operate mainly with two parameters: the frequency of the emission and the thickness of the subsurface channel.

Referring now to the experimental curve, we may conclude that the average channel thickness along the track was most likely 36 m rather than 30 m, as measured at the initial (reception) point of the track. As a consequence, the minimal losses are observed in a lower frequency band (1200–1400 Hz) than expected for a 30-m thick channel. As the frequency increases further, the losses again begin to increase due to the sound scattering by the rough sea surface.

Summarizing, we note the following. The presence of the subsurface channel in the ocean causes a noticeable insonification of shadow zones at frequencies below the critical frequency of this channel. The ray methods cannot correctly describe the sound propagation in the channel itself and the sound field in the shadow zone formed due to the energy leakage from the channel. The true physical pattern of the sound field may be obtained by wave methods of computation. A convenient and useful tool in this respect is Avilov's code [7], which allows one to compute not only the field levels over a wide dynamic range (above 150 dB), but the form of the impulse signals in a wide frequency band as well. This allows one to estimate the contributions of weak energy signals, which are considered in this paper, to the total field with a reasonable accuracy.

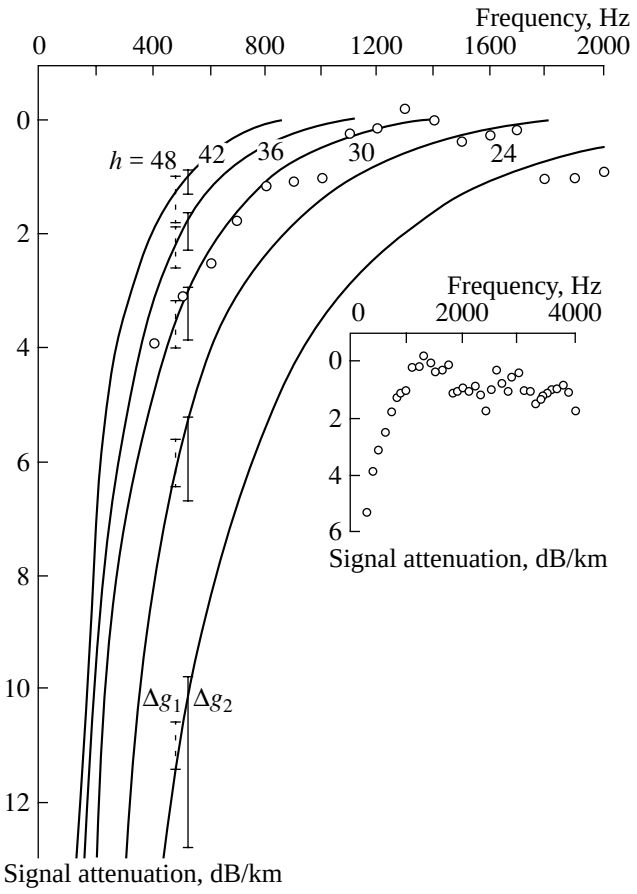

Fig. 8. Dependence of the signal attenuation on frequency (with respect to the spherical decay law) for several values of the subsurface channel thickness h. For a frequency of 500 Hz, the changes in the attenuation are shown for variations of g_1 from 0.001 to 0.018 s^{-1} (Δg_1) and g_2 from 0.237 to 1.570 s^{-1} (Δg_2). The circles in the main plot and in the inset show the experimental data (the bandwidth of analysis is 100 Hz).

The computation results and the experimental data showed that the propagation velocity of the signals from the subsurface channel almost does not depend on the frequency and is close to the sound velocity near the lower boundary of the channel. Starting from frequencies and distances when one may ignore the diffraction penetration of sound through the boundary of a shadow zone, the sound levels in the subsurface channel are higher than at different depths in the shadow zone. However, the sound decay laws with distance remain the same in both cases: the spherical law with additional decay that is determined by the energy leakage from the channel. In the frequency range lower than the critical frequency of the channel, the frequency dependence of losses is determined mainly by the channel thickness and, to a lesser degree, by the sound velocity gradients on both sides of the lower boundary of the channel. The critical frequency of the channel, which is determined by the given environment parameters, is the

optimal frequency for the sound penetration from the channel into the shadow zone. The high sensitivity of losses to the slightest changes of the channel thickness makes it very difficult to use the characteristics of the investigated signals as a tool for monitoring the oceanic medium. From the applied point of view, the above-mentioned high correlation of the signals studied in our experiments is a very important fact.

ACKNOWLEDGMENTS

This work was supported by the Russian Foundation for Basic Research, project no. 00-02-17694.

REFERENCES

1. C. L. Pekeris, J. Acoust. Soc. Am. **18**, 295 (1946).
2. D. E. Weston, C. G. Esmond, and A. Ferris, J. Acoust. Soc. Am. **89**, 156 (1991).
3. V. S. Gostev and R. F. Shvachko, Akust. Zh. **31**, 800 (1985) [Sov. Phys. Acoust. **31**, 487 (1985)].
4. S. V. Burenkov, V. S. Gostev, N. I. Knyazeva, *et al.*, Akust. Zh. **41**, 336 (1995) [Acoust. Phys. **41**, 293 (1995)].
5. M. B. Porter and F. B. Jensen, J. Acoust. Soc. Am. **94**, 510 (1993).
6. V. S. Gostev, L. N. Nosova, and R. F. Shvachko, Akust. Zh. **44**, 201 (1998) [Acoust. Phys. **44**, 162 (1998)].
7. K. V. Avilov, Akust. Zh. **41**, 5 (1995) [Acoust. Phys. **41**, 1 (1995)].
8. A. C. Kibblewhite and R. N. Dencham, J. Acoust. Soc. Am. **38**, 63 (1965).
9. W. A. Kuperman, G. L. D'Spain, and K. D. Heaney, J. Acoust. Soc. Am. **109**, 1935 (2001).
10. B. D. Seckler and J. B. Keller, J. Acoust. Soc. Am. **31**, 192 (1959).
11. L. M. Brekhovskikh and I. D. Ivanov, Akust. Zh. **1**, 23 (1955) [Sov. Phys. Acoust. **1**, 23 (1955)].

Translated by Yu. Lysanov

Acoustical Physics, Vol. 48, No. 6, 2002, pp. 665–672. Translated from Akusticheskiĭ Zhurnal, Vol. 48, No. 6, 2002, pp. 751–759.

Some Features of the Sound Field Formation in the Kamchatka Region of the Pacific Ocean

R. A. Vadov

Andreev Acoustics Institute, Russian Academy of Sciences, ul. Shvernika 4, Moscow, 117036 Russia

e-mail: vadov@akin.ru

Received December 4, 2001

Abstract—The data of three experiments on the long-range propagation of explosion-generated sound signals in the coastal Kamchatka region of the Pacific Ocean are analyzed. The experimental conditions correspond to summertime (July) with a fully-developed underwater sound channel. The propagation paths are oriented towards the coast and cross the cold Kamchatka current. A considerable spatial variability of the hydrological environment on the 250-km deep-water parts of the paths leads to pronounced deviations from the cylindrical law of the geometric spread of the sound field level. The time structure of the sound field formed in conditions of channel-type sound propagation in this region is analyzed. For the classical quartets of signals reflected from the surface, reduced t/N–R/N diagrams are obtained. The diagrams are found to be slightly different for three different paths. The "purely water" signals arriving at the receiver are nearly unresolved in time. One of the experiments reveals pronounced changes in the structure of the explosion-generated signals at distances of 100–120 km from the reception point: the terminal parts of the signals show a sharp increase in level. For the same part of the path, a pronounced level increase is also observed in the range dependence of the sound field. The hydrological data obtained for the water medium in this experiment show that these distances correspond to the boundary of the cold current. From the decay of the sound field level, the attenuation coefficient is determined by the differential method for the frequencies within 400–2000 Hz. The experimental data on the attenuation of low-frequency sound in the Kamchatka region of the Pacific Ocean noticeably exceed the calculated values of the sound absorption coefficient. © *2002 MAIK "Nauka/Interperiodica".*

In different years, in the coastal waters of the Pacific Ocean near the Kamchatka Peninsula with a fully-developed underwater sound channel (USC), experiments have been repeatedly performed to study the long-range propagation of explosion-generated sound signals. The objective of the experiments was to reveal the features of the formation of the time and intensity structures of the sound field in that region. As a rule, the studies were carried out on propagation paths oriented perpendicularly to the coastline. The paths crossed the cold Kamchatka current and the continental slope, including part of the shelf zone. The receiving system was located far from the coast, at a distance of ~400–450 km. Some results obtained by analyzing the experimental data were published earlier [1]. In the present paper, we mainly address the specificity of the time structure of an explosion-generated signal, including the decay of the sound field with distance in the deep-water (about 2000 m deep) part of the paths.

THE HYDROLOGICAL ENVIRONMENT IN THE REGION OF THE EXPERIMENTS

For the Kamchatka region of the Pacific Ocean, a considerable spatial variability of its hydrological parameters is typical.

In this region, the field of the sound speed is formed under the influence of cold runoff waters and the cold Kamchatka current, which leads to considerable changes in the depth of the USC axis in summertime. In July and August, the depth of the USC axis is 40–60 m in the coastal areas and about 100 m at distances of 300–400 km from the coast. At 100–120 km from the coastal shelf, a relatively sharp change in the axis depth occurs along with a change in the USC shape due to the intrusion of cold waters of the coastal Kamchatka current (which penetrates down to depths of 200–300 m and reaches about 100 km in width). The difference in the sound speeds near the surface and the USC axis reaches 28–35 m/s; the sound speed difference between the USC axis and the near-bottom water layers is about 35 m/s at a sea depth of 2000 m and increases up to 80 m/s at a sea depth of 5000 m.

Figures 1a, 1b, and 1c show the vertical sound speed profiles that are typical of the coastal area influenced by the runoff waters, the region affected by the Kamchatka current, and the deep-water part of the Pacific Ocean 300–400 km away from the coast, respectively.

By analyzing a great body of experimental data on hydrological parameters in the north-western part of the Pacific Ocean, Rostov [2] concludes that thermal

1063-7710/02/4806-0665$22.00 © 2002 MAIK "Nauka/Interperiodica"

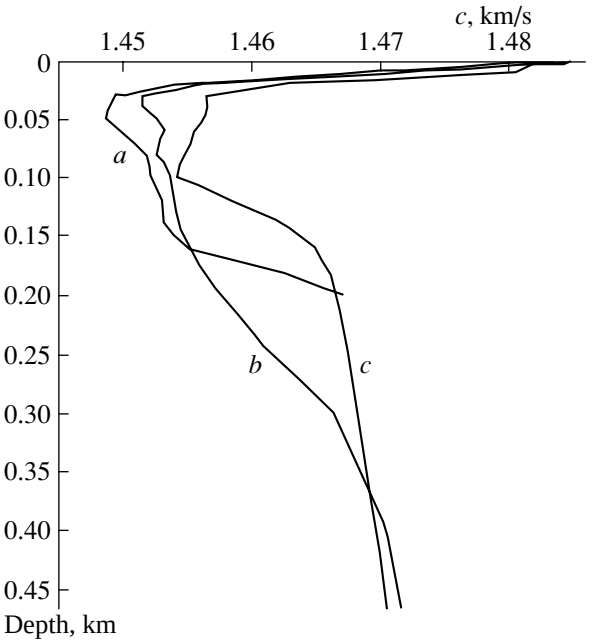

Fig. 1. Vertical profiles of the sound velocity that are typical of different parts of the paths under study: (*a*) parts influenced by the runoff waters, (*b*) parts influenced by the cold Kamchatka current, and (*c*) parts that are most distant from the coastline.

inhomogeneities exist in the region of the Kamchatka current, which take the form of thin layers. For such inhomogeneities in the region of the current and in nearby areas, the mean square fluctuation of the acoustic refraction index is $\mu^2 \approx 10^{-5}$–10^{-7}.

EXPERIMENTAL TECHNIQUE

The experiments were carried out in summertime (July), in different years, on three different paths about 300 km long each. The length of deep-water (more than 2000 m deep) parts of the paths was 230–250 km. The zones where different paths crossed the Kamchatka current were 130–150 km apart from each other.

Two research vessels participated in the experiments. The receiving vessel drifted 350–400 km away from the coast. The transmitting vessel moved at a speed of 10–14 knots from the coast towards the reception point along the path perpendicular to the 150- to 200-m isobaths. The explosive charges were dropped from the transmitting vessel and exploded by pressure-sensitive detonators. The depth of explosions somewhat varied in different experiments: it was 200 and 250 m on the first and second paths and 150 m on the third one. In each of the three experiments, from 25 to 40 charges were exploded within the deep-water parts of the paths. The successive explosions were separated by 15–30 min in time, this interval corresponding to 6.5–10 km in distance. At the moment of each charge dropping, the distance between the vessels was determined from the propagation time of a sound signal and recalculated by navigational observations periodically performed on both vessels. The explosion-generated signals were received by omnidirectional systems located at the depths of 80, 100, or 150 m, which differed from experiment to experiment.

Before or after each experiment, vertical profiles of water temperature and electric conductivity (subsequently recalculated to salinity) were measured by the ISTOK-3 apparatus at 6–7 points of the path. Such a probing was performed for the depths reaching 500–1000 m. The values of temperature, salinity, and hydrostatic pressure were recalculated to the sound speed according to Wilson [3].

During the experiment, the wind speed was no higher than 6–7 m/s and the sea state was Beaufort 1–3.

TIME STRUCTURE OF THE SOUND FIELD

The explosion-generated signal was received in the frequency band from 10–20 Hz to 1–2 kHz, at distances of 10–20 km and longer. In the case of a single-ray sound propagation, the received signal consists of two short (less than 1 ms) pulses that are equal in amplitude and have the same signs: the shock wave and the first oscillation of the gas bubble. The interval between the pulses corresponds to the period T_o of the gas-bubble oscillation. In our experiments, T_o varied from 12 ms for an explosion depth of 250 m to 20 ms for that of 150 m. In the case of a multi-ray reception, each ray yields a pair of the aforementioned pulses in the time structure of the signal.

Figure 2 shows a pattern of changes in the time structure of the explosion-generated signals as a function of distance. This pattern obtained in one of the experiments resembles the classical *t*–*R* diagram proposed by Ewing and Worzel [4] to describe the details of the sound field structure in the USC. The explosion-generated signals shown in Fig. 2 are normalized to the maximal amplitude of each of them and leveled with respect to the moment of their termination. The classical quartets of the elementary (single-ray) signals lie on individual branches that differ in the number of full cycles produced by the rays along which the central signals of the quartets propagate. The quartet that is the first to arrive at the receiver is composed by well-resolved signals propagating over the rays with maximal deviations from the USC axis. In the Kamchatka region, well-resolved signals in the quartets can be observed at distances no longer than 200 km from the source. At distances longer than 200 km, the quartets transform into relatively compact groups of nearly unresolved signals. In the signals received at distances shorter than 200 km, no more than two or three signal quartets can be observed simultaneously. According to

the shapes of the elementary (single-ray) signals in the quartet that arrives first (see inset in Fig. 2), they can be attributed to the signals that are surface-reflected (except for the first signal of the quartet received at distances shorter than 60 km from the source). For the first branch of the quartets received at distances longer than 35–40 km, a phase shift that is a multiple of 180° is obvious (instead of 90°, which arises when the ray touches the caustic). This conclusion is also confirmed by the ray-approximation calculations of the sound field structure. According to the calculation, the quartets of the first branch, which exist in the time structure of the explosion-generated signals received at distances of up to 35–40 km, are produced by the rays that do not touch the surface: surface reflections occur starting from 35–40 km. The main energy of the total explosion-generated signal comes from purely water components that are nearly unresolved in time.

From the data, obtained on the first path, we have earlier concluded in [1] that, although the source and receiver are set off the USC axis, a terminal part exists in the group of the unresolved signals, whose duration is about 50% of the total signal duration and which cannot be explained in the framework of ray considerations. In comparing the experimental and calculated time structures of the explosion-generated signal, we matched them according to the positions of individual quartets and the beginning of the group of the signals unresolved in time. With such a matching, the observed termination of this signal group corresponds to the velocity of sound propagation along the USC axis (Fig. 3).

We calculated the group velocity and the degrees of excitation for the initial ten modes at a frequency of 200 Hz by using the computer code by Mal'tsev [5] (the medium was assumed to be horizontally layered, with one of the measured $c(z)$ profiles). Such a calculation allowed us to partially explain the aforementioned experimental fact. The six initial modes had the calculated group velocities that nearly did not differ from the sound speed at the USC axis, and four modes had rather high excitation factors. A more comprehensive study of the problem was made by Belov *et al.* [6]. In this work, the wave-approximation code of Avilov [7] was applied to one of the $c(z)$ profiles measured on the second path to compute the time structure of the explosion-generated signal at the frequencies 20–200 Hz. A satisfactory agreement with the experimental signal structure was obtained for the signal received at a distance of 105 km in the second experiment. According to the results reported in [6], the horizons that are far from the USC axis were insonified by the exponential tails of the vertical distributions of the mode amplitudes.

At the same time, for the third path, the ray-approximation calculations of the sound field structure showed that the horizontal component of the propagation velocity along some rays crossing the USC axis at angles that were noticeably different from 0° nearly coincides with the sound speed at the axis. For this experiment, the experimental and ray-approximation-calculated time structures of the explosion-generated signal agreed well.

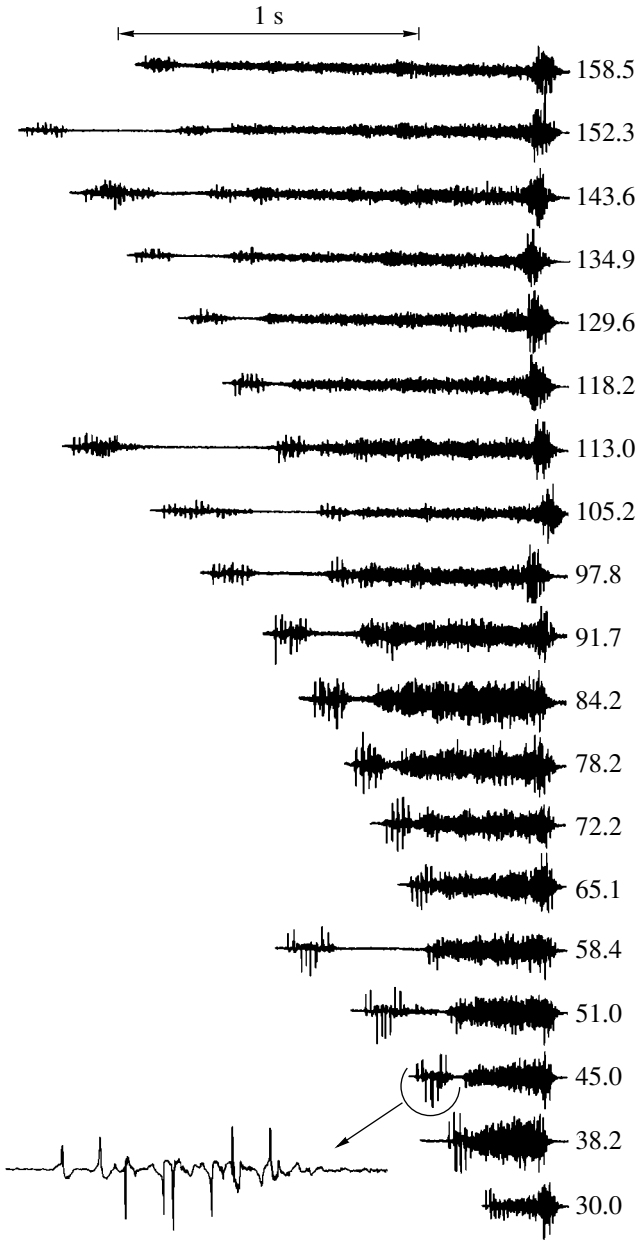

Fig. 2. Time structure of the explosion-generated signal received at different distances from the source on the third path. The source depth is 150 m, and the reception depth, 80 m. The distance between the source and the receiver (in kilometers) is indicated to the right of the signal oscillograms.

Figure 2 presents the time structure of the explosion-generated signals received on the third path. Note the pronounced changes in the signal structure when

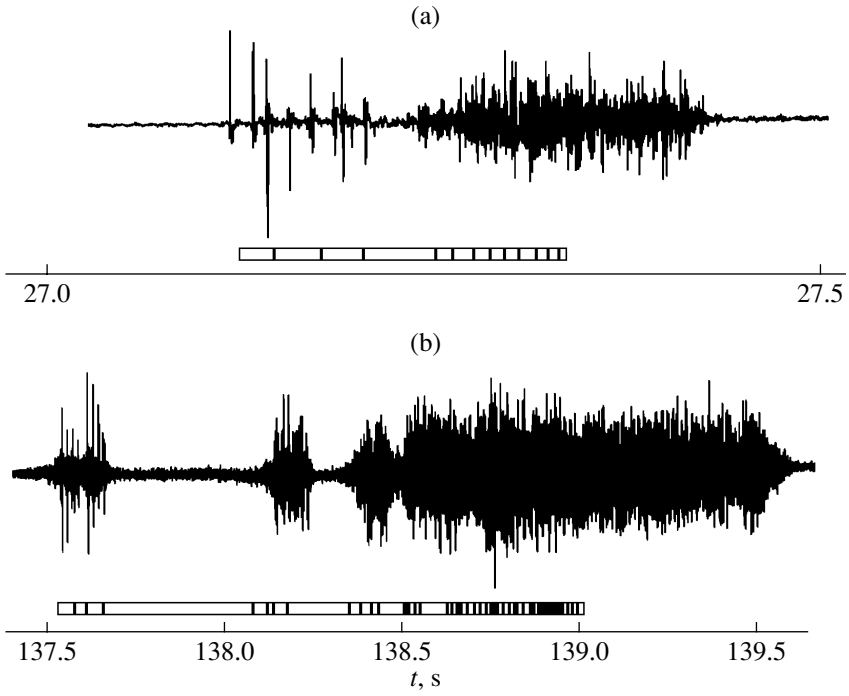

Fig. 3. Time structure of the explosion-generated signal received at the distances (a) 40 and (b) 203 km from the source. The source depth is 200 m, and the reception depth is 100 m. The comparison of the experimental record and the calculated results (the ribbon with vertical dashes under the records shows the signal travel times for individual rays). The computations are performed with Vagin's computer code.

crossing the south-eastern boundary of the cold Kamchatka current, namely, a sharp increase in the amplitude of the terminal part of the signal. These amplitude changes correspond to a distance of 90–95 km from the reception point. The field of the sound speed, which was measured in the same experiment and is presented in Fig. 4, evidences that, at this distance from the nearest reception point, a boundary of the cold current exists with rather sharp changes in the position of the USC axis. Similar, though smoother, changes in the terminal signal part were obtained for the distance increase from 50 to 150 km by ray-approximation calculations with the computer code by Vagin [8] (in view of the sound-speed profile changes along the path).

To simplify the comparative analysis of the time structures of the sound field for different ocean regions, we [9] proposed using the reduced $t/N–R/N$ diagram, which consists of a single curve representing the $t–R$ relation for the signals that propagate along the rays producing N full cycles. Such a diagram fully determines the propagation times for individual quartets, including their positions in the time structure of the multi-ray signal at an arbitrary distance from the source. By simple recalculations, the reduced $t/N–R/N$ diagram can be obtained for the entire body of experimental data obtained in each experiment.

The results of such a recalculation for the third path are shown in Fig. 5. The recalculation was performed for $N = 1, 2, 3$. In addition to the experimental data, the approximating curve is plotted in Fig. 5. In spite of the considerable spatial variability of the hydrological environment along the path, the recalculated values obtained for different N agree well with each other at distances up to 160 km. The scatter of the experimental data is insignificant. A rather high degree of order has been also mentioned by other researchers (see, e.g., [10]) for individual ray groups in long-range sound propagation in variable hydrological environments.

A similar recalculation was also performed for the first and second paths. For those measurements, Fig. 5 shows the $t/N–R/N$ diagrams in the form of curves that approximate the experimental data. The difference between the $t/N–R/N$ diagrams constructed for different paths is more significant. Such a difference can be caused both by space–time changes in the hydrological parameters of the paths (space separation of them, different years of experimenting) and by different depths of the transmitter and receiver relative to the USC axis in these measurements.

The change in the terminal unresolved part of the explosion-generated signal (that is, the elongation of the signal part formed by purely water arrivals) was proportional to the distance with a proportionality factor of 0.005 s/km for the first path, 0.008 s/km for the second, and 0.007 s/km for the third.

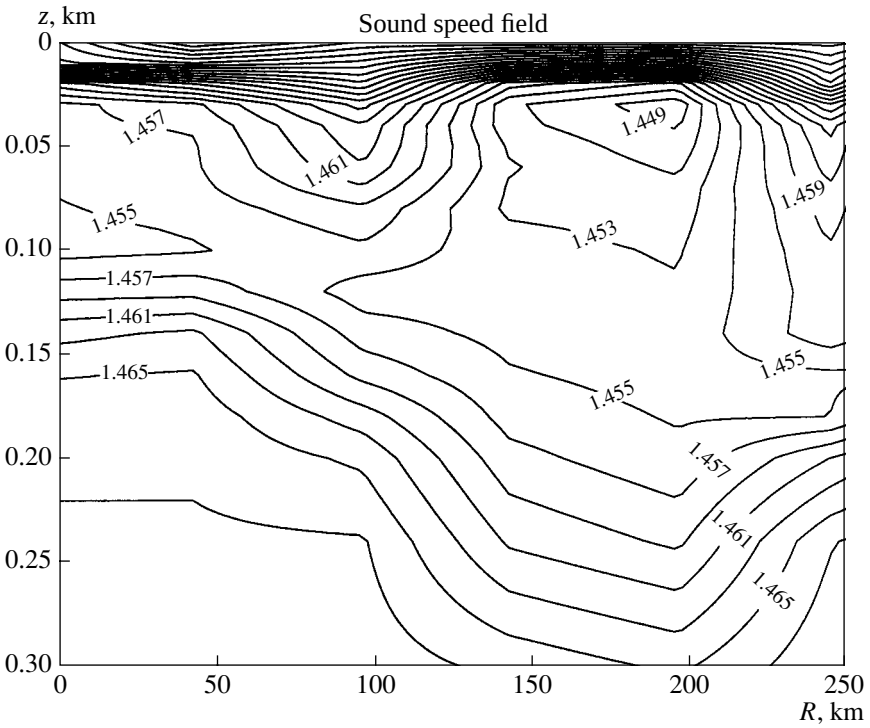

Fig. 4. Sound speed field obtained from the data of the hydrological survey carried out on the third path during the acoustic experiment.

SOUND FIELD DECAY AND THE FREQUENCY DEPENDENCE OF ATTENUATION

With the explosion-generated sound signals, the following sound field characteristic equivalent to the signal energy within a frequency band Δf is used:

$$E_f = \int_0^T p_f^2(t)dt,$$

where T is the signal duration, and $p_f(t)$ is the sound pressure in the explosion-generated signal, which is normalized to the frequency band Δf. In computer signal processing, this equivalent value can be obtained from the power spectrum of the signal.

By processing the signals received on each of the paths, the experimental decay laws were estimated for the sound field levels at different frequencies. The obtained decay laws were used as starting data for estimating the frequency dependence of the attenuation coefficient.

Figure 6 illustrates the decay of the sound field corrected for the cylindrical law of geometric spread for the frequencies 200, 400, and 800 Hz on the first and third experimental paths. Both on the first and on the third paths, a moderate (3–4 dB) elevation in the sound field level is observed for the region of the current boundary nearest to the reception point. The corresponding distances are 120–150 km for the first path and 90–10 km for the third one.

For the frequency band 100–2000 Hz, we used the deviation of the experimental sound field decay from the cylindrical law of geometric spread to estimate the attenuation coefficient. Strictly speaking, the cylindrical law is valid for a channel-type sound propagation in a horizontally stratified medium. In our case, the atten-

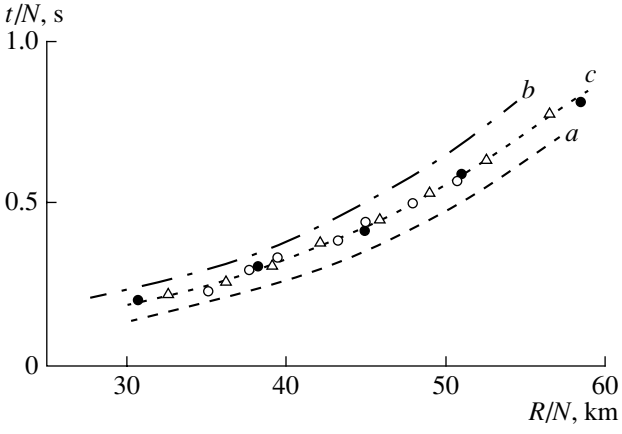

Fig. 5. The t/N–R/N diagram plotted on the basis of the experimental data obtained on the (*a*) first, (*b*) second, and (*c*) third paths. The symbols ●, ×, and ○ indicate the experimental values of t/N for $N = 1$, 2, and 3, respectively, on the third path.

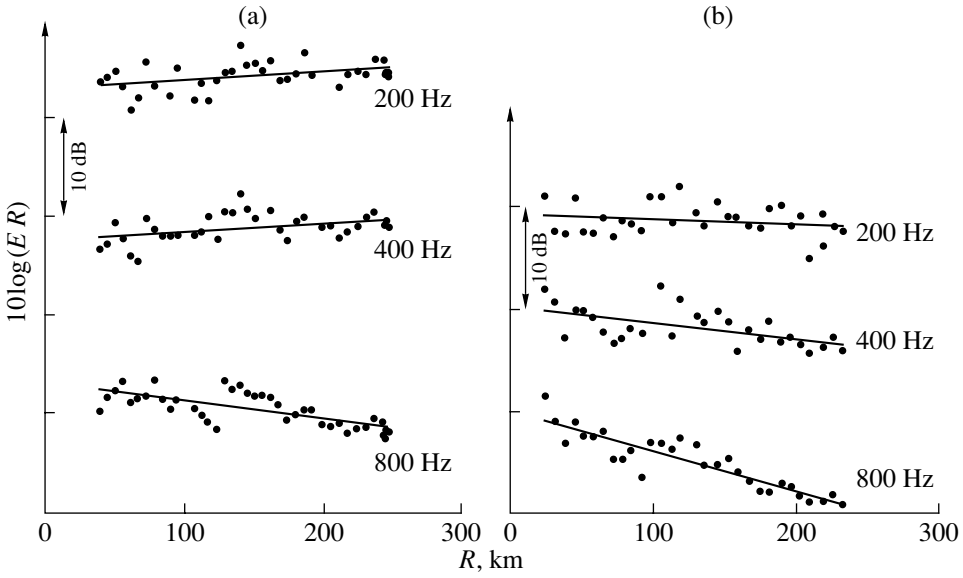

Fig. 6. Experimental decay laws for the sound field on the (a) first and (b) third paths at the frequencies 200, 400, and 800 Hz.

uation coefficient estimated in this way is nothing but a quantitative parameter that characterizes the steepness of the decrease in the sound field level with distance, i.e., the departure of the decay from the cylindrical law. To exclude terminological ambiguity, let us call the aforementioned value the formally determined value of the attenuation coefficient β_f. The values of β_f estimated from the experimental data obtained on the propagation paths are summarized in Table 1.

The experimental law of the sound field decay is also governed by the changes in the USC parameters along the path, including its shape and the depth of its axis. This statement is especially true for low frequencies at which the sound absorption and scattering by inhomogeneities of the sea medium are weak. As was noted in [11], the deviations from the cylindrical law can be observed toward both increase and decrease in the steepness of the decay, the decrease leading to negative values β_f.

Table 1. Experimental values of β_f for the three paths

Frequency, Hz	Path 1, β_f, dB/km	Path 2, β_f, dB/km	Path 3, β_f, dB/km
100	−0.014	−0.004	−0.0055 (−0.006)
125	−0.004	−0.003	−0.0055 (−0.006)
160	−0.021	−0.002	0.000 (−0.004)
200	−0.0095	−0.001	0.0045 (0.005)
250	−0.002	−0.001	0.0043 (0.002)
315	−0.005	0.000	0.0083 (0.008)
400	−0.009	0.0105	0.0165 (0.0155)
500	0.0035	0.011	0.020 (0.018)
630	0.009	0.017	0.029 (0.028)
800	0.018	0.029	0.0395 (0.0395)
1000	0.027	0.036	0.044 (0.043)
1250	0.037	0.047	0.0575 (0.0575)
1600	0.052	0.057	0.069 (0.0685)
2000	0.069	0.078	0.083 (0.083)

According to Table 1, we observed a decrease in the decay steepness (relative to the cylindrical law) on all three paths. This decrease manifested itself at the frequencies 400 Hz and lower on the first path, at 250 Hz and lower on the second, and at 125 Hz and lower on the third. At frequencies higher than 400 Hz, the values of β_f presented in the table increase from the first to the third path. On average, the difference in the decay rates was about 0.0085 dB/km between the second and first paths and 0.018 dB/km between the third and first paths, remaining almost independent of frequency.

For the third path, Table 1 additionally shows the values of β_f (in parentheses) that were obtained from truncated explosion-generated signals. From the whole signals, segments were artificially cut out that contained the quartets of resolved elementary (single-ray) signals reflected by the sea surface (the sea state reached Beaufort 2–3 in this case). By doing so, we tried to exclude the influence of the wavy surface from the values of β_f. However, as the comparison of the data presented in Table 1 shows, this influence proved to be negligibly small in our case.

With the parameters of the medium changing along the path, one cannot determine the law of geometric spread to a sufficient accuracy. To estimate the attenuation coefficient, one should use the so-called differen-

tial method proposed [12] in the mid-1950s. This method of estimating the attenuation is based on two assumptions: first, that the law of geometric spread is unknown but the same for the entire frequency band at hand, and, second, that the frequency dependence of the attenuation coefficient can be approximated by a power-low curve with a zero constant component. At individual frequencies, the levels of the sound field are normalized to the level at one of the frequencies, which is chosen as a reference. This procedure serves to fully exclude the unknown law of geometric spread. From the normalized decays at each frequency, the "differential" attenuation coefficient is determined. By approximating the frequency dependence of the differential attenuation coefficient and by omitting the free term, we obtain the following relation for the total attenuation coefficient:

$$\beta = a f^n. \quad (1)$$

The relatively small lengths of the paths did not allow us to attain sufficient reliability in estimating the attenuation coefficient at lower frequencies (100–315 Hz). The estimates were obtained for the range 400–2000 Hz. The differential values of the attenuation coefficient were estimated for all the paths studied. These values are summarized in Table 2. The 800-Hz frequency was specified as the reference.

In transforming the differential values into the common ones of the attenuation coefficient, we took into account the experimental data obtained on all three paths. To describe the frequency dependence of the attenuation by Eq. (1) with the frequency in kilohertz and attenuation in decibels per kilometer, we obtained the following parameter values: $a = 0.063$ and $n = 0.7$.

For the sake of comparison, in addition to the experimental values, Table 3 shows the attenuation coefficients calculated according to Eq. (1) and according to the expression presented in [13] for the frequency dependence of the absorption coefficient (in view of the relaxation processes caused by magnesium sulphate and boron which are present in sea water).

According to the hydrological surveys of the propagation paths, which were performed prior to all experiments, the characteristic values 4°C and 34‰ were found for the temperature and salinity at depths of 20–400 m. The concentration of hydrogen ions was not determined in the surveys. However, the archival data existing for the region at hand lead to the pH values 7.9–8.1 for these depths. In accordance with Table 3, in the Kamchatka region of the Pacific Ocean, the attenuation coefficients are two to three times higher than the absorption coefficient at the frequencies 400–1000 Hz.

Together with the Norwegian Sea [14], the deep-water southern part of the Sea of Okhotsk [15], and the Greenland Sea [16] (at least, its eastern part), the Kamchatka region should be attributed to the regions of the ocean that are characterized by an increased low-frequency sound attenuation. The most probable mechanism of such attenuation in these regions is the sound scattering by fine-structure thermal inhomogeneities generated by the cold Kamchatka current [2].

Table 2. Experimental values of the differential attenuation coefficient (the reference frequency is $f_0 = 800$ Hz)

Frequency, Hz	Path 1, attenuation, dB/km	Path 2, attenuation, dB/km	Path 3, attenuation, dB/km
400	−0.027	−0.018	−0.023
500	−0.015	−0.018	−0.020
630	−0.009	−0.011	−0.011
800	0	0	0
1000	0.009	0.008	0.005
1250	0.019	0.018	0.018
1600	0.034	0.029	0.030
2000	0.051	0.049	0.044

To conclude, let us formulate the main results obtained in analyzing the data of the three experiments on long-range propagation of the explosion-generated signals on different paths in the Kamchatka region of the Pacific Ocean.

For the three 230 to 250-km-long paths, a considerable spatial variability of their hydrological environments is typical, which leads to pronounced deviations of the geometric spread from the cylindrical law at frequencies below 200–400 Hz.

The experimental time structure of the explosion-generated signals contains well resolved classical quartets produced by elementary (single-ray) signals reflected from the sea surface. The reduced *t*/*N*–*R*/*N* diagrams obtained from the experimental data are somewhat different for the three paths, although the scatter of the values of *t*/*N* for an individual path is negligibly small. The purely water elementary (single-ray) signals are nearly unresolved in time and arrive as a compact group, whose duration increases in proportion with the distance from the source. The proportionality factor varies from 0.005 to 0.008 s/km for different paths.

On one of the paths, sharp changes in the structure of the aforementioned signal group were observed at the point where the path crosses the Kamchatka current boundary nearest to the receiver: the amplitude of the terminal part of this group (which constitutes about 10% of its duration) sharply increased and became three to four times higher than the amplitude of the main signal part.

The attenuation coefficients determined by the differential method from the level decay at 400–1000 Hz exceed the calculated values of the attenuation coeffi-

Table 3. Comparison of the experimental data obtained for the attenuation in the coastal Kamchatka region of the Pacific Ocean with the absorption coefficient calculated for the experimental region

Frequency, Hz	Attenuation, dB/km, calculation by Eq. (1)	Experimental attenuation, dB/km			Absorption, dB/km, calculation according to [13]
		path 1	path 2	path 3	
400	0.033	0.028	0.037	0.032	0.007–0.009
500	0.039	0.041	0.038	0.036	0.011–0.014
630	0.045	0.047	0.044	0.045	0.016–0.020
800	0.054	0.055	0.055	0.055	0.023–0.029
1000	0.063	0.065	0.063	0.060	0.031–0.039
1250	0.073	0.074	0.074	0.073	0.042–0.052
1600	0.087	0.089	0.084	0.085	0.058–0.070
2000	0.102	0.107	0.104	0.099	0.078–0.091

cient by a factor of 2 to 3. Thus, this region of the ocean should be ascribed to the regions with increased attenuation, like the previously studied regions of the Norwegian Sea, the Sea of Okhotsk, and the Greenland Sea.

ACKNOWLEDGMENTS

I am grateful to A.V. Mikryukov and V.V. Nemchenko from the Acoustics Institute for their valuable assistance in performing some of the experiments and for discussing the experimental data.

This work was supported by the Russian Foundation for Basic Research, project nos. 01-02-16636 and 01-05-64711.

REFERENCES

1. R. A. Vadov, Akust. Zh. **43**, 606 (1997) [Acoust. Phys. **43**, 521 (1997)].
2. I. D. Rostov, Candidate's Dissertation in Geography (TOI DVNTs, Vladivostok, 1985).
3. W. D. Wilson, J. Acoust. Soc. Am. **34**, 866 (1962).
4. M. Ewing and J. Worzel, in *Sound Propagation in the Ocean* (Inostrannaya Literatura, Moscow, 1951).
5. A. V. Vagin and N. E. Mal'tsev, Vopr. Sudostr., Ser. Akust., No. 9, 61 (1977).
6. A. I. Belov, A. V. Mikryukov, and O. E. Popov, Akust. Zh. **45**, 157 (1999) [Acoust. Phys. **45**, 127 (1999)].
7. K. V. Avilov, Akust. Zh. **41**, 5 (1995) [Acoust. Phys. **41**, 1 (1995)].
8. A. V. Vagin, *Report of Institute of Acoustics, USSR Acad. Sci.* (Moscow, 1974).
9. R. A. Vadov, Akust. Zh. **40**, 930 (1994) [Acoust. Phys. **40**, 824 (1994)].
10. M. A. Wolfson and S. Tomsovic, J. Acoust. Soc. Am. **109**, 2693 (2001).
11. R. A. Vadov, in *Problems of the Ocean Acoustics* (Nauka, Moscow, 1984), pp. 31–42.
12. M. J. Sheehy and R. Halley, J. Acoust. Soc. Am. **29**, 464 (1957).
13. R. A. Vadov, Akust. Zh. **46**, 624 (2000) [Acoust. Phys. **46**, 544 (2000)].
14. R. A. Vadov, Akust. Zh. **48**, 28 (2002) [Acoust. Phys. **48**, 24 (2002)].
15. R. A. Vadov, Akust. Zh. **45**, 174 (1999) [Acoust. Phys. **45**, 143 (1999)].
16. R. A. Vadov, Akust. Zh. **46**, 47 (2000) [Acoust. Phys. **46**, 37 (2000)].

Translated by E. Kopyl

Acoustical Physics, Vol. 48, No. 6, 2002, pp. 673–677. Translated from Akusticheskiĭ Zhurnal, Vol. 48, No. 6, 2002, pp. 760–765.

Elastic and Mechanical Properties of Films Formed by Dense Layers of Carbon Nanotubes

K. V. Gogolinskiĭ*, Z. Ya. Kosakovskaya, V. N. Reshetov***, and A. A. Chaban******

** Technological Institute of Superhard and Novel Carbon Materials, ul. Tsentral'naya 7a, Troitsk, Moscow oblast, 142190 Russia*

*** Institute of Radioengineering and Electronics, Russian Academy of Sciences, ul. Mokhovaya 11, Moscow, 103907 Russia*

**** Moscow State Engineering Physics Institute, Kashirskoe sh. 31, Moscow, 115409 Russia*

***** Andreev Acoustics Institute, Russian Academy of Sciences, ul. Shvernika 4, Moscow, 117036 Russia*

e-mail: chaban@akin.ru

Received December 25, 2001

Abstract—The elastic and mechanical properties of thin films formed by carbon nanotubes differently oriented with respect to the substrate are studied. The penetration depth of a probe tip into the film is measured as a function of the pressing force by using a scanning-probe atomic force microscope. The effect of pressing the tip into the films on their mechanical stability and the unusual behavior of the films scratched by the tip are investigated. It is found that films with different tube orientation with respect to the substrate exhibit radically different properties. © *2002 MAIK "Nauka/Interperiodica".*

Great interest has been recently shown in the new carbon nanotube materials [1, 2]. This is related to their unique physical properties, including the elastic, mechanical, and electric ones. For electronic applications, the dense-film devices are no less promising than those based on isolated nanotubes or their bundles. However, it seems very important for a film to contain only one layer of nanotubes. In this case, each tube can have its own independent contact on both sides of the film. At present, quite a number of laboratories all over the world can grow dense layers of nanotubes [3–5], but there are few examples of single layers of oriented tubes. It is precisely this type of single-layer films of nanotubes identically oriented with respect to the substrate that is used in the present study. It should be emphasized that we also managed to obtain unusual films with the tubes oriented not at the habitual 90° angle to the substrate (below, we call them 90-degree films) but at an angle of 45° (below, we call them 45-degree films). These are quite interesting objects due to the giant anisotropy of the physical properties of individual nanotubes.

The elastic and mechanical properties of individual isolated tubes and their bundles have been much investigated. As for the properties of dense films, their study is only just beginning [6–8]. Below, we report on the study of films with various tube orientations. The following characteristics were obtained:

(1) the penetration depth of a probe tip into the film as a function of the pressing force (the so-called loading curves);

(2) the presence of indentations produced in the film by the pressing tip;

(3) the character of the damage caused by the tip scratching the film (the scratch sclerometry);

(4) the effect of silicon doping on the elastic properties of the films.

In the experiments, a Nanoscan scanning-probe atomic force microscope was used. Its description and parameters can be found in [9, 10]. An elastic oscillatory system was brought into contact with the analyzed surface by means of a hard tip. When the tip was pressed into the sample, both the frequency and amplitude of elastic oscillations changed. By this change, it was possible to determine the elastic parameters of the sample.

Let the curvature radius of the tip be R and the stiffness of the oscillatory system (the cantilevel fixing the tip) be k_0. Now, we lift the sample and fix the moment of contact with the tip. Then, we lift the sample still further. As a result, the tip moves into the sample to the depth h, and the cantilevel shifts upward by a certain distance x. The total lift of the sample after the moment of contact is $x + h$. This total length can be easily measured. The resistance force F acting from the side of the sample on the pressing tip depends on h. At equilibrium, we have

$$k_0 x = F(h). \quad (1)$$

For evaluation purposes, we limit our consideration to the case of a very hard tip (in our case, it is a diamond

1063-7710/02/4806-0673$22.00 © 2002 MAIK "Nauka/Interperiodica"

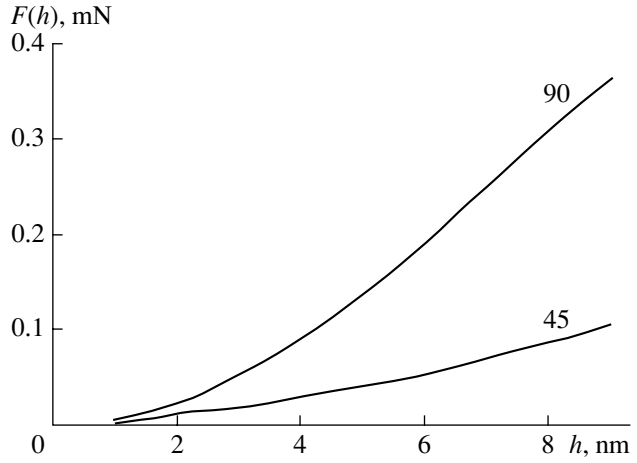

Fig. 1. Pressing force as a function of the tip's penetration depth into the film for 90-degree and 45-degree films.

one) contacting a semi-infinite isotropic medium, because there is no Hertz theory of contact (even a qualitative one) for crystalline media and textures. Since the force $F(h)$ is proportional to $h^{3/2}$ [11], there exists a region of sufficiently small values of h, for which $k_0 h \gg F(h)$. Taking into account Eq. (1), we obtain for this case $x \ll h$. Hence, for the sufficiently small h, the lift of the cantilevel is small compared to the displacement of the tip, and the total displacement can be considered as equal to the tip's penetration into the sample. Neglecting the tip deformation and applying the Hertz theory [11], we obtain a simple condition for this approximation:

$$h \ll \frac{9k_0^2}{16R}\left(\frac{1-\sigma^2}{E}\right)^2. \qquad (2)$$

Here, E is the Young modulus and σ is the Poisson ratio. A characteristic property of our microscope is the value of stiffness (1.3×10^5 N/m), which is very high for the atomic-force microscopy. This considerably increases the region determined by inequality (2). For a sample with $E = 1.7 \times 10^{11}$ Pa and $\sigma = 0.2$, inequality (2) holds for $h \ll 80$ nm, even with the tip's curvature radius $R =$ 4 μm. (Such a large curvature radius of the tip is necessary to measure the macroscopic characteristics of the films formed by elements as massive as nanotubes.)

Consider now the frequency shift of the oscillatory system of the microscope that occurs when the tip is pressed into the sample. The stiffness of the system is now determined not only by the cantilevel, but also by the resistance force of the sample. If the amplitude of elastic oscillations is much less than the penetration depth, the total stiffness is

$$k = k_0 + \frac{dF(h)}{dh}. \qquad (3)$$

Hence, one can easily obtain the pressing force:

$$F(h) = 2k_0\int_0^h \frac{f - f_0}{f_0}dh. \qquad (4)$$

Here, f_0 is the frequency of the unloaded system and $f - f_0$ is the oscillation frequency shift caused by pressing of the tip. In deriving Eq. (4), we assumed that the frequency shift is small compared to the frequency of the unloaded system. Using the Hertz theory, one can easily show that this condition is satisfied for the above parameters and $h \ll 80$ nm.

Thus, using the nonstandard parameters of our scanning-probe atomic force microscope, we can reliably measure the loading curves at the nanometer level and the penetration depths down to at least 10 nm. This opens up interesting prospects for investigating different types of thin films, as for them there are still no adequate measuring techniques and the experimental data are contradictory.

Now, we discuss our experimental results. The films were deposited on a silicon substrate. They consisted of one layer of nanotubes with a characteristic tube length of about 110 nm. The tubes were practically parallel to each other for both tube orientations with respect to the substrate. They were mostly multilayer nanotubes with diameters from 3 to 5 nm. The surface relief was studied for both film types. The relief was studied with a tip of curvature radius about 4 μm and that of curvature radius about 100 nm. In both cases, a rather smooth surface was observed, which was quite similar to the surface described in our previous paper [8], the characteristic inhomogeneities being about 1–2 nm in height.

The loading curves for the films with different orientation of nanotubes, taken with the diamond tip whose curvature radius was about 4 μm, are shown in Fig. 1. As distinct from the previous work [8], we present here the quantitative dependence of the pressing force on the depth of penetration of the tip into a thin film formed by nanotubes. Such an approach has many advantages. If we need to create a pressure contact or introduce an impurity into some surface area by means of atomic force microscopy, or to treat the surface mechanically, then, having performed the corresponding measurements according to this method, we can determine the pressure necessary for obtaining a contact of a desired diameter, irrespective of the surface character (a hard tip is not subject to deformation). One does not need to know what contribution to the sample response is made by the substrate and what is made by the film. One does not need to choose a region with a very smooth surface, as was the case in our previous work. Figure 1 demonstrates the results for the most common region with a considerable roughness. The part of the curve corresponding to the tip penetration depth of less than 1 nm was deliberately omitted, because the amplitude of the tip oscillations was finite, although we chose the minimal possible oscillation

intensity during the observations. As a result, we had to reject the region where this circumstance could have affected the results.

One can see at once a strong difference between the elastic properties of nanotubes with the 45-degree orientation and those with the 90-degree one. For such a complex anisotropic medium, this difference can be analyzed in detail only on the basis of a full set of elastic moduli, but the latter can hardly be obtained in the near future for a thin film with a single layer of tubes. However, the measurement data give a general idea of the enormous anisotropy of elastic properties. Comparative measurements on samples of some other materials have been carried out. Since such results were given in [8], we need not dwell on them. We only note that the elastic stiffness of the high-quality 90-degree film used in this study proved to be considerably higher than that of the sample used before [8].

In the cited paper [8], we noted that the square of frequency shift in nanotube films is proportional to the indentation depth, as should be the case in isotropic media. This allowed us to ascribe a certain effective Young modulus to the nanotube film. (Unfortunately, we have not emphasized that it could differ from the real Young modulus and that it plays the role of the latter to characterize the indentation only.) The same dependence can be represented as the proportionality of $F^{2/3}$ to the penetration depth of the tip. For the new 90-degree film, such a law really holds in the regions with a smooth surface. But it was quite unexpected to find that this law manifests itself for the 45-degree films as well, although, in this case, the elastic force problem is not even an axially symmetric one. Lacking a qualitative Hertz contact theory for crystals and textures, one can hardly be successful in analyzing this fact, but some more or less general relation could possibly be found. (Note that a generalization of the Hertz theory to the case of an arbitrary nonspherical shape of contacting surfaces leads, for isotropic materials, to the abovementioned dependence [11].)

The mechanical properties of the films are also of interest. We searched for the traces of the tip after it was pressed into the film to a penetration depth of several tens of nanometers. For this purpose, the tip was pressed into the same place several times in succession. We tried to detect the change in the time of initial contact and the shape of the loading curve. Within the measurement accuracy (no worse than 1 nm), we could not find any traces of previous pressing for both film types.

It was very interesting to carry out the sclerometric investigations (scratch hardness testing) for such an unusual medium. For this purpose, a tip with a curvature radius of about 100 nm was used. The tip was pressed into the film and moved parallel to its surface. The results obtained for a 90-degree film were remarkable (Fig. 2). If the tip was pressed into the surface through no more than 60 nm, the trace of scratching actually disappeared on the most part of the analyzed surface within one minute after scratching (this is the maximal speed at which the relief study was possible with the equipment used). Figure 2a shows the relief observed along the line of scratching to a depth of 30 nm after 2 min after the scratching procedure. No distinct trace is visible. If there was any, it should have been healed. There are isolated damage regions seen in the picture as dark spots. Figure 2b shows the relief cross section for one of such regions. The section was made at an angle of 75° to the line of scratching for two time instants: within 2 min after the scratching and within 7 min (in Fig. 2a, the section is marked by the straight

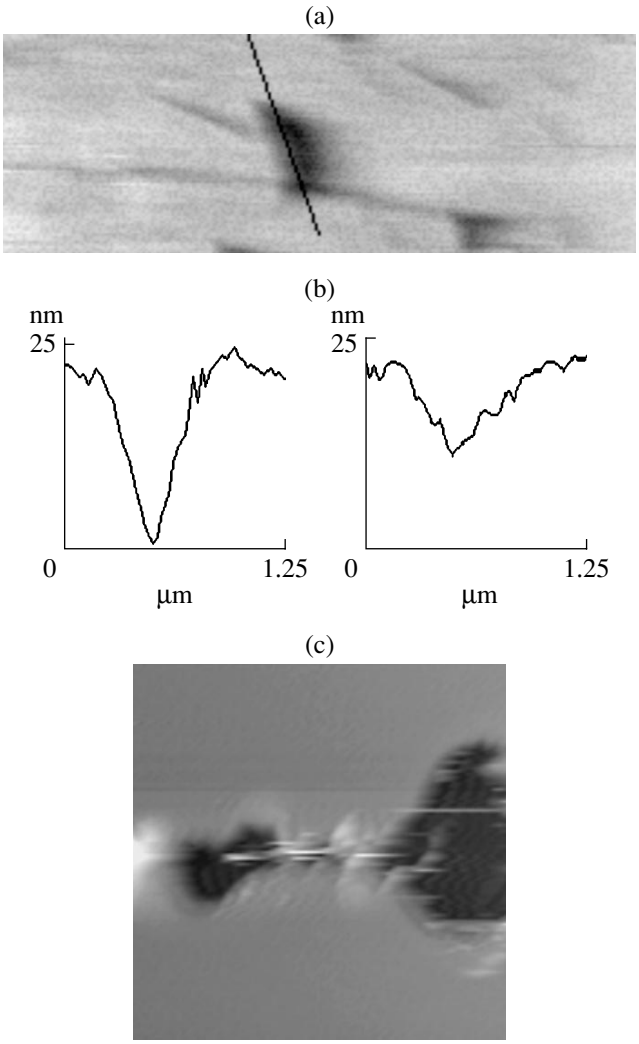

Fig. 2. Traces of scratching for the 90-degree film. (a) Surface relief along the scratch line. The tip is pressed into the film to a depth of 30 nm. The dark regions correspond to depressions. The frame size is 3.5×1.2 μm^2. The straight line corresponds to the cross section in Fig. 2b. (b) Cross section of the surface relief at 75° to the scratch direction, 2 min (left) and 7 min (right) after scratching. (c) Permanent scratch observed after the tip was pressed through the whole thickness of the film. The frame size is 6×6 μm^2. The dark regions show depressions, and the light regions correspond to the raising relief.

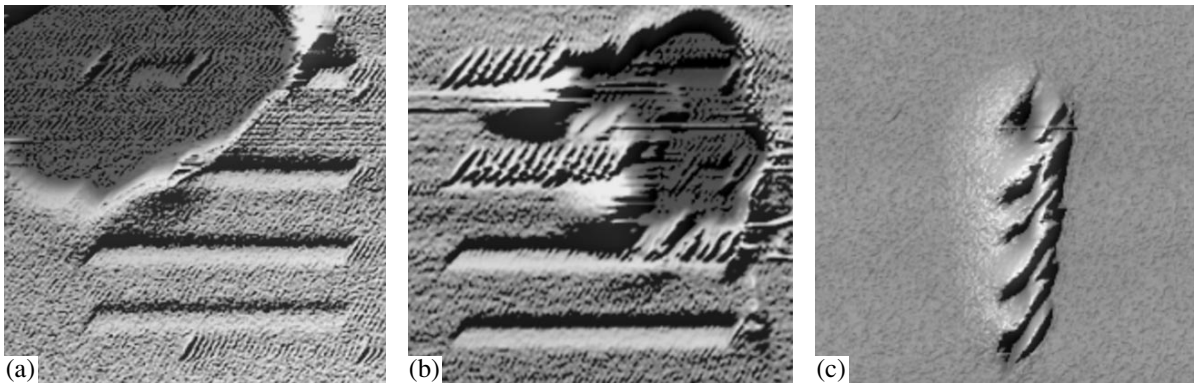

Fig. 3. Scratches on the surface of the 45-degree film. A three-dimensional relief pattern with "illumination." (a) Scratches along the direction of the tube slope (right to left). The depth increases upwards from 30 nm to the full thickness of the film. (b) Scratches in the opposite direction (left to right). The depth increases upwards from 30 nm to the full thickness of the film. (c) Scratch across the direction of the tube slope (upwards) through the full thickness of the film.

line). We see that the residual trace of the scratch on the 90-degree film continues healing. After several tens of minutes, the main (though, not all) traces of scratching disappear, and even some surface defects that existed before the scratching disappear as well. Apparently, this is related to the following two circumstances. The nanotubes are remarkably stable and restore their shape after a strong deformation. The weak bond between individual tubes does not prevent their rearrangement in the course of the surface healing and the transition of the whole system to the state with the minimal potential energy.

The situation drastically changes when the tip becomes close to the silicon substrate or reaches it. The separation of the film from the substrate (most likely, a temporary one) leads to a permanent scratch in the form of a large damage region (Fig. 2c). However, its depth is much smaller than the penetration depth of the tip. The film relief in the scratch region is highly nonuniform not only on the scale of hundreds of nanometers, but on the nanometer scale as well. Most likely, it is connected with pushing individual nanotubes or their bundles out of the layer.

When the 45-degree films are scratched, the situation is entirely different (Fig. 3). The films were scratched in three directions: across the tube slope direction, along the slope, and in the opposite direction. In all three cases, no trace of healing was observed. Note that we cannot guarantee that the tip is moving strictly parallel to the slope direction of the tubes. The error is about several degrees. The tip cannot be strictly perpendicular to the surface either, the error being of the same order of magnitude. As long as the depth of scratching is much smaller than the film thickness, the scratches are smooth and regular, with no fundamental difference observed for the three orientations.

When the probing depth approaches the film thickness, the film is likely to partially separate from the substrate. Unlike the case of the 90-degree film, the depth of the residual trace is comparable to the film thickness. The relief around the scratch is noticeably raised. The elasticity of the surrounding region is lower than that of the rest of the film. At the same time, unlike the case of the 90-degree film, the relief of nanometer-scale regions proves to be smooth. This means that isolated areas of the film are deformed as a whole, without pushing individual tubes or their bundles out of the layer.

In the case of a deep scratching, there are considerable differences for different directions. Figure 3a shows several scratches made along the direction of the tube slope, and Fig. 3b shows scratches made in the opposite direction. In Figs. 3a and 3b, the probing depth grows in the upward direction. The relief pattern is shown as if the surface were illuminated from some point above it. The two lower traces in both figures correspond to the tip pressing to a depth that is much smaller than the film thickness. Such traces are similar for all scratch directions. The upper traces are obtained by scratching to a depth close to the film thickness. In the case of the deep scratching along the tube slope (in Fig. 3, from right to left), the trace is at first smooth, and then a large distorted surface region appears. When deep scratching occurs in the opposite direction (in Fig. 3, from left to right), the trace is at first striped, and then it also transforms to a large distorted surface region. In the case of deep scratching across the tube slope, a complex cocoonlike structure is observed, which is shown in Fig. 3c. The fundamental difference between this and the scratching of 90-degree films is related to the fact that, in the case of 45-degree films, the motion of the scratching tip has a considerable velocity component across the tubes (remember that we cannot scratch strictly along the tube slope). The tip should either break a tube or bend it strongly together with all neighboring tubes.

It is well known that nanotubes actively absorb various chemical elements. Hence, the atoms from the silicon substrate should inevitably move into the film in

considerable amounts. Therefore, the measurements of the loading curves were performed regularly over two months. No changes in the elastic properties were found within the accessible accuracy of measurements for both film types. This fact, which is strange at first sight, has a simple explanation. Apparently, the diffusion of silicon atoms into the film mainly goes through the internal cavity of the multilayer tube. It is well known that individual layers inside a multilayer nanotube are weakly bound to each other. Therefore, the appearance of impurities and a structure modification within the tube does not affect the external layers' response to the mechanical action. In the case of silicon diffusion between the layers inside a multilayer nanotube, or between the nanotubes, one should expect a quite different result.

Thus, in the present study, we managed to obtain the quantitative loading curves for the tip pressed to small depths into two different types of films manufactured on the basis of nanotubes. The mechanical resistance of such films to the external action was investigated.

ACKNOWLEDGMENTS

We are grateful to the Russian Foundation for Basic Research for supporting this study (grant nos. 00-02-16473 and 01-02-18017).

REFERENCES

1. R. Saito and M. S. Dresselhaus, *Physical Properties of Carbon Nanotubes* (Imperial College Press, London, 1998).
2. A. V. Eletskiĭ, Usp. Fiz. Nauk **167**, 945 (1997) [Phys.–Usp. **40**, 899 (1997)].
3. Z. Ya. Kosakovskaya, L. A. Chernozatonskiĭ, and V. A. Fedorov, Pis'ma Zh. Éksp. Teor. Fiz. **56** (1), 26 (1992) [JETP Lett. **56** (1), 26 (1992)].
4. J. S. Suh and J. S. Lee, Appl. Phys. Lett. **75** (14), 2047 (1999).
5. D. A. Walters, M. J. Casavant, X. C. Qin, *et al.*, Chem. Phys. Lett. **338** (1), 14 (2001).
6. P. Calvert, Nature **399**, 210 (1999).
7. V. N. Popov, V. E. van Doren, and M. Balkanski, Solid State Commun. **114** (7), 395 (2000).
8. I. S. Grudzinskaya, Z. Ya. Kosakovskaya, V. N. Reshetov, and A. A. Chaban, Akust. Zh. **47**, 632 (2001) [Acoust. Phys. **47**, 548 (2001)].
9. K. V. Gogolinskiĭ and V. N. Reshetov, Zavod. Lab. **64** (6), 30 (1998).
10. Description of the NanoScan Scanning Probe Microscope, http://www.mtu-net.ru/nanoscan.
11. L. D. Landau and E. M. Lifshits, *Course of Theoretical Physics*, Vol. 7: *Theory of Elasticity*, 4th ed. (Nauka, Moscow, 1987; Pergamon, New York, 1986).

Translated by A. Kruglov

Acoustical Physics, Vol. 48, No. 6, 2002, pp. 678–680. Translated from Akusticheskiĭ Zhurnal, Vol. 48, No. 6, 2002, pp. 766–769.

Properties of Acoustic Boundary Waves Propagating along the Interface between Two Piezoelectric Media

M. Yu. Dvoesherstov, V. I. Cherednik, A. P. Chirimanov, and S. G. Petrov

Lobachevskiĭ State University, Nizhni Novgorod,
pr. Gagarina 23, Nizhni Novgorod, 603600 Russia
e-mail: dvoesh@rf.unn.runnet.ru

Received October 23, 2001

Abstract—The properties of electroacoustic boundary waves propagating in a system of two piezoelectric crystalline media are theoretically analyzed. A numerical experiment is used to determine the specific pairs of piezoelectric media and their orientations that allow the propagation of this type of waves with optimal properties. © *2002 MAIK "Nauka/Interperiodica".*

A wave that propagates without dispersion along the interface between two isotropic halfspaces is called a Stoneley wave [1]. This type of wave can exist only when certain relationships between the elastic parameters of the bordering media are valid [2]. In a system of two semi-infinite piezoelectric crystalline media that have an acoustic contact with each other, an electroacoustic boundary wave (BW) can also exist [2, 3]. The electroacoustic waves that propagate in a layered system formed by a film and a piezoelectric substrate when the film thickness h is sufficiently large (comparable to the wavelength λ) are also called BW [4].

No system of two bordering piezoelectric media has yet been manufactured by the epitaxial growth of a piezoelectric crystalline film on a piezoelectric substrate of another type (except for the ZnO films [5]). The piezoelectric films of SiO_2, $LiNbO_3$, $LiTaO_3$, etc. have not yet been obtained by epitaxial technology. However, recently, some technologies appeared (the direct bonding of piezoelectric materials) that allow one to create a direct acoustic contact between two previously grown piezocrystals of different symmetry [4, 6]. Accordingly, interest in the properties of BW has grown considerably. The application of BW in acoustoelectronic devices can give a number of important advantages over the common surface acoustic waves (SAW): unlike a SAW, a BW has no direct contact with the atmosphere, and, hence, there is no need to encase the structure obtained, which considerably reduces the final dimensions of the device [4]; in some cases, the phase velocity of transverse BW can be higher than that of SAW [3]; by choosing specific piezoelectric media, one can considerably improve the technical parameters of the wave, namely, raise the electromechanical coupling coefficient K^2 and, simultaneously, improve the thermal stability of the wave [7].

The aim of the present study is the theoretical determination of various pairs of piezoelectric crystals and their orientations that allow the existence of BW, as well as the numerical analysis of the main parameters of BW.

Following the solution-searching technique used for SAW [8], one can also find the solution for BW. In the last case, since the energy of BW is mainly localized in the vicinity of the interface between two piezoelectric media, the amplitudes of mechanical displacements and the corresponding electric potential should exponentially decay on both sides of the interface.

By numerical calculation, we determined the solutions for a quasi-transverse BW propagating in a system of two identical bordering piezoelectric crystals of $LiNbO_3$, $LiTaO_3$, $Li_2B_4O_7$, etc., separated by an infinitely thin short-circuited metallic layer (see table). The electric short-circuiting of the interface leads to the condition of the existence of this type of wave. For comparison, the table also shows the calculated phase velocities of SAW (V_0 for a free surface and V_M for a metallized surface) and the bulk wave velocities (V_{t1}, V_{t2}, and V_L) for the given crystal orientations (which are represented by three Euler angles ϕ, θ, and Ψ [9]). It can be seen that the velocity of the quasi-transverse BW V_{BW} is close to that of the slow shear bulk wave V_{t1}. Figure 1 demonstrates the calculated normalized amplitudes of the mechanical displacements u_1, u_2, u_3 and the potential $u_4 = \varphi$ of the BW on both sides of the interface (along the X_3 axis) in the system of two identical YX-cut (0°, 90°, 0°) lithium niobate piezoelectric media separated by an infinitely thin short-circuited metallic layer. Figure 1 shows that the boundary wave mainly consists of two shear components of mechanical displacements u_2 and u_3. The displacement amplitudes decay along the X_3 axis at a relatively large distance from the interface:

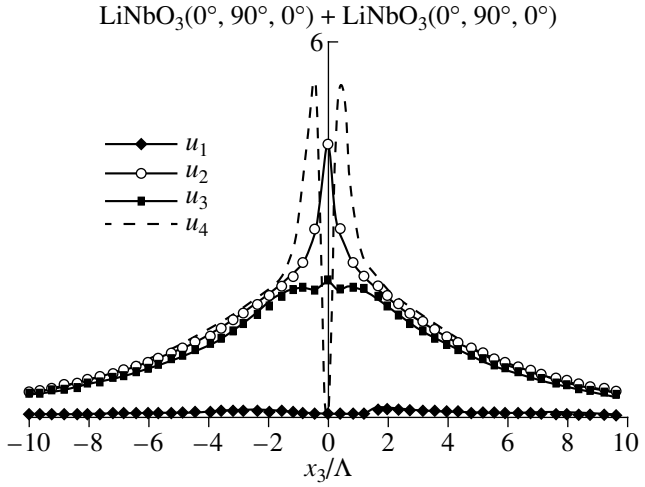

Fig. 1. Normalized amplitudes of the displacements (curves u_1, u_2, and u_3) and the potential (curve u_4) of the BW along the X_3 axis in a system of two identical bordering piezoelectric media (YX-cut $LiNbO_3$) separated by metal.

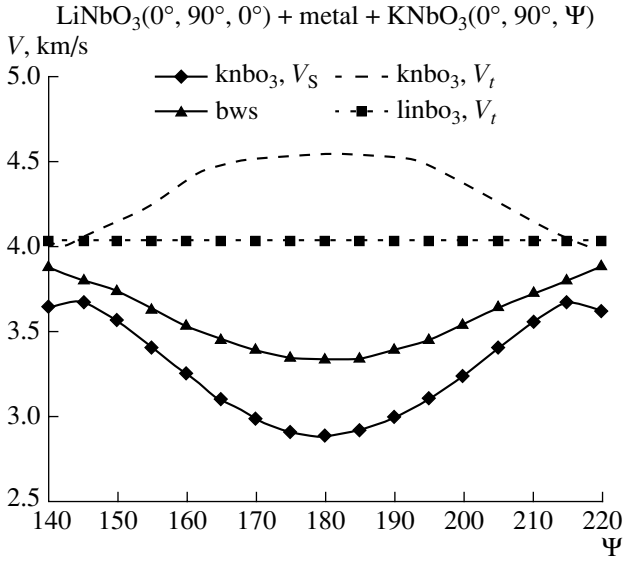

Fig. 2. The BW phase velocity (curve bws) in the (0°, 90°, 0°)$LiNbO_3$/metal/(0°, 90°, Ψ)$KNbO_3$ system, the SAW velocity (curve $knbo_3$,V_S), and the velocity of slow shear bulk waves in $KNbO_3$ (curve $knbo_3$, V_t) and in $LiNbO_3$ (curve $linbo_3$, V_t) versus the angle Ψ.

about ten wavelengths, which is far greater than in the SAW case.

By means of a numerical experiment, the regions for the existence of BW solutions in a system of two different piezoelectric crystals were also determined. Figure 2 demonstrates the calculated dependences of the velocity V_{BW} (curve bws) in the $LiNbO_3$(0°, 90°, 0°)/metal/$KNbO_3$(0°, 90°, Ψ = 140°–220°) system. The same figure shows for comparison the calculated velocities of a slow shear bulk wave in $KNbO_3$ and $LiNbO_3$ crystals (curves $knbo_3$, V_t and $linbo_3$, V_t) and the SAW velocity on a metallized surface of $KNbO_3$ (curve $knbo_3$, V_S).

It can be seen that, in this case, the phase velocity of BW is considerably smaller than the velocities of the bulk waves in both piezoelectric crystals and is close to the SAW velocity in YX-$LiNbO_3$ (V_{LiNbO_3} = 3.691 km/s). Figure 3 demonstrates the normalized amplitudes of the displacements of a BW as functions of the distance from the contact boundary of two crystals in the (0°, 90°, 0°)$LiNbO_3$/metal/(0°, 90°, 175°)$KNbO_3$ system. In this case, only one transverse displacement component u_2 is predominant ($u_2 \gg u_1, u_3$). Contrary to the situation in Fig. 1, the displacement amplitudes are no more symmetric on the left and on the right of the interface ($X_3 = 0$), and the amplitude u_2 with the electric potential φ decay much faster on both sides of the interface, namely, at distances of about 1.5 wavelengths. Besides, the electric potential in the $KNbO_3$ crystal is higher than that in the $LiNbO_3$ crystal, because the piezoelectric parameters of $KNbO_3$ are an order of magnitude higher [10]. Note also that a BW exists in this pair of piezocrystals in the absence of a metallic layer at the interface. In this case, the value of its phase velocity lies between those of SAW phase velocities in both media, and its electromechanical coupling coefficient K^2 is

Table

Piezoelectric crystals	V_t, km/s V_{t2}, km/s V_L, km/s	SAW V_M, km/s V_0, km/s	V_{BW}, km/s
Orientation (0°, 90°, 0°) $LiNbO_3$/metal/$LiNbO_3$	4.03078 4.7524 6.547	3.691 3.7178	4.02907
Orientation (0°, –49°, 0°) $LiNbO_3$/metal/$LiNbO_3$	4.03078 4.7524 6.547	3.637 3.641	4.0302
Orientation (0°, 90°, 0°) $LiTaO_3$/metal/$LiTaO_3$	3.350833 4.2265 5.5885	3.158 3.161	3.350831
Orientation (0°, 75°, 75°) $Li_2B_4O_7$/metal/$Li_2B_4O_7$	3.6889 4.936 6.4385	3.2945 3.309	3.3759
Orientation (0°, 90°, 0°) PKN/metal/PKN	3.0546 4.936 6.4385	3.2945 3.309	2.6942

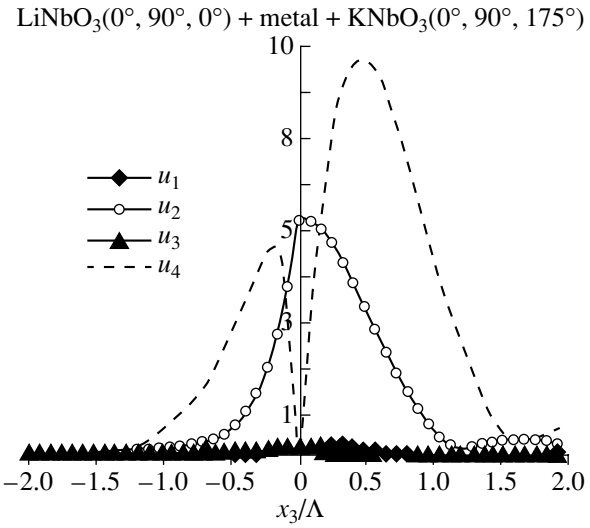

Fig. 3. Normalized amplitudes of the displacements (curves u_1, u_2, and u_3) and the potential (curve u_4) of the BW along the X_3 axis in the (0°, 90°, 0°)$LiNbO_3$/metal/(0°, 90°, 175°)$KNbO_3$ system.

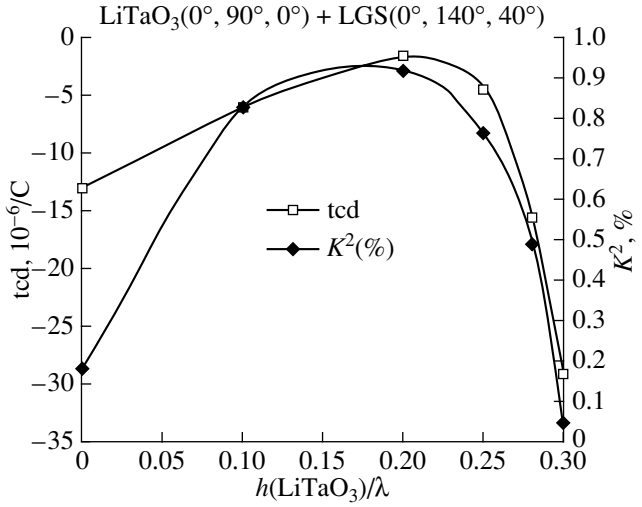

Fig. 4. Dependences of the tcd (10^{-6}/C) and K^2 (%) on h/λ for the system consisting of a (0°, 90°, 0°)$LiTaO_3$ film on (0°, 140°, 40°)LGS.

higher than that of $LiNbO_3$ but lower than that of $KNbO_3$.

Earlier [4], a structure consisting of an *YX*-$LiNbO_3$ film on *YX*-quartz was proposed, in which the BW has the "optimal" characteristics ($K^2 \approx 1.5\%$ and the temperature coefficient of delay tcd < 10^{-6}/C) with the thickness of the lithium niobate film being $h \approx 0.3\lambda$ (λ is the wavelength).

In this paper, we propose a structure consisting of an *YX*-$LiTaO_3$ film on (0°, 140°, 40°) LGS (langasite). Figure 4 demonstrates the calculated dependences of K^2 (%) and tcd (10^{-6}/C) on h/λ for BW in this layered structure. It can be seen that, in this system, at $h/\lambda \approx 0.2$, the BW has the maximal coefficient $K^2 \approx 0.96\%$ and a practically zero value of the tcd.

For piezoelectric crystals with strong piezoelectric coupling ($LiNbO_3$, $KNbO_3$, and $LiTaO_3$), the orientations are found that allow the propagation of BW. It is shown that, in the case of two identical piezoelectric media separated by an infinitely thin metallic layer, the BW has a quasi-transverse structure and its phase velocity is close to that of the slow shear bulk wave. The $LiTaO_3$/LGS layered structure is proposed. In this structure, the BW has optimal parameters: a high electromechanical coupling coefficient and a zero temperature coefficient of delay.

REFERENCES

1. R. Stoneley, Proc. R. Soc. London, Ser. A **106**, 416 (1924).
2. K. Yamanouchi, K. Iwahashi, and K. Shibayama, IEEE Trans. Sonics Ultrason. **25**, 384 (1978).
3. S. Camou and S. Ballandras, in *Proceedings of IEEE Ultrasonics Symposium* (2000).
4. K. Eda, K. Onishi, and H. Sato, in *Proceedings of IEEE Ultrasonics Symposium* (2000).
5. E. Adler and L. Solie, in *Proceedings of IEEE Ultrasonics Symposium* (Seattle, USA, 1995), p. 341.
6. H. Sato, K. Onishi, and T. Shimamura, in *Proceedings of IEEE Ultrasonics Symposium* (1999).
7. T. Irino, T. Y. Watanabe, and Y. Shimizu, in *Proceedings of IEEE Ultrasonics Symposium* (1987), p. 257.
8. M. Yu. Dvoesherstov, V. I. Cherednik, and A. P. Chirimanov, Izv. Vyssh. Uchebn. Zaved., Radiofiz. **43** (9), 801 (2000).
9. M. P. Shaskol'skaya, *Acoustic Crystals* (Nauka, Moscow, 1982), p. 632.
10. M. Yu. Dvoesherstov, V. I. Cherednick, A. P. Chirimanov, and S. G. Petrov, Proc. SPIE **3900**, 290 (1999).

Translated by A. Kruglov

Acoustical Physics, Vol. 48, No. 6, 2002, pp. 681–686. Translated from Akusticheskiĭ Zhurnal, Vol. 48, No. 6, 2002, pp. 770–776.

Sound Signal Scintillation Approach in the Acoustic Modeling of the Current Speed Profile in the Fram Strait

I. B. Esipov*, O. M. Johannessen, K. A. Naugolnykh***, O. B. Ovchinnikov*, and Yu. I. Tuzhilkin***

** Andreev Acoustics Institute, Russian Academy of Sciences, ul.Shvernika 4, Moscow, 117036 Russia*
e-mail: ibesipov@akin.ru
*** Nansen Environment and Remote Sensing Center, N–5037 Bergen, Norway*
**** Environmental Technologies Laboratory NOAA (Zeltech), University of Colorado, 80303 Boulder, USA*
Received March 27, 2002

Abstract—The results of mathematical model measurements of the speed of the transverse current in the Fram Strait are presented. The method is based on the statistical processing of the propagation time fluctuations of the probing signals along 16 acoustic tracks. The dependence of the sound velocity on depth is assumed to correspond to winter conditions. For the imitation of the current, the three-dimensional field of environmental inhomogeneities observed in the strait is computed. The complex profile of the current in the direction across the strait is represented by the motion of 10 layers of this field that move with different velocities. The measuring system consists of four transmitters and four receivers positioned near both coasts of the strait. The rays used for the measurements do not touch the bottom and do not change their type under the effect of environmental inhomogeneities crossing the acoustic tracks. © *2002 MAIK "Nauka/Interperiodica".*

In recent years, interest among scientists in the problem of predicting global changes in the Earth's climate has increased. Global warming will lead to an increase in the ocean level, floods covering seaside cities, and other consequences, which are necessary to know beforehand. An important role in the formation of the climate of the Northern Hemisphere is played by the temperature of waters of the Arctic Ocean. The temperature, in turn, depends on the amount of heat transferred to the ocean through straits and estuaries. Most of the heat enters with the Gulf Stream through the Fram Strait [1, 2], which explains the interest taken by researchers in arranging a monitoring of the temperature of its waters and the speed of their currents. Some aspects of temperature monitoring by the acoustic method are considered in our previous paper [3]. Here, we will dwell on the problems of using acoustics for the observation of currents.

The currents along the acoustic tracks are measured by the travel time difference of the sound signals in the reciprocal transmission [4–7]. However, one of the main features of the current in the Fram Strait is its variability in the direction across the strait. Therefore, obtaining the total run of the current needs a great number of measurements. Methods of measuring currents directed across the acoustic track seem to be more attractive. These methods are considered in [8–11]. The main feature of these works is the assumption that the field of currents is uniform over the whole acoustic track, which does not hold for the conditions in the Fram Strait.

The most adequate method for solving this problem is the scintillation approach. It was developed in optics, where it obtained its name [12]. The method is based on the analysis of the amplitude and phase fluctuations that occur in the received signal because of the inhomogeneities transferred by a current through the acoustic track. The theory of the method is given in [13]. The results of the sea tests are described in [14]. The method uses horizontal arrays of large dimensions, which allows phasing the array not only by azimuth but also by distance along the acoustic track. The resolution in distance increases if both arrays (i.e., the transmitting and receiving ones) are phased to the same part of the track. The theory is developed for cases where the reflection of acoustic rays from the waveguide boundaries and the deformation of rays under the effect of hydrological conditions are not taken into account. The experimental validation of the theory was performed in [14] on a short track with the separation of the direct signal by means of time gating.

The possibility of using such methods for monitoring transverse currents on long tracks in conditions close to real ones can be investigated by means of mathematical modeling. Such a modeling for the conditions in the Fram Strait is the goal of our paper.

We begin with considering the features of the test region and the choice of the acoustic track. Then, we

1063-7710/02/4806-0681$22.00

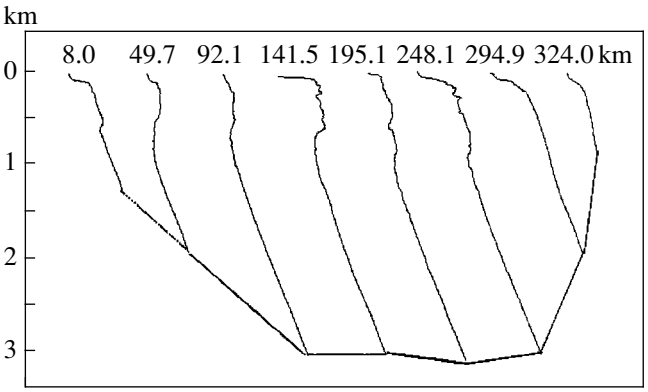

Fig. 1. Sound velocity profiles in different parts of the Fram Strait. East is on the left.

describe the technique for obtaining the three-dimensional field of the water medium inhomogeneities and the model of the distribution of currents. Next, the technique used for the signal processing by horizontal arrays is justified. Finally, the results of estimating the speed distribution in the current along the acoustic track crossing the strait are discussed.

For modeling, we chose the strait region along 79° W, between the Spitsbergen and Greenland islands. The width of the central deep-water part of the strait is close to 300 km, and the average sea depth is 2500 m. The hydrological conditions in this region were determined by the data of the run completed by the R/V *Polarstern* in March of 1993. Therefore, our modeling refers to winter conditions. Typical dependencies of the sound velocity on depth for different parts of the strait are shown in Fig. 1. The distance is measured from the Spitsbergen archipelago. Therefore, in Fig. 1, the east is on the left, as if one is looking on the strait from its northern side. It is seen that the sound velocity minimum is located on the strait surface. The second minimum is seen in its eastern part, at a depth of about 600 m. The overlying layer of higher sound velocity is formed by warm Atlantic waters entering with the West-Spitsbergen current. Owing to high salinity, these waters sink under layers of cooler but less saline waters forming a subsurface minimum of the sound velocity. The thickness of the subsurface layer increases westward where the East-Greenland current carrying low-salinity waters of the Arctic Ocean to the south predominates [15]. The structure of currents in the strait is very complex [16]. Therefore, for modeling, we chose a simplified version, which, however, retains the basic features of this structure. In accordance with [17], it is assumed that, in the eastern one-third of the strait, the current in the surface water layers is directed to the north, while in the remaining part, to the south. The speed distribution in the current is shown in Fig. 5 (the solid line). For simplicity, the speed of the current is assumed to be depth-independent.

The dependence of the sound velocity on depth is not described by smooth functions. This is explained by the turbulent nature of the current. The inhomogeneities transferred by it are clearly seen in Fig. 2, which displays the sound velocity isolines. It is seen that the inhomogeneities are concentrated in the upper 1-km layer. According to the data of [1, 18], the typical dimensions of mesoscale inhomogeneities are within 20 to 50 km, their lifetime is up to 20 days, and the speed of their motion is 5 to 15 km per day. Unfortunately, small-scale inhomogeneities in the strait are poorly investigated.

The conditions in the Fram Strait are rather complicated for describing the sound propagation features. In the modal approximation, one needs to take into account the mode interaction, while in the ray approximation, the variability of ray types. In this paper, as previously in [3], we used the ray approximation. Such a choice seems to be justified, since the length of the acoustic track is much smaller than that where the ray chaos begins leading to strong unpredictable variations of ray trajectories under the effect of small changes in environmental conditions [19]. However, this method is justified only when there are rays that do not change their type (i.e., retain the number of reflections from the sea surface and the number of lower turning points) under the effect of inhomogeneities transferred by the current. Such rays are lacking among those propagating in the upper turbulent layer. On the other hand, rays emerging from the source at large angles touch the bottom, whose characteristics are not exactly known. As a compromise, we chose the rays that do not touch the bottom and experience five reflections from the surface. They allow us to determine the speed of the current at a rather larger number (5) of track segments. In addition, they penetrate to depths where the sound velocity exceeds that in subsurface layers even in the presence of most intense inhomogeneities. This is the necessary condition for retaining the type of rays. The depth of the lower turning points of these rays is close to 1800 m, where the sound velocity is 1475 m/s. In subsurface layers, the sound velocity is 1460 m/s. With such a velocity difference of 15 m/s, the ray does not touch the bottom. These circumstances limit the length of the acoustic track by the deep-water part of the Fram Strait. The locations of the source (T) and the receiver (R) are shown in Fig. 2. It is assumed that the source is at depths of 100 and 1500 m, at a distance of 80 km from Prince Carl Land. The length of the acoustic track was 210 km. Computations were carried out for different depths of the reception points. Varying the depth within several hundreds of meters, we could shift the coordinates of tangency points of rays on the sea surface. This allowed the estimation of the speed of current at ten segments of the track.

As noted above, the scintillation method is based on the analysis of signal fluctuations caused by environ-

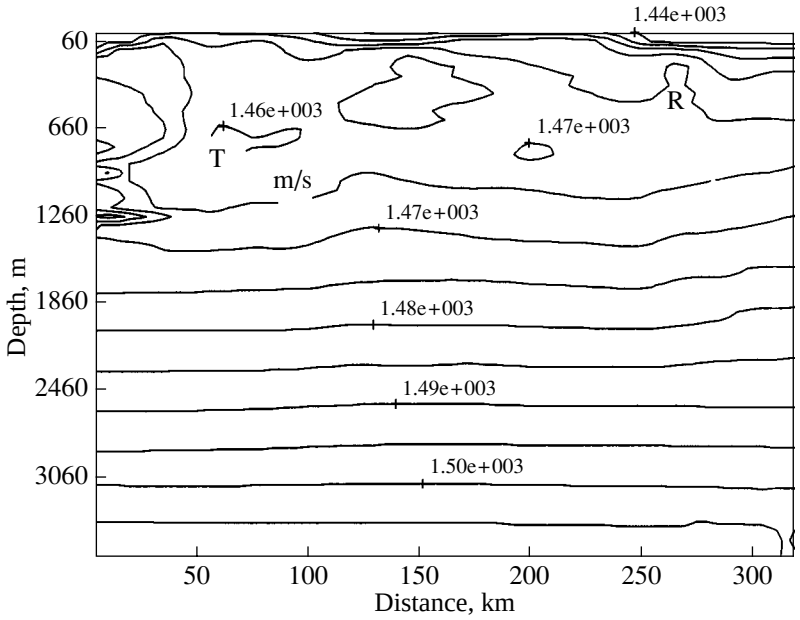

Fig. 2. Sound velocity isolines in the transverse section of the current.

mental inhomogeneities transferred by the current. Therefore, for modeling, it was necessary to generate the three-dimensional field of inhomogeneities with given characteristics. The transfer of this field across the acoustic track can imitate a current. The transfer of the field with the same speed over the whole track imitates a uniform current. Otherwise, the current will be nonuniform along the track, which is characteristics of the Fram Strait. In its imitation, the field is separated into several branches moving with different speeds. Since the sound velocity $c(z, r)$ in the strait depends not only on the presence of inhomogeneities but on the specific segment of the acoustic track as well, we must determine what will be understood as inhomogeneities. As initial material, we used the distribution $c(z, r)$ obtained from the measurements of R/V *Polarstern* (Fig. 2). It is represented by sampling values in z at 64 depths and in the distance r with a step of 5 km. For each r_i, using the method of least squares, the function z_j, r_i is represented by a third-degree polynomial. The resulting functions $c_0(z, r_i)$ are taken as regular components of the sound velocity field. The field inhomogeneities are determined as the difference

$$\delta c_0(z_j, r_i) = c(z_j, r_i) - c_0(z_j, r_i). \quad (1)$$

As statistical characteristics of inhomogeneities, their variance Δ_0^2 and the spatial spectrum were calculated. Subsequent field realizations were obtained by adding a random component at each field point. To provide the slowness of the field variations, these components were small (no greater than $\pm 0.1\Delta_0$). Its spatial characteristics remained relatively stable under two additional conditions: the random component was introduced to the kth realization only if the following inequalities were satisfied:

$$[\delta c_k(z_j, r_i) - \delta c_{k-1}(z_j, r_i)] \times [\delta c_{k-1}(z_j, r_{i+1}) - \delta c_{k-1}(z_j, r_i)] \geq 0, \quad (2)$$

$$[\delta c_k(z_j, r_i) - \delta c_k(z_{j-1}, r_i)] \times [\delta c_{k-1}(z_j, r_i) - \delta c_{k-1}(z_{j-1}, r_i)] \geq 0. \quad (3)$$

In other words, the sound velocity at a point z_j, r_i can increase or decrease in passing to the kth realization if in the previous realization it increased or decreased with increasing r [condition (2)]. Condition (3) requires the coincidence of signs of the derivatives of δc_k with respect to the depth z. At every step of the computations, 100 random numbers were given. When none of them satisfied inequalities (2) and (3), the sound velocity gradients were set equal to zero. As a result, the sound velocity gradient could change its sign. After filtering and normalization, the computed field appeared to be homogeneous. Its variances and spatial spectra along the z and r axes were the same in all realizations. The spectra along the k axis (k is the number of realization) were also computed. Equating the field correlation intervals along the r and k axes, we obtain an equation that allows one to determine the spatial scale to which the step along the k axis corresponds in the inhomogeneous field isotropic in the horizontal plane at a chosen depth. In modeling, the field was assumed to be isotropic at a depth of the location of most intense inhomogeneities. It is clear that, introducing some coefficient in this equation, we can model the field of inhomogeneities, compressed or expanded in the direction of the current. Average statistical characteristics can be

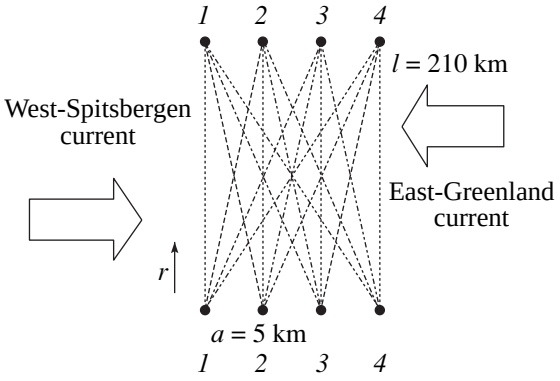

Fig. 3. Schematic positions of the sources and receivers of the measuring system.

obtained if the amount of the field data is rather large. In this paper, 12000 runs similar to those shown in Fig. 2 represent the random field of inhomogeneities.

The ray code used allows one to compute the fluctuations of the amplitudes and travel times of signals propagating along the rays. In this paper, we consider only time fluctuations. They arise when the realizations of the field of inhomogeneities change on the acoustic track. Large-scale inhomogeneities generate slow fluctuations at a constant speed of current u, while small-scale inhomogeneities generate fast fluctuations. When a measuring scheme consists of two parallel tracks separated along the current by the distance d, fluctuations at both receivers should be correlated after the compensation of the time delay d/u. When the tracks have a common source and two separated receivers, correlated fluctuations are generated only by the inhomogeneities located within the parts of divergent tracks where the distance between them is close to d. Fluctuations generated by inhomogeneities in other parts of the tracks are uncorrelated and play the role of noise. The correlated part of fluctuations can be accumulated using a group of divergent and convergent tracks. When the fluctuations are added up, their correlated part is accumulated faster than noise. The measured system used is shown in Fig. 3. It consists of four sources and four receivers forming two parallel chains at both ends of the strait of width l. In the chains, the distance a between the elements is much smaller than the strait width. The system allows one to arrange 16 acoustic tracks that differ from one another by the element numbers and the frequency of the transmitted signal. The fluctuations of signal travel times are added up over all 16 tracks after introducing the necessary delays. Choosing them, we can tune the system to the speed u measured at the distance r from the sources, which is about the same along any track. The value of the delay $t_{i,j}$ between the ith source and the jth receiver is taken from the table.

To measure the speed u of the current at the distance r, we need to substitute this value into the expression for the delays $t_{i,j}$ and, using the method of item-to-item examination, find the value of u corresponding to the maximal sum of fluctuations. For the measuring system to be wide-band with respect to the spatial frequencies, its dimensions along the current must be moderate: the distance between end elements (aperture) equals 15 km at $a = 5$ km. The system is most sensitive to inhomogeneities with dimensions of 4–7 km. Based on the hypothesis of frozen turbulence, we can assume that such inhomogeneities retain their form within the aperture of the measuring system. The inhomogeneities of greater dimensions generate fluctuations correlated over all tracks and are unsuitable for the measurements. They were filtered out from the spatial spectrum. The results of modeling are shown in Fig. 4. In this case, the system was tuned to the distances $r = 20$, 40, and 160 km. The maxima of the variance of the sums of fluctuations averaged over 12000 realizations were near the current speeds –0.1, –0.05, and 0.02 m/s. The negative values of the speed correspond to the northward direction.

Figure 5 exhibits the results of the total distribution of the speed of current in the strait. They were obtained by the following procedure. First, on the basis of the atlas data [17], we determined the function describing the direction and speed of current in the transverse section of the strait (the solid line in Fig. 5). In contrast to [17], in our case the current was assumed to be barotropic. Then, the current was imitated by the motion of the three-dimensional field of inhomogeneities. The current was divided by the vertical planes into 10 layers of about the same width, so that the middle of each layer was at a point where the ray exits to the sea surface. Remember that, in computations, two sets of depths were used for the source and receiver locations. This doubled the number of ray tangents to the strait surface. Each layer moves across the track with the speed given at this segment of the track. The measuring system was tuned beforehand to the coordinates of the points of the ray exit to the surface, and, at each such point, the enumeration of all possible values of speeds was performed with a step of 0.025 m/s. The results of calculations are shown in Fig. 5 by rectangles. One can easily see that the modeling provides an appropriate pattern of the speed distribution for currents in the strait, which offers the possibility of remote tracking this current by remote acoustic sensing. The maximal error is close to 0.03 m/s.

In discussing the results, it is expedient to begin with the adopted model of the current. It does not take into account the effect of surface roughness, internal waves, and ice cover. Each of these factors can lead to arrival time fluctuations of the probing signals of the order of 10 ms [20–22]. Due to such a model of inhomogeneities, the mean square deviation of fluctuations is close to 5 ms; i.e., the useful effect has the same order of magnitude as noise. However, the situation can be improved using the accumulation in time. Indeed, the measurement of the current structure is carried out by the arrival time fluctuations of the probing signals along

Table

$t_{44} = 0$	$t_{34} = \frac{a(l-r)}{ul}$	$t_{24} = \frac{2a(l-r)}{ul}$	$t_{14} = \frac{3a(l-r)}{ul}$
$t_{43} = \frac{ar}{ul}$	$t_{33} = \frac{a}{u}$	$t_{23} = \frac{a(2l-r)}{ul}$	$t_{13} = \frac{a(3l-2r)}{ul}$
$t_{42} = \frac{2ar}{ul}$	$t_{32} = \frac{a(l+r)}{ul}$	$t_{22} = \frac{2a}{u}$	$t_{12} = \frac{a(3l-r)}{ul}$
$t_{41} = \frac{3ar}{ul}$	$t_{31} = \frac{a(l+r)}{ul}$	$t_{21} = \frac{a(2l+r)}{ul}$	$t_{11} = \frac{3a}{u}$

the acoustic tracks. The accuracy of the arrival time measurement depends on the pulse form and the signal-to-noise ratio at the point of reception [23]. If the envelope of the probing pulse has, e.g., the Gaussian form

$$\frac{1}{\sigma\sqrt{2\pi}}\exp\left(-\frac{(t-t_0)^2}{2\sigma^2}\right)$$

with the variance σ^2, the mean square error in determining the arrival time t_0 is

$$\sigma_t \geq \frac{\sigma N}{S},$$

where S is the average amplitude of the pulse at the point of reception and N is the mean square amplitude value of noise when the signal is absent. If the waveguide has no inhomogeneities, then, using rather powerful sources, one can decrease σ_t up to a required value. Unfortunately, σ is determined to a considerable extent by the waveguide inhomogeneities and the roughness of its upper boundary caused by sea waves or by the ice cover. After its scattering from the surface, the signal arrives at the receiver at times that differ from the arrival time of the main signal, which spreads the total pulse. For a symmetric spreading, one can use the accumulation over the envelope of several pulses. Indeed, the characteristic period of fluctuations caused by inhomogeneities is determined by the time of their presence at the acoustic track. The average dimension of inhomogeneities in use is 6 km. Assuming that the speed of current is 1 m/s, which is certainly an overstated value, we obtain the time of crossing equal to 100 min. When transmitting one pulse per minute and combining the received signals by their envelopes, the signal-to-noise ratio can be increased by a factor of 10 due to the averaging of fast fluctuations caused by the sea waves and the roughness of the ice cover. When a pulse expands asymmetrically, some shifts occur in the estimates of the arrival times. Their determination needs a separate investigation.

The system considered can be used in practice. The main difficulty in using it is the necessity to determine the real location of the transmitting and receiving elements of the system secured on the cable stretched between the anchor and the neutral-buoyancy buoy. At the present time, this problem is solved by means of bottom acoustic beacons located near the transmitters and receivers.

It remains to note that the measurements were carried out with signals arriving over rays that did not change their type in the course of measurements. In modeling, they were singled out by the arrival times of

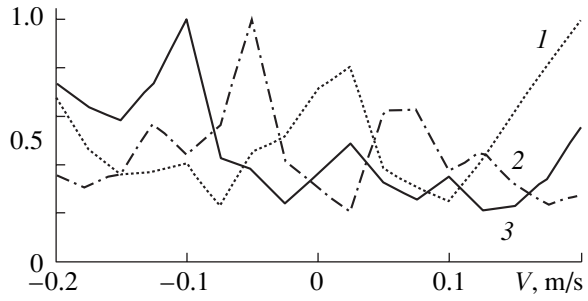

Fig. 4. Dependence of the variance of the total signal on the speed of current with the system tuned to r = (*1*) 20, (*2*) 40, and (*3*) 160 km.

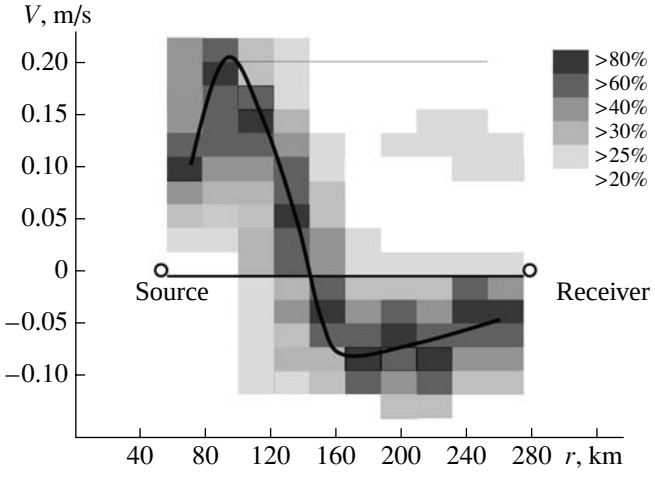

Fig. 5. Preset distribution of the speed of current in the transverse section of the strait (the solid line) and the results of its estimation by the scintillation approach.

the signals within a certain time interval. In practice, the arrival angle can also be taken into account. To this end, the chain of the receivers must be replaced by a chain of vertical arrays.

Let us summarize the results. The mathematical modeling shows that, in the Fram Strait, it is possible to develop an acoustic system that allows one to measure the speed of the current in separate parts of the transverse section of the strait. The system consists of horizontal chains of transmitters and receivers positioned along both sides of the strait and forming a set of acoustic tracks. Among the rays connecting the sources and the receivers, those rays that do not touch the bottom and do not change their type under the effect of inhomogeneities transferred by the current are singlet out. The separation of the rays is performed through the time gating and, in more complicated cases, by the arrival angle as well. On each track, the travel time fluctuations are measured for signals propagating over these rays. It is assumed that, at distances of an order of three characteristic dimensions of inhomogeneities of the water medium, the hypothesis of frozen turbulence is valid. In this case, the travel time fluctuations of the signals travelling along these rays will be partially correlated after the introduction of time delays calculated for a given distance from the source and a given speed of current. The variance of the sum of fluctuations over all tracks is maximal for correct values of the distance and the speed of current. The necessary condition for the presence of rays that do not touch the bottom and do not change their type in the turbulent flow is the sufficiently large depth of the strait. A ray exits to the surface if the sound velocity at its lower turning point is greater than the sound velocity in the subsurface layers filled with inhomogeneities. The deep-water part of the Fram Strait satisfies this condition.

ACKNOWLEDGMENTS

This work was supported by the CRDF, project no. RG2-2333-MO-02, and the EST.CLG, project no. 977890.

REFERENCES

1. K. Aagard and E. C. Carmack, in *Polar Oceans and Their Role in Shaping Global Environment. Geophysical Monography* (Am. Geophys. Union, 1994), Vol. 85, pp. 5–20.
2. O. M. Johannessen, E. Bjargo, and M. W. Milas, Science **271**, 129 (1996).
3. K. Naugolnykh, O. Johannessen, I. Esipov, *et al.*, J. Acoust. Soc. Am. **104**, 738 (1998).
4. P. F. Worcester, J. Acoust. Soc. Am. **52**, 895 (1977).
5. W. H. Munc, P. Worcester, and C. Wunch, *Ocean Acoustic Tomography* (Cambridge Univ. Press, Cambridge, 1995).
6. O. A. Godin, D. Yu. Mikhin, and S. A. Molchanov, Izv. Ross. Akad. Nauk, Fiz. Atmos. Okeana **29** (2), 194 (1993).
7. O. A. Godin, D. Yu. Mikhin, and A. V. Mokhov, Akust. Zh. **42**, 501 (1996) [Acoust. Phys. **42**, 441 (1996)].
8. B. F. Kur'yanov and L. M. Nefedov, in *Proceedings of 9th All-Union Acoustical Conference, Sec. D* (Acoustics Institute, USSR Academy of Sciences, Moscow, 1977), pp. 65–68.
9. I. M. Fuks, Radiotekh. Élektron. (Moscow), No. 3, 515 (1975).
10. I. Fuks, K. Naugolnykh, and M. Charnotskii, J. Acoust. Soc. Am. **106**, 2119 (1999).
11. I. Fuks, M. Charnotskii, and K. Naugolnykh, J. Acoust. Soc. Am. **109**, 2730 (2001).
12. R. W. Lee, J. Opt. Soc. Am. **64** (10), 1295 (1974).
13. G. B. Crawford, R. J. Lataitis, and S. F. Clifford, J. Acoust. Soc. Am. **88**, 442 (1990).
14. D. M. Farmer and G. B. Crawford, J. Acoust. Soc. Am. **90**, 1582 (1991).
15. E. G. Nikiforov and A. O. Shpaĭkher, *Formation of Large-Scale Fluctuations of the Hydrological Conditions in the Arctic Ocean* (Gidrometeoizdat, Leningrad, 1980).
16. A. G. Gladfelder, *Oceanography of the Greenland Sea. V/59 Atka (AGB-3) Survey Summer 1962* (US Nav. Ocean Off., Washington, 1964).
17. *Ocean Atlas. The Arctic Ocean* (Minoborony SSSR, 1980).
18. O. M. Johannessen, J. A. Johannessen, E. Svendsen, *et al.*, Science **236**, 427 (1987).
19. K. B. Smith, V. G. Brown, and F. D. Tappert, J. Acoust. Soc. Am. **91**, 1939 (1992).
20. J. F. Lynch, G. Jin, R. Pawlowicz, *et al.*, J. Acoust. Soc. Am. **99**, 803 (1996).
21. K. J. Noble and S. M. Flatte, J. Acoust. Soc. Am. **107**, 747 (2000).
22. J. S. Gerber and S. M. Flatte, J. Acoust. Soc. Am. **109**, 528 (2001).
23. S. M. Flatte and R. B. Stoughton, J. Geophys. Res. **91** (C6), 7709 (1986).

Translated by Yu. Lysanov

Acoustical Physics, Vol. 48, No. 6, 2002, pp. 687–696. Translated from Akusticheskiĭ Zhurnal, Vol. 48, No. 6, 2002, pp. 777–787.

Relaxation Nature of the Domain Structure in a Cholesteric Liquid Crystal under the Effect of Ultrasound

E. N. Kozhevnikov

Samara State University, ul. Akad. Pavlova 1, Samara, 443114 Russia

e-mail: kozhev@ssu.samara.ru

Received January 24, 2002

Abstract—The relaxation of the orientational order in liquid crystals in a sound field is taken as the basis for the theoretical description of the spatially modulated structures arising in a layer of a cholesteric liquid crystal under the effect of ultrasound. Two mechanisms of the destabilization of a cholesteric liquid crystal layer with planar initial orientation are analyzed: the vortex mechanism, which takes into account the contribution of relaxation processes to the formation of an oscillating vortex flow in the layer of a cholesteric liquid crystal, and the nonlinear relaxation mechanism based on the stationary nonlinear stress and moments arising due to the relaxation of the orientational order in a sound field and unrelated to the vortex flows. It is demonstrated that, when both these mechanisms are simultaneously in effect, the formation of a domain structure must be observed in a wide frequency range. The results of calculations are compared with experimental data. © *2002 MAIK "Nauka/Interperiodica".*

Nematic and cholesteric liquid crystals demonstrate the variety of spatially modulated dissipative structures (domains), which may arise in them as a result of the periodic deformation of crystals in oscillating flows, viscous waves, and sound fields. The domain form depends on the initial orientation of a crystal, the geometry of a liquid-crystal cell, and the type and frequency of action. The theoretical analysis of domain structures was performed in papers published earlier (see, e.g., [1–8]) within the framework of linear hydrodynamics of Leslie and Ericsen [9, 10], where the viscous stress and moments are a linear combination of the gradients of velocity and rate of director rotation and the processes of structural relaxation are not taken into account. Such an approach provides an opportunity to develop an adequate description of a dissipative structure arising in a crystal in the case of a low-frequency deformation but can be insufficient at ultrasonic frequencies. The necessity to take into account the relaxation processes and the nonlinear terms in rheological relations in describing the dissipative structures in liquid crystals is substantiated below using the example of a theoretical description of domains that arise in a layer of a cholesteric liquid crystal when the crystal is compressed in an ultrasonic field.

Experimental studies [1, 11, 12] show that, in the case of the ultrasonic wave incidence upon a layer of a cholesteric liquid crystal (LC) with the planar orientation of molecules, periodic structure distortions arise in the LC. These distortions are observed as domains, and the effect is of a threshold character. The structure form depends on the initial geometry of an LC sample, and its spatial period decreases with advancing over the effect threshold. An attempt to describe theoretically the formation of a spatially-modulated structure in a layer of a cholesteric LC in the case of normal incidence of an ultrasonic wave upon it was made in [13] on the basis of the Leslie–Ericsen hydrodynamics. The mechanism of domain formation under the effect of periodic compression within the framework of linear hydrodynamics is as follows. A random deviation, periodic along the layer, of the director from the equilibrium orientation $\delta\mathbf{n}$ gives rise to shear stress and moments of the form $\delta\sigma_{ij} \sim \delta n_i n_k v_{kj}$ and $\delta\Gamma_i^v \sim \delta n_k v_{ik}$ (σ_{ij} and $\mathbf{\Gamma}^v$ are the viscous stress and moments and v_{ij} is the rate of deformation of the medium). This results in the appearance of oscillating vortex flows in the crystal. The phase delay of the particle displacement in the flows relative to the deformation caused by the sound field gives rise to stationary flows, which can enhance the initial rotation of the director. The initial structure of the crystal is stabilized by the elastic Frank's moments. The actions of the destabilizing and elastic moments become equal at the effect threshold, and domains form with a further increase in the action intensity. Calculation [13] predicts the formation of a domain structure in a layer of a cholesteric LC under the effect of ultrasound. At the same time, a significant qualitative disagreement with experimental data, which was revealed by a detailed comparison [12], indicates that it is impossible, within the framework of the classical hydrodynamics of cholesteric LC, to adequately describe the domain structure formed as a result of the compression of a layer of a cholesteric LC at ultrasonic frequencies.

1063-7710/02/4806-0687$22.00

Let us analyze the effect of ultrasound on a layer of a cholesteric LC once more with allowance for the effects connected with the relaxation of the parameter of orientational order. The inclusion of the relaxation leads to the following mechanisms of destabilization of the structure of the cholesteric LC layer. The first of them is the vortex one. It is analogous to the mechanism described in [13], but it takes into account the displacement delay in the oscillating flows because of the relaxation processes in the medium and the viscoelastic character of the crystal deformation at high frequencies. The second mechanism is the nonlinear relaxation one. It takes into account that the Leslie viscosity coefficients involved in the expression for the viscous stress and moments depend on the orientational order of the crystal and change together with it in the course of the medium deformation in sound and viscous waves. The relaxation delay of these changes relative to the deformation in an external field must give rise to the stationary stress σ_{ij} and moments Γ_i of the form

$$\sigma_{ij}^{(2)} \sim \overline{\left\{ \mathrm{Re}\left[\frac{\delta\alpha}{\delta\varepsilon_{pq}}\varepsilon_{pq}\right] v_{ij} \right\}},$$
$$\Gamma_i^{(2)} \sim \overline{\left\{ \mathrm{Re}\left[\frac{\delta(\gamma_2/\gamma_1)}{\delta\varepsilon_{pq}}\delta\varepsilon_{pq}\right] v_{ik} \right\}} n_k. \tag{1.1}$$

Here, the overbar means averaging over the oscillation period, ε_{pq} are the components of the strain tensor, $v_{pq} = \dot{\varepsilon}_{pq}$, and α and γ are the Leslie viscosity coefficients. These stress and moments nonlinear in the strain have a relaxation nature and are not connected with the rise of additional vortex flows in a medium.

This paper shows that the indicated mechanisms lead to the destabilization of the structure of a planar layer of a cholesteric LC in the case of normal incidence of an ultrasonic wave upon it and, as a result, to the formation of domains. The threshold intensity of sound and the size of domains are determined. It is possible to judge the importance of the relaxation processes in macroscopic phenomena by comparing the theoretical and experimental threshold parameters of the effect.

HYDRODYNAMIC EQUATIONS OF CHOLESTERIC LIQUID CRYSTALS

Describing the effect, we treat a cholesteric crystal as a twisted nematic. Adding the terms nonlinear in the strain rate in the medium to the equations of motion and rotation, we represent them in the form

$$\rho\dot{\mathbf{v}} = -\nabla P + \nabla\cdot\hat{\sigma} + \nabla\cdot\hat{\sigma}^{(2)} + \mathbf{F},$$
$$\gamma_1\mathbf{N} + \gamma_2[\hat{v}\cdot\mathbf{n} - (\mathbf{n}\cdot\hat{v}\cdot\mathbf{n})\mathbf{n}] - \mathbf{\Gamma} + \mathbf{\Gamma}^{(2)} = 0. \tag{2.1}$$

Here, ρ is the density, $\mathbf{v}$ is the velocity, $\mathbf{n}$ is the director, $\mathbf{N} = \dot{\mathbf{n}} - 1/2(\mathrm{rot}\,\mathbf{v}\times\mathbf{n})$ is the velocity of the director rotation with respect to the surrounding medium, $\hat{v}$ is the strain rate tensor, P is the pressure, $\hat{\sigma}$ is the viscoelastic stress tensor [14]

$$\sigma_{ij} = n_i n_j(\Delta E\varepsilon_{\alpha\alpha} + \mu_3 v_{\alpha\alpha}) + \alpha_1 v_{\alpha\beta}n_\alpha n_\beta n_i n_j + \alpha_2 N_i n_j + \alpha_3 N_j n_j + \alpha_4 v_{ij} + \alpha_5 v_{ik}n_k n_j + \alpha_6 v_{jk}n_k n_i, \tag{2.2}$$

$\Delta E = \mathrm{DE}F(\omega\tau)/2$ and $\mu_3 = \mathrm{DE}\tau/[2(1+\omega^2\tau^2)]$ are the anisotropic part of the local elastic modulus and the coefficient of volume viscosity, $\mathrm{DE} = (E_\parallel - E_\perp)\big|_{\omega=0}^{\omega=\infty}$ is the dispersion jump of the anisotropy of the elastic modulus determined along and perpendicularly to the director, $F(\omega\tau) = \omega^2\tau^2/(1+\omega^2\tau^2)$, ω is the frequency of a sound wave, τ is the time of relaxation of the orientational order parameter, α_i are the viscosity coefficients, $\mathbf{\Gamma}$ and $\mathbf{F}$ are the elastic moments and forces arising in a deformed cholesteric structure and determined through the Frank's elastic energy, and $\mathbf{\Gamma}^{(2)}$ and $\hat{\sigma}^{(2)}$ are the nonlinear relaxation moments and stress of the form of Eq. (1.1) (these quantities are constructed using statistical methods). The viscosity coefficient α_3 is assumed to be small by analogy with nematic crystals, and we further assume it to be equal to zero. In this case, the coefficients of rotational viscosity are equal: $\gamma_1 = -\gamma_2 = \gamma$.

Let us specify the form of Eqs. (2.1) for the Cartesian coordinate system, where the z axis determines the direction of the unperturbed axis of the cholesteric helix. In the unperturbed state, the director lies in the cholesteric planes parallel to (x, y) and rotates uniformly with the period P_0 in passing from one plane to another. Let us set the structure distortions by the angles θ and φ determining the deviation of molecules from the unperturbed cholesteric plane and from the initial orientation in this plane, respectively. The density of the Frank's elastic energy g has the following form, when expressed through the variables θ and φ in the two-constant approximation with allowance for the possible tension of the crystal along the cholesteric axis $\delta_z' = \Delta h/h$ [14]:

$$g = \frac{1}{2}K_{33}\{(\nabla_\perp\varphi)^2(1-\delta_z') + \lambda(\nabla_\parallel\varphi)^2 + (\nabla\theta)^2 + q^2\theta^2 + 4q\theta(\mathbf{n}\nabla)\varphi + (\lambda-1)[n_x(\partial_y\theta) - n_y\partial_x\theta]^2\}, \tag{2.3}$$

where $K_{11} = K_{33}$ and K_{22} are the Frank's elastic constants, $\lambda = K_{22}/K_{33}$, and $q = 2\pi/P_0$.

The minimum of the elastic energy for the perturbations of the angles θ and φ that are periodic along the layer leads to the possibility of the formation of domains of the square-grid type at the critical tensile strain δ_0. The strain δ_0, the structure wave number k_0,

and the domain size d_0 at the effect threshold are equal to

$$\delta_0 = \frac{P_0}{4h}\sqrt{2\lambda(3+\lambda)}, \quad k_0 = \frac{2\pi}{\sqrt{P_0 h}}\left(\frac{2\lambda}{3+\lambda}\right)^{1/4}, \qquad d_0 = \frac{\pi\sqrt{2}}{k_0} = \sqrt{hP_0}\left(\frac{3+\lambda}{8\lambda}\right)^{1/4}. \tag{2.4}$$

The elastic moments Γ_θ and Γ_φ conjugate to the angles θ and φ in a distorted cholesteric structure are determined by the Euler equations using the free energy:

$$\Gamma_\varphi = \nabla\frac{\partial g}{\partial\nabla\varphi} - \frac{\partial g}{\partial\varphi} = K_{33}[(1-\delta')\Delta_\perp\varphi + \lambda\varphi_{zz} + 2qn_\alpha\theta_\alpha],$$

$$\Gamma_\theta = \nabla\frac{\partial g}{\partial\nabla\theta} - \frac{\partial g}{\partial\theta} = K_{33}[\Delta\theta - q^2\theta - 2qn_\alpha\varphi_\alpha + (\lambda-1)(n_x^2\theta_{yy} + n_y^2\theta_{xx} - 2n_xn_y\theta_{xy})].$$

Here and below, the index α runs over the values $\alpha = x$, y and $\Delta_\perp = \partial_x^2 + \partial_y^2$.

The force **F** in Eq. (2.1) is determined by the differentiation of the energy g with respect to the displacements **u** at fixed spatial angles of molecule rotation. The following expressions are obtained for the components of **F** [14]:

$$F_z = -q\Gamma_\varphi + n_\alpha\Gamma_{\theta,\alpha}, \qquad F_{x,y} - F_{y,x} = \frac{1}{2}\Delta_\perp\Gamma_\varphi, \quad F_{\alpha,\alpha} = 0.$$

The inequality $\eta\omega/\rho c^2 \ll 1$ is valid at ultrasonic frequencies. It provides an opportunity to eliminate the acoustic modes from the equation of motion (2.1) by using the double rotor operation. We retain the square terms in the equations, which are proportional to the product of the rotation angles of molecules θ and φ by the velocities, and take into account the change of the wave number q_0 in a sound field that is connected with the geometrical tension of the medium. Performing the necessary transformations, we arrive at the following equations:

equations of rotation

$$\gamma_1\left[\varphi_{,t} + q_0v_z - q_0\varepsilon_{zz}v_z - \frac{1}{2}(\mathrm{rot}\mathbf{v})_z + n_xn_y(v_{xx} - v_{yy}) + (n_x^2 - n_y^2)v_{xy}\right] - \Gamma_\varphi + \Gamma_\varphi^{(2)} = 0, \tag{2.5}$$

$$\gamma_1(\dot\theta - n_\alpha v_{z,\alpha} - \theta v_{zz}) - \Gamma_\theta + \Gamma_\theta^{(2)} = 0$$

and equations of motion

$$(\rho\partial_t\Delta - \eta\hat D_1)v_z = -\gamma\Delta_\perp n_\alpha\dot\theta_{,\alpha} + [\Delta E\varepsilon_{zz}\Delta_\perp + (\mu_3+\alpha_5)v_{zz}\Delta_\perp]n_\alpha\theta_\alpha + [\mathrm{rotrot}\mathbf{g}]_z$$
$$-\alpha_6\partial_z^2(v_{zz}n_\alpha\theta_\alpha) - \gamma\Delta_\perp\{q_0[\varphi_t + q_0v_z - \Omega_z + n_xn_y(v_{xx}-v_{yy}) + (n_x^2-n_y^2)v_{xy} - n_\beta\partial_\beta(\dot\theta - n_\alpha v_{z,\alpha} - \theta v_{zz})\} + \Delta_\perp\sigma_{zk,k}^{(2)} - \partial_z(\nabla\cdot\nabla\cdot\hat\sigma^{(2)}), \quad \beta = x,y;$$

$$\left[\rho\partial_t - \left(\eta + \frac{1}{4}\alpha_5\right)\Delta_\perp - \eta\partial_z^2\right]\Omega_z + \frac{1}{4}n_x^2 - n_y^2\left\{\alpha_5(\partial_x^2 - \partial_y^2)\Omega_z - \alpha_6(v_{xy,z^2} + v_{zz,xy}) + \frac{\alpha_6}{2}((3\partial_x^2+\partial_y^2)v_{x,y} + (3\partial_y^2+\partial_x^2)v_{y,x})\right\}$$
$$+\alpha_5n_xn_y\partial_x\partial_y\Omega_z = -\frac{1}{2}\gamma\left\{\Delta_\perp\dot\varphi_m + n_xn_y\left[\partial_x\partial_y\dot\varphi_m + \frac{1}{2}\Delta_\perp(v_{xx}-v_{yy})\right] + \frac{1}{2}(n_x^2-n_y^2)\Delta_\perp v_{xy}\right\} - \frac{1}{2}\alpha_6\partial_z[v_{zz}(n_y\theta_{,x} - n_y\theta_{,y})]$$
$$+\partial_z(\mathrm{rot}\mathbf{g})_z + \sigma_{yk,kx}^{(2)} - \sigma_{xk,ky}^{(2)}, \quad k = x,y,z; \qquad \mathrm{div}\mathbf{v} = 0. \tag{2.6}$$

Here, $\mathbf{g} = \rho[(\mathbf{v}\nabla)\mathbf{v} + \mathbf{v}(\nabla\mathbf{v})]$ is the convective force, $\dot\varphi_m = \varphi_{,t} + q_0v_z - \Omega_z$ is the spatial rate of molecule rotation around the z axis, $\mathbf{\Omega} = 1/2\mathrm{rot}\mathbf{v}$, and $\hat D_1$ is the differentiating operator of the form

$$\hat D_1 = \frac{2\alpha_4 + \alpha_5 + 2\gamma}{4\eta}\Delta_\perp^2 + \frac{\alpha_4 + \alpha_5/2 + 3/8\alpha_1}{\eta}\Delta_\perp\partial_z^2 + \partial_z^4, \qquad \eta = \frac{1}{2}(\alpha_4 + \alpha_6/2).$$

Let us consider an ultrasonic wave with the frequency ω and compression amplitude ε_0 that is incident normally upon a planar layer of a cholesteric LC with the thickness h and analyze its effect upon this layer on the basis of Eqs. (2.5) and (2.6). The axis of the cholesteric helix in the unperturbed state of the crystal (the z axis) is directed along the normal to the layer, and the cholesteric layers are parallel to the layer boundaries $z = 0$ and $z = h$. Assuming that the first boundary of the LC layer in the path of the sound wave ($z = 0$) is acous-

tically transparent and the second one ($z = h$) is hard, we represent the compression of the layer in the sound field by the standing wave

$$\varepsilon \approx 2\varepsilon_0 \cos[k_s(h-z)]\sin\omega t, \tag{2.7}$$

where $k_s = \omega/c$ is the wave number of sound in the layer and c is the sound velocity.

Analyzing the effect, we restrict ourselves to the frequencies at which the sound wavelength in the cholesteric crystal is greater than the helix pitch, and, in the equations for perturbations, we replace the square of liquid compression averaged over the oscillation period and determining the effect by its value averaged over the layer thickness:

$$\overline{\varepsilon^2} = \varepsilon_0^2[1 + \sin(2k_s h)/(2k_s h)].$$

VORTEX MECHANISM OF THE DESTABILIZATION OF A CHOLESTERIC STRUCTURE

Let us consider separately the contribution of viscoelastic stress to the destabilization of the structure of a cholesteric LC by excluding the nonlinear relaxation moments $\mathbf{\Gamma}^{(2)}$ and the stress $\hat{\sigma}^{(2)}$ from Eqs. (2.5) and (2.6). We represent θ, φ, and the velocity perturbations $\delta\mathbf{v}$ as the sums of the stationary (index 2) terms and the terms oscillating (prime) with the sound frequency:

$$\theta = \theta_2 + \theta', \quad \varphi = \varphi_2 + \varphi', \quad \delta\mathbf{v} = \mathbf{v}_2 + \mathbf{v}',$$

and we separate the equations for stationary and nonstationary variables. Let us consider the structure distortions with the minimal free energy, when $\theta = n_\alpha\tau_\alpha$ and the functions τ_α and φ change slowly along the crystal axis. We assume the velocity perturbations also to be functions that slowly vary with z. Let us average all the terms in the equations for φ and $\mathbf{v}$ over the helix pitch P_0 and eliminate the elastic moments, which are small in comparison with the viscous ones, from the equation for oscillating variables.

We assume the stationary perturbations to be equal to zero at the boundaries,

$$\varphi_2\big|_{z=0,h} = \tau_2\big|_{z=0,h} = 0,$$
$$\Omega_z\big|_{z=0,h} = 0; \quad v_{2z}\big|_{z=0,h} = 0,$$

and, ignoring the effects in the boundary layers with the thickness of the order of the viscous wavelength, we determine the oscillating variables v_z' and θ' as a particular solution to the corresponding inhomogeneous equations. The existence condition for a nonzero solution to Eqs. (2.5) and (2.6) corresponds to the threshold of the domain formation.

We represent stationary perturbations in the form of the functions depending periodically on the coordinates x and y and satisfying zero boundary conditions

$$\varphi_2, \tau, v_{2z}, \Omega_z \sim \exp(ik_x x + ik_y y)\sin(k_z z), \tag{3.1}$$

where k_x and k_y are the wave numbers determining the form of the domain structure; $k_z = 2\pi/h$; and, in this case, $\partial_\alpha = ik_\alpha$ and $\Delta_\perp = -k_x^2 - k_y^2 = -k^2$.

We assume that the inequalities

$$k_z < k < q_0 \tag{3.2}$$

are valid and consider the formation of the structure of the square-grid type, where $k_x = k_y$. In the case of such a structure, the terms averaged over the helix pitch, $n_x\theta'_{,y} - n_y\theta'_{,x}$, $n_x\theta_{2,y} - n_y\theta_{2,x}$, and $(\mathrm{rot}\,\mathbf{g})_z$, vanish, and, as a consequence, the rate of rotation of the medium also vanishes: $\Omega_z' = 0$.

We omit the equations for oscillating perturbations because of their length and give expressions for the oscillations of the velocity v_z' and the angles θ' and φ':

$$v_z' = \frac{k^2}{2B}\tau_{2\alpha,\alpha}\{[\eta|D_1|\Delta E + |\Delta|\rho(\mu_3+\alpha_6)\omega^2]\varepsilon_{zz} + [\eta(\mu_3+\alpha_6)|D_1| - |\Delta|\rho\Delta E]v_{zz}\},$$

$$\theta' = \frac{k^2}{2B}n_\beta\tau_{2\alpha,\alpha\beta}\{[\eta(\mu_3+\alpha_6)|D_1| - |\Delta|\rho\Delta E]\varepsilon_{zz} - [\eta|D_1|\Delta E - |\Delta|\rho(\mu_3+\alpha_6)\omega^2]\omega^{-2}v_{zz}\},$$

$$\varphi' = -q_0(u_z' + u_z);$$

we also present the coupled equations for stationary perturbations:

$$\gamma A q_0 v_{2z} - M\varepsilon_0^2 q_0\tau_{\alpha,\alpha} + K_{33}\{[k^2(1-\delta_z') + \lambda k_z^2]\varphi - q_0\tau_{\alpha,\alpha}\} = 0,$$

$$\gamma A k^2 v_{2z} - M\varepsilon_0^2 k^2\tau_{\alpha,\alpha} + K_{33}\left[\left(2q_0^2 + \frac{3+\lambda}{4}k^2\right)\tau_{\alpha,\alpha} - 2q_0 k^2\varphi\right] = 0, \tag{3.3}$$

$$\gamma A v_{2z} - N\varepsilon_0^2\tau_{\alpha,\alpha} = 0.$$

Here,

$$A = (\eta + \alpha_5/4)/(\gamma/2 + \eta + \alpha_5/4),$$

$$M = \frac{2\gamma k^2[1 + \sin(2k_s h)/2k_s h]}{B} \times (\eta|D_1|\Delta E + |\Delta|\rho(\mu_3+\alpha_6)\omega^2),$$

$$N = \frac{[1 + \sin(2k_s h)/2k_s h]}{2Bq_0^2}$$

$$\times\left\{2\rho k^2\omega^2[\rho k^2\Delta E - \eta(\mu_3 + \alpha_6)|D_1|]\right.$$

$$\left. + \mathrm{DE}\Delta E\left[1 + 2\left(\frac{\alpha_6}{\mu_{3,0}}\right) + \left(\frac{\alpha_6}{\mu_{3,0}}\right)^2(1 + \omega^2\tau^2)\right]\right\},$$

$$B = \eta^2[|D_1|^2 + 4\sigma^4|\Delta|^2], \quad \sigma = \sqrt{\rho\omega/2\eta},$$

$$|D_1| = \frac{2\alpha_4 + \alpha_5 + \gamma}{4\eta}k^4 + \frac{\alpha_4 + \alpha_5/2 + 3/8\alpha_1}{\eta}k^2k_z^2 + k_z^2,$$

$$|\Delta| = k^2 + k_z^2,$$

$\mu_{3,0} = \mathrm{DE}\tau/2$ is the viscosity coefficient μ_3 at low frequencies ($\omega\tau \ll 1$), and $\sigma = \sqrt{\rho\omega/2\eta}$ is the wave number in the viscous wave propagating along the crystal axis $\eta = \alpha_4/2 + \alpha_6/4$.

We determine the value of ε_0, at which perturbations with the wave number k start to increase, by setting the determinant of the system of equations (3.3) equal to zero:

$$\varepsilon_0(\omega, k) = \left\{\frac{K_{33}}{4k^2}[(3 + \lambda)(1 - \delta_z')k^4 + 8\lambda k_z^2q^2\right.$$

$$- 8k^2q^2\delta_z' + \lambda(3 + \lambda)(1 - \delta_z')k_z^2k^2] \qquad (3.4)$$

$$\left.\times[(M - N)(2q^2 + k^2 + \lambda k_z^2)]^{-1}\right\}^{1/2}.$$

The wave number k at the effect threshold and the threshold value of ε_{th} is determined by the minimization of $\varepsilon_0(\omega, k)$ with respect to k.

The finite expression for ε_{th} as a function of the parameters of the crystal and the cell is lengthy. We give a simplified expression for ε_{th} that is obtained taking into account the inequality

$$|N/M| \ll 1 \qquad (3.5)$$

and inequalities (3.2). Their validity for typical crystal parameters, helix pitch, layer thickness, and frequencies, which are examined below, is proved by a direct testing.

If conditions (3.2) and (3.5) are valid, the expression for ε_0 is determined by the formula

$$\varepsilon_0(\omega, k) = \left\{\frac{\eta K_{33}k_0^4(3 + \lambda)}{8[1 + \sin(2k_s h)/2k_s h]\gamma\mathrm{DE}q^2}\right.$$

$$\left.\times\frac{(\xi^4 + 1 - 2\xi^2\delta)(\xi^4 + a^2\omega^2\tau^2)}{\xi^4 + a\xi^2}\frac{1 + \omega^2\tau^2}{\omega^2\tau^2}\right\}^{1/2}, \qquad (3.6)$$

where $\xi = k/k_0$, $\delta = \delta'/\delta_0$ is the ratio of the layer extension to the critical one; $a = \rho/(\eta\tau k_0^2)$; and, in the real case, the inequality $a \gg 1$ is valid.

The minimal value of ε_0 in Eq. (3.6) at the frequencies $\tau^{-1}a^{-1} < \omega < \tau^{-1}$ is attained at $\xi = 1$, and the threshold compression ε_{th} in this case depends only slightly on frequency:

$$\varepsilon_{th}^{(1)} = \frac{k_0}{q}\left\{\frac{\rho K_{33}(3 + \lambda)}{4[1 + \sin(2k_s h)/2k_s h]\gamma\tau\mathrm{DE}}(1 - \delta)\right\}^{1/2}, \qquad (3.7)$$

while the characteristic size of the domain structure is equal to $d = d_0$.

The value of ε_{th} increases beyond this frequency interval away from it. At high frequencies, when $\omega > \tau^{-1}$, we obtain $\varepsilon_{th} \approx \varepsilon_{th}^{(1)}\sqrt{a\,\omega\tau} \sim \omega$ and the domain size in this case is equal to $d \approx d_0$. At low frequencies, when $\omega < (a\tau)^{-1}$, we obtain $\varepsilon_{th} \approx \varepsilon_{th}^{(1)}\sqrt{2a/\omega\tau} \sim \omega^{-1/2}$ and $d \approx d_0/\sqrt{a\omega\tau} \sim \omega^{-1/2}$ [14], respectively. Thus, the action of the vortex mechanism in the formation of acoustic domains is most effective within the frequency range $\tau^{-1}a^{-1} < \omega < \tau^{-1}$.

NONLINEAR RELAXATION MECHANISM OF THE DESTABILIZATION OF A CHOLESTERIC STRUCTURE

Let us consider the action of stationary nonlinear relaxation stress and moments while ignoring the oscillating variables in Eqs. (2.5) and (2.6). We use a statistical approach to determine $\mathbf{\Gamma}^{(2)}$ and $\hat{\sigma}^{(2)}$. The microscopic model of a nematic crystal that was proposed in [15–19] lies at its basis. The equation of rotation of a single molecule is constructed within the framework of this model, which serves as the basis for an equation describing the density evolution of the angular distribution of molecule orientations. The microscopic stress arising in this case is determined simultaneously. The averaging of the microscopic stress over the equilibrium distribution provides an opportunity to develop a hydrodynamic description of LC and to determine the Leslie viscosity coefficients, viscoelastic properties of crystals, and anisotropy of their acoustic properties [20–26]. Here, the averaging of the microscopic stress and evolutionary equation is performed over the nonequilibrium density of the orientational distribution of molecules of a nematic LC, which results in the hydrodynamic description of a medium that is nonlinear in the strain rate.

According to [17, 18, 23], we describe the angular dependence in the distribution of the molecule orientation and the microscopic stress in the components of the vector $\mathbf{L}(|\mathbf{L}| = 1)$ and represent the equations of rotation

of a single molecule and the microscopic stress σ'_{ij} arising in this case in the form

$$\dot{L}_i = (\boldsymbol{\Omega} \times \mathbf{L})_i + \Lambda \kappa_{ijk} v_{jk} + bG_i, \tag{4.1}$$

$$\begin{aligned}\sigma'_{ij} = -b^{-1}(&a_2 N_{L,i} L_j + a_3 N_{L,j} L_i + a_5 v_{i\alpha} L_\alpha L_j \\ &+ a_6 v_{j\alpha} L_\alpha L_i + a_1 v_{\alpha\beta} L_\alpha L_\beta L_i L_j),\end{aligned} \tag{4.2}$$

where $\mathbf{N}_L = \dot{\mathbf{L}} - (\Omega \times \mathbf{L})$; $\mathbf{G}$ is the force thermodynamically conjugate to $\mathbf{N}_L$, which arises in the case of the nonequilibrium angular distribution of molecule orientation;

$$\kappa_{ijk} = \frac{1}{2}[\delta_{ij} L_k + \delta_{ik} L_j - 2L_i L_j L_k];$$

b is the rotational mobility; and a_k are the kinetic coefficients. In this case,

$$a_2 - a_3 = 1, \quad a_2 + a_3 = a_6 - a_5 = \Lambda.$$

The coefficient Λ depends on the molecule shape and changes from $\Lambda = 1$ for elongated ellipsoid molecules to $\Lambda = -1$ for disk-shaped molecules [20]. We take $\Lambda = 1$, assuming the molecules to be of elongated shape.

The forces $\mathbf{G}$ can be presented in the form [18, 19]

$$G_i = -T\left(\frac{\partial}{\partial L_i} - L_i L_j \frac{\partial}{\partial L_j}\right) f'. \tag{4.3}$$

Here, $f' = (f - f_0)/f_0$ is the relative deviation of the angular distribution density of molecule axes $f = f(\mathbf{L})$ from the quasi-equilibrium Boltzmann distribution $f_0 = \text{const} \exp\{-E/T\}$, where $E = E(\mathbf{L})$ is the orientational energy of molecules and T is the temperature in the energy representation. The instant values of the temperature T, pressure P, director $\mathbf{n}$, and angular distribution moments $\langle L_{i_1} L_{i_2} \ldots L_{i_k} \rangle$ averaged over the nonequilibrium density of the distribution f are involved in the quasi-equilibrium distribution f_0. In the case of the equilibrium distribution f_{00}, the unperturbed values of the indicated quantities are used.

From Eqs. (4.2) and (4.3), we obtain the following expression for the microscopic stress tensor:

$$\begin{aligned}\sigma'_{ij} = &T\left(L_j \frac{\partial}{\partial L_i} - L_j L_i L_k \frac{\partial}{\partial L_k}\right) f' \\ &- \frac{1}{2} b^{-1}(1 + a_5 + a_6)(v_{i\alpha} L_\alpha L_j + v_{j\alpha} L_\alpha L_i) \\ &- b^{-1}(a_1 - 1) v_{\alpha\beta} L_\alpha L_\beta L_i L_j.\end{aligned} \tag{4.4}$$

Its averaging over the nonequilibrium distribution $f = f_0(1 + f')$ yields nonlinear relaxation stress.

The density of the angular distribution f satisfies the continuity equation in the form

$$\frac{\partial f}{\partial t} + \left[\frac{\partial}{\partial L_i} - L_i L_j \frac{\partial}{\partial L_j}\right](\dot{L}_i f) = 0, \tag{4.5}$$

which, together with the equation of molecule rotation (2.1) and Eq. (2.3), leads to the equation of angular diffusion for the function f'. We describe the orientational interaction of molecules by a self-consistent field with the Maier–Saupe potential $E(L) = -d\langle P_2(L_1)\rangle P_2(L_1)$, where d is the field constant, P_k are the Legendre polynomials, $L_1 = \mathbf{nL}$ is the projection of the vector $\mathbf{L}$ onto the crystal axis, and the angular brackets here and further mean averaging over the equilibrium angular distribution f_{00}. The equation for f' was obtained and studied in [22, 23]. Solving it and restricting ourselves to the relaxation of the parameter of orientational order only, we represent the perturbation f' and the nonequilibrium distribution density in the form

$$\begin{aligned}f' &= (P_2 - \langle P_2 \rangle) A_{11}, \\ f &= f_{00}\{1 + 3d_T L_1 L_s \delta n_s \\ &+ (P_2 - \langle P_2 \rangle)\{-K\beta_S^{-1}\varepsilon + \beta A_{11}\}.\end{aligned} \tag{4.6}$$

Here, $A_{11} = \beta^{-1}\{K\beta_S^{-1}[F\varepsilon + (1 - F)\tau\dot{\varepsilon}] - 3R[F\epsilon_{11} + (1 - F)\tau\dot{\epsilon}_{11}]\}$, β_S is the adiabatic compressibility; $R = 1 - d_T/7 + 12d_T R_{24}/(35R_{22})$, $R_{nm} = \langle P_n P_m \rangle - \langle P_n \rangle \langle P_m \rangle$, $d_T = d\langle P_2 \rangle/T$, $\epsilon_{11} = \varepsilon_{ik} n_i n_k - 1/3\varepsilon$; the parameters K and β have the forms

$$K = \beta d_T \frac{1}{T}\left(\frac{\partial T_c}{\partial p} - \frac{\alpha T V}{C_p}\right),$$

$$\beta = \left(1 + nR_{22}\frac{d_T^2}{C_p} - R_{22}\frac{d}{T}\right)^{-1};$$

T_c is the temperature of orientational melting of the crystal; α is the volumetric coefficient of thermal expansion; V is the volume; C_p is the specific heat at constant pressure; and the function $F = F(\omega\tau)$ determines the relaxation dependence of the angular distribution perturbation on the action frequency.

The stress $\hat{\sigma}^{(2)}$ in a one-dimensional sound field with the oscillation direction determined by the unit vector $\mathbf{m}$ is reduced to the form

$$\hat{\sigma}^{(2)} = nT\bar{\varepsilon}^2 \hat{\Sigma}(\omega, \mathbf{m}, \mathbf{n}), \tag{4.7}$$

where the dimensionless tensor function $\hat{\Sigma}(\omega, \mathbf{m}, \mathbf{n})$ determines the dependence of nonlinear stress on the molecular parameters of the medium and on the frequency and direction of sound propagation; its components are

$$\begin{aligned}\Sigma_{ij} = &\beta^{-1}[K\beta_S^{-1} + R(3m_1^2 - 1)] \\ &\times F(\omega\tau)\left\{-\frac{3}{2}\langle P_2 \rangle m_1(m_i n_j - m_j n_i)\right. \\ &\left. - 3R_{22}(a_5 + a_6)R\left[m_1(m_i n_j + m_j n_i) - \frac{2}{3}m_i m_j\right]\right.\end{aligned}$$

$$-6a_1R\left[\langle P_2^2(P_2-\langle P_2\rangle)\rangle(m_1^2-1/3)+\frac{1}{3}R_{22}\right] \quad (4.8)$$

$$\times(n_in_j-\delta_{ij}/3)-6a_1R\langle P_2^2(P_2-\langle P_2\rangle)\rangle(m_1^2-1/3)\delta_{ij}$$

$$-\frac{3}{4}a_1R\langle(1-L_1^2)^2(P_2-\langle P_2\rangle)\rangle$$

$$\times[2m_im_j-m_1^2n_in_j-(\mathbf{n}\times\mathbf{m})_i(\mathbf{n}\times\mathbf{m})_j]\Bigg\}.$$

We derive the equation of the director rotation directly from the balance equation of the distribution density (2.6). Let us multiply all the terms in the equation by L_1L_s ($s = 2, 3$) and integrate with respect to the directions of the vector $\mathbf{L}$. Taking into account the relation $\langle L_1^2 - L_1^4\rangle = 2d/3T$, which can be readily obtained for the Boltzmann distribution with the Maier–Saupe potential, we reduce the equation of the director rotation to the form

$$\dot{n}_s+\frac{bT}{\langle P_2\rangle}\int f(n_iL_s+L_1\delta_{is})\left[\frac{\partial}{\partial L_i}-L_iL_j\frac{\partial}{\partial L_j}\right]f'd\mathbf{L}$$

$$-\frac{1}{\langle P_2\rangle}\int f(n_iL_s+L_1\delta_{is})\{\nu_{i,p}L_p-\nu_{pq}L_pL_qL_i\}d\mathbf{L}=0.$$

Transforming this equation with the help of Eq. (4.6), we arrive at the nonlinear equation of director rotation. We separate the part in it that describes the director evolutions that are slow in comparison with the frequency of the external action. For this purpose, we average each term over the oscillation period. Adding also the Frank's elastic moments $\mathbf{\Gamma}$, which are not included in the initial molecular model of a nematic LC, we obtain a finite equation for the slow rotation of the director in a one-dimensional sound field:

$$\delta\dot{\mathbf{n}}-\frac{1}{2}(\mathrm{rot}\mathbf{v}\times\mathbf{n})+\frac{\gamma_2}{\gamma_1}[\hat{\nu}\cdot\mathbf{n}-(\mathbf{n}\cdot\hat{\nu}\cdot\mathbf{n})\mathbf{n}]$$
$$-\frac{1}{\gamma_1}\mathbf{\Gamma}-\omega_2F\varepsilon_0^2m_1(\mathbf{m}-m_1\mathbf{n})=0, \quad (4.9)$$

where

$$\omega_2=\frac{[1+\sin(2k_sh)/2k_sh]}{\tau\langle P_2\rangle}[K\beta_S^{-1}$$

$$+R(3m_1^2-1)]\left\{\frac{1}{7}\left(R_{22}+\frac{16}{5}R_{24}\right)\right.$$

$$\left.+\frac{1}{6}(\langle P_2\rangle+2-10T/d)\right\}$$

is the parameter with the dimension of frequency.

In the given geometry of the effect of a sound field upon the layer of a cholesteric LC, we obtain $\mathbf{n} = (0, 0, 1)$, $\mathbf{n} = (n_x, n_y, \theta)$, and $m_1 = \theta$. Further more, we omit the small term containing ω_2 in the expression for m_1^2. Determining the matrix elements Σ_{ij} according to Eq. (4.8), we write down the components of the stress tensor that are necessary for the equations:

$$\sigma_{zs}^{(2)}=-2\gamma\omega_1^+\varepsilon_0^2F\theta n_s,\quad \sigma_{sz}^{(2)}=2\gamma\omega_1^-\varepsilon_0^2F\theta n_s, \quad (4.10)$$

where

$$\omega_1^{\pm}=\frac{nT}{2\gamma}\beta^{-1}\left[1+\frac{\sin(2k_sh)}{2k_sh}\right](K\beta_S^{-1}-R)$$

$$\times\left\{\frac{3}{2}\langle P_2\rangle\pm R[3R_{22}(a_5+a_6)\right. \quad (4.11)$$

$$\left.+2a_1(R_{22}-\langle P_2^2(P_2-\langle P_2\rangle)\rangle)]\right\}$$

are the parameters, which also have the dimension of frequency.

The stress $\sigma_{xy}^{(2)}$ is symmetric with respect to the transposition of indices, and the diagonal elements of the stress tensor $\hat{\sigma}^{(2)}$ coincide. These components will not be used in the equation of motion.

Let us again consider the structure distortions with the minimal free energy when $\theta = n_\alpha\tau_\alpha$ and the functions τ_α and φ and the flow velocities change slowly along the crystal axis. We determine the periodic dependence of the variables on the coordinates according to Eq. (3.1). Retaining only the nonlinear relaxation terms in Eqs. (2.5) and (2.6), we separate the equations for τ, φ_2, $\nu_{2,z}$, and Ω_z with the coefficients containing the external action ε_0^2:

$$\gamma(q\nu_z-\Omega_z)+K_{33}\{[k^2(1-\delta_z')+\lambda k_z^2]\varphi-q\tau_{\alpha,\alpha}\}=0,$$

$$\gamma k^2\nu_z-\gamma\omega_2F\varepsilon_0^2k^2\tau_{\alpha,\alpha}$$

$$+K_{33}\left[\left(2q^2+\frac{3+\lambda}{4}k^2\right)\tau_{\alpha,\alpha}-2qk^2\varphi\right]=0, \quad (4.12)$$

$$q(q\nu_z-\Omega_z)+\omega_1^+F\varepsilon_0^2\tau_{\alpha,\alpha}=0,$$

$$\left(\eta+\frac{1}{4}\alpha_5\right)\Omega_z-\frac{1}{2}\gamma(q\nu_z-\Omega_z)=0.$$

We determine the value of ε_0, at which the perturbations with the wave number k start to grow, by setting to zero the determinant of the set of equations (4.12):

$$\varepsilon_0(\omega,k)$$

$$=\left\{\frac{(3+\lambda)K_{33}}{4\gamma(2\omega_1^+A+\omega_2)}\frac{k^4+k_0^4-2k^2k_0^2\delta}{k^2}F^{-1}(\omega\tau)\right\}^{1/2},$$

where $A = (\eta + \alpha_5/4)/(\gamma/2 + \eta + \alpha_5/4)$.

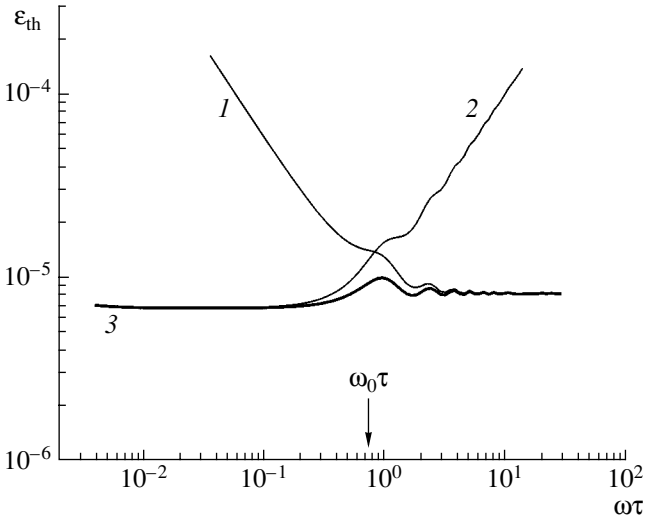

Fig. 1. Dependence of the threshold compressibility on frequency. (*1*) Vortex mechanism, (*2*) nonlinear relaxation mechanism, and (*3*) complete theory. The parameters of the layer of a cholesteric LC are $h = 100$ μm, $P_0 = 10$ μm, and $\delta = 0.8$.

The wave number of the domain structure at the effect threshold k_{th} and the threshold value of $\varepsilon_{th}^{(2)}$ are determined by the minimization of $\varepsilon_0(\omega, k)$ with respect to k:

$$k_{th} = k_0 = \frac{2\pi}{\sqrt{P_0 h}}\left(\frac{2\lambda}{3+\lambda}\right)^{1/4},$$
$$\varepsilon_{th}^{(2)} = \left\{\frac{(3+\lambda)K_{33}k_0^2}{\gamma(2\omega_1^+ A + \omega_2)}\frac{1+(\omega\tau)^2}{(\omega\tau)^2}(1-\delta)\right\}^{1/2}. \quad (4.13)$$

DISCUSSION

Let us compare the effects of the two aforementioned mechanisms of the structure destabilization for a layer of cholesteric LC with each other and with experimental data. Experimental observation of domains in a layer of a cholesteric LC under the effect of ultrasound in the frequency range 0.3–3.6 MHz is described in [1, 11, 12]. These publications report on the formation of a domain structure of the square-grid type with sides that are parallel and perpendicular to the rubbing lines of the boundary surface. The grid appears only in separate parts of the layer of a cholesteric LC, where, presumably, the layer extension at disclinations takes place.

The parameters of a cholesteric LC in the numerical analysis were assumed to be equal to the typical ones for nematic crystals: $K_{33} \approx 0.5 \times 10^{-11}$ N, $\alpha_4 \approx \gamma_1 \approx 0.1$ Pa [10], $c = 1.5 \times 10^3$ m/s, $\tau = 3 \times 10^{-8}$ s, $\beta_S = 0.5 \times 10^{-9}$ N^{-1} m^2 [27], DE $= 2 \times 10^7$ N/m^2 [28], $\alpha_6 \approx 0$, $\rho \approx 10^3$ kg m^{-3} [29], $\partial T_c/\partial P = 3.5 \times 10^{-7}$ deg m^2 N^{-1} [30], $C_p = 2 \times 10^6$ J m^{-3} [31], $d \approx 0.45 T_c$ [12], and $T_c = 319$ K [10]. The threshold compressibility and the size of domains were determined for the temperature $T = 310$ K, at which the molecular parameters of the medium are $\langle P_2 \rangle = 0.6$, $\beta \approx 5$, and $d_T \approx 2.5$. Equaling d_0 [Eq. (2.4)] to the experimental size of domains $d \approx 18.5$ μm observed at the static extension of the layer of a cholesteric LC with the thickness $h = 22$ μm and the helix pitch $P_0 = 4.3$ μm [12], we obtain the value $\lambda = K_{22}/K \approx 2.8 \times 10^{-2}$. The kinetic coefficients a_1 and $a_5 + a_6$ in the parameter ω_1^+ remain undetermined within the framework of the model in use. Let us estimate their value according to the publications [18, 19, 24, 25], where the anisotropic part of the Leslie stress with the viscosity coefficients α_k ($k \neq 4$) is mainly caused by the gradients f'. In this case, the second and third terms in Eq. (4.4) must be small, which gives the values $a_1 \approx 1$ and $a_5 + a_6 \approx -1$ that are used for the numerical calculation of $\varepsilon_{th}^{(2)}$.

Both vortex and nonlinear relaxation mechanisms lead to the destabilization of the structure of a cholesteric LC in a sound field and to the formation of a domain structure in the layer of a cholesteric LC. Their effect manifests itself in different frequency ranges: the first one manifests itself in the interval $(a\tau)^{-1} < \omega < \tau^{-1}$ and the second, for $\omega > \tau^{-1}$. The numerical comparison of the vortex and relaxation thresholds of the effect is given in Fig. 1, where the curves for the threshold values ε_{th} as the functions of the reduced frequency $\omega\tau$ are plotted according to Eqs. (3.6) and (4.13) for the layer thickness $h = 100$ μm and the helix pitch $P_0 = 10$ μm. It was assumed in Eq. (3.6) that $\xi = 1$. The relative extension of the layer in both cases was assumed to be equal to $\delta = 0.8$.

A curve for the frequency dependence of the threshold amplitude of compression ε_{th}, obtained by taking into account the simultaneous effects of both mechanisms, is plotted in the same figure. The expression for ε_{th} is constructed by summation of the inverse squares of $\varepsilon_{th}^{(1)}$ and $\varepsilon_{th}^{(2)}$:

$$\varepsilon_{th} = \left\{\frac{1}{[\varepsilon_{th}^{(1)}]^2} + \frac{1}{[\varepsilon_{th}^{(2)}]^2}\right\}^{-1/2}. \quad (5.1)$$

Figure 1 demonstrates that the vortex and relaxation mechanisms of destabilization of the structure of a cholesteric LC and the domain formation in the layer of a cholesteric LC are governing in different frequency ranges. The boundary between these ranges $\omega = \omega_0$ can be estimated using the relation $\omega_0 \approx 2.25 \times 10^{-2} h/P_0\tau^{-1}$. The two mechanisms complement each other and expand the frequency range where the effect must be observed. The value of $\varepsilon_{th}^{(1)}$ at $\omega\tau \ll 1$ and the value of $\varepsilon_{th}^{(2)}$ at $\omega\tau \gg 1$ differ little, which leads to a slight

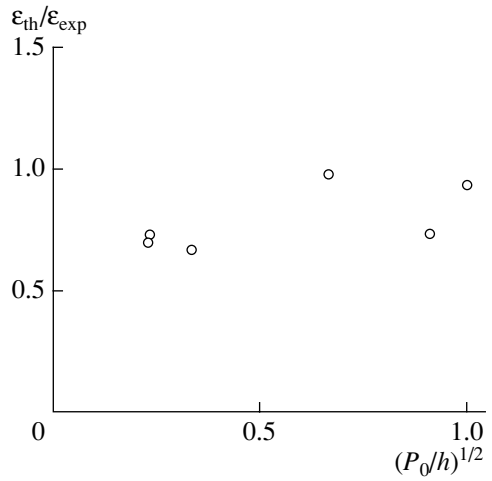

Fig. 2. Ratio of the theoretical compressibility ε_{th} to the experimental compressibility ε_{exp} for different values of P_0/h.

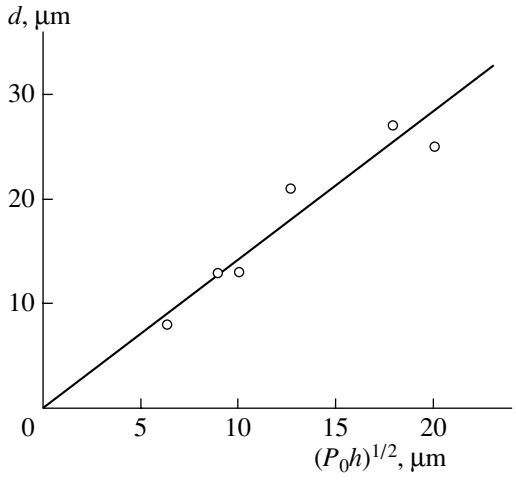

Fig. 3. Theoretical (straight line) and experimental sizes of domains for different values of P_0 and h.

dependence of the threshold compression ε_{th} on frequency. For example, in the case of the layer thickness $h = 100$ μm and the helix pitch $P_0 = 4$ μm, the threshold compression changes from the value $\varepsilon_{th} \approx 0.7 \times 10^{-5}$ at low frequencies to $\varepsilon_{th} \approx 0.8 \times 10^{-5}$ at high frequencies. The corresponding value of the threshold intensity of sound in the wave incident upon the layer is equal to $I_{th} = \varepsilon_{th}^2 \rho c^3 \approx 0.02$ W/cm^2.

Both vortex and relaxation mechanisms lead to the formation of acoustic domains of the same size d_0 in a layer of a cholesteric LC. This size does not depend on frequency, and the visual manifestations of these mechanisms are similar. However, they lead to different dependences of the threshold compressibility on the pitch of the cholesteric helix: $\varepsilon_{th} \sim 1/\sqrt{P_0}$ for the nonlinear relaxation mechanism and $\varepsilon_{th} \sim \sqrt{P_0}$ for the vortex one, and their effects can be identified experimentally.

A comparison of the theoretical and the experimental thresholds of the effect, i.e., ε_{th} and ε_{exp}, respectively, is represented in Fig. 2. The values of $\varepsilon_{th}/\varepsilon_{exp}$ are plotted there as functions of $\sqrt{P_0 h}$ for different ω, h, and P_0. The threshold compression ε_{th} was determined according to Eqs. (5.1), (3.6), and (4.13) at $\xi = 1$, and the values of ε_{exp} were recalculated according to the experimental data given in [1, 12]. The comparison of the theoretical and experimental sizes of domains is given in Fig. 3, where the theoretical curve for $d = d_0$ as the function of $\sqrt{P_0 h}$ is plotted and the experimental data [1, 12] are indicated.

Figures 2 and 3 demonstrate a good agreement between theoretical calculations and experimental data. The closeness of the theory developed with allowance for the relaxation processes and the experimental data indicates that the processes of structural relaxation can play a decisive role in the formation of spatially modulated structures in LC affected by ultrasound, and they must be taken into account in the theory of the corresponding phenomena.

In conclusion, we present some numerical estimates for the parameters used above for the layer of a cholesteric LC:

$$\frac{k_{th}}{q} \approx 0.16, \quad \frac{k_z}{k_{th}} \approx 0.5, \quad \frac{N}{M} \sim 10^{-2}.$$

These values testify to the validity of inequalities (3.2) and (3.5) used in the derivation of Eq. (3.6).

ACKNOWLEDGMENTS

This work was supported by the Russian Foundation for Basic Research, project no. 00-02-17732.

REFERENCES

1. A. P. Kapustin and O. A. Kapustina, *Acoustics of Liquid Crystals* (Nauka, Moscow, 1986), p. 247.
2. *Pattern Formation in Liquid Crystals*, Ed. by A. Buka and L. Kramer (Springer, New York, 1996).
3. E. Demus, in *Physical Properties of Liquid Crystals* (Wiley–VCH, Weinheim, 2000), Vol. 1, pp. 447–466.
4. E. N. Kozhevnikov, Sov. Phys. JETP **64**, 793 (1986).
5. S. J. Hogan, T. Mullen, and P. Woodford, Proc. R. Soc. London, Ser. A **441**, 559 (1993).
6. A. P. Krekhov, T. Börsönyi, P. Tótch, *et al.*, Phys. Rep. **337**, 171 (2000).
7. H. Moritake, T. Seike, and K. Toda, Jpn. J. Appl. Phys., Part 1 **38**, 3076 (1999).
8. M. Inoue, H. Moritake, and K. Toda, Jpn. J. Appl. Phys., Part 1 **39**, 3125 (2000).

9. M. J. Stephen and J. P. Straley, Rev. Mod. Phys. **46** (4), 617 (1974).
10. P. De Gennes, *The Physics of Liquid Crystals* (Clarendon, Oxford, 1974; Mir, Moscow, 1977).
11. I. N. Gurova, O. A. Kapustina, V. N. Lupanov, and G. S. Chilaya, in *IV International Conference of Socialistic Countries on Liquid Crystals* (Tbilisi, 1981), Vol. 2, p. 74.
12. I. N. Gurova and O. A. Kapustina, Akust. Zh. **43**, 338 (1997) [Acoust. Phys. **43**, 290 (1997)].
13. E. N. Kozhevnikov, Zh. Éksp. Teor. Fiz. **92**, 1306 (1987) [Sov. Phys. JETP **65**, 731 (1987)].
14. E. N. Kozhevnikov, Akust. Zh. **47**, 501 (2001) [Acoust. Phys. **47**, 430 (2001)].
15. M. Doi and S. F. Edwards, J. Chem. Soc., Faraday Trans. 2 **74**, 560 (1978).
16. M. Doi and S. F. Edwards, J. Chem. Soc., Faraday Trans. 2 **74**, 918 (1978).
17. V. N. Pokrovskiĭ, *Statistical Mechanics of the Dilute Suspensions* (Nauka, Moscow, 1978), p. 178.
18. A. N. Semenov, Zh. Éksp. Teor. Fiz. **85**, 549 (1983) [Sov. Phys. JETP **58**, 321 (1983)].
19. M. A. Osipov and E. M. Terentjev, Phys. Lett. A **134** (5), 301 (1989).
20. V. I. Stepanov, Preprint, IMSS UNTs URO AN SSSR (Sverdlovsk Inst. of Mechanics of Continua, Ural Division, USSR Academy of Science, 1983), pp. 46–57.
21. V. I. Stepanov, Preprint No. 106, IMSS UNTs URO AN SSSR (Sverdlovsk Inst. of Mechanics of Continua, Ural Division, USSR Academy of Science, 1982), pp. 39–61.
22. E. N. Kozhevnikov, Akust. Zh. **40**, 613 (1994) [Acoust. Phys. **40**, 544 (1994)].
23. E. N. Kozhevnikov, Akust. Zh. **42**, 800 (1996) [Acoust. Phys. **42**, 705 (1996)].
24. A. Chrzanowska and K. Sokalski, Phys. Rev. E **52**, 5228 (1995).
25. A. Chrzanowska, M. Kroger, and H. S. Seller, Phys. Rev. E **60**, 4226 (1999).
26. A. Chrzanowska, Phys. Rev. E **62**, 1431 (2000).
27. D. Eden, C. W. Garland, and R. C. Williamson, J. Chem. Phys. **58** (5), 1861 (1973).
28. C. A. Castro, A. Hikata, and C. Elbaum, Phys. Rev. A **17** (1), 353 (1978).
29. J. S. Lee, S. L. Golub, and G. H. Brown, J. Chem. Phys. **76**, 2409 (1972).
30. M. A. Tikhomirova, A. K. Vistin', and V. N. Nosov, Kristallografiya **17** (5), 100 (1972).
31. A. S. Sonin, *Lectures on Liquid Crystals* (Mosk. Gos. Univ., Moscow, 1979), Part 1, p. 122.

Translated by M. Lyamshev

Acoustical Physics, Vol. 48, No. 6, 2002, pp. 697–706. Translated from Akusticheskiĭ Zhurnal, Vol. 48, No. 6, 2002, pp. 788–798.

Attenuation Features of the Coherent Sound Field Component in Deep-Water Regions of the Arctic Ocean

V. D. Krupin

Andreev Acoustics Institute, Russian Academy of Sciences, ul. Shvernika 4, Moscow, 117036 Russia

e-mail: bvp@akin.ru

Received November 14, 2001

Abstract—On the basis of the WKB method and the theory of sound scattering by a stochastically rough surface of an elastic layer, the normal mode attenuation coefficients (NMAC) are analyzed for the coherent component of the sound field generated by a tone source in the deep-water acoustic waveguide extending along the Spitsbergen–Barrow Point oceanographic section. For an arctic waveguide with an ice cover in the form of a flat homogeneous absorbing elastic layer, the NMAC are explicitly obtained as analytical functions of the whole set of the waveguide parameters and the parameters of the sound velocity profiles in characteristic water layers with consideration for the typical features of thermohaline stratification observed in the central region of the Arctic Ocean. It is shown that the results of calculating the values of the NMAC and their dependences on the ice cover thickness by the derived formulas are very close to the exact results obtained with the use of the mode program. A number of regularities were found in the behavior of the NMAC as functions of the mode number and the ice cover thickness, as well as in the sensitivity of the sound field formed in the arctic waveguide to the variability of the ice cover thickness. Specific features are revealed in the distribution of the sound field intensity along a vertical receiving acoustic array. It is shown that the aforementioned WKB approximations for the NMAC and all mentioned regularities also hold for arctic waveguides with ice cover described by more realistic models with stochastically rough surfaces in the domain of applicability of the methods used for calculating the coherent reflection coefficient at the water–ice boundary. It is pointed out that the use of the WKB approximations of NMAC can considerably improve the efficiency of computer programs used for acoustic remote monitoring of the thermohaline structure of the underice medium and the ice cover of the Arctic Ocean and for sound source localization in arctic regions. © *2002 MAIK "Nauka/Interperiodica".*

The thermohaline structure of the underice medium in the Arctic basin is of primary importance in the ice formation, the global oceanic circulation, and the formation of the Earth's climate. Methods for modeling the acoustic monitoring of this structure have been developed in the last few years in the framework of the international scientific projects Arctic ATOC (Arctic Acoustic Thermometry of Ocean Climate) and ACOUS (Arctic Climate Observation using Underwater Sound) [1–7]. Both modeling and the full-scale experiments on thermometry of the Arctic Ocean along deep-water transarctic acoustic paths showed that the measurements of the variations in the arrival times of normal modes offer the possibility of monitoring the average temperature of the intermediate layer of warm water intruding from the Atlantic [1–4] and affecting the thermohaline structure in the upper water layers. A similar technique can be applied [5–7] in modeling the acoustic monitoring of salinity of the uppermost desalinated water layer whose temperature is always about the freezing point. It is precisely this layer with reduced salinity that plays the crucial role in the existence of the permanent ice cover and the formation of the inclement climate in the Arctic basin.

It is obvious that the data on normal mode propagation times alone are insufficient for realizing the acoustic monitoring of the ice cover in the Arctic Ocean and the thermohaline structure in the water layers intermediate between the aforementioned layers, because the ice cover with its typical material parameters only slightly affects these propagation times [8], and the velocity of sound in these layers depends on both temperature and salinity. In this context, it is advantageous to use the normal mode attenuation coefficients (NMAC) of several first numbers as additional informative data. These coefficients are very sensitive to variations in both the parameters of the ice cover and the vertical gradient of the sound velocity in the adjacent upper layers of the medium under the ice cover. The magnitudes of NMAC can be reconstructed from the expansion coefficients of the sound pressure along the vertical array in normalized eigenfunctions of the arctic waveguide. The eigenfunctions, in turn, can be calculated, with the use of mode filtration algorithms, from the measured sound pressure values of the narrow-band or broadband signals at the hydrophones of the receiving acoustic arrays [9–18]. In this connection, the study of regularities in the NMAC as functions of the parameters of the ice cover and the underice medium is of considerable interest for the development of methods of modeling the acoustic monitoring in the Arctic basin.

1063-7710/02/4806-0697$22.00

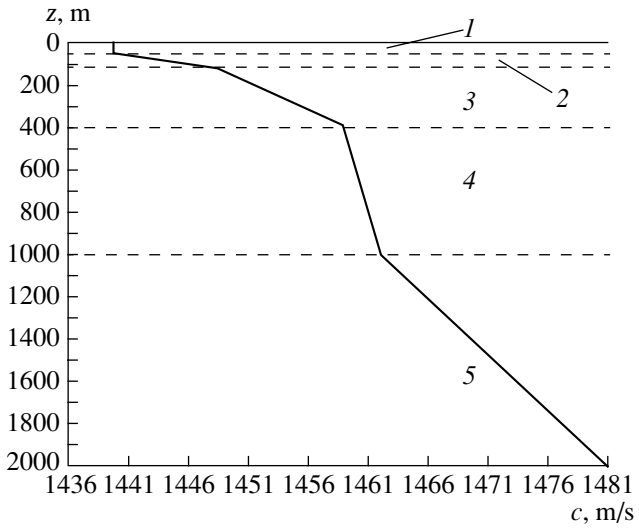

Fig. 1. Typical vertical sound velocity profile in water after averaging over the 2000-km segment of the European part of the Spitsbergen–Barrow Point oceanographic section.

This paper deals with the study of these regularities in the absorption of normal modes and uses the deep-water waveguide with the vertical sound field profile typical of the Central Arctic basin (see Fig. 1) as an example. Results of similar investigations in the case of a shallow-water arctic waveguide can be found in [19, 20]. The paper also presents the normal mode attenuation coefficients and analyzes the distribution of the sound field intensity generated by a tone source on a vertical acoustic array and the sensitivity of the horizontal sections of intensity levels in the subsurface sound channel to the variation of the ice cover thickness. All results are obtained both numerically and using the WKB method, for a horizontally homogeneous waveguide with the aforementioned sound velocity profile in the water layer and the ice cover in the form of a homogeneous absorbing elastic layer of constant thickness with flat boundaries. The results of some known theoretical studies of the sound reflection and scattering by an elastic layer with stochastically rough boundaries are used to extend the regularities established for the normal mode attenuation coefficients in such a waveguide to the model of an arctic waveguide whose ice cover is characterized by rough boundaries. Some aspects of possible applications of the established regularities are discussed.

MODELS OF THE SOUND FIELD PROFILE AND THE ICE COVER OF AN ARCTIC WAVEGUIDE

As is known [21–23], five characteristic layers can be distinguished in the underice medium of the deep-water region of the Arctic Ocean: (*1*) the uppermost desalinated water layer characterized by low salinity and a temperature of about the freezing point, (*2*) the cold halocline layer with a high positive vertical gradient of salinity, (*3*) the layer of warm and saline Atlantic waters characterized by a considerable positive gradient of temperature and reaching the Arctic basin through the eastern part of the Fram Channel, (*4*) the core of Atlantic water masses, and (*5*) the deep-water layer extending to the bottom and characterized by a nearly constant vertical hydrostatic gradient of sound velocity. Layers *1–4* with a total thickness of about several hundreds of meters below the ice undersurface form a fully developed subsurface sound channel. Outside this channel, with a further depth increase to the bottom, the sound velocity increases almost linearly and with a much smaller gradient due to the hydrostatic pressure. The mixed surface layer *1* with low salinity is formed by the inflow of fresh waters arriving mainly from four river systems (McKenzie, Ob, Eniseĭ, and Lena) and due to the arrival of low-salinity water masses from the Bering Sea through the Bering Strait to the Chukotsk Sea. The latter arrival measures up to 40% of the income portion of freshwater balance of the Arctic Ocean. The origin of the cold halocline layer *2* is caused both by the wintertime advection of the cold saline shelf waters from the periphery of the Arctic Ocean to the deeper (below 100 m) layers located between the desalinated layer *1* and the Atlantic saline warm waters and by the autumnal and wintertime convection of saline water masses from the subsurface layer. This process is completed by the intrusion of cold desalinated shelf waters into this layer [22, 23]. The subsurface layer isolates the ice cover from the warm waters of Atlantic origin and prevents it from being melted (indeed, the heat of Atlantic waters of even a few watts per square meter would be sufficient to melt a considerable portion of ice in the case of the absence of this layer), thus favoring the ice formation process [23]. The reduced salinity of the upper layer is the most important factor affecting the formation of the ice cover and climate of the Arctic basin.

With the aim of establishing the relationships for the NMAC as functions of the above features of the underice medium, we approximate the sound field profile in the water layer by an ascending piecewise linear function

$$c(z) = c_j + g_j(z - \bar{z}_j) \text{ for } \bar{z}_j \le z \le \bar{z}_{j+1}, \quad j = (1, 2, 3, 4, 5), \tag{1}$$

where c_j are the values of the sound velocity at the boundaries $z = \bar{z}_j = \sum_{m=1}^{j} h_m$ of the aforementioned characteristic water layers; h_j are the widths of these layers; $g_j = (c_{j+1} - c_j)/h_j$ are the positive vertical gradients of sound velocity in these layers; and $c_1 = c_2 = c_0 = c(0)$ and $c_6 = c(H)$ are sound velocities at the ice undersurface $\bar{z}_1 = 0$ and at the bottom $\bar{z}_6 = H$, respectively. In calculating the normal mode characteristics, we used

Table 1. Model of the sound velocity profile $c(z)$ along the European part of the Spitsbergen–Barrow Point oceanographic section, the depths of the boundaries separating the characteristic layers, the thicknesses of the layers, and the gradients of the sound velocity in the layers

Boundary number j	Boundary depth $\bar{z}_j$, m	Sound velocity c_j, m/s	Number of layer j	Layer thickness h_i, m	Sound velocity gradient g_i, s^{-1}
1	0	1440	1	50	0
2	50	1440	2	70	1.1143×10^{-1}
3	120	1448	3	280	3.9286×10^{-2}
4	400	1459	4	600	5.0000×10^{-3}
5	1000	1462	5	2000	1.9000×10^{-2}
6	3000	1500			

Table 2. Parameters of the ice cover

Ice thickness l, m	Longitudinal wave velocity c_p, m/s	Shear wave velocity c_s, m/s	Longitudinal wave attenuation δ_p, dB/m/kHz	Shear wave attenuation δ_s, dB/m/kHz	Density ρ_i, g/cm^3
0–5	3832.7	1903.5	0.058	0.348	0.9

the sound field profile whose parameters are given in Table 1. Figure 1 shows this profile only to a depth of 2000 m. This profile was obtained by averaging the sound field profiles calculated from the measured vertical temperature and salinity profiles during the Sever expedition [21] for intermediate points of the European part of the Spitsbergen–Barrow Point oceanographic section 2000 km in length with the average depth H = 3000 m.

For the ice cover, we used the model in the form of a homogeneous absorbing elastic layer. In accordance with the available experimental data [24], we approximated the attenuation coefficients β_P [dB/km] and β_s [dB/km] by linear functions of frequency: $\beta_P = \delta_p f$ and $\beta_s = \delta_s f$, where the frequency f is measured in hertz and the attenuation factors δ_p and δ_s are related by the formula $\delta_s = 6\delta_p$ and have the dimension [dB/m/kHz]. Table 2 presents the parameters of the ice cover.

REPRESENTATION OF THE PRESSURE IN THE SOUND FIELD OF A TONE SOURCE IN AN ARCTIC WAVEGUIDE WITH ICE COVER OF CONSTANT THICKNESS IN THE FORM OF A SERIES EXPANSION IN NORMAL MODES

Consider first the model of an arctic waveguide with the sound field profile shown in Fig. 1 and ice cover in the form of a homogeneous absorbing elastic layer with flat boundaries. The pressure p of the sound field generated at an arbitrary point (r, z) of the water layer by a harmonic point source with the angular frequency $\omega = 2\pi f$ under the condition $kr \gg 1$ ($k = \omega/c(0)$ is the wave number) is determined as the sum of normal modes [19]:

$$p(r, z, z_0\omega) = -\omega\rho_0 Q \sum_{n=1}^{\infty} A_n w_n(z, \xi_n^2), \tag{2}$$

$$A_n = (8i\pi\xi_n r)^{-1/2} w_n(z_0) \times \exp[i\mathrm{Re}(\xi_n)r - \beta_n r/(20\log_{10} e)], \tag{3}$$

where ρ_0 is the density of water, Q is the volume velocity of the source, z_0 and z are the source and receiver depths, and r is the horizontal distance between the source and the receiver. In these formulas, the quantities $w_n(z)$ and $\lambda_n = \xi_n^2$ (ξ_n is the complex horizontal wave number of a normal mode with number n) are the nth normalized eigenfunction and the nth eigenvalue of the spectral boundary-value problem

$$\frac{d^2 w}{d^2 z} + \left[\frac{\omega^2}{c^2(z)} - \xi^2\right] w = 0, \tag{4}$$

$$\left[\frac{dw}{dz} + G_s(\xi^2)w\right]_{z=0} = \left[\frac{dw}{dz} + G_b(\xi^2)w\right]_{z=H} = 0, \tag{5}$$

where ξ is the spectral parameter (the horizontal wave number); H is the thickness of the water layer; $c(z)$ is the sound velocity in the water layer; and G_s and G_b are the input admittance of the homogeneous absorbing ice cover at the surface $z = 0$ and the input admittance of the stratified absorbing bottom at the water–bottom boundary $z = H$, respectively. In the following consideration,

we will use only the expression for the admittance G_s derived in [19]:

$$G_s = m_i^{-1}\alpha G_1/G_2, \tag{6}$$

$$G_1 = k_s^4[(2\xi^2 - k_s^2)^2\coth(\alpha l) - 4\alpha\beta\xi^2\coth(\beta l)], \tag{7}$$

$$\begin{aligned} G_2 = &\left[(2\xi^2 - k_s^2)^2 - 4\alpha\beta\xi^2\tanh\left(\frac{\alpha l}{2}\right)\coth\left(\frac{\beta l}{2}\right)\right] \\ &\times\left[(2\xi^2 - k_s^2)^2 - 4\alpha\beta\xi^2\coth\left(\frac{\alpha l}{2}\right)\tanh\left(\frac{\beta l}{2}\right)\right], \end{aligned} \tag{8}$$

where $a = \sqrt{\xi^2 - k_p^2}$, $b = \sqrt{\xi^2 - k_s^2}$, $k_p = (\omega/c_p)(1 + i\eta_p)$, $k_s = (\omega/c_s)(1 + i\eta_s)$, $\eta_p = 10^{-3}c_p\delta_p/[40\pi\log_{10}(e)]$, and $\eta_s = 10^{-3}c_s\delta_s/[40\pi\log_{10}(e)]$ are the coefficients of losses for the longitudinal and shear waves in the ice layer; l is the thickness of the ice cover; $m_i = \rho_i/\rho_0$ is the ice-to-water density ratio; and $i = \sqrt{-1}$. The quantity β_n in Eq. (3) is the attenuation coefficient of the nth mode (in [dB/km]); it is caused by the sound wave absorption by the ice cover and the ocean bottom and is related to the imaginary part $\mathrm{Im}(\xi_n)$ [Neper/m] of the wave number ξ_n by the formula

$$\beta_n = (20\log_{10}(e))\mathrm{Im}(\xi_n)\times 10^3. \tag{9}$$

WKB APPROXIMATIONS OF THE NORMAL MODE ATTENUATION COEFFICIENTS IN AN ARCTIC WAVEGUIDE WITH ICE COVER OF CONSTANT THICKNESS

For a more illustrative interpretation of the numerical results obtained for the NMAC in terms of the above model of the arctic waveguide with the use of a mode program that modifies the program [25] to allow for expressions (6)–(8) for the input admittance G_s of the absorbing ice layer and to control the calculation correctness, we first obtain approximate explicit expressions for the NMAC on the basis of the asymptotic WKB method. For convenience, we represent the pressure p as the sum of two components $p = p_1 + p_2$. The pressure p_1 is the sum of sound pressures of the least attenuating normal modes with the numbers $n = 1, 2, \ldots, N$; for sufficiently high frequencies, these modes correspond to rays refracted upward and reflected only from the ice undersurface. The pressure p_2 is the sum of pressures of normal modes with the numbers from $N + 1$ to infinity; these modes correspond to rays multiply reflected from two absorbing boundaries of the water layer. For sufficiently large distances r from the source, normal modes with the numbers $n = 1, 2, \ldots, N$ predominate in the total sound field; for this reason, the analytical and numerical results given below refer to these modes. By the WKB method, the attenuation coefficients β_n [dB/km] of the normal modes with the numbers $n = 1, 2, \ldots, N$ are given by the expressions [26]

$$\beta_n = -20\log_{10}|V_s(\chi_n, kl)|\times 10^3/(\Delta_n + D_n), \tag{10}$$

$$\Delta_n = -\left(\frac{\partial\varphi_s}{\partial\xi}\right)_{\xi = \xi_n}, \tag{11}$$

$$D_n = 2\cos\chi_n\int_0^{z_t}[c_0^2/c(z)^2 - \cos^2\chi_n]^{-1/2}dz, \tag{12}$$

where χ_n is the grazing angle of the ray corresponding to the nth mode near the ice cover; this angle can be determined from the relationship $\mathrm{Re}(\xi_n) = k\cos\chi_n$. The parameters $|V_s|$ and φ_s are the magnitude and phase of the reflection coefficient from the water–ice boundary, respectively; D_n is the cycle length of the geometric ray with the grazing angle χ_n at the water–ice boundary (this length is equal to the distance between two successive reflections from the ice undersurface); Δ_n is the horizontal displacement of the beam of rays at the reflection from the surface of the ice cover; and z_t is the depth of the point at which the ray with the grazing angle χ_n is turned back and which is the unique root of the equation $c_0/c(z_t) - \cos\chi_n = 0$. The grazing angles χ_n are determined from the equations

$$k\int_0^{z_t}\sqrt{c_0^2/c(z)^2 - \cos^2\chi_n}dz + \varphi_s(\chi_n, kl)/2 = (n + 1/4)\pi \tag{13}$$
$$(n = 1, 2\ldots N).$$

These expressions hold for all modes with grazing angles $\chi_n \le \chi_4$, where $\chi_4 = \arccos[c_0/c(H)]$ is the grazing angle of the ray touching the bottom.

Calculating the integral in Eq. (12) with the use of piecewise linear approximation (1) for the sound velocity $c(z)$, we obtain the following recursion relations for the cycle length of the sound ray with the grazing angle χ_n:

$$D_n = \begin{cases} D_{n,1} = 2h_1/\tan\chi_n + 2c_0\tan\chi_n/g_2 & \text{(14a)} \\ \text{for } \chi_n < \chi_1 \\ D_{n,j+1} = D_{n,j} + 2c_0(g_{j+1}^{-1} - g_j^{-1}) \\ \times\sqrt{\tan^2\chi_n - [(c_{j+1}/c_0)^2 - 1]} & \text{(14b)} \\ \text{for } (\chi_j \le \chi_n \le \chi_{j+1}, j = 1, 2, 3, 4), \end{cases}$$

where $\chi_j = \arccos(c_0/c_{j+2})$ ($j = 1$, 2, 3, and 4) are the grazing angles of the boundary rays touching three characteristic boundaries of the water layer and bottom $z = \bar{z}_{j+2}$. Because only the modes with small grazing angles (less than the boundary angle χ_4) are of interest

in our consideration, we can approximate the magnitude of the reflection coefficient by the relationship

$$|V_s(\chi_n, kl)| \approx \exp(-\gamma \sin\chi_n), \quad \gamma = |(\partial|V_s|/\partial\chi)_{\chi=0}|. \tag{15}$$

Then, taking into account the expressions for the reflection coefficient V_s and its magnitude,

$$V_s = [ik\sin\chi - G_s(k\cos\chi)]/[ik\sin\chi + G_s(k\cos\chi)], \tag{16}$$

$$|V_s| = \{1 - 4k^{-1}\mathrm{Im}(G_s) \times \sin\chi/[\sin^2\chi + k^{-2}|G_s|^2 + 2k^{-1}\mathrm{Im}(G_s)\sin\chi]\}^{1/2}, \tag{17}$$

and calculating the derivative of expression (17) with respect to the grazing angle χ at $\chi = 0$, we obtain an expression for γ:

$$\gamma = 2\mathrm{Im}(1/\tilde{G}_s), \tag{18}$$

where $\tilde{G}_s = k^{-1}(G_s)_{\chi=0}$. As follows from Eqs. (6)–(8) for the admittance G_s and from Eq. (18), the expression for γ has the following form:

$$\gamma = 2\mathrm{Im}(\gamma_2\gamma_3/\gamma_1), \tag{19}$$

where

$$\gamma_1 = \frac{\nu^4}{m_i}\sqrt{1-\mu^2}\{(2-\nu^2)^2\coth[(kl)\sqrt{1-\mu^2}] - 4\sqrt{1-\nu^2}\sqrt{1-\mu^2}\coth[(kl)\sqrt{1-\nu^2}]\},$$

$$\gamma_2 = \left\{(2-\nu^2)^2 - 4\sqrt{1-\nu^2}\sqrt{1-\mu^2} \times \tanh\left[\frac{kl}{2}\sqrt{1-\mu^2}\right]\coth\left[\frac{kl}{2}\sqrt{1-\nu^2}\right]\right\};$$

$$\gamma_3 = \left\{(2-\nu^2)^2 - 4\sqrt{1-\nu^2}\sqrt{1-\mu^2} \times \coth\left[\frac{kl}{2}\sqrt{1-\mu^2}\right]\tanh\left[\frac{kl}{2}\sqrt{1-\nu^2}\right]\right\};$$

$$\mu = (c_0/c_p)(1 + i\eta_p), \quad \nu = (c_0/c_s)(1 + i\eta_s).$$

Then, using Eqs. (1), (10), and (11) and taking into account the fact that $\Delta_n \ll D_n$ for the attenuation coefficients β_n [dB/km] of normal modes captured by the underice sound channel, we obtain the approximate expression

$$\beta_n = 20\log_{10}(e)\gamma\sin\chi_n \times 10^3/D_n(\chi_n), \tag{20}$$

where the quantities χ_n and $D_n(\chi_n)$ are determined by Eqs. (13) and (14). In particular, in the case of the sound

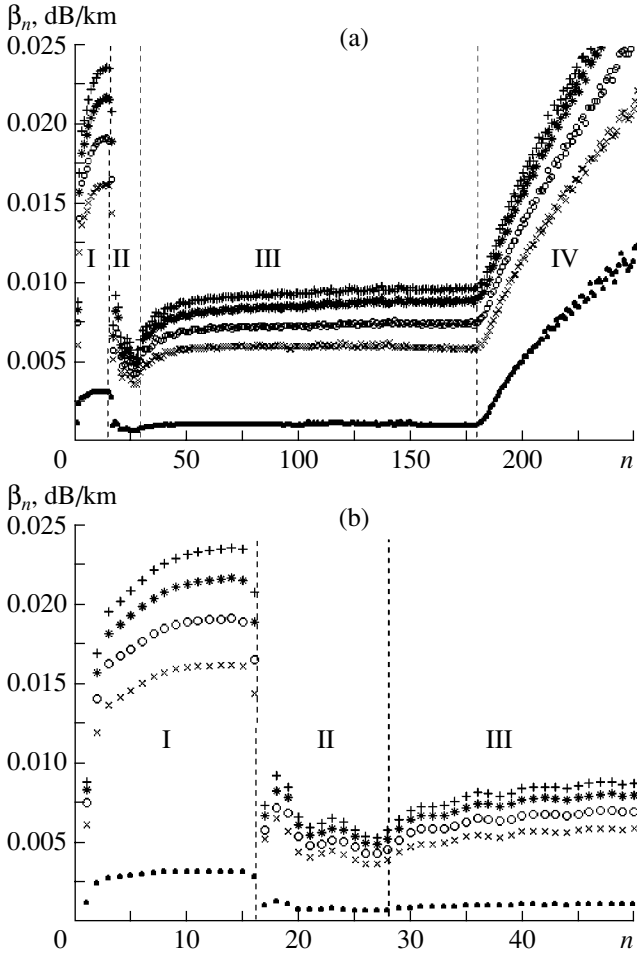

Fig. 2. Attenuation coefficients β_n (dB/km) of normal modes as functions of mode numbers for (a) $n = 1, \ldots, 250$ and (b) $n = 1, \ldots, 50$ at a frequency of 250 Hz for different values of the ice cover thickness: l = (•) 1, (×) 2, (+) 3, (*) 4, and (○) 5 m.

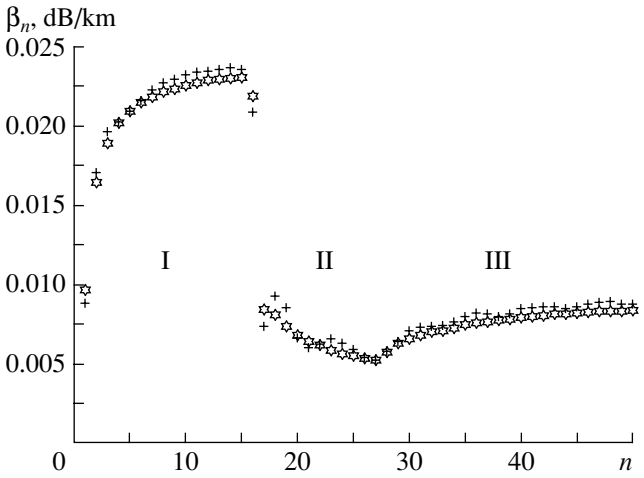

Fig. 3. Attenuation coefficients β_n (dB/km) of normal modes as functions of mode numbers for $n = 1, \ldots, 50$ at a frequency of 250 Hz for the ice cover thickness $l = 3$ m: (+) the exact mode program and (☆) the WKB method.

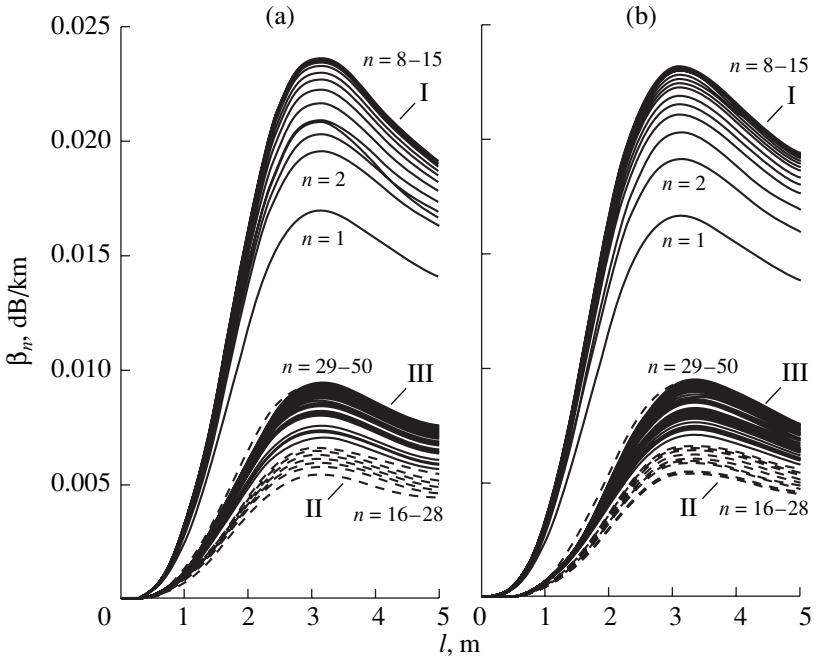

Fig. 4. Normal mode attenuation coefficients β_n at a frequency of 250 Hz as functions of the ice cover thickness l = 0–5 m for the mode numbers n = 1, …, 50: (a) the exact mode program and (b) the WKB method.

velocity profile described by a linear or bilinear function of depth, which occurs, e.g., in the Greenland Sea [27] in winter and spring, the attenuation coefficients of lower normal modes captured by the subsurface sound channel only slightly depend on the number n and are given by the simple expression [19, 20]

$$\beta_n = 20\log_{10}(e)\gamma g_2 \times 10^3/c_2 = \beta = \text{const}, \quad (21)$$

where g is the gradient of sound velocity in the subsurface sound channel.

NUMERICAL ANALYSIS OF THE NORMAL MODE ATTENUATION COEFFICIENTS AND ITS INTERPRETATION IN TERMS OF THE WKB APPROXIMATION

Now, we analyze the regularities that the sound absorption by the ice cover causes in the distribution of the NMAC over the mode numbers for different ice thickness values ranging from 0 to 5 m. As can be seen from Fig. 2a, the sequence of NMAC $\{\beta_n\}$, n = 1, 2, …, 250, is divided into four groups of numbers separated by the vertical dashed lines and marked by roman numbers I, II, III, and IV. In group I, coefficients β_n take on maximal values and correspond to the modes of lower numbers n = 1, 2, …, N_1 = 15 with phase velocities $c_{p,n}$ in the interval $c_0 = c_1 = 1440 < c_{p,n} \le c_4 = 1459$, or to water-path rays that are refracted in the upward direction, turn back at the depths $z_t \le \bar{z}_4$, have grazing angles $\chi \le \chi_2$, and cross the desalinated and halocline cold layers. In group II, the coefficients β_n take on minimal values and correspond to the modes with the numbers $N_1 + 1 \le n = 16$, …, $N_2 = 28$ with phase velocities c in the interval $c_4 = 1459 \le c_{p,n} \le c_5 = 1462$, or to rays that turn back at depths $z_t \le \bar{z}_5$ and cross all four upper layers. The vast group III, which includes modes with the numbers $N_2 + 1 \le n = 29$, … $N_3 = 100$ and phase velocities in the interval $c_5 = 1462 \le c_{p,n} \le c_6 = c(H) = 1500$, is characterized by the NMAC only slightly increasing with the number n and corresponds to rays with grazing angles $\chi_3 < \chi \le \chi_4$ and turning points lying in the thick lowest layer with a constant hydrostatic gradient of sound velocity. Group IV includes the NMAC for modes with the numbers $N_3 + 1 \le n = N_4 = 250$; these coefficients rapidly increase with the mode number n and correspond to rays multiply reflected from both the ice cover and the arctic waveguide bottom. The above features in the distribution of NMAC over the mode numbers appear more prominent in Fig. 2b, where the distribution is shown for modes with the numbers n = 1, 2, …, 50 on an enlarged scale. As can be seen from Figs. 2a and 2b, the values of NMAC are nonmonotone functions of the ice cover thickness. Furthermore, the values of NMAC for group I of modes are more sensitive to variation of the ice cover thickness in comparison with those for groups II and III. Figure 3 shows a comparison of the exact values $\{\beta_n\}$, n = 1, 2, …, 50, calculated with the modified mode program [25] for the ice thickness l = 3 m with the corresponding values calculated by formulas (10), (14), (19), and (20) based on the WKB method. From this comparison, it follows that the above WKB approximations for the coefficients

$\{\beta_n\}$, $n = 1, 2, \ldots$ practically coincide with their exact values obtained with the use of the numerical procedures of searching for complex eigenvalues of the spectral boundary-value problem (4)–(8).

The above features in the behavior of NMAC versus the mode number are prominent in Fig. 4, where the coefficients β_n for mode numbers $n = 1, 2, \ldots, 50$ are shown as functions of the ice cover thickness l in the interval from 0 to 5 m. The comparison of the curves presented in Figs. 4a and 4b shows that, within the whole range of ice thickness, the curves $\beta_n(l)$ calculated by the WKB formulas (10), (14), (19), and (20) coincide to a high accuracy with those obtained using digital procedures of determining the complex eigenvalues of the boundary-value problem (4)–(8). As seen from Fig. 4, the curves $\beta_n(l)$ for mode groups I and III show a curious geometrical feature that consists in the fact that they nearly merge forming two contrast concentration regions in the $l\beta$ plane; these regions are shown by the solid lines and marked by arrows and roman numerals. The closely spaced curves shown by the dashed lines correspond to the least attenuated modes of group II. In addition, Fig. 4 shows that the coefficients β_n are two-valued functions of l and have maxima at certain values of ice cover thickness. As can be seen from Fig. 4, the curves $\beta_n(l)$ are ordered in the $l\beta$ plane in a fairly complex nonmonotone way, and regions appear where they approach one another, which is unlike the case of a shallow-water arctic waveguide [20], where the curves $\beta_n(l)$ are ordered from bottom to top in ascending order of mode numbers n.

SOUND INTENSITY LEVEL AT THE VERTICAL ACOUSTIC ARRAY AS A FUNCTION OF DISTANCE AND ICE COVER THICKNESS

Now, we discuss the features of the sound field intensity $I(r, z, z_0)$ produced at a vertical acoustic array (a chain of hydrophones) by a tone source as a function of the horizontal distance r between the source and the array. For simplicity, we assume that the sound intensity at a single receiving element of the array is determined as the incoherent sum of the mode energies $|A_n|^2|w_n(z)|^2$ of the required maximal number $n_{\max}$ of normal modes [where z is the depth of an array receiver and the quantities A_n for the numbers $n = 1, 2, \ldots, n_{n\max}$ are determined from Eq. (3)]. For modes of group IV, the attenuation coefficients rapidly increase with the number n, and the amplitudes A_n are, according to our calculations, very small in comparison with the amplitudes of modes of groups I–III. For this reason, the sound field in the case of middle and long distances r is mainly formed by modes of groups I, II, and III, the attenuation coefficients of the modes of group III being only slightly dependent on the mode number. We denote by δ_1 and δ_2 the average attenuation coefficients of modes of group I and of combined group II + III, respectively. One can see from Fig. 5 that the magnitudes of the functions $|w_n|$ for the modes of group I ($n =$ 1–15) are noticeably greater than the magnitudes of the functions $|w_n|$ for the modes of groups II and III in the depth interval $0 < z < h$, and they are exponentially small for the depths $h \le z \le H$, where $h = h_1 + h_2 + h_3 =$ 400 m. For this reason, the sound intensity curves $J = 10\log_{10}[I(r, z, z_0)/I_0]$ (I_0 is the sound intensity at the distance $r = 1$ km in free space) corresponding to the source located at some depth $z_0 \le h$ ($z_0 = 100$ m) in the region with a high sound velocity gradient and two receiving array elements lying at the depths $z_1 < h$ and $z_2 > h$ cross each other at a certain distance r_0 (Fig. 6a). An approximate formula for r_0 follows from Eqs. (2) and (3):

$$r_0 \approx (\delta_1 - \delta_2)^{-1} \times \log_{10}\left|\frac{\sum_{\mathrm{I}}[|w_n(z_2)w_n(z_0)|^2 - |w_n(z_1)w_n(z_0)|^2]k_n^{-1}}{\sum_{\mathrm{II+III}}[|w_n(z_2)w_n(z_0)|^2 - |w_n(z_1)w_n(z_0)|^2]k_n^{-1}}\right|, \quad (22)$$

where the figures I and II + III mean the summation over the mode numbers of group I and the combined group II + III.

Figure 6a shows that for a distance of several hundreds of kilometers from the source $r \le r_0$, the sound field produced at the array segment $0 < z < h$ by a source located at the depth $z_0 = 100$ m $\le h$ is formed predominantly by the modes of groups I and II with the numbers $n = 1, \ldots, 29$, which are captured by the subsurface sound channel. At the same time, the contribution of all modes of group III to the sound field intensity at this array segment is appreciably smaller and does not exceed 0.5 dB. For longer distances r, the sound field at this array segment is formed by all modes of groups I–III. For the remainder of the array located at depths $h < z < H$, only the least attenuated modes of groups II and III contribute to the sound intensity for all distances r, because the quantities $|w_n(z)|$ are exponentially small for the modes of group I. For a source located at a depth $z_0 > h$, the modes of group I are practically not generated in the waveguide, so that the sound field is formed predominantly by the modes of groups II and III along the whole length of the array and for all distances r.

Figure 6b shows the family of the horizontal sections of the intensity level J in the subsurface sound channel for different values of the ice cover thickness $l = 0$–5 m (the light solid line corresponds to $l = 0$). As can be seen, the magnitude of the intensity level J as a function of the ice cover thickness l correlates, at a given r, with the features in the behavior of the curves $\beta_n(l)$ shown in Figs. 2 and 4. It appears that the curves of the intensity level $J(r)$ are most sensitive to variations in the ice thickness for $l = 1$–2 m.

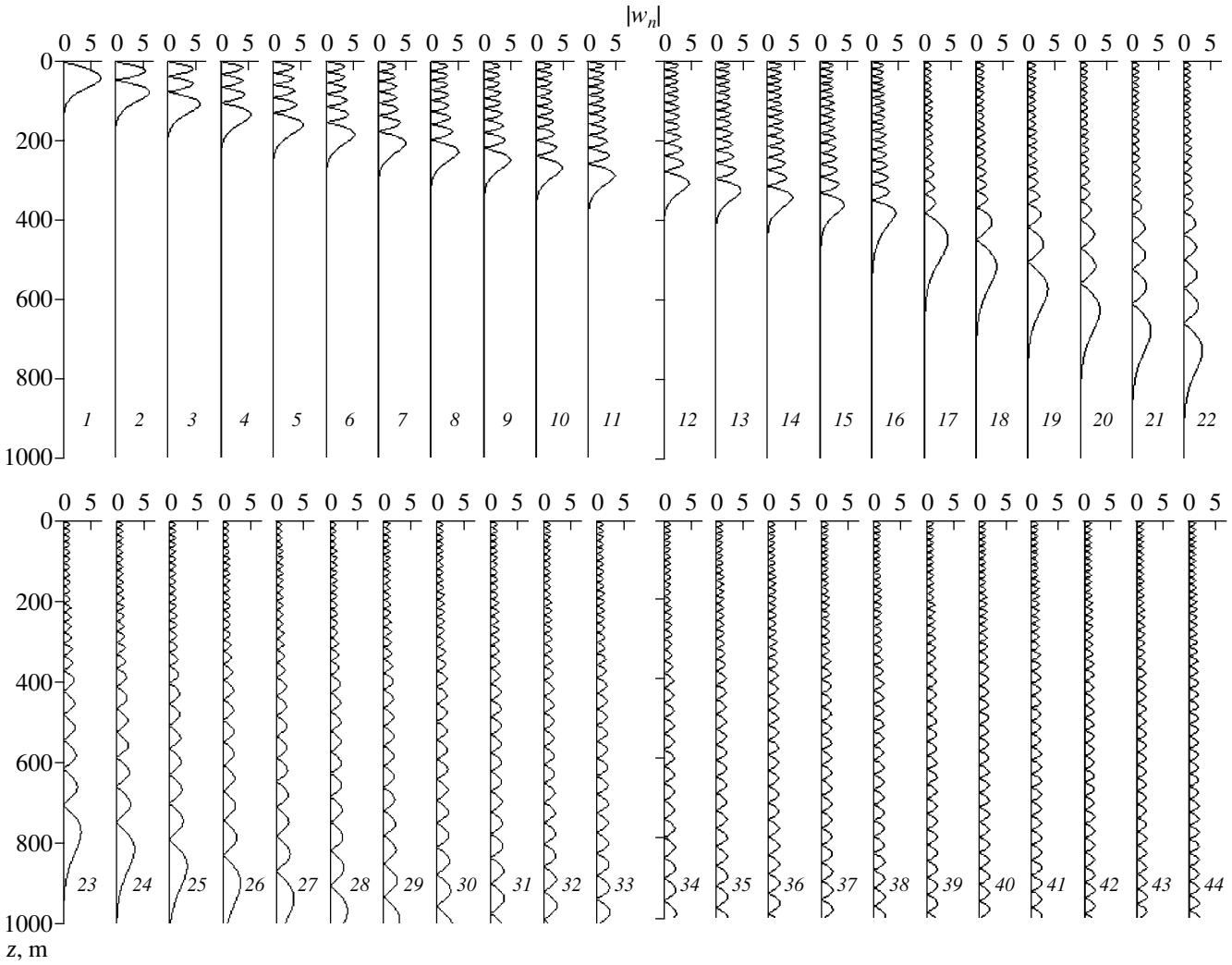

Fig. 5. Magnitudes of the normalized eigenfunctions w_n as functions of depth at a frequency of 250 Hz and at the ice cover depth l = 3 m. The integers are the mode numbers: numbers from *1* to *15* correspond to group I, from *16* to *29*, to group II, and from *30* to *44*, to group III.

EXTENSION OF THE RESULTS TO THE MODEL OF AN ARCTIC WAVEGUIDE WITH STOCHASTICALLY ROUGH BOUNDARIES OF THE ICE COVER

The above results were extended to several realistic models of the ice cover with stochastically rough boundaries. For such models, an adequate characteristic of the sound field is (see [28, 29]) the average intensity $\langle I \rangle$ of the coherent component of the sound field, in which the pressure is calculated as the incoherent sum of the waveguide modes corresponding to the flat average water–ice boundary characterized by the coherent reflection coefficient $\langle V_s \rangle$ (here, the averaging is performed over the statistical ensemble of realizations of the ice cover roughness). If the reflection coefficient $\langle V_s \rangle$ is known, the corresponding attenuation coefficients of these modes $\{ \bar{\beta}_n \}$, $n = 1, 2, \ldots, N$, due to the absorption in the bulk of ice and the scattering of sound and elastic waves from the rough boundaries of the ice cover, as well as their mode-number average values $\bar{\delta}_1$ and $\bar{\delta}_2$ for modes of group I and the combined group II + III, are determined in the WKB approximation by the expressions similar to Eqs. (10), (14), (19) and (20), in which the quantity γ should be replaced with $\bar{\gamma}$ equal to the absolute value of the partial derivative of the magnitude of $\langle V_s \rangle$ with respect to the grazing angle at zero: $\bar{\gamma} = |(\partial |\langle V_s \rangle| / \partial \chi)_{\chi = 0}|$. The quantity $\bar{\gamma}$ governs the dependence of the attenuation coefficients $\{ \bar{\beta}_n \}$, $n = 1, 2, \ldots, N$ on the geometrical parameters of the ice cover (such as the rms amplitudes of different types of roughness relative to the average boundary, the spatial radius of roughness correlation, and the average ice thickness), the acoustic and elastic material param-

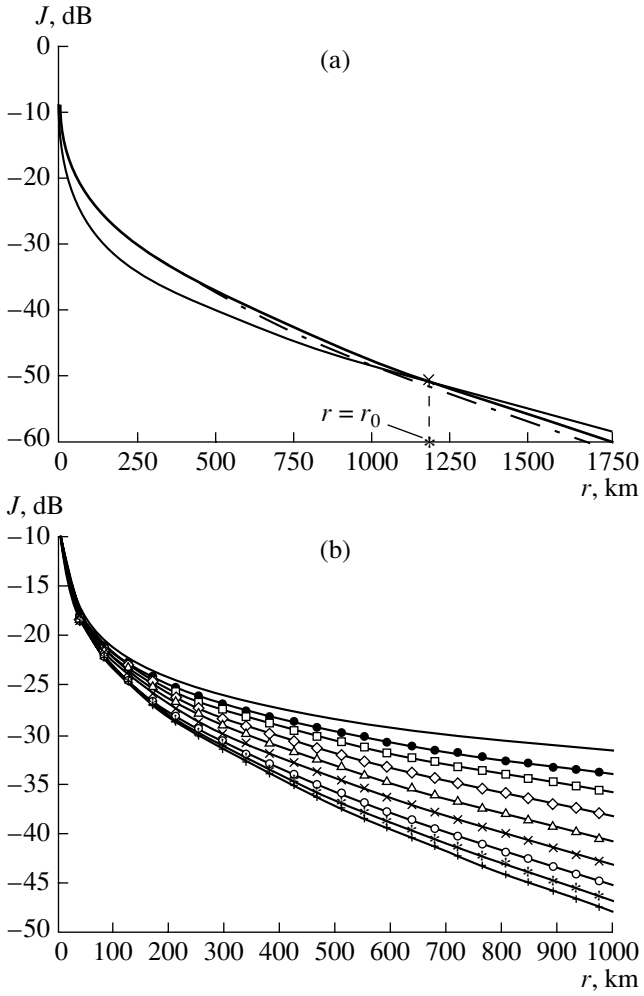

Fig. 6. Sound field intensity levels J (dB) as functions of distance r at a frequency of 250 Hz and at the source depth z_0 = 100 m: (a) (—) l = 3 m, z = 200 m, and n_{max} = 400; (—) l = 3 m, z = 500 m, and n_{max} = 400; (— - — - —) l = 3 m, z = 200 m, and n_{max} = 29; and (b) z = 200 m, n_{max} = 400, l = (●) 1, (□) 1.25, (◇) 1.5, (△) 1.75, (×) 2, (+) 3, (*) 4, and (○) 5 m.

eters of ice, and the frequency. Numerically, the quantity $\bar{\gamma}$ can, in principle, be determined using the known formulas and methods [28–32] for calculating the reflection coefficient $\langle V_s \rangle$ as a function of the grazing angle χ.

Since the only difference between the quantities $\{\bar{\beta}_n\}$ (n = 1, 2, …, N) and the quantities $\{\bar{\beta}_n\}$ (n = 1, 2, …, N) consists in the constant factors $\bar{\gamma}$ and γ, all regularities obtained above for the normal mode characteristics and the spatial distribution of the sound intensity in an arctic waveguide with a flat elastic absorbing ice layer will hold (in the regions where the aforementioned methods of calculating the coherent reflection coefficient $\langle V_s \rangle$ and the quantity $\bar{\gamma}$ are valid) also for the arctic waveguide models with stochastically rough ice cover.

CONCLUSIONS

The WKB approximations proposed above for the attenuation coefficients of normal modes of the coherent component of the sound field generated by a tone source and the established regularities in the distribution of the intensity of this component over a vertical acoustic array can be useful for the development of methods for the acoustic monitoring of the ice cover state and the thermohaline structure in the Arctic basin. Simple formulas (14) and (20) derived in the framework of the WKB method, combined with formula (13), the known asymptotic expressions for the eigenfunctions w_n, and an empirical function relating the sound velocity to temperature, salinity, and depth (e.g., like the Chen–Millero–Lee equation), form the key set for deriving the optimal estimators of the stochastic average geometrical, acoustic, and elastic parameters of the ice cover, as well as the thickness, temperature, and salinity of the characteristic layers in the underice medium, from the experimentally measured attenuation coefficients of normal modes of groups I and II $\{(\bar{\beta}_n)_e\}$, n = 1, 2, …, N_2, which carry important fundamental information about the ice cover parameters and the oceanographic characteristics of the subsurface sound channel. These estimators can be obtained with the use of digital procedures for solving, on the basis of the least squares method [33], the system of nonlinear equations $\{(\bar{\beta}_n)_e - \bar{\beta}_n\} = 0$, n = 1, 2, …, N_2, where $\bar{\beta}_n$ are the theoretically calculated NMAC, in the vector of the parameters to be estimated. The coefficients $(\bar{\beta}_n)_e$ are determined from Eq. (3) by using the coefficients A_n, which are the expansion coefficients of the sound field at the vertical array in the eigenfunctions w_n. The expansion coefficients, in turn, can be calculated using the methods of modal decomposition [9–11, 14, 18] and the matched-field processing [12, 13–17] from the sound field pressures measured with the hydrophones of the vertical receiving array segment located at the depths $0 < z < h$ in the subsurface sound channel. As was shown above, under the condition that $z_0 < h$, these pressures are formed by the modes of groups I and II for a wide range of distances $r < r_0$.

Note that the derived WKB approximations for the coefficients $\bar{\beta}_n$ provide the possibility of a fast and high-accuracy calculation of their distribution over the mode numbers and their dependences on the ice cover parameters, the thermohaline structure of the underice medium, and the frequency. They offer the possibility of circumventing multiple calculations of the complex wave numbers of normal modes with the use of procedures for searching for the complex eigenvalues of a non-self-conjugate spectral boundary-value problem for the second-order differential equation. In turn, these formulas, together with the asymptotic expressions for modal eigenfunctions, provide the possibility of a fast calculation of the sound field intensity generated by a

tone source as a function of the horizontal distance r, various parameters of the ice cover and the underice medium, and the frequency. Therefore, the use of these formulas may significantly improve the efficiency of computer programs used both in the acoustic tomography of the ocean and for the localization of a sound source in the oceanic waveguide, which are based on the matched-field processing [15] requiring multiple calculations of the sound field characteristics for numerous values of the parameters to be estimated.

ACKNOWLEDGMENTS

This work was supported by the Russian Foundation for Basic Research, project no. 01-02-16636.

I thank Professor K.D. Sabinin (Andreev Acoustics Institute, Russian Academy of Sciences) for useful discussions on the oceanological aspects of the problem of the acoustic monitoring of the Arctic Ocean.

REFERENCES

1. A. N. Gavrilov and P. N. Mikhalevsky, in *Proceedings of the Oceans'95 Conference* (1995), Vol. 1, p. 247.
2. A. N. Gavrilov, M. M. Slavinskiĭ, and A. Yu. Shmelev, Usp. Fiz. Nauk **165**, 836 (1995) [Phys. Usp. **38**, 797 (1995)].
3. A. N. Gavrilov and P. N. Mikhalevsky, in *Proceedings of 3rd European Conference on Underwater Acoustics* (1996), Vol. 2, p. 851.
4. P. N. Mikhalevsky, A. N. Gavrilov, and A. B. Baggeroer, IEEE J. Oceanic Eng. Soc. **24** (2), 183 (1999).
5. G. I. Kozubskaya, V. M. Kudryashov, and K. D. Sabinin, Akust. Zh. **45**, 250 (1999) [Acoust. Phys. **45**, 217 (1999)].
6. V. M. Kudryashov, Akust. Zh. **46**, 798 (2000) [Acoust. Phys. **46**, 700 (2000)].
7. Yu. A. Kravtsov, V. D. Krupin, S. S. Lappo, and K. D. Sabinin, in *Proceedings of the 1st International Congress of Seas and Oceans* (West Pomeranian Univ. Press, Szczecin–Miedzdrolje, 2001), p. 187.
8. Guoliang and P. Wadhams, Prog. Oceanogr. **22**, 249 (1989).
9. T. C. Yang, J. Acoust. Soc. Am. **82**, 1736 (1987).
10. E. C. Shang, H. P. Wang, and Z. Y. Huang, J. Acoust. Soc. Am. **83**, 103 (1988).
11. T. C. Yang, J. Acoust. Soc. Am. **85**, 1139 (1989).
12. E. Livingston and O. Diachok, J. Acoust. Soc. Am. **86**, 1909 (1989).
13. D. F. Gingras, J. Acoust. Soc. Am. **86**, 1940 (1989).
14. A. G. Voronovich, V. V. Goncharov, A. Yu. Nikol'tsev, and Yu. A. Chepurin, Akust. Zh. **38**, 661 (1992) [Sov. Phys. Acoust. **38**, 365 (1992)].
15. A. B. Baggeroer, W. A. Kuperman, and P. N. Mikhalevsky, IEEE J. Ocean. Eng. **18** (4), 401 (1993).
16. J. V. Candy and E. J. Sullivan, J. Acoust. Soc. Am. **98**, 1455 (1995).
17. J. V. Candy and E. J. Sullivan, J. Acoust. Soc. Am. **104**, 275 (1998).
18. Lu I-Tai, R. C. Qiu, and Kwak Jaeyoung, J. Acoust. Soc. Am. **104**, 288 (1998).
19. V. D. Krupin, Akust. Zh. **46**, 789 (2000) [Acoust. Phys. **46**, 692 (2000)].
20. V. D. Krupin, in *Proceedings of the VIII School–Seminar of Academician L.M. Brekhovskikh: Acoustics of the Ocean* (GEOS, Moscow, 2000), p. 48.
21. I. V. Polyakov and L. A. Timokhov, Meteorol. Gidrol., No. 7, 68 (1994).
22. K. Aagaard, L. K. Coachman, and E. C. Carmack, Deep-Sea Res., Part A **28**, 529 (1981).
23. M. Steele and T. Boyd, J. Geophys. Res. **103** (C5), 10419 (1998).
24. D. F. Common and S. T. McDaniel, J. Acoust. Soc. Am. **77**, 499 (1985).
25. V. D. Krupin, Sudostr. Prom., Ser. Akust., No. 2, 82 (1989).
26. C. T. Tindle and D. E. Weston, J. Acoust. Soc. Am. **67**, 1614 (1980).
27. P. J. Sutton, P. F. Worcester, G. Masters, *et al.*, J. Acoust. Soc. Am. **94**, 1517 (1993).
28. W. A. Kuperman and H. Schmidt, J. Acoust. Soc. Am. **86**, 1511 (1989).
29. F. I. Kryazhev and V. M. Kudryashov, Akust. Zh. **47**, 101 (2001) [Acoust. Phys. **47**, 85 (2001)].
30. R. Rubenstein and D. Greene, J. Acoust. Soc. Am. **89**, 866 (1991).
31. V. M. Kudryashov, Akust. Zh. **42**, 247 (1996) [Acoust. Phys. **42**, 215 (1996)].
32. V. M. Kudryashov, Akust. Zh. **45**, 529 (1999) [Acoust. Phys. **45**, 472 (1999)].
33. D. W. Marquardt, J. Soc. Ind. Appl. Math. **11** (2), 431 (1963).

Translated by A. Vinogradov

Acoustical Physics, Vol. 48, No. 6, 2002, pp. 707–712. Translated from Akusticheskiĭ Zhurnal, Vol. 48, No. 6, 2002, pp. 799–804.

Natural Oscillations of a Fluid-Filled Vessel Shaped Like a Spherical Cone

Yu. A. Lavrov* and V. D. Luk'yanov**

** St. Petersburg State University of Transport, Moskovskiĭ pr. 9, St. Petersburg, 190031 Russia*

*** St. Petersburg Military Engineering University, Zakhar'evskaya ul. 22, St. Petersburg, 191194 Russia*

e-mail: lvv@vl2771.spb.edu

Received January 21, 2002

Abstract—An analytical solution to the problem of determining the frequencies and modes of free axisymmetric oscillations of a spherical cone is obtained and studied. The spherical cone is filled with an ideal compressible liquid. The spherical surface of the cone is represented by a thin elastic shell rigidly fixed along its boundary to the perfectly rigid radial wall of the cone. Approximate equations for the eigenfrequencies are presented. The dependences of the frequencies on the mechanical properties of the shell and on the geometric dimensions of the resonator are analyzed. *© 2002 MAIK "Nauka/Interperiodica".*

Oscillations of fluid-filled elastic spherical shells are considered in many papers, which present both analytical solutions [1–6] and numerical techniques, such as a combination of the boundary-element and finite-element methods [3]. Oscillations of both a complete sphere [1–3, 6] and a hemisphere [4, 5, 7] have been studied. In this paper, we consider a case that has not been adequately investigated in the literature: we study free oscillations of a spherical cone with an arbitrary vertex angle and an ideal compressible liquid filling its inner volume. The spherical cone is bounded by a thin elastic spherical shell and a perfectly rigid radial wall.

The spherical cone occupies the region $\Omega = \{0 < r < R, 0 \le \varphi < 2\pi, 0 \le \vartheta < \alpha\}$, where r, φ, and ϑ are spherical coordinates. The region Ω is filled with an ideal compressible liquid characterized by the density ρ_0 and the sound velocity c. The shell represents the spherical surface of radius R. For the spherical cone defined above, we seek the axisymmetric modes of oscillation that do not depend on the azimuth angle φ. Therefore, this variable is absent in our calculations.

The sound pressure $P(r, \vartheta)$ in the medium in the region Ω satisfies the Helmholtz homogeneous equation

$$\left(\frac{1}{r^2}\frac{\partial}{\partial r}r^2\frac{\partial}{\partial r} + \frac{1}{r^2\sin\vartheta}\frac{\partial}{\partial\vartheta}\sin\vartheta\frac{\partial}{\partial\vartheta} + k^2\right)P(r, \vartheta) = 0, \quad (1)$$

where $k = \omega/c$ is the wave number (ω is the circular frequency). The dependence of the wave process on time is assumed to be harmonic and determined by the factor $\exp(-i\omega t)$, which is omitted from here on.

The boundary condition that determines the absence of motion for the wall of the angular region has the form

$$\left.\frac{\partial P(r, \vartheta)}{\partial\vartheta}\right|_{\vartheta = \alpha} = 0. \quad (2)$$

The displacements of the points of the elastic shell are described by a system of ordinary differential equations from the Vlasov theory of shell oscillations [8] with allowance for the contact with the acoustic medium. The equations describing the shell movement harmonic in time are as follows:

$$-\rho h\omega^2 U(\vartheta) = G\left(1 - \sigma + \frac{d}{d\vartheta}L\right)U(\vartheta) + G\frac{d}{d\vartheta}((1 + \sigma - \beta(\Delta_\perp + 2))W\vartheta), \quad (3)$$

$$-\rho h\omega^2 W(\vartheta) = -G(1 + \sigma - \beta\Delta_\perp)LU(\vartheta) - G(2(1 + \sigma) + \beta(\Delta_\perp^2 + (1 - \sigma)(\Delta_\perp + 2)))W(\vartheta) + P(R, \vartheta). \quad (4)$$

Here, $U(\vartheta)$ and $W(\vartheta)$ are the displacements of the shell points in the meridian and radial directions, respectively;

$$L\Phi(\vartheta) = \frac{1}{\sin\vartheta}\frac{d}{d\vartheta}(\sin\vartheta\Phi(\vartheta));$$

$$\Delta_\perp\Phi(\vartheta) = L\left(\frac{d}{d\vartheta}\Phi(\vartheta)\right);$$

$G = Eh/(R^2(1 - \sigma^2))$; $\beta = h^2/(12R^2)$; h is the thickness of the shell; and E, σ, and ρ are the Young modulus, Poisson ratio, and density of the shell material, respectively.

The equality of the radial displacements of the shell points and the displacements of the liquid at the shell

1063-7710/02/4806-0707$22.00

surface in the direction normal to the latter is expressed as follows:

$$W(\vartheta) = \frac{1}{\rho_0\omega^2}\frac{\partial P(r,\vartheta)}{\partial r}\bigg|_{r=R}. \quad (5)$$

The condition that the shell is fixed along its perimeter means the absence of displacements and rotations at the shell boundary:

$$U(\alpha) = 0, \quad (6)$$

$$\frac{dW(\vartheta)}{d\vartheta}\bigg|_{\vartheta=\alpha} = 0, \quad (7)$$

$$W(\alpha) = 0. \quad (8)$$

To make the problem unambiguously solvable, it is necessary to define the behavior of the pressure near the vertex of the angular region. Near the vertex and near the fixed points of the shell boundary, the Meixner conditions must be satisfied [9].

The construction and testing of the solution to the above-stated problem for the shell–liquid coupled system rely on the solution to the problem of natural oscillations of a shell in vacuum. Free oscillations of a spherical shell were considered in [2, 3, 10], and free oscillations of a hemispherical shell, in [5, 7, 11].

The solution $U_0(\vartheta)$, $W_0(\vartheta)$ to the auxiliary problem of the oscillations of a shell with an arbitrary cone angle should satisfy conditions (3), (4), and (6)–(8), where in Eq. (4), for the time being, we set $P(R, \vartheta) \equiv 0$. The following relationships should be applied: $U_0(\vartheta) = AF_1(q, \vartheta)$ and $W_0(\vartheta) = BF_0(q, \vartheta)$, where $F_0(q, \vartheta) = P_q(\cos\vartheta)$, $F_1(q, \vartheta) = \dfrac{\partial P_q(\cos\vartheta)}{\partial\vartheta}$, and $P_q(z)$ is the Legendre function of the first kind of order q. Here, q is the sought quantity.

To determine the constants A and B, we use a homogeneous system of linear algebraic equations in the unknown quantity $\chi = q(q+1)$:

$$\begin{cases}(a_{11}(\chi) + \rho h\omega^2)A + a_{12}(\chi)B = 0\\ a_{21}(\chi)A + (a_{22}(\chi) + \rho h\omega^2)B = 0\end{cases}, \quad (9)$$

where the coefficients are determined by the expressions

$$a_{11}(\chi) = (-\chi + 1 - \sigma)G,$$
$$a_{12}(\chi) = ((\chi - 2)\beta + 1 + \sigma)G,$$
$$a_{21}(\chi) = \chi(\chi\beta + 1 + \sigma)G,$$
$$a_{22}(\chi) = -((\chi^2 - (\chi - 2)(1 - \sigma))\beta + 2(1 + \sigma))G.$$

For system (9) to have a nonzero solution, the following condition should be satisfied:

$$\Delta(\chi) = (a_{11}(\chi) + \rho h\omega^2)(a_{22}(\chi) + \rho h\omega^2) - a_{12}(\chi)a_{21}(\chi) = 0. \quad (10)$$

The determinant $\Delta(\chi)$ is a third-degree polynomial in χ. Therefore, Eq. (10) has three roots. For each of these roots χ_s, there is a pair of quantities $q_s = (-1 + \sqrt{1 + 4\chi_s})/2$, $\tilde{q}_s = (-1 - \sqrt{1 + 4\chi_s})/2$. From the property of the Legendre functions $P_q(z) = P_{-1-q}(z)$, we obtain $P_{\tilde{q}_s}(z) = P_{q_s}(z)$. Then, for each pair q_s, $\tilde{q}_s$, there exist linearly dependent solutions to the system of differential equations (3), (4). Thus, three linearly independent solutions to the system of equations are determined by the three roots q_1, q_2, and q_3 obtained by using the characteristic equation (10). Each root corresponds to a particular solution

$$U_{0s}(\vartheta) = a_{12}(\chi_s)F_1(q_s, \vartheta),$$
$$W_{0s}(\vartheta) = -(a_{11}(\chi_s) + \rho h\omega^2)F_0(q_s, \vartheta).$$

The general solution to the system of equations with boundary conditions (6) and (7) has the form

$$U_0(\vartheta) = C\sum_{s=1}^{3} m_s U_{0s}(\vartheta), \quad W_0(\vartheta) = C\sum_{s=1}^{3} m_s W_{0s}(\vartheta),$$

where C is an arbitrary constant, $m_1 = U_{03}(\alpha)W'_{02}(\alpha) - U_{02}(\alpha)W'_{03}(\alpha)$, $m_2 = U_{01}(\alpha)W'_{03}(\alpha) - U_{03}(\alpha)W'_{01}(\alpha)$, and $m_3 = U_{02}(\alpha)W'_{01}(\alpha) - U_{01}(\alpha)W'_{02}(\alpha)$.

When condition (8) is satisfied, we can construct an equation for the determination of the eigenfrequencies of an isolated shell:

$$\sum_{s=1}^{3} m_s W_{0s}(\alpha). \quad (11)$$

The method proposed in [13–15] for constructing a solution to the problem of coupled oscillations of a shell with a liquid yields the following result:

$$P(r, \vartheta) = C\sum_{n=0}^{\infty} p_n Q_n(r, \vartheta),$$

$$Q_n(r, \vartheta) = \frac{f_0(\lambda_n, kr)}{f_0(\lambda_n, kR)}\frac{F_0(\lambda_n, \vartheta)}{F_0(\lambda_n, \alpha)},$$

$$U(\vartheta) = C\sum_{n=0}^{\infty} u_n\frac{F_1(\lambda_n, \vartheta)}{F_0(\lambda_n, \alpha)},$$

$$W(\vartheta) = C\sum_{n=0}^{\infty} w_n\frac{F_0(\lambda_n, \vartheta)}{F_0(\lambda_n, \alpha)},$$

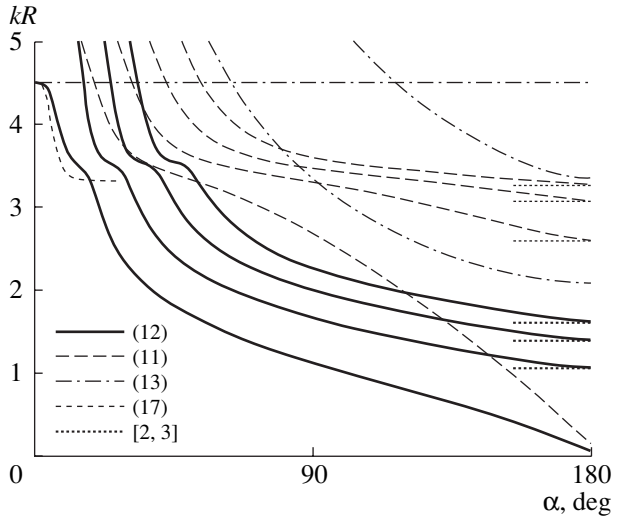

Fig. 1. Dependences of the lower eigenfrequencies on the vertex angle of the spherical cone at a fixed R (the solid lines); $h/R = 0.01$. The dashed and dot-and-dash lines correspond to the oscillation frequencies of an isolated shell and a resonator with perfectly rigid walls. The dotted lines are plotted using the frequency equation from [2, 3].

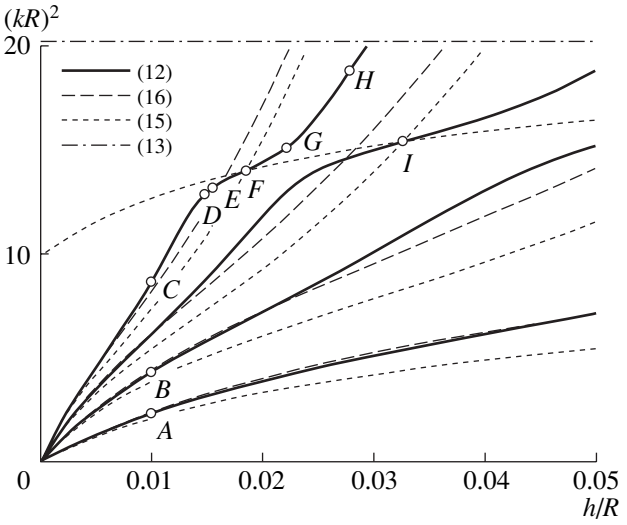

Fig. 2. Dependences of the lower eigenfrequencies ω_s (s = 1, 2, 3, 4) on the shell thickness for $\alpha = 60°$ (the solid lines). The dashed lines are obtained from the approximate equation (16). The pole lines are represented by short-dash lines.

where

$$p_n = \varepsilon_n f_0(\lambda_n, kR)\rho_0\omega c(\rho h\omega^2 + a_{11}(\mu_n))/z_n,$$
$$u_n = -\varepsilon_n f_1(\lambda_n, kR)a_{12}(\mu_n)/z_n,$$

$$w_n = w_n(\omega) = \varepsilon_n f_1(\lambda_n, kR)(\rho h\omega^2 + a_{11}(\mu_n))/z_n,$$
$$z_n = z_n(\omega) = f_0(\lambda_n, kR)\rho_0\omega c(\rho h\omega^2 + a_{11}(\mu_n))$$
$$+ f_1(\lambda_n, kR)\Delta(\mu_n),$$
$$\varepsilon_n = -\alpha(\lambda_n + 1/2)F_0(\lambda_n, \alpha)\left(\frac{\partial F_1(\lambda_n, \alpha)}{\partial\lambda_n}\right)^{-1},$$

$$f_0(\lambda, z) = \frac{J_{\lambda+1/2}(z)}{\sqrt{z}}, \quad f_1(\lambda, z) = \frac{\partial f_0(\lambda, z)}{\partial z},$$

$\mu_n = \lambda_n(\lambda_n + 1)$, and $J_m(z)$ is the Bessel function of order m. The expression for ε_n is chosen to obey the asymptotics $\varepsilon_n \xrightarrow[n\to\infty]{} 1$ [16]. The discrete set of values λ_n, where $n = 0, 1, 2, \ldots$, is determined from the equation

$$F_1(\lambda, \alpha) = 0$$

on condition that $\lambda_0 = 0$ and $\lambda_n \underset{n\to\infty}{\sim} \pi(n + 1/4)/\alpha - 1/2$ [16].

The proposed expressions for the fields satisfying conditions (1)–(7) will correspond to a free process, if we impose the last condition (8) on $W(\vartheta)$. Then, the equation for the determination of the discrete set of eigenfrequencies ω_s, where $s = 1, 2, 3, \ldots$, takes the form

$$\sum_{n=0}^{\infty} w_n(\omega) = 0. \qquad (12)$$

To perform a numerical study of free oscillations of the resonator under consideration, it is convenient to use a comparison with the behavior of isolated shells and containers with perfectly rigid walls.

A formal substitution of $\rho_0 \equiv 0$ in Eq. (12) allows us to determine the frequencies of free oscillations of a shell in vacuum. In this case, we avoid the labor-intensive search for the real-valued roots of a complex-valued function, as is necessary in the case of using Eq. (11). The results obtained by the two approaches coincide.

Oscillations of a liquid-filled hemispherical container with perfectly rigid walls have been studied in [5, 12].

The eigenfrequencies of a resonator with an arbitrary cone angle and perfectly rigid conic and spherical walls are determined from the equation

$$f_1(\lambda_s, kR) = 0, \quad s = 0, 1, 2, \ldots. \qquad (13)$$

If the spherical surface is perfectly soft, one should use the equation

$$f_0(\lambda_s, kR) = 0, \quad s = 0, 1, 2, \ldots. \qquad (14)$$

The numerical experiments performed for a steel shell–water coupled system are illustrated in Figs. 1–5.

First of all, it should be noted that the spectrum of the coupled system under consideration lies in a region of much lower frequencies compared to both the spec-

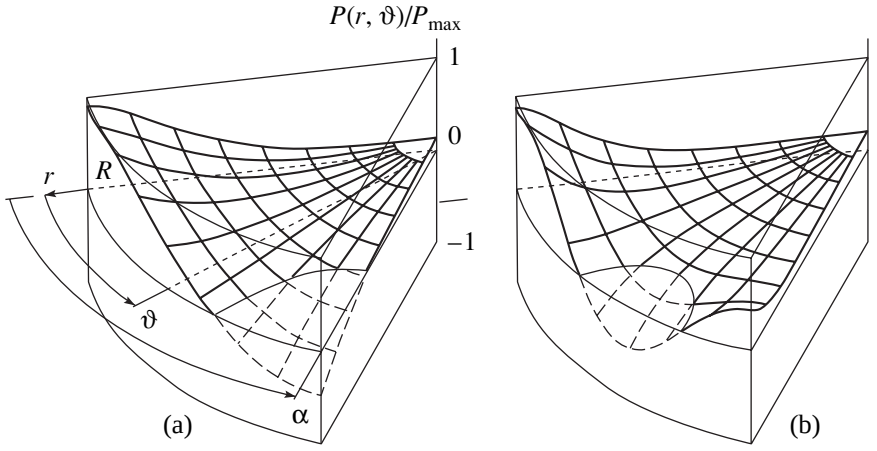

Fig. 3. Modes of free pressure oscillations in the resonator at the frequencies (a) ω_1 and (b) ω_2 (points *A* and *B* in Fig. 2); $\alpha = 60°$ and $h/R = 0.01$.

trum of an isolated shell and the spectrum of a perfectly rigid resonator (Fig. 1).

When $h/R \longrightarrow 0$, the convergence of the series in Eq. (12) becomes rather slow, which hinders the computations. Simultaneously, the eigenfrequencies approach the roots of the equation

$$z_s(\omega) = 0, \quad s = 1, 2, 3, \ldots . \tag{15}$$

The lowest of these roots for each index *s* are below denoted as $\tilde{\omega}_s$. Applying the algorithm described in [15], we construct the relation

$$\omega_s \underset{n \to \infty}{\approx} \sqrt{\frac{hE\lambda_s(\mu_s - 2)}{R^3\rho_0(\mu_s - 1 + \sigma)}},$$

or a finite transcendental equation for an approximate frequency determination:

$$w_s(\omega) + \frac{R^2\sqrt{R}\sqrt[4]{3(1-\sigma^2)}}{Eh\sqrt{h}} = 0, \quad s = 1, 2, 3, \ldots . \tag{16}$$

Equation (16) provides an acceptable accuracy in rather wide limits of variation of the quantity h/R (Fig. 2).

The modes of pressure oscillations in the medium are shown in Figs. 3 and 4, where

$$P_{\max} = \max_{\substack{0 \le r \le R \\ 0 \le \vartheta \le \alpha}} |P(r, \vartheta)|.$$

As long as the eigenfrequency line is immediately adjacent to the line of the roots $\tilde{\omega}_s$ of Eq. (15) (Fig. 2), the standing wave $Q_s(r, \vartheta)$ dominates in the wave packet of the oscillatory process. Figure 4 shows the dynamics of the coefficients p_n of this packet.

At the frequency $\tilde{\omega}_s$, the wave $Q_s(r, \vartheta)$ satisfies conditions (1)–(7) of the problem, while condition (8) fails. However, at the points of intersection of the lines of roots of Eq. (15) with different indices s_1 and s_2 (the points *F* and *I* in Fig. 2), the free process in the resonator is represented by a linear combination of just the two waves $Q_{s_1}(r, \vartheta)$ and $Q_{s_2}(r, \vartheta)$. The relation between the coefficients p_{s_1} and p_{s_2} of this combination is such that condition (8) is also satisfied.

The use of the asymptotics $\lambda_n \underset{n \to \infty}{\sim} j_{0n}/\alpha - 1/2$, $n > 0$, where j_{0n} is the set of positive roots of the equation $J_1(z) = 0$, allows us to construct a finite transcendental equation suitable for the determination of the lower eigenfrequencies at small angles α:

$$\frac{\tan(kR)}{kR}\left(1 + \frac{\alpha^3\tan(\alpha/2)R\rho_0\omega^2}{96G(1-\beta)\beta + \alpha^3\tan(\alpha/2)(2G(1+\sigma+(1-\sigma)\beta) - \rho h\omega^2)}\right) = 1. \tag{17}$$

In the derivation of Eq. (17), we took into account that $\sum_{n=1}^{\infty} j_{0n}^{-4} = 1/192$ (as in [14]).

If $\alpha \longrightarrow 0$ while *R* and *h* are constant, the rigidity of the shell increases with a decrease in its diameter, which results in the desired frequencies approaching the roots of Eq. (13) (Fig. 1).

The special case of small angles α when the quantity $R_c = R\alpha$ is constant is also of interest. In this case, as $\alpha \longrightarrow 0$ and, hence, $R \longrightarrow \infty$, the spherical shell

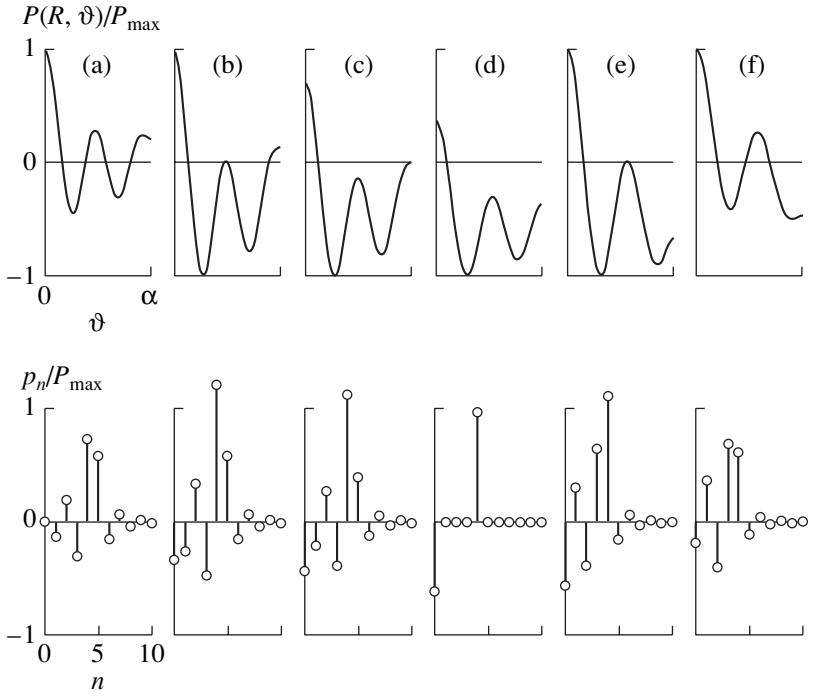

Fig. 4. Evolution of the modes of pressure oscillations and the standing wave packet with the displacement along the line of the fourth eigenfrequency; $\alpha = 60°$. The plots (and the corresponding values of h/R) refer to the points (a) *C*, (b) *D*, (c) *E*, (d) *F*, (e) *G*, and (f) *H* in Fig. 2.

becomes less curved and its oscillations become similar to those of a flat circular plate of a constant radius R_c. It is appropriate to compare the frequencies of free oscillations of the resonator under study with the eigenfrequencies of a cylindrical resonator of radius R_c and height $H_c = R$. The eigenfrequencies of such a resonator, which has a perfectly rigid cylindrical surface, a soft surface at one end, and an elastic plate at the other end, can be determined from the equation

$$\sum_{n=0}^{\infty}\left(q_n^4 - \frac{\rho h\omega^2}{D} - \frac{\rho_0\omega^2}{D}\frac{\tan(H_c\sqrt{k^2-q_n^2})}{\sqrt{k^2-q_n^2}}\right)^{-1} = 0, \quad (18)$$

where $q_n = j_{0n}/R_c$ and $D = Eh^3/(12(1-\sigma^2))$. Equation (18) is a particular case of the result obtained in [14].

The expected coming together of the roots of Eqs. (12) and (18) is confirmed by Fig. 5. It is important to note that, in contrast to Fig. 1, in the special case under discussion, the shell behaves at the lower frequencies as a soft shell rather than as a rigid one. The dimensions and the shape of the shell vary insignificantly, its rigidity does not grow, and the effect of inertia, by contrast, decreases with decreasing frequency of its oscillations. As in the previous publications [13–15], where a similar effect was described, an increase in *R* is accompanied by an increase in the acoustic volume covered by the shell, and, hence, the role of the compressibility of the medium becomes more important.

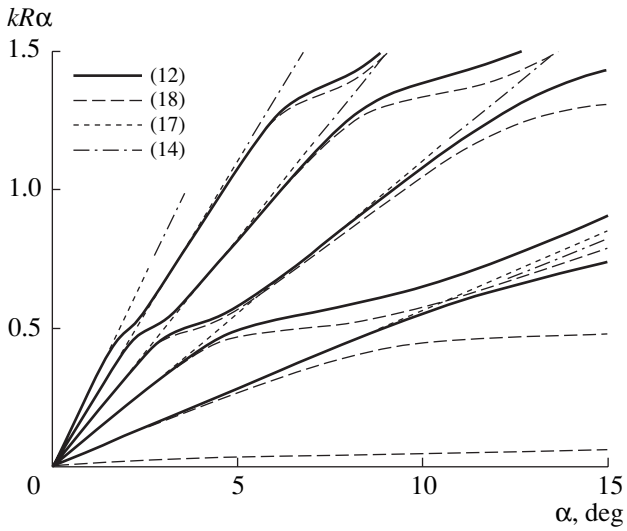

Fig. 5. Dependences of the lower eigenfrequencies on the cone angle at a fixed parameter $R\alpha$ (the solid lines); $h/(R\alpha) = 0.02$. The dashed, short-dash, and dot-and-dash lines correspond to the calculations by Eqs. (18), (17), and (14), respectively.

REFERENCES

1. V. S. Kobychkin and V. P. Shmakov, Stroit. Mekh. Raschet Sooruzheniĭ, No. 2, 49 (1969).
2. A. E. Engin, J. Acoust. Soc. Am. **46**, 186 (1969).
3. M. R. Bai and K. Wu, J. Acoust. Soc. Am. **95**, 3300 (1994).

4. E. A. Samoĭlov and B. S. Pavlov, Izv. Vyssh. Uchebn. Zaved., Aviats. Tekh. **7** (3), 73 (1964).
5. Chintsum Hwang, Trans. ASME, J. Appl. Mech. **32** (3), 665 (1965).
6. C. Scandrett, J. Acoust. Soc. Am. **111**, 893 (2002).
7. Kohsetsu Yuji, Trans. Jpn. Soc. Mech. Eng., Ser. A **65** (636), 50 (1999).
8. V. Z. Vlasov, *Selected Works* (Akad. Nauk SSSR, Moscow, 1962), Vol. 1.
9. R. Mittra and S. W. Lee, *Analytical Techniques in the Theory of Guided Waves* (Macmillan, New York, 1971; Mir, Moscow, 1974).
10. P. M. Naghdi and A. Kalnins, Trans. ASME, J. Appl. Mech. **29** (1), 65 (1962).
11. S. I. Hayek, in *142nd Meeting of Acoustical Society of America* (2001), p. 2772.
12. M. Utsumi, Trans. ASME, J. Appl. Mech. **67** (2), 344 (2000).
13. Yu. A. Lavrov, V. D. Luk'yanov, and G. L. Nikitin, Akust. Zh. **35**, 302 (1989) [Sov. Phys. Acoust. **35**, 180 (1989)].
14. Yu. A. Lavrov, Prikl. Mekh. **27(37)** (4), 53 (1991).
15. Yu. A. Lavrov, Akust. Zh. **43**, 425 (1997) [Acoust. Phys. **43**, 364 (1997)].
16. E. W. Hobson, *The Theory of Spherical and Ellipsoidal Harmonics* (Cambridge Univ. Press, Cambridge, 1931; Inostrannaya Literatura, Moscow, 1952).

Translated by E. Golyamina

Acoustical Physics, Vol. 48, No. 6, 2002, pp. 713–719. Translated from Akusticheskiĭ Zhurnal, Vol. 48, No. 6, 2002, pp. 805–812.

Symmetry of the Rayleigh Equation and the Analysis of Nonlinear Gas Bubble Oscillations in Liquid

A. O. Maksimov

Pacific Oceanological Institute, Far East Division, Russian Academy of Sciences, ul. Baltiĭskaya 43, Vladivostok, 690041 Russia

e-mail: pacific@online.marine.su

Received June 20, 2000

Abstract—The Rayleigh equation describing nonlinear oscillations of a gas bubble in a liquid is analyzed using the theory of groups. The group of scale transformations is calculated and then used as the basis for constructing the solutions to the Rayleigh equation. The analytical description of the essentially nonlinear dynamics of a bubble allows one to use the aforementioned solutions as a model for analyzing such phenomena as cavitation, shock wave propagation in liquids with phase inclusions, and sonoluminescence. © *2002 MAIK "Nauka/Interperiodica".*

The application of the theory of continuous groups for analyzing the symmetry of equations of nonlinear acoustics [1, 2] made it possible to obtain new integrals of motion and exact analytical solutions.

This paper deals with the symmetry of the Rayleigh equation that describes nonlinear oscillations of a gas bubble in an acoustic field.

The Rayleigh equation has the form

$$R\ddot{R} + \frac{3}{2}\dot{R}^2 = \frac{P_i(R) - P(t)}{\rho_0}, \qquad P_i(R) = P_0(R_0/R)^{3\gamma}, \tag{1}$$

where R and R_0 are the current end equilibrium radii of the bubble, P_i is the gas pressure in the bubble, P_0 is the equilibrium pressure, $P(t)$ is the external pressure, and ρ_0 is the density of the liquid.

In Eq. (1), we omitted small (outside the small time interval of bubble collapse) terms describing dissipative processes. The contribution of these terms can be taken into account either using the perturbation theory or as an adiabatic perturbation along the trajectories of Hamiltonian system (1) [3, 4] or numerically.

We begin our analysis of the symmetry of Eq. (1) with the construction of infinitesimal generators of the desired continuous groups. We represent Eq. (1) in terms of normalized variables $u = R/R_0$, $\dot{u} = du/d\tau$, $\tau = t\Omega_0$, $\Omega_0^2 = (3\gamma P_0/\rho_0 R_0^2)$, and $u_1 = P(t)/P_0$:

$$\ddot{u} = \frac{1}{u}\left[-\frac{3}{2}\dot{u} + \frac{1}{3\gamma}\left(\frac{1}{u^{3\gamma}} - u_1\right)\right]. \tag{2}$$

The procedure for determining the tangent vector field of the group of symmetry $\mathbf{V} = \xi(\tau, u)\partial_\tau + \eta(\tau, u)\partial_u$ is given in monographs [5–7] and consists of the construction of the prolongations of the first and second kinds to the space $\tau, u, \dot{u}, \ddot{u}$:

$$pr^{(1)}\mathbf{V} = \mathbf{V} + \varsigma_1(\tau, u, \dot{u})\partial_{\dot{u}},$$

$$\varsigma_1 = D_1(\eta) - \dot{u}D_1(\xi), \quad D_1 = \partial_\tau + \dot{u}\partial_u;$$

$$pr^{(2)}\mathbf{V} = \mathbf{V} + \varsigma_1(\tau, u, \dot{u})\partial_{\dot{u}} + \varsigma_2(\tau, u, \dot{u}, \ddot{u})\partial_{\ddot{u}},$$

$$\varsigma_2 = D_2(\varsigma_1) - \ddot{u}D_2(\xi), \quad D_2 = \partial_\tau + \dot{u}\partial_u + \ddot{u}\partial_{\dot{u}};$$

and the solution of the equation of group

$$pr^{(2)}\mathbf{V}\left\{\ddot{u} - \frac{1}{u}\left[-\frac{3}{2}\dot{u} + \frac{1}{3\gamma}\left(\frac{1}{u^{3\gamma}} - u_1\right)\right]\right\} = 0, \tag{3}$$

under the condition that $\ddot{u} = \frac{1}{u}\left[-\frac{3}{2}\dot{u} + \frac{1}{3\gamma}\left(\frac{1}{u^{3\gamma}} - u_1\right)\right]$.

Rewriting Eq. (3) in an explicit form and collecting the coefficients of equal powers of $\dot{u}$, we obtain

$$C_0 + C_1\dot{u} + C_2\dot{u}^2 + C_3\dot{u}^3 = 0,$$

where

$$C_0 = \left[\frac{\partial^2\eta}{\partial\tau^2} + \left(\frac{\partial\eta}{\partial u} - \frac{\partial\xi}{\partial\tau}\right)\frac{1}{3\gamma u}\left(\frac{1}{u^{3\gamma}} - u_1(\tau)\right)\right.$$

$$\left. - \left(\xi\frac{\partial}{\partial\tau} + \eta\frac{\partial}{\partial u}\right)\frac{1}{3\gamma u}\left(\frac{1}{u^{3\gamma}} - u_1(\tau)\right)\right], \tag{4}$$

$$C_1 = \left[\left(2\frac{\partial^2\eta}{\partial\tau\partial u} - \frac{\partial^2\xi}{\partial\tau^2}\right) - \frac{2}{\gamma u}\frac{\partial\xi}{\partial u}\left(\frac{1}{u_2^{3\gamma}} - u_1(\tau)\right) + \frac{3}{u}\frac{\partial\eta}{\partial\tau}\right],$$

$$C_2 = \left[\left(\frac{\partial^2\eta}{\partial u^2} + \frac{3}{2u}\frac{\partial\eta}{\partial\tau} - \frac{3}{2u^2}\eta\right) - \frac{\partial^2\xi}{\partial\tau^2}\right],$$

$$C_3 = \left[-\frac{\partial^2\xi}{\partial u^2} + \frac{3}{2u}\frac{\partial\xi}{\partial\tau}\right].$$

Since $\dot{u}$ is an independent variable, we must equate each of the above coefficients to zero. From the condition $C_3 = 0$, we have $\xi(\tau, u) = \alpha(\tau) + u^{5/2}\beta(\tau)$. The condition $C_2 = 0$ can be represented in the form

$$\frac{1}{u^{3/2}}\frac{\partial}{\partial u}\left[\frac{1}{u^{3/2}}\frac{\partial}{\partial u}u^{3/2}\eta\right] = 2\frac{1}{u^{3/2}}\frac{\partial}{\partial u}\frac{\partial\xi}{\partial\tau}, \quad (5)$$

which yields $\eta(\tau, u) = \dfrac{\sigma(\tau)}{u^{3/2}} + \nu(\tau)u + \beta(\tau)u^{7/2}$.

Substituting the expressions derived above for η and ξ in equations $C_1 = 0$ and $C_0 = 0$ and equating the coefficients of equal powers of u, we obtain the following relationships for the unknown functions $\alpha(\tau)$, $\beta(\tau)$, $\sigma(\tau)$, and $\nu(\tau)$:

$$\beta = 0, \quad 5\frac{\partial\nu}{\partial\tau} = \frac{\partial^2\alpha}{\partial\tau^2} \text{ (from the condition } C_1 = 0), \quad (6a)$$

$$\sigma = 0, \quad \frac{\partial^2\nu}{\partial\tau^2} = 0, \quad \frac{(2+3\gamma)}{2}\nu = \frac{\partial\alpha}{\partial\tau}, \quad (6b)$$

$$\frac{1}{u_1}\frac{\partial u_1}{\partial\tau} = \frac{2}{\alpha}\left[\nu - \frac{\partial\alpha}{\partial\tau}\right] = -\frac{6\gamma}{(2+3\gamma)}\frac{1}{\alpha}\frac{\partial\alpha}{\partial\tau} \text{ from } C_0 = 0.$$

From relationships (6), it follows that

$$\xi = c_0 + c_1\tau, \quad \eta = c_1\frac{2}{(2+3\gamma)}u$$
$$\text{and} \quad u_1(\tau) = u_1(0)\left(\frac{c_0}{c_0 + c_1\tau}\right)^{6\gamma/(2+3\gamma)}. \quad (7)$$

In the case of a steady external pressure, we have $\partial u_1/\partial\tau = 0$, $u_1 = \text{const}$, and $c_1 = 0$, and the group generator is

$$\mathbf{V}_1 = \partial_\tau. \quad (8)$$

This group is the group of time translation G_1: $(u_2, u_3, \tau + \varepsilon)$. Its presence has the result that the Rayleigh equation has an integral of motion, i.e., a Hamiltonian [3, 4]:

$$H = \frac{u^3\dot{u}^2}{2} + \frac{1}{3\gamma}\left(\frac{1}{3(\gamma-1)u^{3(\gamma-1)}} - \frac{u^3u_1}{3}\right) = \text{const}. \quad (9)$$

The second nontrivial solution to Eqs. (7) appears for

$$u_1(\tau) = u_1(0)\left(\frac{\tau_0}{\tau + \tau_0}\right)^{6\gamma/(2+3\gamma)}, \quad c_0/c_1 \equiv \tau_0.$$

Changing the variable $\tilde{\tau} = (\tau + \tau_0)$, we obtain $u_1(\tilde{\tau}) = U\tilde{\tau}^{-6\gamma/(2+3\gamma)}$, where $U = u_1(0)\tau_0^{6\gamma/(2+3\gamma)}$. An external perturbation of this form corresponds to the shock wave $P(t) = P_m t_0/(t + t_0)^{6\gamma/(2+3\gamma)}$ with the pressure drop P_m at the leading edge and with the characteristic fall time t_0 $(\tau_0 \equiv t_0\Omega_0)$.

In this case, the group generator has the form

$$\mathbf{V}_2 = \tilde{\tau}\partial_\tau + \frac{2}{2+3\gamma}u\partial_u. \quad (10)$$

This group is the group of scaling transformations

$$G_2\colon u' = \lambda^{2/(2+3\gamma)}u(\tilde{\tau}), \quad \tilde{\tau}' = \lambda\tilde{\tau},$$

which translates the solution of the Rayleigh equation into another solution; i.e., the function u' is also a solution to Eq. (2) if it is considered as a function of the new variable $\tilde{\tau}'$: $u'(\tilde{\tau}') = \lambda^{2/(2+3\gamma)}u(\lambda^{-1}\tilde{\tau}')$.

Thus, only two symmetry groups, namely, the time translation and the scaling transformations, can exist for the Rayleigh equation.

Let us investigate the behavior of the solutions under the condition that the group of scaling transformations is available. The invariant solution $u'(\tilde{\tau}') = \lambda^{2/(2+3\gamma)}u(\lambda^{-1}\tilde{\tau}') = u(\tilde{\tau}')$ has the form

$$u(\tilde{\tau}) = z\tilde{\tau}^{2/(2+3\gamma)}, \quad U = \frac{18(\gamma-1)\gamma z^2}{(2+3\gamma)^2} + \frac{1}{z^{3\gamma}}. \quad (11)$$

To find the general solution, we will use the fact that the availability of a certain continuous group of symmetry generally offers the possibility of reducing the order of the corresponding differential equation. Namely, it appears possible to introduce new coordinates (w, z) in such a way that the vector field $\mathbf{V}_2$ and its prolongations $\mathbf{pr}^{(1)}\mathbf{V}_2$ and $\mathbf{pr}^{(2)}\mathbf{V}_2$ represent the shift: $\mathbf{V}_2 = \partial/\partial w$ [7]. Thus, to be invariant in the new coordinate system, differential equation (2) must be independent of w.

The change of variables is constructed with the use of the group invariants; in our case, it is reduced to the substitution $z(w) = u(\tilde{\tau})\tilde{\tau}^{-2/(2+3\gamma)}$, $w = \ln\tilde{\tau}$. It is convenient to introduce the new variable $z_1(\tilde{\tau}) = \tilde{\tau}^{3\gamma/(2+3\gamma)}\dot{u}(\tilde{\tau})$ and rewrite the second-order differential equation (2) as a system of two first-order equations. It turns out that the variable w does not appear explicitly in the resulting system:

$$\frac{dz}{dw} = -\frac{2}{2+3\gamma}z + z_1,$$
$$\frac{dz_1}{dw} = \frac{3\gamma}{2+3\gamma}z_1 + \frac{1}{z}\left[-\frac{3}{2}z_1^2 + \frac{1}{3\gamma}\left(\frac{1}{z^{3\gamma}} - U\right)\right]. \quad (12)$$

From this system, we derive

$$\frac{dz_1}{dz} = \left\{\frac{3\gamma}{2+3\gamma}zz_1 + \left[-\frac{3}{2}z_1^2 + \frac{1}{3\gamma}\left(\frac{1}{z^{3\gamma}} - U\right)\right]\right\} \times z^{-1}\left(z_1 - \frac{2}{2+3\gamma}z\right)^{-1}. \quad (13)$$

Indeed, Eq. (13) is an ordinary differential equation of the first order.

Let us analyze the phase portrait of dynamic system (12). Stationary states are determined from the condition that the right-hand sides of Eqs. (12) vanish:

$$\frac{18\gamma(\gamma-1)}{(2+3\gamma)^2}z^2 + \frac{1}{z^{3\gamma}} = U, \quad z_1 = \frac{2}{(2+3\gamma)}z. \quad (14)$$

This equation has no roots for $U < U_c$, where

$$U_c = \frac{1}{2}\frac{12(\gamma-1)^{3\gamma/(2+3\gamma)}}{(2+3\gamma)^{(3\gamma-2)/(2+3\gamma)}}, \quad (15)$$

one root for $U > U_c$ and $\gamma = 1$, and two roots for $U > U_c$ and $\gamma > 1$. Explicit expressions for these stationary points can be found either if the polytropic exponent only slightly deviates from unity $(\gamma - 1) \ll 1$ or for $\gamma = 4/3$. In the latter case, Eq. (14) is the bicubic equation $z^6 - 9/2Uz^4 + 9/2 = 0$ and its solutions (that make sense for $U \geq U_c = 3^{-1/3} = 0.694$) are described by the formulas

$$z_s^2 = 3^{2/3}U/U_c \times 1/2 + \cos(\alpha/3),$$
$$z_n^2 = 3^{2/3}U/U_c \times 1/2 + \cos(\alpha/3 - 2\pi/3), \quad (16)$$

where $\cos\alpha = 1 - 2U_c^3/U^3$ ($z_s^2 = z_n^2 = 3^{2/3}$ if $U = U_c\cos\alpha = -1$). The type of these singular points is determined from the linear stability analysis and from the calculation of the corresponding Lyapunov exponents λ, which can be expressed explicitly through the solutions of Eq. (14) $z_{s,n}$:

$$\lambda_{1,2} = -\frac{(8-3\gamma)}{2(2+3\gamma)} \pm \sqrt{\frac{(8-3\gamma)^2}{4(2+3\gamma)^2} + \frac{12(\gamma-1)}{(2+3\gamma)^2} - \frac{1}{z_{2s,2n}^{(2+3\gamma)}}}. \quad (17)$$

Stationary states appear at $U = U_c$ (15) at the point with coordinates $z_c = [(2+3\gamma)^2/12(\gamma-1)]^{1/(2+3\gamma)}$, $z_{1c} = 2/(2+3\gamma)z_c$ ($z_{2c} = 3^{1/3}$ for $\gamma = 4/3$). The Lyapunov exponents for this point are $\lambda_{1,2} = (0, -(8-3\gamma)/(2+3\gamma))$. For $U > U_c$, Eq. (14) has two roots, $z_n < z_c$ and $z_s > z_c$. As follows from Eq. (17), a nodal point corresponds to the stationary state z_n (because $\lambda_{1n,2n} < 0$), and a saddle point corresponds to the stationary state z_c (because $\lambda_{1s} < 0$ and $\lambda_{2s} > 0$). With further increase in U, the node is transformed to the focus at $z_n = \left[\frac{25 + 18(\gamma-1) + 9(\gamma-1)^2}{4(2+3\gamma)^2}\right]^{-1/(2+3\gamma)}$ (this transformation occurs at $U = U_f \approx 1$ for $\gamma = 4/3$). In the case of $\gamma \longrightarrow 1$, the bifurcation point at which the node and the saddle merge tends to infinity $z_c \longrightarrow \infty$ ($U_c \longrightarrow 0$, $z_n \longrightarrow U^{1/3}$).

We will investigate the behavior of trajectories far away from the origin using the mapping of the phase plane onto the Poincaré sphere (which is the unit radius sphere touching the (z, z_1) plane at the origin) [8]. On the sphere, two points correspond to every point (z, z_1) of the plane; they lie on the straight line passing through the center of the sphere and the point under consideration. The point of the plane located at an infinite distance is mapped onto the equator of the sphere. In this mapping, the integral curves on the plane are transformed into the corresponding curves on the sphere, and this transformation will not change the characteristic behavior of saddles, nodes, and focuses. However, new singular points will appear on the equator. The transformation $z = (1/c)$, $z_1 = (m/s)$ offers the possibility of studying singular points on the equator of the Poincaré sphere, except for the points corresponding to the ends of the z_1 axis (however, an analysis shows that the system under consideration has no singular points in this region of the phase space).

Two singular points are located on the equator. They are unstable ($s = 0$, $m = 0$) and stable ($s = 0$, $m = 5/2$) nodes. At long distances from the origin, all trajectories tend to this equilibrium state along certain directions, and these directions are the m axis (along which only two trajectories arrive at the node) and the s axis (along which an infinite set of semi-trajectories arrive at the node). On the initial (z, z_1) phase plane, the angular coefficient of the direction along which the trajectories tend to the simple equilibrium state measures 2/5. In the case of time reversal, the trajectories will tend to the unstable node along the direction coinciding with the z axis.

The figure illustrates the above analysis. It shows the behaviors of trajectories calculated for characteristic values of the amplitude parameter $U = 0.5$, 1, and 10 and the polytropic exponent $\gamma = 4/3$. These values are chosen with the goal of characterizing the trajectory behaviors in typical situations:

(a) a small amplitude parameter $U < 1$: here, we use $U = 0.5$, which is less than unity but is sufficiently close to the critical value $U_c = 0.694$, to demonstrate how the singularities appear;

(b) an intermediate amplitude parameter $U \sim 1$: in this case, we use $U = 1$ to illustrate the change of the singular point behavior (the node-focus transformation); and

(c) large amplitude parameters: here, we use $U = 10$.

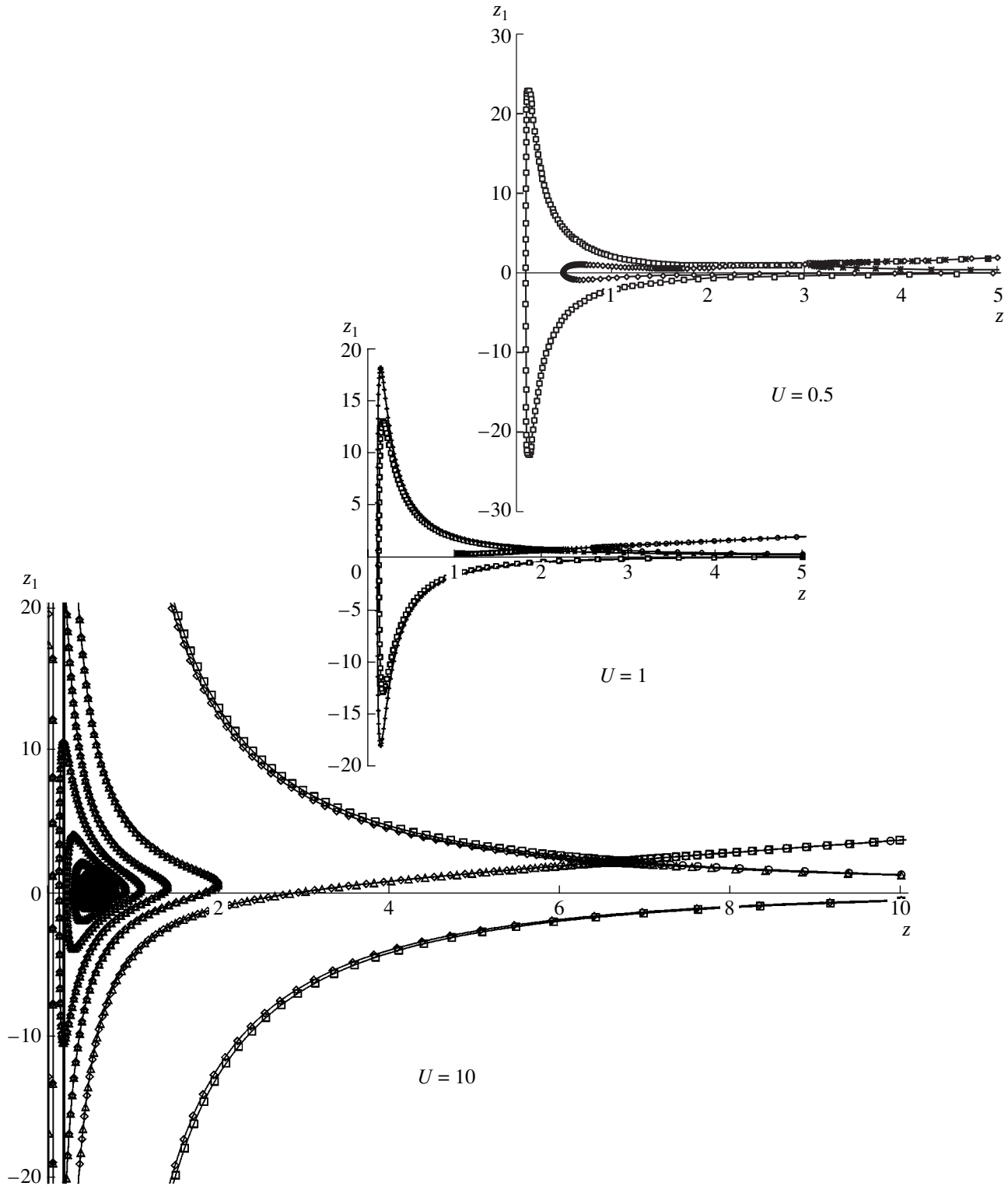

Phase portraits of dynamic system (12) for different values of the governing parameter $U = 0.5$, 1, and 10.

For $U = 0.5$, the system has no singular points in any finite region of the phase space. Trajectories begin from the unstable nodal point at infinity along the direction corresponding to the z axis and go to infinity for $w \longrightarrow \infty$ ($\tilde{\tau} \longrightarrow \infty$) along the direction $z_1/z = 2/5$. The figure shows three trajectories for different initial conditions that are specially chosen to illustrate the appearance of the singular point. The motion along the

direction $z_1/z = 2/5$ corresponds to the known Rayleigh law (the 2/5 law) describing the expansion of an empty bubble.

Note that, for $U \ll 1$, the solution to the Rayleigh equation can be obtained in an explicit form. Indeed, since $P_m \geq P_0$ ($u_1(0) \geq 1$) in the shock wave, the condition $U \ll 1\ u_1(0)\tau_0^{6\gamma/(2+3\gamma)} \ll 1$ can be satisfied only in the case of short pulses $t_0\Omega_0 \ll 1$ ($\tau_0 \ll 1$) and a not too intense wave, because only the inertial term compensates the varying external force. The radius will only slightly vary during the action of the pulse, and the velocity will also be small. Assuming that the bubble under consideration was at rest at the moment of pulse arrival ($\dot{u}(\tau = 0) = 0$, $u(\tau = 0) = 1$), we have

$$\ddot{u} = \frac{1}{3\gamma}\left[1 - \frac{U}{(\tau + \tau_0)^{6\gamma/(2+3\gamma)}}\right],$$

$$\dot{u}(\tau) = \tau/3\gamma - \frac{U}{3\gamma}\frac{(2+3\gamma)}{(3\gamma-2)} \times \left[\left(\frac{1}{\tau_0}\right)^{(3\gamma-2)/(3\gamma+2)} - \left(\frac{1}{\tau+\tau_0}\right)^{(3\gamma-2)/(3\gamma+2)}\right]. \quad (18)$$

The speed of bubble compression reaches its maximal value $u_{\max}$ at the moment $\tau_* = U^{(2+3\gamma)/6\gamma} - \tau_0 = \tau_0[u_1(0)^{(2+3\gamma)/6\gamma} - 1]$ (for $\gamma = 4/3$, $\tau_* = \tau_0[u_1(0)^{3/4} - 1]$); this maximal value is

$$\dot{u}_{\max} = \frac{\tau_0}{3\gamma}\left[u_1(0)^{(2+3\gamma)/6\gamma} - 1 - \frac{(2+3\gamma)}{(3\gamma-2)}\left(1 - \frac{1}{u_1(0)^{(3\gamma-2)/6\gamma}}\right)\right]. \quad (19)$$

For $u_1(0) \sim 1$, we have $u_{\max} \sim -\tau_0$, and for $u_1(0) \gg 1$, we have $u_{\max} \sim -\tau_0 u_1(0)$.

The applicability of this approximation is restricted more severely than follows from the condition $U \ll 1$, because the speed of the bubble wall is small only for $1 \leq u_1(0) \ll (1/\tau_0)$, and from the above condition it follows that there is a subregion $(1/\tau_0) \leq u_1(0) \ll (1/\tau_0)^{6\gamma/(2+3\gamma)}$ where this velocity is high.

At the moment $\tau = \tau_{**}$,

$$\frac{\tau_{**}}{3\gamma} = \frac{U}{3\gamma}\frac{(2+3\gamma)}{(3\gamma-2)}\left(\frac{1}{\tau_0^{(3\gamma-2)/(2+3\gamma)}} - \frac{1}{(\tau_{**}+\tau_0)^{(3\gamma-2)/(2+3\gamma)}}\right) \quad (20)$$

[$\tau_{**} \sim \tau_0$ for $u_1(0) \sim 1$ and $\tau_{**} \approx \tau_0 u_1(0)\ (2+3\gamma)/(3\gamma - 2)$ for $u_1(0) \gg 1$], the bubble radius reaches its minimal value $u_{\min}$,

$$u_{\min} - 1 = \frac{\tau_{**}^2}{6\gamma} - \frac{U}{3\gamma}\left(\frac{2+3\gamma}{3\gamma-2}\right)\left[\frac{\tau_{**}}{\tau_0^{(3\gamma-2)/(2+3\gamma)}} - \frac{(3\gamma+2)}{4}(\tau_{**}+\tau_0)^{4/(2+3\gamma)} - \tau_0^{4/(2+3\gamma)}\right]. \quad (21)$$

We have $u_{\min} \approx 1 - \tau_0^2 u_0^2(0)\ 2/3\gamma[(2+3\gamma)/(3\gamma-2)^2]$ for $u_1(0) \gg 1$ and $u_{\min} \sim (1 - \sim\tau_0^2)$ for $u_1(0) \sim 1$.

For times noticeably exceeding the characteristic duration of the pulse ($\tau \gg \tau_0$), the behavior of trajectories is governed by the integral of energy (9) calculated at $u_1 = 0$. Finally, for $\tau \gg 1$, in which case $u \gg 1$ and the compressibility of gas can be neglected, the bubble will expand according to the Rayleigh law $u \sim \tau^{2/5}$. In the figure, this process corresponds to motion along the straight line $z_1 = (2/5)z$ as mentioned above.

We note that the maximal speed $\dot{u}_{\max}$, the minimal radius $u_{\min} = R_{\min}/R_0$, and the collapse time τ_{**} depend on the parameters of the acoustic pulse, as in the case of the exponential pulse $P(t) = P_m\exp(-t/t_0)$ that was studied in detail in [9, 10]. This fact is not surprising, because only integral characteristics of the shock wave govern the effect in the case of short pulses.

Two singular points appear in the phase portrait corresponding to $U = 1$. They are the node and the saddle separated by a small distance. The initial data for three calculated trajectories were chosen so as to decorate the separatrixes of the saddle point and to distinguish the domain of attraction of the nodal point. In this region of the initial data, the intensity and duration of the shock wave are sufficient to capture the bubble and to govern its dynamics.

In the figure, the phase portrait for $U = 10$ illustrates the bubble oscillations under the action of an intense shock wave ($U \gg 1$). Note that, in this case, the singular points are spaced rather widely. Three calculated trajectories decorate the separatrixes of the saddle point and the domain of attraction of the focus. In this region of the parameter U, the bubble collapse ($z \ll 1$) is so intense ($|z_1| \gg 1$) that trajectories go beyond the frame of the figure and one has to follow the branches of a trajectory by using markers.

This case also allows an analytical description. For $\tau_0 \gg 1$, the external force acting on the bubble varies slowly, which results in the existence of an adiabatic invariant [4, 11].

Note that the initial Rayleigh equation (2) can be written in the Hamiltonian form

$$\dot{u} = \frac{\partial H}{\partial p}, \quad \dot{p} = -\frac{\partial H}{\partial u}, \quad p = u^3\dot{u},$$
$$H = \frac{u^3\dot{u}^2}{2} + \frac{1}{3\gamma}\left[\frac{1}{3(\gamma-1)u^{3(\gamma-1)}} + \frac{u^3 u_1(\tau)}{3}\right]. \quad (22)$$

However, the above variables $z(w) = u(\tilde{\tau})\tilde{\tau}^{-2/(2+3\gamma)}$ and $w = \ln\tilde{\tau}$ are more convenient for the analysis. Applying a canonical transformation with the generation function $\Phi(u, P, \tilde{\tau}) = z(u)P$,

$$p = u^3\dot{u} = \frac{\partial\Phi}{\partial u}, \quad z = \frac{\partial\Phi}{\partial P}, \quad H'(\tilde{\tau}) = H(\tilde{\tau}) + \frac{\partial\Phi}{\partial\tilde{\tau}}, \quad (23)$$

we obtain the expressions for the canonical momentum P and the Hamiltonian H' in new variables:

$$P = \left[\left(\frac{\partial z}{\partial u}\right)_{P=\text{const}}\right]^{-1} p = \tilde{\tau}^{2/(2+3\gamma)} p,$$

$$\tilde{H}(\tilde{\tau}) = H(\tilde{\tau}) - \frac{2}{2+3\gamma}\frac{Pz}{\tilde{\tau}}.$$

With the use of the new temporal variable w, we finally obtain

$$\frac{dz}{dw} = \frac{\partial \tilde{H}}{\partial P}, \quad \frac{dP}{dw} = -\frac{\partial \tilde{H}}{\partial z};$$

$$\lambda_{ad}(w) \equiv \exp[4/2 + 3\gamma^w],$$

$$\tilde{H}(z, P, w) = H\tilde{\tau} = \frac{P^2}{2z^3\lambda_{ad}(w)} \tag{24}$$

$$+ \frac{\lambda_{ad}(w)}{3\gamma}\left[\frac{1}{3(\gamma-1)z} + \frac{z^3 U}{3}\right] - \frac{2}{2+3\gamma}Pz.$$

Since the Hamiltonian $\tilde{H}$ depends on the time w slowly, as compared to the period of the fundamental bubble oscillations, the dynamic system (24) has the adiabatic invariant [11]

$$I = \frac{1}{2\pi}\oint P dz,$$

in the form of an integral along the trajectory for a given energy $\tilde{E} = \tilde{H}(z, P, \lambda_{ad})$ and a given adiabatic parameter λ_{ad}. We emphasize that only a fixed value of Hamiltonian (22) has the direct physical meaning of energy. Under the canonical transformation (23), the Hamiltonian is changed and its value will not describe the energy directly; however, we will use this term in single quotation marks to designate a fixed value of the Hamiltonian.

To avoid cumbersome exponents, we perform the calculations for $\gamma = 4/3$. In this case,

$$I = \frac{\lambda_{ad}}{\pi}\int_{z_{\min}}^{z_{\max}} \sqrt{\frac{z^2}{9} + \frac{2\tilde{E}}{\lambda_{ad} z^3} - \frac{1}{2}\left[\frac{1}{z^4} + \frac{U}{3}\right]}\, z^3 dz, \tag{25}$$

where $z_{\max}$ and $z_{\min}$ correspond to the turning points $dz/dw = 0$. At these values of z, the argument of the root in Eq. (25) vanishes. The period of motion along this trajectory is given by the expression

$$W = 2\int_{z_{\min}}^{z_{\max}} \frac{dz}{\sqrt{\frac{z^2}{9} + \frac{2\tilde{E}}{\lambda_{ad} z^3} - \frac{1}{2}\left[\frac{1}{z^4} + \frac{U}{3}\right]}}. \tag{26}$$

If the bubble that was initially in equilibrium ($u = 1$, $\dot{u} = 0$ $z(w_0) = \tau_0^{-1/3} = \lambda_{ad}(w_0)^{-1/2}$, and $P = 0$) is driven by the shock wave at the moment $\tau = 0$ $w_0 = \ln\tau_0$, its "energy" will be $\tilde{E}(w_0) = \frac{\lambda_{ad}(w_0)}{4}\left[1 + \frac{u_1(0)}{3}\right]$, and adiabatic invariant (25) calculated in the first approximation with respect to the parameter $u_1 \gg 1$ will be equal to

$$I = \frac{\sqrt{u_1(0)}}{\pi\sqrt{6}}\int_0^1 du u\sqrt{u(1-u^3)} \approx 0.036\sqrt{u_1(0)}. \tag{27}$$

Since the magnitude of the adiabatic invariant does not vary with time w, we can equate the left-hand side of expression (25) to the initial value (27) of the invariant, thus obtaining an expression implicitly specifying the "energy" $\tilde{E} = \tilde{E}(w)$ as a function of time w.

The calculation of the integral in Eq. (25) becomes an essentially simpler problem in the asymptotic limit $w \gg w_0$ $z(w) \longrightarrow z_n + \Delta z(w)$, $|\Delta z(w)| \ll z_n$, which corresponds to the dynamic bubble trajectory approaching the focus of system (12). In this case, $z = z_n + \Delta z$, $|\Delta z| \ll z_n$, and $P = P_n(w) + \Delta P$, where P_n is determined from the condition

$$\frac{dz}{dw} = \frac{P}{\lambda(w)z^3} - \frac{z}{3} = 0, \quad P_n(w) = \lambda(w)\frac{z_n^4}{3}$$

and ΔP satisfies the equation

$$\frac{d\Delta P}{dw} = -\frac{\partial \tilde{H}}{\partial z} - \frac{d\lambda(w)}{dw}\frac{z_n^4}{3} = -\frac{\partial}{\partial \Delta z}\left(\tilde{H} + \frac{2}{9}\lambda(w) z_n^4 \Delta z\right).$$

The replacement of variable P by ΔP is, in essence, the canonical transformation with the generating function

$$\Phi_1(z, \Delta P, w) = P(z - z_n) = P_n(w) + \Delta P \Delta z,$$
$$P = \partial\Phi_1/\partial z, \quad \Delta z = \partial\Phi_1/\partial \Delta P, \tag{28a}$$

as a result of which the Hamiltonian is also transformed into the form

$$\tilde{H}' = \tilde{H} + \partial\Phi_1/\partial w = \tilde{H} + \Delta z \partial P_n(w)/\partial w$$
$$= \tilde{H} + 2/9\lambda(w) z_n^4 \Delta z. \tag{28b}$$

To consider Eq. (12) linearized near the focus, we must expand the Hamiltonian $\tilde{H}'$ in Δz and ΔP to quadratic terms:

$$\tilde{H}' = \lambda(w)\left[\frac{1}{3}\left(\frac{1}{z_n} - \frac{z_n^5}{9}\right) + \frac{\Delta P^2}{2\lambda^2(w) z_n^3}\right.$$
$$\left. - \frac{4}{3}\frac{\Delta P \Delta z}{\pi(w)} + \left(\frac{7}{9}z_n^3 + \frac{1}{2}\frac{1}{z_n^3}\right)\frac{\Delta z^2}{2}\right]. \tag{29}$$

This expression allows further simplifications. Since $U \gg 1$ and $z_n \ll 1$, we have, to the first approximation,

$$\left(\frac{\tilde{H}'}{\lambda(w)}\right) = \frac{1}{3z_n} + \frac{\Delta P^2}{2\lambda(w)z_n^3} + \frac{\Delta z^2}{4z_n^3}. \quad (30)$$

Now, the adiabatic invariant can be easily calculated. From Eq. (30), we find the variable ΔP as a function of Δz at constant "energy" $\tilde{E}'$ and adiabatic parameter λ:

$$\Delta P = \pm\frac{1}{\sqrt{2}}\lambda\sqrt{4z_n^3\left(\frac{\tilde{E}' - \tilde{E}_n}{\lambda}\right) - \Delta z^2}, \quad \tilde{E}_n \equiv \lambda\frac{1}{3z_n}. \quad (31)$$

Using this expression, we obtain

$$\begin{aligned} I &= \frac{1}{\pi}\oint P_n + \Delta P\, d(\Delta z) \\ &= \frac{2}{\pi\sqrt{2}}\lambda\int_{\Delta z_{\min}}^{\Delta z_{\max}}\sqrt{4z_n^3\left(\frac{\tilde{E}' - \tilde{E}_n}{\lambda}\right) - \Delta z^2}\, d(\Delta z) \\ &= 4\sqrt{2}z_n^3\tilde{E}' - \tilde{E}_n. \end{aligned} \quad (32)$$

Since the adiabatic invariant does not vary with time, we can equate expression (32) to the initial value of I determined by Eq. (27), thus finding the temporal behavior of the "energy" $\tilde{E}'$ and its dependence on the amplitude $u_1(0)$ and the decay time τ_0 of the shock wave:

$$\begin{aligned} \tilde{E}' &= \tilde{E}_n(w) + \frac{I}{4\sqrt{2}z_n^3} = \frac{\exp(2w/3)}{3}U^{1/4} + \frac{I}{4\sqrt{2}}U^{3/4} \\ &= \frac{\tau_0 u_1(0)^{1/4}}{3}\left[\left(\frac{\tilde{\tau}}{\tau_0}\right)^{2/3} + 0.019u_1(0)\right]. \end{aligned} \quad (33)$$

The real energy of bubble oscillations of Eqs. (22), when averaged over the period $2\pi/(\mathrm{Im}\lambda)$, where λ is determined by expression (17), is obtained from Eq. (33) as $\tilde{E}'$ divided by $\tilde{\tau}$, which follows from the canonical transformation formulas (23), (28a), and (28b).

In the stationary regime described by Eq. (33), two superimposed motions govern the variation of the bubble radius:

$$\begin{aligned} R(t) &= R_0\left(\frac{P_0}{P_m}\right)^{1/4}\left(\frac{t + t_0}{t_0}\right)^{1/3} \\ &+ 0.01R_0\left(\frac{P_m}{P_0}\right)t_0\Omega_0^{1/3}\sin\left\{\left(\frac{P_m}{P_0}\right)^{3/4}t_0\Omega_0\ln[\Omega_0 t + t_0] + \alpha\right\}. \end{aligned} \quad (34)$$

One of these motions is the increase in the radius according to the power law with an exponent that is noticeably different from the exponent in the Rayleigh law. The other motion is the oscillation with a constant amplitude and a logarithmically increasing period. The constant phase α cannot be calculated explicitly in the framework of our approach.

It appears thus possible to analytically describe the nonlinear dynamics of a bubble driven by an external perturbation in conditions ensuring the scale invariance of the Rayleigh equation.

This fact offers the possibility of using the class of solutions obtained above as a convenient model for analyzing such phenomena as cavitation, shock wave propagation in liquids with phase inclusions, and sonoluminescence.

ACKNOWLEDGMENTS

This work was partially supported by the Russian Foundation for Basic Research (project no. 01-02-9690).

REFERENCES

1. A. G. Kudryavtsev and O. A. Sapozhnikov, Akust. Zh. **44**, 628 (1998) [Acoust. Phys. **44**, 541 (1998)].
2. A. G. Kudryavtsev and O. A. Sapozhnikov, Akust. Zh. **44**, 808 (1998) [Acoust. Phys. **44**, 704 (1998)].
3. L. I. Sedov, *A Course in Continuum Mechanics*, 3rd ed. (Nauka, Moscow, 1976; Wolters-Noordhoff, Groningen, 1972), Vol. 2.
4. S. Smereka, B. Binir, and S. Banerjee, Phys. Fluids **30** (11), 3342 (1987).
5. L. V. Ovsyannikov, *Group Analysis of Differential Equations* (Nauka, Moscow, 1978; Academic, New York, 1982).
6. N. Kh. Ibragimov, *Transformation Groups Applied to Mathematical Physics* (Nauka, Moscow, 1983; Reidel, Dordrecht, 1985).
7. P. J. Olver, *Applications of Lie Groups to Differential Equations* (Springer, New York, 1986; Mir, Moscow, 1989).
8. N. N. Bautin and E. A. Leontovich, *Methods and Approaches for Qualitative Investigations of Dynamic Systems on a Plane* (Nauka, Moscow, 1990).
9. R. I. Soloukhin, *Gas Bubble Fluctuations in an Incompressible Liquid* (Novosibirsk, 1961), pp. 27–29.
10. V. K. Kedrinskiĭ, *Hydrodynamics of Explosions: Experiment and Models* (Ross. Akad. Nauk, Novosibirsk, 2000).
11. L. D. Landau and E. M. Lifshits, *Mechanics*, 2nd ed. (Nauka, Moscow, 1965; Pergamon, Oxford, 1976).

Translated by A. Vinogradov

Acoustical Physics, Vol. 48, No. 6, 2002, pp. 720–727. Translated from Akusticheskiĭ Zhurnal, Vol. 48, No. 6, 2002, pp. 813–821.

Acoustic Field Produced by a Concave Radiating Surface with Allowance for the Diffraction

O. A. Sapozhnikov and T. V. Sinilo

Moscow State University, Vorob'evy gory, Moscow, 119899 Russia

e-mail: oleg@acs366b.phys.msu.su

Received January 30, 2002

Abstract—Strongly focused ultrasonic beams are widely used in such modern applications as nondestructive testing and ultrasonic diagnostics and surgery. In these applications, it is important to theoretically predict the acoustic field distribution. The field is usually focused with the help of concave piezoelectric sources, which may consist of one or several radiating elements. The field produced by such sources is usually calculated in terms of the widely known Rayleigh integral, which neglects the multiple scattering of the field by the nonplanar radiating surface. However, at wide focusing angles, the contribution of this effect may be significant. This paper reports results of a numerical simulation of the acoustic field produced by an axially symmetric concave radiator by the method of matched expansions modified for sources whose size is large in terms of the wavelength and for a strong focusing (with convergence angles up to 180°). The results are compared with the calculations by the Rayleigh integral. The spatial structure of the additional acoustic field resulting from the diffraction by the edges and the multiple scattering from the radiating surface itself is considered. The effect of the concave shape of the radiating surface is shown to be significant not only near the source, but also at the beam axis, near the focal point, as well as in the region where the beams issued from the edge arrive after their reflection from the concave surface. *© 2002 MAIK "Nauka/Interperiodica".*

INTRODUCTION

Recent medical and nondestructive-testing ultrasonic applications increasingly use strongly focused acoustic beams. Therefore, much attention has been focused on the theoretical description of the corresponding sources that operate in continuous [1, 2] and pulsed [3–5] operating modes. The field is usually focused with the help of concave piezoelectric transducers; less frequently, by a combination of a plane source and an acoustic lens. Phased arrays have also been used recently [6]. At wide focusing angles, a much more complex theory should be used to allow for the diffraction by the curved surface of the radiator or the lens. However, the field is usually described in terms of the Rayleigh integral, which is the exact solution to the diffraction problem for a plane radiating surface [7]. This representation is equivalent to the Huygens–Fresnel principle, which regards the field of an extended source as interference of spherical waves produced by elementary point sources distributed over the radiating surface. This approach ignores the secondary waves produced by multiple scattering from the curved surface of the radiator. To find an adequate solution to the problem with allowance for the diffraction from the curved surface, one can use the method of matched expansions proposed by Coulouvrat [8]. However, in its initial form as described in [8], this method imposes limitations on the maximal aperture dimension and on the maximal focusing angle. The present paper proposes a modification of this method that significantly extends its range of application [9].

DESCRIPTION OF THE METHOD

Consider the problem whose geometry is illustrated in Fig. 1. Let an axially symmetric spherical bowl Γ_S built in an infinite rigid screen Γ_B oscillate radially as $\exp(-i\omega t)$. Let a, f, and F be the aperture radius, radius of curvature, and center of curvature, respectively. The observation point M will be characterized by its spherical coordinates r and θ with the origin at the point O where the plane of the screen intersects the source's axis of symmetry. The acoustic field is described by the Helmholtz equation $\Delta p + k^2 p = 0$ with the Sommerfeld radiation condition at infinity and with the boundary conditions $\partial p/\partial n = ik\rho_0 c_0 u$ on Γ_S and $\partial p/\partial n = 0$ on Γ_B. Here, p is the amplitude of the sound pressure; $k = \omega/c_0$ is the wave number; ω is the circular frequency; ρ_0 and c_0 are the density of the medium and the acoustic velocity in it, respectively; and u is the amplitude of the normal component of the radiating surface velocity, the normal being directed toward the medium.

Consider an additional hemisphere Γ_L of radius a centered at the origin O. This surface separates the interior domain Ω_i from the exterior domain Ω_e. Denote the acoustic field in these domains as p_i and p_e, respectively. Then the original problem splits in two:

$$\Delta p_i + k^2 p_i = 0, \tag{1a}$$

$$\left.\frac{\partial p_i}{\partial n}\right|_{\Gamma_S} = ik\rho_0 c_0 u, \tag{1b}$$

$$\Delta p_e + k^2 p_e = 0, \tag{2a}$$

$$\left.\frac{\partial p_e}{\partial n}\right|_{\Gamma_B} = 0. \tag{2b}$$

These two problems are related by the conditions that the pressure and normal velocity be continuous at the separating surface Γ_L:

$$p_i|_{\Gamma_L} = p_e|_{\Gamma_L}, \tag{3a}$$

$$\left.\frac{\partial p_i}{\partial n}\right|_{\Gamma_L} = \left.\frac{\partial p_e}{\partial n}\right|_{\Gamma_L}. \tag{3b}$$

Following the procedure described in [8], represent the general solution to Eqs. (1) and (2) in terms of the spherical function expansions. Due to the condition that the acoustic pressure be finite at the origin *O* and to the Sommerfeld radiation condition, we obtain

$$p_i = \sum_{n=0}^{\infty} \xi_n P_n(\cos\theta) j_n(kr), \tag{4}$$

$$p_e = \sum_{n=0}^{\infty} \eta_n P_n(\cos\theta) h_n^{(1)}(kr), \tag{5}$$

where the coefficients ξ_n and η_n of the expansions are determined by boundary conditions (1) and (2) and by continuity conditions (3); P_n are the Legendre polynomials; and j_n, $h_n^{(1)} = j_n + iy_n$, and y_n are the *n*th-order spherical Bessel, first-kind Hankel, and Neumann functions, respectively.

Note that it is not evident whether expansion (4) can be used in the interior domain Ω_i, because the boundary surface is not spherical and solution (4) can in general fail to satisfy the boundary condition. An encouraging circumstance is the fact that, in the limiting case of a zero curvature, this approach gives excellent agreement with the exact solution [8]. In more general cases, the possibility of representing the solution in form (4) requires a special theoretical study and is not a simple problem [10]. However, a direct checking method exists: if, in numerical simulations after finding coefficients ξ_n, expansion (4) reconstructs the boundary condition to a high accuracy, then, as follows from the existence and uniqueness theorem for the Helmholtz equation, the expansion found is the solution to the problem. Leaping ahead, we note that the solutions we found did reconstruct the boundary condition to a high accuracy (see Fig. 4).

As follows from boundary condition (2b), all odd coefficients in Eq. (5) vanish. Thus, we have

$$p_e = \sum_{n=0}^{\infty} \eta_n P_{2n}(\cos\theta) h_{2n}^{(1)}(kr). \tag{6}$$

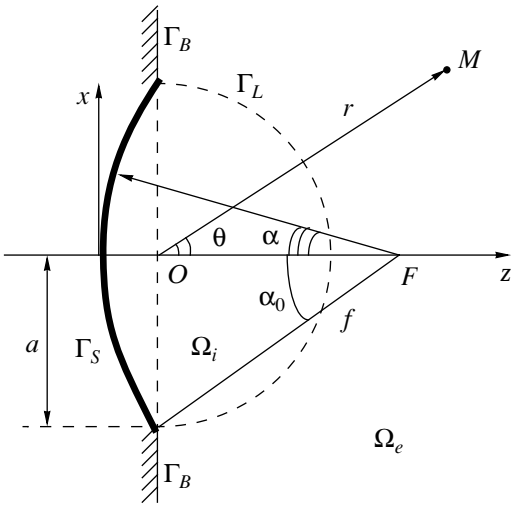

Fig. 1. Geometry of the problem.

Matching conditions (3) relate the coefficients of the interior and exterior expansions; i.e., the quantities η_n can be expressed in terms of ξ_n. In addition, all even coefficients ξ_{2n} of the interior expansion can be represented as infinite combinations of the odd coefficients ξ_{2n+1}. Applying the boundary condition at a number of points of the radiating surface, we obtain an infinite system of linear equations for the unknown expansion coefficients ξ_n. For more details, refer to the original paper [8].

To obtain a finite system of equations, one has to reduce the number of terms in expansions (4) and (6) retaining the first *NB* terms in the interior expansion and *NA* terms in the exterior expansion and hoping that the series converge rapidly enough. In this case, *NA* equations for *NB* unknowns (*NB* > *NA*) are obtained from the matching conditions, while the remaining *NP* = *NB* – *NA* equations are obtained from the boundary condition applied at the corresponding number of points of the radiating surface.

The Bessel and Neumann functions can be calculated by recurrent formulas (see Appendix). The problem is thus reduced to the numerical solution of a finite system of linear equations, which can be performed by standard methods.

High-order Bessel and Neumann functions are known to have the following asymptotics [11]:

$$j_n(\varsigma) \sim [4\varsigma(n+1/2)]^{-1/2}[e\varsigma/2(n+1/2)]^{n+1/2}, \tag{7a}$$

$$y_n(\varsigma) \sim -[\varsigma(n+1/2)]^{-1/2}[e\varsigma/2(n+1/2)]^{-(n+1/2)}. \tag{7b}$$

It can be seen that, as the order increases above $n > e\varsigma/2$, especially at high ς (in this problem, at $\varsigma \sim ka$), the Bessel functions become very small and the Neumann functions become very large. Therefore, the accuracy of solving the system of linear equations becomes low, because the magnitudes of the basis functions appear

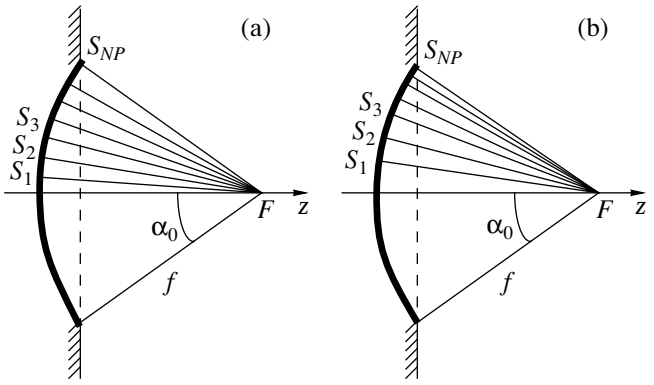

Fig. 2. (a) Uniform and (b) nonuniform distribution of the points at which the amplitude of the normal velocity of the radiating surface is specified.

widely different in their order, and, hence, part of the terms of the series are products of very large and very small quantities and, as a result, are calculated with insufficient accuracy. The higher the order of the functions used, the greater they differ in magnitude from the approximate unit amplitude of lower order functions. Therefore, a too high *NB* leads to significant errors and makes numerical simulations impossible. On the other hand, in order to reduce the error due to the truncation of series (4)–(6), the method should use the spherical Bessel and Neumann functions of up to very high orders. Thus, an optimal value of *NB* exists. Our calculations have shown that sufficiently good results are obtained at $NB \approx (2–3)ka$. This means that this method is difficult to apply to radiators whose size *ka* is large in terms of wavelength, because the maximal order of the Bessel and Neumann functions becomes very high and they reach computer zero or computer infinity at orders smaller than $(2–3)ka$ due to asymptotics (7).

To sidestep this difficulty, we wrote expansions (4) and (6) in terms of normalized Bessel and Hankel functions whose magnitudes are close to unity:

$$p_i = \sum_{n=0}^{NB} \xi_n P_n(\cos\theta)\bar{j}_n(kr), \tag{8}$$

$$p_e = \sum_{n=0}^{NA} \eta_n P_{2n}(\cos\theta)\bar{h}_{2n}^{(1)}(kr). \tag{9}$$

For the sake of simplicity, we denote the expansion coefficients as ξ_n and η_n as before, though their values are different from those in formulas (4) and (6). The new normalized basis functions are as follows:

$$\bar{j}_n(\varsigma) = j_n(\varsigma)\exp(-\varepsilon_n), \tag{10}$$

$$\bar{y}_n(\varsigma) = y_n(\varsigma)\exp(\varepsilon_n), \tag{11}$$

$$\bar{h}_n^{(1)}(\varsigma) = \bar{j}_n(\varsigma)\exp(-2\varepsilon_n) + i\bar{y}_n(\varsigma). \tag{12}$$

The normalization exponents ε_n are independent of ς and their values are noticeably smaller than computer infinity. The formulas for coefficients ε_n and normalized functions are given in Appendix B.

Expansions (8) and (9) considerably extend the range in which the aperture radius can be specified (to $ka \sim 10^3$) maintaining a sufficiently high accuracy of calculations.

Another improvement of the method is to use the nonuniformly distributed spatial points where the normal velocity of the radiating surface Γ_S is specified. As we mentioned above, part of the equations in the system are determined by the boundary conditions imposed at *NP* points of the surface Γ_S. Our calculations have shown that the distribution of these points over the surface strongly affects the accuracy of the boundary condition reconstruction and, therefore, the accuracy of the method. More accurate results were obtained when the point spacing was greater far from the edge and smaller near edge (Fig. 2b) rather than uniform (Fig. 2a). Such a nonuniform distribution provides a better description of the rapid acoustic field variation near the edge of the source.

NUMERICAL RESULTS

As an example of the calculation of the field produced by a large focusing aperture, Fig. 3 shows the axial sound pressure amplitude distribution for an aperture with $ka = 1000$, the focusing angle $\alpha_0 = 60°$, and a constant velocity over the radiating surface:

$$\begin{cases} u = u_0, & \alpha < \alpha_0 \\ u = 0, & \alpha \geq \alpha_0. \end{cases} \tag{13}$$

The focusing angle is understood hereinafter as half of the convergence angle (see Fig. 1). The solid line in Fig. 3 is calculated by the modified method of matched expansions; the dashed line, by the Rayleigh integral

$$p(\mathbf{r}) = -\frac{i\omega\rho_0}{2\pi}\int\int_{\Gamma_S} u(\mathbf{r}')\frac{e^{ik|\mathbf{r}-\mathbf{r}'|}}{|\mathbf{r}-\mathbf{r}'|}dS'. \tag{14}$$

Here, $\mathbf{r}$ is the position vector of the observation point and $\mathbf{r}'$ is the position vector of the element dS' of the radiating surface Γ_S. The noticeable difference between these two theoretical curves in the region near the radiating surface, which can be attributed to the diffraction by the surface of the source or to multiple scattering of the elementary waves by the curved radiator, is visible.

As we noted above, the validation criterion for the solution is the accuracy of reconstructing the boundary conditions, because spherical-harmonics expansions (8) and (9) give a particular solution to the Helmholtz equation, whatever the expansion coefficients ξ_n and η_n. Figure 4 demonstrates a high accuracy of reconstructing boundary condition (1b) and matching condi-

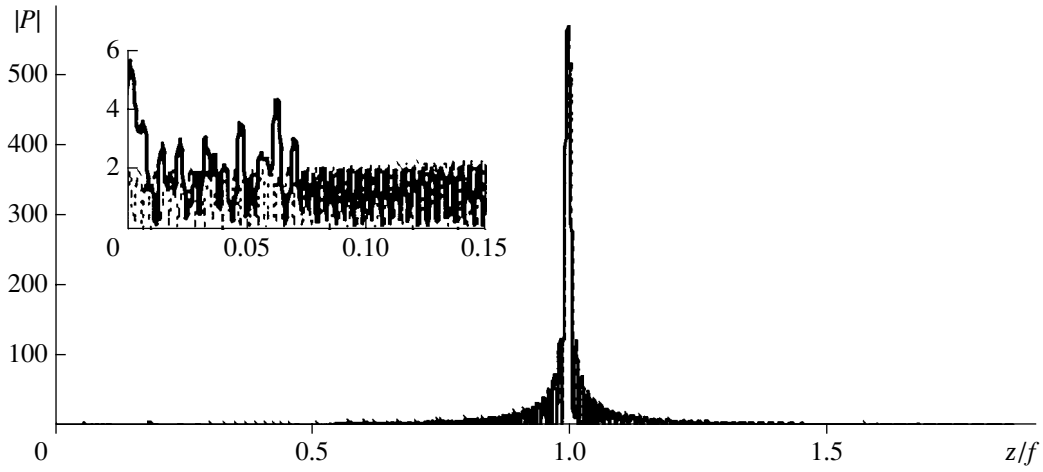

Fig. 3. Normalized amplitude of the acoustic pressure $|P| = |p|/\rho_0 c_0 u_0$ at the radiator axis for $ka = 1000$, $\alpha_0 = 60°$, and a uniform velocity distribution over the radiating surface: the method of matched expansions (solid line) and the Rayleigh integral (dashed line).

tion (3b) for the normal component of the particle velocity. In this case, we used Eqs. (13) as boundary condition (1b), the aperture radius was $ka = 200$, and the focusing angle was $\alpha_0 = 80°$. The velocity distribution is plotted versus the spherical angle θ (Fig. 1), while the curve in Fig. 4 reconstructs conditions (3b) and (1b) within the intervals [0°, 90°] and [90°, 180°], respectively. The normal velocity component of the radiating surface is reconstructed to within 0.03%, and the calculated normal derivative of the pressure is continuous along the matching surface to within 3% relative to the velocity on the radiator, the maximal error being observed at the edge.

The nonuniform distribution of the points where the boundary condition was imposed on the surface of the radiator was in many cases found to improve the accuracy of the calculations by a factor of about 10, all other conditions being the same. Figure 5 illustrates this situation by the results of reconstructing boundary condition (1b) at $ka = 150$, $\alpha_0 = 60$, and a uniform velocity distribution (13) over the radiating surface.

Aside from improving the accuracy, the modification of the method was also found to considerably extend the range of the focusing angles admissible for calculations up to 90°. Figure 6 presents the acoustic field calculated at the axis of the radiator with the aperture radius $ka = 200$ and the focusing angle $\alpha_0 = 88°$. This case cannot be simulated in the framework of the nonmodified approach [8]. The thick line in Fig. 6 is obtained by the modified method of matched expansions; the thin line, by the Rayleigh integral. The figure also shows on an enlarged scale the corresponding distributions near the source and behind the focal point.

From the viewpoint of applications, it is of interest to calculate corrections given by the theory reported in this paper relative to the field predicted by Rayleigh integral (14). These corrections represent the multiply scattered field due to the diffraction by the curved surface. Figure 7 shows the two-dimensional spatial amplitude distributions of this scattered field over the plane passing through the source axis. The field amplitude was calculated as $|\Delta p| = |p_1 - p_2|$, where p_1 and p_2 are the complex amplitudes of the sound pressure obtained by the modified method of matched expansions and by the Rayleigh integral, respectively. The plots refer to $ka = 200$ and the considerably wide focusing angles $\alpha_0 =$ (a) 80° and (b) 88°. For illustration, we use a nonuniformly shaded scale to make the diffracted

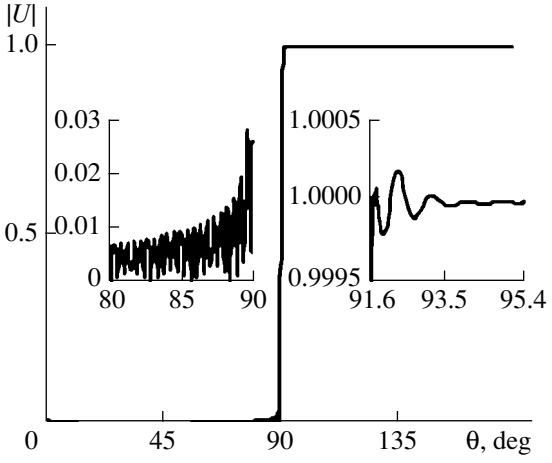

Fig. 4. Reconstructed boundary condition and the matching condition for the normal component of the particle velocity at $ka = 200$ and $\alpha_0 = 80°$: $|U| = \left|\frac{\partial(p_i - p_e)}{\partial n}\right| / k\rho_0 c_0 u_0$ is the jump in the dimensionless velocity at the matching surface for $0° \le \theta \le 90°$, and $|U| = \left|\frac{\partial p}{\partial n}\right| / k\rho_0 c_0 u_0$ is the dimensionless velocity on the radiating surface for $90° < \theta \le 180°$. The exact solution provides $|U| = 0$ for $0° \le \theta \le 90°$ and $|U| = 1$ for $90° < \theta \le 180°$.

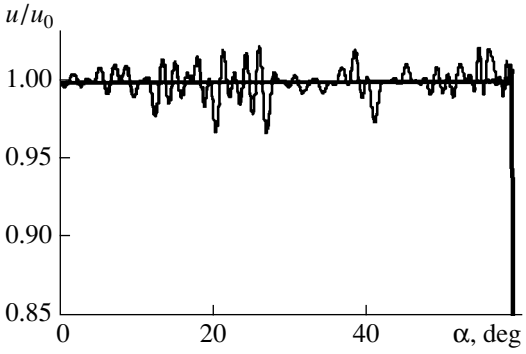

Fig. 5. Reconstructed boundary condition for the uniform distribution of the amplitude of the normal velocity over the radiating surface at $ka = 150$ and $\alpha_0 = 60°$: uniform (thin line) and nonuniform (thick line) distributions of the points over the surface.

field structure in the prefocal region more pronounced. The multiply scattered field is seen to be particularly intense near the axis of the radiator, especially beginning from a certain distance behind the geometrical focal point. As noted in [8], the concentration of the additional field at the axis behind the focal point can be explained by geometrical considerations: rays multiply reflected from the curved surface cannot cross the axis closer than at the distance $z_{min}/f = 1 - \cos\alpha_0/\cos 2\alpha_0$. At this distance, the axis is crossed by the rays issuing from the edge points of the radiator after the specular reflection from the opposite points (the dash-and-dot line in Fig. 8). All other multiply reflected rays cross the acoustic axis at the distances $z > z_{min}$.

In the off-axis region, the rescattered field has a particular structure (see Fig. 7). An oval domain is observed between the focal point and the radiator, where the rescattered field is very small (except, perhaps, near the axis). In this domain, the Rayleigh integral predicts the acoustic field rather accurately. The existence of this domain also follows from geometrical considerations. The analysis of all possible rays issuing from the radiator points and reflected by the curved surface clearly shows that, after the specular reflection, the rays issuing from the edge exhibit the maximal deviation from the surface. Note that the edge is also the strongest source, which generates the so-called edge wave. The dotted lines in Fig. 8 show the rays that go from the edge to the concave surface (the corresponding acoustic field is taken into account by the Rayleigh integral); the thin solid lines show these rays after their reflection (these rays are disregarded by the Rayleigh integral). The envelope of all rays that emanated from the edge and were singly reflected from the surface has a typical arc shape shown in Fig. 8 by a thick line. The analysis shows that this envelope can be written as $R(\beta)$ in the following parametric form:

$$R = f\frac{\tan\gamma\cos\varphi + \sin\varphi}{\tan\gamma\cos\beta + \sin\beta}, \tag{15}$$

$$\beta = \arctan\left(\frac{\left(\tan^2\gamma - \frac{3}{2\cos^2\gamma}\right)\sin\varphi - \tan\gamma\cos\varphi}{\left(1 - \frac{3}{2\cos^2\gamma}\right)\cos\varphi - \tan\gamma\sin\varphi}\right), \tag{16}$$

where $\gamma = \pi - (3\varphi \pm \alpha_0)/2$ and φ varies in the range $\pi - \alpha_0 < \varphi < \pi + \alpha_0$. It is precisely the surface of revolution produced by this envelope that bounds the oval shadow region in which corrections to the Rayleigh integral are small. The rays that experienced one or more reflections pass outside this shadow region. At first sight, it may seem from Fig. 7 that the amplitude of the multiply scattered field formed by these rays is small compared to the axial values. However, the off-axis amplitude of the primary field is also small; i.e., the relative level of

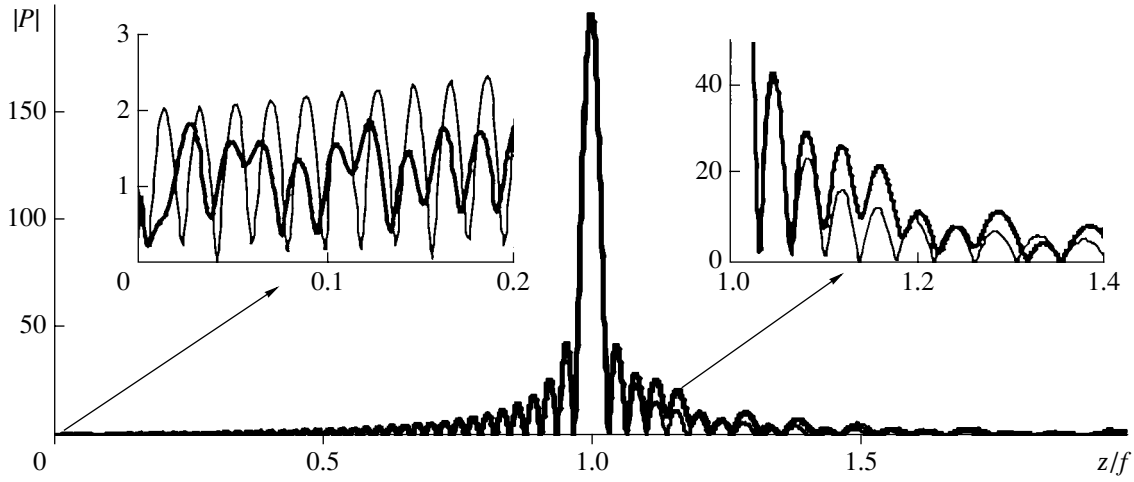

Fig. 6. Amplitude of the sound pressure at the axis of the radiator with $ka = 200$ and $\alpha_0 = 88°$: the modified method of matched expansions (thick line) and the Rayleigh integral (thin line).

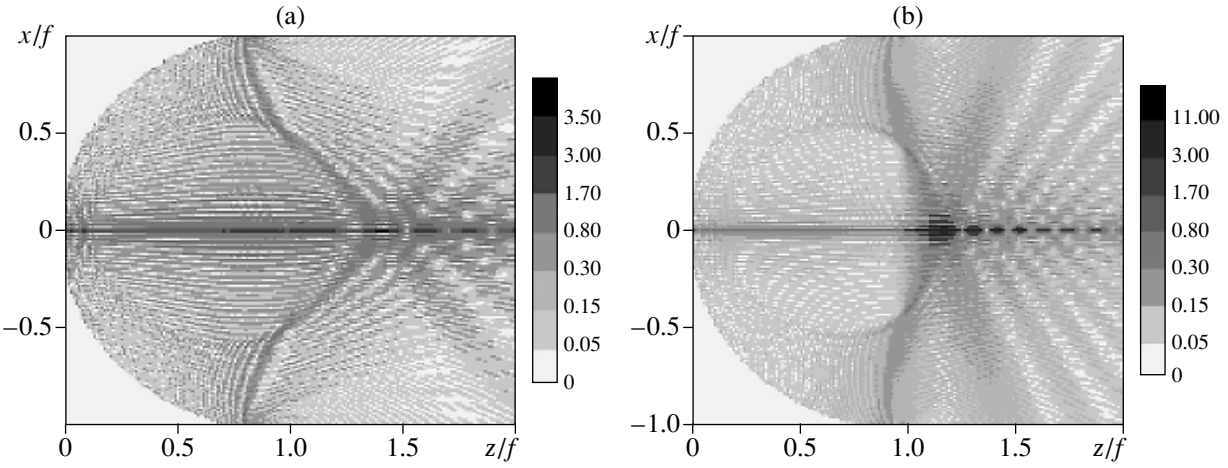

Fig. 7. Two-dimensional amplitude distributions of the multiply scattered acoustic field in the plane that passes through the axis of the radiator with the aperture radius $ka = 200$ and a wide focusing angle α_0 = (a) 80° and (b) 88°. The shading represents the magnitude of the difference between the complex amplitudes of the sound pressure calculated by the method of matched expansions and by the Rayleigh integral.

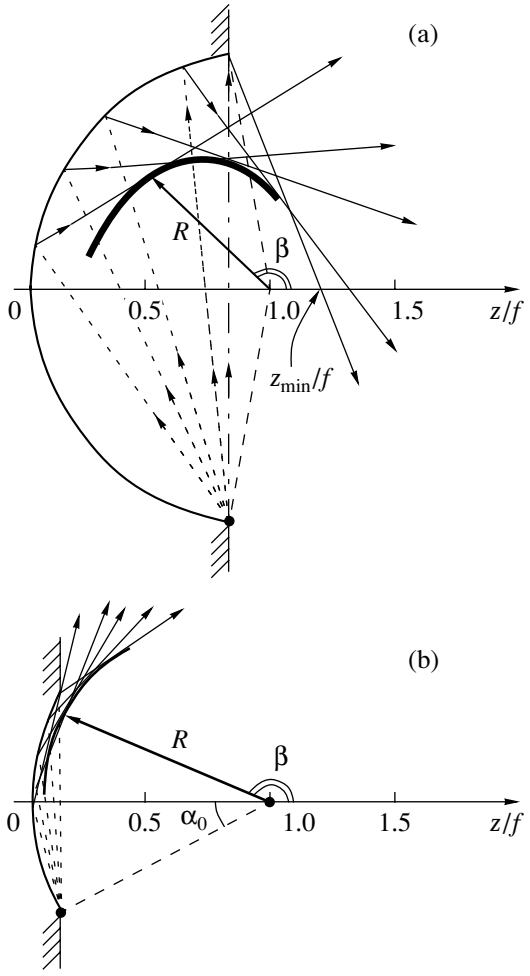

Fig. 8. Geometric structure of the multiply scattered field.

the multiply scattered field is high. For instance, near the radiating surface, the corrections due to the multiply reflected rays may be comparable with the primary field.

For weakly and moderately focused sources, the shadow region (for the multiply scattered field) grows so that it occupies almost the entire halfspace in front of the radiator (Fig. 8b). This observation is validated experimentally [12]. The above acoustic ray patterns give only a qualitative structure of the additional field. For example, they fail to predict the multiply scattered field near the axis in the shadow region, the interference fringes, etc. The value of the method of matched expansions used in this paper is that it calculates the total diffracted field to a high accuracy.

ACKNOWLEDGMENTS

This work was supported by the CRDF, the program "Universities of Russia," and the Russian Foundation for Basic Research.

APPENDIX A

The spherical Bessel and Neumann functions and their derivatives can be calculated by the well-known recurrent formulas [13]

$$s_n(\varsigma) = \frac{2n-1}{\varsigma} s_{n-1}(\varsigma) - s_{n-2}(\varsigma), \qquad \text{(A.1)}$$

$$s_n'(\varsigma) = s_{n-1}(\varsigma) - \frac{n+1}{\varsigma} s_n(\varsigma), \qquad \text{(A.2)}$$

where $s_n(\varsigma)$ denotes any of these spherical functions and ς is the argument of the corresponding function.

Recurrent procedure (A.1) uses the known expressions for the zero- and first-order functions

$$j_0(\varsigma) = \frac{\sin\varsigma}{\varsigma}, \quad j_1(\varsigma) = -j_0'(\varsigma) = -\frac{\cos\varsigma}{\varsigma} + \frac{\sin\varsigma}{\varsigma^2},$$

$$y_0(\varsigma) = -\frac{\cos\varsigma}{\varsigma}, \quad y_1(\varsigma) = -y_0'(\varsigma) = -\frac{\sin\varsigma}{\varsigma} - \frac{\cos\varsigma}{\varsigma^2}.$$

Procedure (A.1) is stable for Neumann functions of any order and for Bessel functions with $n \le \varsigma$. Bessel functions with $n \ge \varsigma$ can be calculated from the inverse recurrent formula [14]

$$j_n(\varsigma) = \frac{2n+3}{\varsigma} j_{n+1}(\varsigma) - j_{n+2}(\varsigma). \tag{A.3}$$

To start procedure (A.3) with a certain number N, one should know the values of $j_{N+2}(\varsigma)$ and $j_{N+1}(\varsigma)$, which are unknown in advance. However, recurrent algorithm (A.3) rather rapidly reaches the branch corresponding to the Bessel functions; i.e., the particular values of the initial functions $s_{N+2}(\varsigma)$ and $s_{N+1}(\varsigma)$ are unimportant. For example, they can be taken as 0 and 1, respectively, while the number N must considerably (by several hundreds) exceed the maximal required n. Recurrent procedure (A.3) then calculates the Bessel functions accurate to within a constant factor: $\tilde{j}_n(\varsigma) = \chi j_n(\varsigma)$.

Functions $\tilde{j}_n$ grow very fast with decreasing n [see asymptotics (7a)] and can, in general, approach computer infinity. Therefore, at certain numbers $n = n_m$ ($m = 1, 2, \ldots, M$), it is reasonable to renormalize these functions. To this end, a coefficient $\chi_m = \chi\mu_1\mu_2\ldots\mu_m$ is introduced for the functions $\tilde{j}_n$ with $n_m \le n < n_{m+1}$; i.e., the functions are redefined as $\tilde{j}_n(\varsigma) = \chi_m j_n(\varsigma)$. The factor μ_m, stored in the computer memory, is chosen so that the n_mth function be equal to unity: $\tilde{j}_{n_m}(\varsigma) = 1$. The factor χ is defined so that the direct and inverse recurrent procedures yield the same value for the Bessel function of the order $n \approx \varsigma$. The final true values of the higher-order Bessel functions are calculated through the inverse normalization of the functions $\tilde{j}_n$ with the numbers $n_m \le n < n_{m-1}$:

$$j_n(\varsigma) = \tilde{j}_n(\varsigma)/\chi_m = \tilde{j}_n(\varsigma)/(\chi\mu_1\mu_2\ldots\mu_m). \tag{A.4}$$

After this, the derivatives are calculated from recurrent formulas (A.2). Thus, the spherical Bessel and Neumann functions of all required orders and their derivatives are determined.

APPENDIX B

In the problem considered in this paper, it is convenient to normalize the spherical Bessel and Hankel functions using the value of the Bessel function at $\varsigma = ka$, i.e., at the boundary of the inner domain, $r \approx a$. In this case, the new functions will not be too small or too large in the range of ς of interest. To calculate the normalization factors ε_n such that $\varepsilon_n = 0$ for $n < ka$ and $\varepsilon_n = -\ln[j_n(ka)]$ for $n \ge ka$, one can use asymptotic formulas (7). However, it is more convenient to rely on the recurrent formulas that follow from the corresponding relationships for the spherical Bessel functions (see Appendix A). To calculate $\varepsilon_n = -\ln[j_n(ka)]$, one can use the logarithms of the auxilliary coefficients χ, μ_1, μ_2, …, μ_m and the functions $\tilde{j}_n(ka)$ introduced in Appendix A,

$$\varepsilon_n = \ln(\chi) + \ln(\mu_1) + \ln(\mu_2) + \ldots + \ln(\mu_m) - \ln(\tilde{j}_n(ka)), \tag{B.1}$$

rather than compute the functions $\tilde{j}_n$ explicitly.

This procedure avoids the use of great numbers, i.e., overcomes the problem of computer infinity.

To calculate the normalized spherical Bessel functions at an arbitrary argument ς for the orders $n \le \varsigma$, we use the transformed direct recurrent relationships

$$\bar{j}_n(\varsigma) = \frac{2n-1}{\varsigma}\bar{j}_{n-1}(\varsigma)\exp(\varepsilon_n - \varepsilon_{n-1}) - \bar{j}_{n-2}(\varsigma)\exp(\varepsilon_n - \varepsilon_{n-2}). \tag{B.2}$$

To calculate the normalized spherical Bessel functions of the orders $n \ge \varsigma$, we use the inverse recurrent procedure described in Appendix A and store the functions $\tilde{j}_n$ and logarithms $\tilde{\varepsilon}_n = \ln(\chi_m)$ of the coefficients χ_m (where $n_m \le n < n_{m+1}$) rather than the functions j_n. Subsequently, the necessary normalization is applied:

$$\bar{j}_n(\varsigma) = \tilde{j}_n(\varsigma)\exp(\tilde{\varepsilon}_n - \varepsilon_n). \tag{B.3}$$

The derivatives of the normalized Bessel functions are calculated by the recurrent formula

$$\bar{j}_n'(\varsigma) = \bar{j}_{n-1}(\varsigma)\exp(\varepsilon_n - \varepsilon_{n-1}) - \frac{(n+1)\bar{j}_n(\varsigma)}{\varsigma}. \tag{B.4}$$

The normalized Hankel functions and their derivatives are determined from the relationships

$$\bar{h}_n^{(1)}(\varsigma) = \bar{j}_n(\varsigma)\exp(-2\varepsilon_n) + i\bar{y}_n(\varsigma),$$
$$\bar{h}_n^{(1)\prime}(\varsigma) = \bar{j}_n'(\varsigma)\exp(-2\varepsilon_n) + i\bar{y}_n'(\varsigma). \tag{B.5}$$

The normalized Neumann functions $\bar{y}_n(\varsigma) = y_n(\varsigma)\exp(\varepsilon_n)$ and their derivatives $\bar{y}'_n$ are computed from the following modified recurrent relationships:

$$\bar{y}_n(\varsigma) = \frac{2n-1}{\varsigma}\bar{y}_{n-1}(\varsigma)\exp(\varepsilon_{n-1}-\varepsilon_n) - \bar{y}_{n-2}(\varsigma)\exp(\varepsilon_{n-2}-\varepsilon_n), \quad \text{(B.6)}$$

$$y'_n(\varsigma) = \bar{y}_{n-1}(\varsigma)\exp(\varepsilon_{n-1}-\varepsilon_n) - \frac{(n+1)\bar{y}_n(\varsigma)}{\varsigma}.$$

REFERENCES

1. A. J. Rudgers, J. Acoust. Soc. Am. **79**, 1211 (1986).
2. D. Cathignol and O. A. Sapozhnikov, Akust. Zh. **45**, 816 (1999) [Acoust. Phys. **45**, 735 (1999)].
3. W. N. Cobb, J. Acoust. Soc. Am. **75**, 72 (1984).
4. D. Guyomar and J. Power, J. Acoust. Soc. Am. **76**, 1564 (1984).
5. H. Djelouah, J. C. Baboux, and M. Perdrix, J. Acoust. Soc. Am. **87**, 76 (1990).
6. L. R. Gavrilov and J. W. Hand, Akust. Zh. **46**, 456 (2000) [Acoust. Phys. **46**, 390 (2000)].
7. J. W. S. Rayleigh, *The Theory of Sound* (Dover, New York, 1945), Vol. 2, p. 47.
8. F. Coulouvrat, J. Acoust. Soc. Am. **94**, 1663 (1993).
9. O. A. Sapozhnikov and T. V. Sinilo, in *Proceedings of X Session of the Russian Acoustical Society: Physical Acoustics. Wave Propagation and Diffraction* (Moscow, 2000), p. 179.
10. V. F. Apel'tsin and A. G. Kyurkchan, *Analytical Properties of Wave Fields* (Mosk. Gos. Univ., Moscow, 1990).
11. F. W. J. Olver, *Asymptotics and Special Functions* (Academic, New York, 1974; Nauka, Moscow, 1990).
12. D. Cathignol, O. A. Sapozhnikov, and Y. Theillere, J. Acoust. Soc. Am. **105**, 2612 (1999).
13. E. Jahnke, F. Emde, and F. Lösch, *Tables of Higher Functions*, 6th ed. (McGraw-Hill, New York, 1960; Nauka, Moscow, 1968).
14. W. H. Press, S. A. Teukolsky, W. T. Vetterling, and B. P. Flannery, *Numerical Recipes in Fortran: The Art of Scientific Computing*, 2nd ed. (Cambridge Univ. Press, Cambridge, 1994), pp. 223–229.

Translated by A. Khzmalyan

Acoustical Physics, Vol. 48, No. 6, 2002, pp. 728–734. Translated from Akusticheskiĭ Zhurnal, Vol. 48, No. 6, 2002, pp. 822–829.

Wide-Angle Mode Adiabatic Parabolic Equations

M. Yu. Trofimov

Pacific Oceanological Institute, Far East Division, Russian Academy of Sciences, ul. Baltiĭskaya 43, Vladivostok, 690041 Russia

e-mail: dominus@poi.dvo.ru

Received September 20, 2000

Abstract—Using the generalized multiscale method, a system of parabolic equations for the normal mode amplitudes is derived to describe wide-angle sound propagation in the horizontal direction. For the simplest case, this system is compared with the wide-angle equation obtained by the formal factorization of the horizontal Helmholtz operator and the rational-linear Padé approximation for the square roots of operators. The problem of energy flux conservation is considered. The formulas obtained are extended to the case when both density and refractive index may have discontinuities at some interfaces. © *2002 MAIK "Nauka/Interperiodica".*

The multiscale method has been used to derive the wide-angle parabolic equations in [1, 2]. It was found that wide-angle equations can be obtained by simply taking into account the subsequent approximations of the multiscale method without the total or partial summation of asymptotic series.

This paper realizes such a procedure to determine the first correction to the narrow-angle parabolic equation [3]. The procedure is found to lead to the wide-angle equations corresponding to the rational-linear approximation of the square root of the horizontal Helmholtz operator in the formal factorization method [4]. The proposed approach improves the results obtained with the use of the factorization method, and the most important improvement consists in taking into account the radiation transformed into other modes (to avoid misunderstanding, note that Abawi *et al.* [5] considered a somewhat different problem). Since the derivation in the general form is rather cumbersome, it is described below for only the simplest case. For the general case, the final formulas are presented without derivation. The problem of energy flux conservation is also considered for the simplest case.

This paper continues the previous study [3], which formulates the initial physical problem and briefly discusses the history of the problem (see also [4]). Note that the applicability of the adiabatic approximation in the context of certain particular problems have been recently investigated in [6].

In the simplest case, the propagation of sound is described by the Helmholtz equation

$$P_{xx} + P_{yy} + P_{zz} + n^2 P = 0, \tag{1}$$

where P is the acoustic pressure, $n = 1/c$ is the refractive index, and c is the velocity of sound. The absorption of sound is taken into account by the imaginary part of the refractive index [4]. The variables are made dimensionless with the use of the length scale $\bar{h} = \bar{c}/\omega$ and the time scale ω^{-1}, where ω is the angular frequency of sound and $\bar{c}$ is the characteristic velocity of sound.

Equation (1) is considered in the domain Ω specified by the condition $-H \le z \le 0$, where H is the depth of an imaginary boundary at the bottom, with boundary conditions

$$P = 0 \quad \text{at } z = 0, \quad P_z = 0 \quad \text{at } z = -H. \tag{2}$$

In addition, appropriate radiation conditions at infinity are assumed to be satisfied for the horizontal variables.

Introduce a small parameter ϵ and the slow variables $X = \epsilon x$ and $Y = \epsilon^{1/2} y$. Such scales of slowness are characteristic of the parabolic approximation; they were discussed in [7] (see also Sect. 1 in [8]). We postulate that the refractive index allows an expansion in the form

$$n^2 = n_0^2(X, z) + \epsilon\nu(X, Y, z), \tag{3}$$

where we assume that n_0 is real and assign the imaginary part of the refractive index (which is responsible for the absorption of sound) to ν. The assumption that the absorption is small holds for the sound frequencies for which the equations derived below are used. In terms of the slow variables, the Helmholtz equation takes the form

$$\epsilon^2 P_{XX} + \epsilon P_{YY} + P_{zz} + (n_0^2 + \epsilon\nu)P = 0. \tag{4}$$

With the introduction of one fast variable, the generalized multiscale method [9] yields the acoustic pressure expansion in the form

$$P = (u_0(X, Y, z) + \epsilon u_1(X, Y, z) + \epsilon^2 u_2(X, Y, z) + \ldots)\exp\left(\frac{i}{\epsilon}\theta(X, Y, z)\right), \tag{5}$$

which was discussed in detail in [3]. The substitution of this expansion into Eq. (4) and boundary conditions (2) leads to the family of boundary-value problems indexed with the orders (degrees) of ϵ. We consider these problems up to the order $O(\epsilon^2)$.

First of all, we note that boundary conditions (2) yield the identical boundary conditions for u_l, $l = 0, 1, \ldots$ in all orders:

$$u_l = 0 \text{ at } z = 0, \quad u_{lz} = 0 \text{ at } z = -H. \tag{6}$$

In the orders $O(\epsilon^{-2})$ and $O(\epsilon^{-1})$, we obtain the following relationships

$$(\theta_z)^2 u_0 = 0, \quad (\theta_Y)^2 u_0 = 0,$$

which can be satisfied by assuming that the function θ is independent of z and Y.

In the order $O(\epsilon^0)$, we obtain the equation

$$u_{0zz} + n_0^2 u_0 - (\theta_X)^2 u_0 = 0 \tag{7}$$

with boundary conditions (6). We restrict our consideration of this problem to the solutions of the form

$$u_0 = A(X, Y)\phi(z, X), \tag{8}$$

where ϕ is the solution to the eigenvalue problem

$$\phi_{zz} + n_0^2\phi - k^2\phi = 0, \quad \phi(0) = 0, \quad \phi_z(-H) = 0 \tag{9}$$

with the spectral parameter $k^2 = (\theta_X)^2$. We assume that solutions to problem (9), i.e., the eigenfunctions, are real and normalized according to the relationship

$$\int_{-H}^{0} \phi^2 dz = 1. \tag{10}$$

It is known that eigenfunctions form a denumerable set, which we will represent as sequence ϕ_l, $l = 0, 1, \ldots$ and mark the corresponding wave numbers using the same indexes k_l, $l = 0, 1, \ldots$. In what follows, we fix a number j and assume that

$$u_0 = A(X, Y)\phi_j(z, X). \tag{11}$$

In the order $O(\epsilon^1)$, we obtain

$$\begin{aligned} &u_{1zz} + n_0^2 u_1 - (\theta_X)^2 u_1 \\ &= -2\theta_X u_{0X} - i\theta_{XX} u_0 - u_{0YY} - \nu u_0 \end{aligned} \tag{12}$$

with boundary conditions (6). The condition of solvability of this problem with respect to u_1 is

$$2ik_j A_X + ik_{jX} A + A_{YY} + \alpha A = 0, \tag{13}$$

where

$$\alpha = \int_{H}^{0} \nu\phi_j^2 dz. \tag{14}$$

Equation (13) is a very particular case of the parabolic equation derived in [3] (see the same paper for the explanation of the concept of solvability conditions).

In view of Eq. (13), Eq. (12) can be rewritten as

$$\begin{aligned} &u_{1zz} + n_0^2 u_1 - k_j^2 u_1 \\ &= A\left(\phi_j \int_{-H}^{0} \nu\phi_j^2 dz - 2ik\phi_{jX} - \nu\phi_j\right). \end{aligned} \tag{15}$$

We seek the solution to problem (15) with boundary conditions (6) in the form

$$u_1 = \sum_{l=0}^{\infty} B_{jl}(X, Y)\phi_l(z, X). \tag{16}$$

In view of the fact that index j has a special meaning, we will denote coefficient B_{jj} as simply B. Substituting Eq. (16) into Eq. (15) and integrating the resulting equality over z from $-H$ to 0, we obtain, after certain rearrangements, an equation valid for $l \neq j$:

$$(k_l^2 - k_j^2)B_{jl} = A\left(-2ik_j \int_{-H}^{0} \phi_{jX}\phi_l dz - D_{jl}\right), \tag{17}$$

where we introduced the notation

$$D_{jl} = \int_{-H}^{0} \nu\phi_j\phi_l dz \tag{18}$$

(which will be convenient for the following consideration). Equation (17) serves to obtain the coefficients B_{jl} for $j \neq l$. The coefficient B will be determined from the parabolic equation that will be derived below from the condition of solvability of the problem in the order $O(\epsilon^2)$. Since the coefficients B_{jl} are proportional to A, it is convenient to introduce the quantities E_{jl} for $j \neq l$:

$$AE_{jl} = B_{jl}. \tag{19}$$

For definiteness, we set $E_{jj} = 0$.

To find the expressions for ϕ_{jX} and k_{jX} appearing in many formulas, we differentiate problem (9) written for ϕ_j, k_j with respect to X to obtain

$$\begin{aligned} \phi_{jXzz} + n_0^2\phi_{jX} - k_j^2\phi_{jX} &= -(n_0^2)_X\phi_j + (k_j^2)_X\phi_j, \\ \phi_{jX}(0) = 0, \quad \phi_{jXz}(-H) &= 0. \end{aligned} \tag{20}$$

The condition of solvability of this problem is

$$(k_j^2)_X = \int_{-H}^{0} (n_0^2)_X\phi_j^2 dz, \tag{21}$$

which makes it possible to determine k_{jX}. We will seek the function ϕ_{jX} in the form

$$\phi_{jX} = \sum_{l=0}^{\infty} C_{jl}\phi_l. \tag{22}$$

In a way similar to that used in the derivation of expressions for the coefficients B_{jl}, we obtain the formulas for the coefficients C_{jl} with $j \neq l$:

$$(k_l^2 - k_j^2)C_{jl} = -\int_{-H}^{0} (n_0^2)_X \phi_j \phi_l dz. \tag{23}$$

From normalization condition (10) differentiated with respect to X, we additionally obtain

$$C_{jj} = 0. \tag{24}$$

Now, we turn our attention to the relationships in the order $O(\epsilon^2)$. In this order, we obtain the equation

$$\begin{aligned} &u_{2zz} + n_0^2 u_2 - (\theta_X)^2 u_2 \\ &= u_{0XX} - 2\theta_X u_{1X} - i\theta_{XX} u_1 - u_{1YY} - \nu u_1 \end{aligned} \tag{25}$$

with boundary conditions (6). Replacing the quantities u_0 and u_1 appearing in this equation by corresponding representations (8) and (16) and using representation (22), we arrive at the condition of solvability in the form

$$2ik_j B_X + ik_{jX} B + B_{YY} + \alpha B + A_{XX} + \beta A = 0, \tag{26}$$

where

$$\begin{aligned} \beta &= -\int_{-H}^{0} (\phi_{jX})^2 dz \\ &+ \sum_{l=0,\, l\neq j}^{\infty} B_{jl}\left(2ik_j \int_{-H}^{0} \phi_{lX}\phi_j dz + D_{lj}\right). \end{aligned} \tag{27}$$

In deriving formula (27), we used the formula

$$\int_{-H}^{0} \phi_{jXX}\phi_j dz + \int_{-H}^{0} (\phi_{jX})^2 dz = 0,$$

which can be obtained by differentiating twice the normalization condition (10). Using the equality

$$C_{jl} + C_{lj} = 0, \tag{28}$$

which can be obtained by differentiating the orthogonality condition for the eigenfunctions

$$\int_{-H}^{0} \phi_j \phi_l dz = 0$$

with respect to X, together with the expression (17) for B_{jl} and taking into account the symmetry of the coefficients D_{jl} with respect to indexes, we obtain (after some rearrangements) convenient expressions for β:

$$\begin{aligned} \beta &= -\sum_{l=0,\, l\neq j}^{\infty} \left(C_{jl}^2 + \frac{1}{k_l^2 - k_j^2}(D_{jl}^2 + 4k_j^2 C_{jl}^2)\right) \\ &= -\sum_{l=0,\, l\neq j}^{\infty} (C_{jl}^2 + (k_l^2 - k_j^2)|E_{jl}|^2). \end{aligned} \tag{29}$$

The system of equations (13), (26) represents the wide-angle adiabatic mode parabolic equations in the framework of our approach. This statement will acquire a more specific content when the results obtained here are compared with those obtained with a more traditional approach.

Consider the case of n_0 independent of X. To compare our system of equations (13), (26) with the equation resulting from the formal factorization of the horizontal Helmholtz operator, we introduce the amplitude

$$U = A + \epsilon B$$

and add Eq. (26) multiplied by ϵ to Eq. (13). We express the term A_{XX} appearing in Eq. (26) with the use of Eq. (13) differentiated with respect to X. As a result, we obtain

$$\begin{aligned} &2ik_j U_X + U_{YY} + \alpha U \\ &+ \epsilon\left(\beta A + \frac{i}{2k_j} A_{YYX} + \frac{i}{2k_j} D_{jjX} A + \frac{i}{2k_j} D_{jj} A_X\right) = 0. \end{aligned} \tag{30}$$

Since we intend to consider this equation only to the terms of $O(\epsilon^2)$, we can replace it with the equation

$$\begin{aligned} &2ik_j U_X + U_{YY} + \alpha U \\ &+ \epsilon\left(\beta U + \frac{i}{2k_j} U_{YYX} + \frac{i}{2k_j} D_{jjX} U + \frac{i}{2k_j} D_{jj} U_X\right) = 0. \end{aligned} \tag{31}$$

Returning to the initial variables $x = \epsilon^{-1}X$ and $y = \epsilon^{-1/2}Y$ and introducing the parameters

$$\bar{\nu} = \epsilon\nu, \quad \bar{D}_{jl} = \epsilon D_{jl} = \int_{-H}^{0} \bar{\nu}\phi_j\phi_l dz,$$

we finally obtain

$$\begin{aligned} &2ik_j U_x + U_{yy} + \bar{\alpha} U \\ &+ \bar{\beta} U + \frac{i}{2k_j} U_{yyx} + \frac{i}{2k_j} \bar{D}_{jjx} U + \frac{i}{2k_j} \bar{D}_{jj} U_x = 0, \end{aligned} \tag{32}$$

where, in this case,

$$\bar{\alpha} = \bar{D}_{jj}, \quad \bar{\beta} = -\sum_{l=0,\, l\neq j}^{\infty} \frac{1}{k_l^2 - k_j^2} \bar{D}_{jl}^2.$$

Now, we apply the method of formal factorization (for details, see [8], [10], and [11]) of the horizontal

Helmholtz operator to Eq. (4) written in the initial variables in the form

$$P_{xx} + P_{yy} + P_{zz} + (n_0^2 + \bar{\nu})P = 0. \quad (33)$$

Following the algorithm from [4], we represent the acoustic pressure P in the form

$$P = \tilde{A}(x, y)\phi_j(z),$$

where ϕ_j is the eigenfunction, and integrate Eq. (33) with respect to z from $-H$ to 0. Taking into account normalization condition (10) and spectral problem (9), we obtain the equation for the amplitude $\tilde{A}$:

$$\tilde{A}_{xx} + \tilde{A}_{yy} + k_j^2\tilde{A} + \bar{\alpha}\tilde{A} = 0. \quad (34)$$

We replace this equation with its factorization:

$$\left(i\frac{\partial}{\partial x} + k_j\sqrt{1 + \frac{1}{k_j^2}\left(\frac{\partial^2}{\partial y^2} + \bar{\alpha}\right)}\right) \times\left(i\frac{\partial}{\partial x} - k_j\sqrt{1 + \frac{1}{k_j^2}\left(\frac{\partial^2}{\partial y^2} + \bar{\alpha}\right)}\right)\tilde{A} = 0. \quad (35)$$

Remember that such a replacement is approximate in the case of variable coefficients.

Retaining only the first factor, we approximate the square root of the operator $\sqrt{1 + Q}$, where

$$Q = \frac{1}{k_j^2}\left(\frac{\partial^2}{\partial y^2} + \bar{\alpha}\right)$$

by a rational-linear combination $(1 + pQ)(1 + qQ)^{-1}$, where p and q are some factors. Using formula $\tilde{A} = \tilde{U}\exp(k_j x)$ to introduce the envelope $\tilde{U}$, we obtain the equation for the envelope

$$i(1 + qQ)\tilde{U}_x + k_j(p - q)Q\tilde{U} = 0.$$

For $p = 3/4$ and $q = 1/4$ (these coefficients correspond to the Padé approximation P_1^1 [12]), we obtain, after some rearrangements, the final equation

$$2ik_j\tilde{U}_x + \tilde{U}_{yy} + \bar{\alpha}\tilde{U} + \frac{i}{2k_j}\tilde{U}_{yyx} + \frac{i}{2k_j}\bar{D}_{jj}\tilde{U}_x = 0. \quad (36)$$

This equation differs from Eq. (32) in that some terms are absent; namely, the term

$$\frac{i}{2k_j}\bar{D}_{jjx}\tilde{U}$$

is absent because of the above assumptions regarding commutativity, and the term $\bar{\beta}\tilde{U}$ is absent because of the exclusion of other modes from our consideration.

Now, we show that, under the assumption that the loss is absent (the refractive index is real), the equations derived above ensure the conservation of the energy flux to the order $O(\epsilon^3)$.

We introduce the notation

$$\langle h, g\rangle = \int_{-\infty}^{\infty}\int_{-H}^{0} hg^* dz dy, \quad (37)$$

where the asterisk means complex conjugation. We multiply Eq. (1) by P^* and integrate it with respect to y from $-\infty$ to ∞ and with respect to z from $-H$ to 0. Integrating by parts with the use of the boundary conditions, we obtain the equality

$$\langle P_{xx}, P\rangle - \langle P_y, P_y\rangle - \langle P_z, P_z\rangle + \int_{-\infty}^{\infty}\int_{-H}^{0} n^2|P|^2 dz dy = 0,$$

which yields

$$\mathrm{Im}\langle P_{xx}, P\rangle = 0.$$

The energy flux across the (y, z) plane is $\mathrm{Im}\langle P_x, P\rangle$. This expression, which is differentiated with respect to x, gives $\mathrm{Im}\langle P_{xx}, P\rangle$. Consequently, we have the energy flux conservation law for Eq. (1):

$$\frac{\partial}{\partial x}\mathrm{Im}\langle P_x, P\rangle = 0. \quad (38)$$

We now turn our attention to the consideration of this law for parabolic equations (13) and (26). Remember that, in these equations, we have

$$P = A\phi_j\exp\frac{i}{\epsilon}\theta + \epsilon B\phi_j\exp\frac{i}{\epsilon}\theta + \epsilon\left(\sum_{l=0,\, l\neq j}^{\infty} B_{jl}\phi_l\right)\exp\frac{i}{\epsilon}\theta + O(\epsilon^2),$$

where A, B, and B_{jl} are functions of low variables $X = \epsilon x$ and $Y = \epsilon^{1/2}y$, θ is a function of X, and ϕ_j and ϕ_l are functions of X and z. Taking into account the fact that

$$\frac{\partial}{\partial x} = \epsilon\frac{\partial}{\partial X},$$

we have $k_j = \theta_X = (1/\epsilon)\theta_x$.

Direct calculations yield

$$\frac{\partial}{\partial x}\mathrm{Im}\langle P_x, P\rangle = \epsilon\left(k_j\int_{-\infty}^{\infty}|A|^2 dy\right)_X + \epsilon^2\left\{\frac{1}{2i}\int_{-\infty}^{\infty}(A_{XX}A^* - A_{XX}^*A)dy + k_{jX}\int_{-\infty}^{\infty}(BA^* + AB^*)dy\right. \quad (39)$$

$$+ k_j \int_{-\infty}^{\infty} (B_X A^* + BA_X + A_X B + AB_X^*) dy \Bigg\}.$$

Note that Eq. (39) is sufficient to obtain the conservation law (38) in the order of $O(\epsilon^0)$. Indeed, multiply Eq. (13) by A^* and integrate the resulting equality with respect to Y from $-\infty$ to ∞. From the equality obtained in this way, subtract the complex conjugate Eq. (13) multiplied by A and integrated with respect to Y in the same limits. As a result, we obtain

$$\left(k_j \int_{-\infty}^{\infty} |A|^2 dy \right)_X = 0,$$

which is the conservation law (38) in the order of $O(\epsilon)$.

To obtain the conservation law in the order of $O(\epsilon^2)$, which is equivalent to a zero factor of ϵ^2 in Eq. (39), we should combine two equalities. The first equality is the difference between Eq. (13) multiplied by B^* and integrated with respect to Y from $-\infty$ to ∞ and the complex conjugate Eq. (13) multiplied by B and integrated with respect to Y from $-\infty$ to ∞. The second equality is the difference between Eq. (26) multiplied by A^* and integrated with respect to Y from $-\infty$ to ∞ and the complex conjugate Eq. (26) multiplied by A and integrated with respect to Y from $-\infty$ to ∞. For a better understanding of the two latter sentences, which are somewhat cumbersome, we note that equations are first multiplied and then integrated.

Now, we present the basic formulas for the case when the sound propagation is described by the equation

$$(\gamma P_x)_x + (\gamma P_y)_y + (\gamma P_z)_z + \gamma n^2 P = 0, \tag{40}$$

where $\gamma = 1/\rho$ and ρ is the density made dimensionless with the use of the characteristic density $\bar{\rho}$ as the density scale.

The domain, where this equation is considered, and the boundary conditions are the same as in the above simplest case.

We introduce slow variables $X = \epsilon x$ and $Y = \epsilon^{1/2} y$ and postulate that the refractive index has the form of Eq. (3) and the parameter γ is representable in the form

$$\gamma = \gamma_0(X, z) + \epsilon \gamma_1(X, Y, z).$$

Substitute these representations and expression (5) into Eq. (40) written in terms of slow variables and in boundary conditions (2) and consider the boundary-value problems in different orders of ϵ.

As in the simplest case, we first obtain that the quantity θ is independent of z and Y. The problem in the order of $O(\epsilon^0)$ leads us to the representation

$$u_0 = A(X, Y)\phi_j(z, X),$$

where (ϕ_j, k_j) is one of the solutions to the eigenvalue problem

$$\begin{gathered} (\gamma_0 \phi_z)_z + \gamma_0 n_0^2 \phi - \gamma_0 k^2 \phi = 0, \\ \phi(0) = 0, \quad \phi_z(-H) = 0 \end{gathered} \tag{41}$$

with the spectral parameter $k^2 = (\theta_X)^2$ and the normalization condition

$$\int_{-H}^{0} \gamma_0 \phi^2 dz = 1. \tag{42}$$

The condition of solvability for the problem in the order of $O(\epsilon^1)$ is the parabolic equation for A

$$2ik_j A_X + ik_{jX} A + A_{YY} + \alpha A = 0, \tag{43}$$

where α is now given by the formula

$$\alpha = \int_{-H}^{0} \gamma_0 \nu \phi_j^2 dz + \int_{-H}^{0} \gamma_1 (n_0^2 - k_j^2) \phi_j^2 dz - \int_{-H}^{0} \gamma_1 (\phi_{jz})^2 dz. \tag{44}$$

The solution to the boundary-value problem in the order of $O(\epsilon)$ is represented in the form

$$u_1 = \sum_{l=0}^{\infty} B_{jl}(X, Y)\phi_l(z, X), \tag{45}$$

where the coefficient B_{jj} is again denoted as B. As below, the coefficients B_{jl} for $j \neq l$ prove to be proportional to A, and we introduce the coefficients E_{jl} for $j \neq l$ by the equality

$$AE_{jl} = B_{jl}. \tag{46}$$

For $j \neq l$, these coefficients satisfy the equation

$$\begin{aligned} (k_l^2 - k_j^2) E_{jl} = {} & -ik_j \int_{-H}^{0} \gamma_{0X} \phi_j \phi_l dz - 2ik_j \int_{-H}^{0} \gamma_0 \phi_{jX} \phi_l dz \\ & + k_j^2 \int_{-H}^{0} \gamma_1 \phi_j \phi_l dz - \int_{-H}^{0} (\gamma_1 \phi_{jz})_z \phi_l dz \\ & - \int_{-H}^{0} \gamma_1 n_0^2 \phi_j \phi_l dz - \int_{-H}^{0} \gamma_0 \nu \phi_j \phi_l dz. \end{aligned} \tag{47}$$

In contrast to the simplest case, we now set

$$E_{jj} = -\frac{1}{2} \int_{-H}^{0} \gamma_1 \phi_j^2 dz. \tag{48}$$

For the derivatives of the eigenfunctions with respect to X, we use the representation

$$\phi_{jX} = \sum_{l=0}^{\infty} C_{jl} \phi_l. \tag{49}$$

The equation for these coefficients is as follows:

$$(k_m^2 - k_j^2)C_{jm} = \int_{-H}^{0} \gamma_{0X}\phi_{jz}\phi_{mz}dz - \int_{-H}^{0} (\gamma_0 n_0^2)_X \phi_j \phi_m dz + (k_j^2)_X \delta_{jm} + k_j^2 \int_{-H}^{0} \gamma_{0X}\phi_j\phi_m dz, \quad (50)$$

where δ_{jm} is the Kronecker delta. For $j \neq m$, this equation gives the coefficients C_{jm}, and, for $j = m$, it gives the formula for k_{jX}. The equation for C_{jj} is obtained by differentiating normalization condition (42) with respect to X:

$$\int_{-H}^{0} \gamma_{0X}\phi_j^2 dz + 2C_{jj} = 0. \quad (51)$$

In contrast to the simplest case considered above, the coefficients C_{jm} are now not antisymmetric in indexes; instead, we have the relationship

$$C_{jm} + C_{mj} = -\int_{-H}^{0} \gamma_{0X}\phi_j\phi_m dz. \quad (52)$$

The analogous formula for E_{jm} has the form

$$E_{jm} + E_{mj} = -\int_{-H}^{0} \gamma_1 \phi_j \phi_m dz + i\frac{1}{k_m - k_j}(C_{mj} - C_{jm}). \quad (53)$$

The solvability condition for the boundary-value problem in the order of $O(\epsilon^2)$ gives the parabolic equation for the amplitude B:

$$2ik_j B_X + ik_{jX}B + B_{YY} + \alpha B + A_{XX} + 4ik_j E_{jj}A_X + 2(E_{jj}A_Y)_Y + \beta A = 0, \quad (54)$$

where

$$\beta = 2ik_j \sum_{l=0,\, l\neq j}^{\infty} E_{jl}(C_{lj} - C_{jl}) - \sum_{l=0,\, l\neq j}^{\infty} (k_l^2 - k_j^2)E_{jl}^2 + C_{jjX} - \sum_{l=0}^{\infty} C_{jl}^2 + 2ik_j E_{jjX} + 2ik_{jX}E_{jj} + \int_{-H}^{0} \gamma_1 \nu \phi_j^2 dz. \quad (55)$$

Assume now that the parameters γ_0 and n_0 have discontinuities of the first kind at the boundaries

$$z = h^{(l)}(X, Y), \quad l = 1, \ldots, N,$$

where the functions $h^{(l)}$ have the form

$$h^{(l)}(X, Y) = h_0^{(l)}(X) + \epsilon h_1^{(l)}(X, Y).$$

For other points, we assume that the functions γ_0 and n_0 are smooth.

Note that, under the condition that $h_1^{(l)} = 0$, the formulas derived above remain valid even in the presence of discontinuities, provided that the solutions to the boundary-value problems are understood in the sense of appropriate distributions (say, belonging to the Sobolev space H^1). Here, we show that these formulas formally include also the case of $h_1^{(l)} \neq 0$ if one includes the perturbations of the boundaries into the perturbations of the parameter γ and the refractive index γ_1 and ν. However, in this procedure, the portions of γ_1 and ν corresponding to the perturbation of the boundaries must be of the order of $O(1/\epsilon)$, because only in this case will they change the values of γ and n by finite values after their multiplication by ϵ. For this reason, the smallness of these perturbations must be understood in some integral sense rather than pointwise. Having mentioned this fact, we will not consider the questions of functional analysis and simply give the formal derivation of formulas, which contains all the information required for a more rigorous consideration.

Let the perturbations of γ_0 and n_0 corresponding to the perturbation of the boundary $z = h^{(l)}$ at a point (X, Y) be described by the function $\chi(z)$ as follows:

$$\tilde{\gamma}_0(z) = \gamma_0(z - \chi(z)), \quad \tilde{n}_0(z) = n_0(z - \chi(z)), \quad (56)$$

where we require that function χ satisfy the conditions

$$\chi(h_0^{(l)}) = h_1^{(l)}, \quad |\chi(z)| < |h_1^{(l)}| \quad \text{for} \quad z \neq h_0^{(l)};$$

χ is a smooth function, and the support of χ has a diameter of about $O(h_1^{(l)})$.

Expand the functions $\tilde{\gamma}_0$ and $\tilde{n}_0^2$ in the Taylor series

$$\tilde{\gamma}_0 = \gamma_0 - \chi\gamma_{0z} + o(|h_1^{(l)}|),$$

$$\tilde{n}_0^2 = n_0^2 - \chi(n_0^2)_z + o(|h_1^{(l)}|).$$

Here, because of the discontinuous behavior of the functions γ_0 and n_0^2, the derivatives are understood in the sense of distributions. The validity of the Taylor formula in this case is shown, e.g., in [13] (Sect. 3.3 of Part 1). In our case, we have

$$\chi\gamma_{0z} = \chi(\gamma_{0+} - \gamma_{0-})\delta(z - h_0^{(l)}) + \text{a smooth fuction of order } O(|h_1^{(l)}|)$$

and a similar formula for n_0^2, where δ is the Dirac delta, $\gamma_{0+} = \lim_{z \to h_0^{(l)},\, z > h_0^{(l)}} \gamma_0$, and $\gamma_{0-} = \lim_{z \to h_0^{(l)},\, z < h_0^{(l)}} \gamma_0$.

If we set

$$\gamma_1 = -\chi\gamma_{0z}, \quad \nu = -\chi(n_0^2)_z,$$

the integrals containing these quantities and appearing in expressions (14) and (27) for the coefficients α and β are

$$\int_{-H}^{0}\gamma_1\phi_j^2 dz = -\int_{-H}^{0}\chi\gamma_{0z}\phi_j^2 dz = -(\gamma_{0+}-\gamma_{0-})h_1^{(l)}\phi_l^2\Big|_{z=h_0^{(l)}} + o(|h_1^{(l)}|), \tag{57}$$

$$\int_{-H}^{0}\gamma_0\nu\phi_j^2 dz + \int_{-H}^{0}\gamma_1 n_0^2\phi_j^2 dz = -\int_{-H}^{0}\chi(n_0^2\gamma_0)_z\phi_j^2 dz = -((n_0^2\gamma_0)_+ - (n_0^2\gamma_0)_-)h_1^{(l)}\phi_l^2\Big|_{z=h_0^{(l)}} + o(|h_1^{(l)}|), \tag{58}$$

$$\int_{-H}^{0}\gamma_1(\phi_{jz})^2 dz = \int_{-H}^{0}\chi\gamma_{0z}(\phi_{jz})^2 dz = \int_{-H}^{0}\chi\left(\frac{1}{\gamma_0}\right)_z(\gamma_0\phi_{jz})^2 dz = \left(\left(\frac{1}{\gamma_0}\right)_+ - \left(\frac{1}{\gamma_0}\right)_-\right)h_1^{(l)}(\gamma_0\phi_{jz})^2\Big|_{z=h_0^{(l)}} + o(|h_1^{(l)}|), \tag{59}$$

and

$$\int_{-H}^{0}\gamma_1\nu\phi_j^2 dz = \int_{-H}^{0}\chi^2\gamma_{0z}(n_0^2)_z\phi_j^2 dz = (\gamma_{0+}-\gamma_{0-})((n_0^2)_+ - (n_0^2)_-)h_1^{(l)}\phi_j^2\Big|_{z=h_0^{(l)}} + o(|h_1^{(l)}|^2). \tag{60}$$

It remains to note that the orders of errors in formulas (57)–(60) correspond to the orders of ϵ, in which these integrals appear in the expressions for the coefficients α and β if one returns to the initial variables in these expressions, as we have done in the comparison with the method of factorization.

It is not difficult to check that the above formulas agree well with the formulas from [3].[1]

Thus, using the generalized multiscale method, the system of parabolic equations (43) and (54) for the amplitudes of the normal acoustic mode was derived to describe the wide-angle propagation of sound in the horizontal plane. For the simplest case, this system was compared with the wide-angle equation obtained by the formal factorization of the horizontal Helmholtz operator with the use of the rational-linear Padé approximation for the square root of the operator. The problem of energy flux conservation was considered. On the basis of the theory of distributions, an approach was developed to extend the formulas obtained for smooth density and refractive index to the case when these parameters are discontinuous at some interfaces.

REFERENCES

1. W. L. Siegmann, G. A. Kreigsmann, and D. Lee, J. Acoust. Soc. Am. **78**, 659 (1985).
2. B. J. Orchard, W. L. Siegmann, and M. J. Jacobson, J. Acoust. Soc. Am. **91**, 788 (1992).
3. M. Yu. Trofimov, Akust. Zh. **45**, 647 (1999) [Acoust. Phys. **45**, 575 (1999)].
4. M. D. Collins, J. Acoust. Soc. Am. **94**, 2269 (1993).
5. A. T. Abawi, W. A. Kuperman, and M. D. Collins, J. Acoust. Soc. Am. **102**, 233 (1997).
6. E. C. Shang, Y. Y. Wang, and T. F. Gao, J. Comput. Acoust. **9** (2), 359 (2001).
7. M. A. Leontovich and V. A. Fok, in *Studies of the Radio Wave Propagation* (Akad. Nauk SSSR, Moscow, 1948), No. 2, pp. 13–39.
8. F. D. Tappert, in *Wave Propagation and Underwater Acoustics*, Ed. by J. B. Keller and J. S. Papadakis, Lecture Notes in Physics (Springer, New York, 1977), Vol. 70.
9. A. H. Nayfeh, *Perturbation Methods* (Wiley, New York, 1973).
10. K. V. Avilov and N. E. Mal'tsev, Akust. Zh. **27**, 335 (1981) [Sov. Phys. Acoust. **27**, 185 (1981)].
11. K. V. Avilov, Akust. Zh. **41**, 5 (1995) [Acoust. Phys. **41**, 1 (1995)].
12. C. M. Bender and S. A. Orszag, *Advanced Mathematical Methods for Scientists and Engineers* (McGraw-Hill, New York, 1978).
13. P. Antosik, J. Mikusiński, and R. Sikorski, *Theory of Distributions* (Elsevier, Amsterdam, 1973).

Translated by A. Vinogradov

[1] Except for the term containing $h_{0X}^{(l)}$, which appeared in the final formulas because of the use of an erroneous formula $\left(\int_{-H}^{0}\frac{1}{\rho_0}\phi^2 dz\right)_X = \int_{-H}^{0}\left(\frac{1}{\rho_0}\right)_X\phi^2 dz + 2\int_{-H}^{0}\frac{1}{\rho_0}\phi_X\phi dz$ (see [3], Appendix). In fact, such integrals must be differentiated as follows (we consider the case of one boundary): $\left(\int_{-H}^{0}\frac{1}{\rho_0}\phi^2 dz\right)_X = \left(\int_{-H}^{h_0^{(l)}}\frac{1}{\rho_0}\phi^2 dz + \int_{h_0^{(l)}}^{0}\frac{1}{\rho_0}\phi^2 dz\right)_X = h_{0X}^{(l)}\left(\left(\frac{1}{\rho_0}\right)_- - \left(\frac{1}{\rho_0}\right)_+\right)\phi^2$ + the terms given above. As a result, the terms containing $h_{0X}^{(l)}$ are cancelled.

Acoustical Physics, Vol. 48, No. 6, 2002, pp. 735–740. Translated from Akusticheskiĭ Zhurnal, Vol. 48, No. 6, 2002, pp. 830–835.

Geometrooptical Representation of the Field Produced by an Extended Source in a Two-Dimensional Inhomogeneous Medium

B. P. Sharfarets

ul. Kubinskaya 14–70, St. Petersburg, 196128 Russia

e-mail: sharg@mail.rcom.ru

Received December 3, 2001

Abstract—An asymptotic solution to the two-dimensional inhomogeneous Helmholtz equation in the R^2 space with a variable refractive index is considered. The volume density of the source is nonzero in a finite region D. A special conformal transformation of the original space is used to show that this asymptotic solution can be represented as a geometrooptical series. Algorithms for calculating all characteristics of this series are presented. The results can be applied to a real three-dimensional oceanic waveguide. © *2002 MAIK "Nauka/Interperiodica".*

The problem of calculating the fields and responses produced by linear antennas in oceanic waveguides attracted considerable interest in recent years [1–8]. The studies concerned with this problem used the assumption that the properties of the medium are either constant [2–4, 8] or change negligibly [6] over the aperture, or the field was calculated by simple summation over all the antenna elements (integration over the antenna aperture) paying no attention to the variation of the properties of the medium within the antenna aperture [1, 5, 7]. In the first and second cases, the authors quite correctly keep using the notion of the directional pattern of the antenna in free space, which is, however, invalid in the general case when the variations in the properties of the medium over the antenna aperture cannot be neglected. The third approach, which is valid in this case, is nevertheless ineffective and physically unclear.

In this paper, we study the field produced by an antenna in a two-dimensional inhomogeneous medium with allowance for the variation of the properties of the medium over the antenna aperture and retaining the efficiency and clarity characteristic of the first two approaches.

One of the most efficient techniques for solving the Helmholtz equation with a variable refractive index is the method of canonical operator (see, e.g., [9] and other works by V.P. Maslov and other authors). Note that, as a rule, the procedure consists in solving the homogeneous equation with inhomogeneous boundary conditions. The solution thus obtained is called the formal asymptotic solution (FAS) or quasi-classical asymptotics. In [10] and a number of other publications, the FAS was obtained for the fundamental solution (Green's function) of the Helmholtz equation with a variable refractive index in a space of an arbitrary dimension. For an arbitrary source function, the solution can formally be obtained as a convolution of the corresponding Green's function with the volume density of the source. The question of whether this solution can be represented as a geometrooptical series remains, however, open. For a space of an arbitrary dimension with a constant refractive index, this question has been solved positively: a solution to the respective boundary problem can be represented as a geometrooptical series [11].

This paper shows that the FAS to the inhomogeneous two-dimensional Helmholtz equation with a variable refractive index can be represented as a geometrooptical series.

Let us formulate the problem as follows:

$$\begin{aligned} &L(x, y, -j\partial/\partial x, -j\partial/\partial y)u(x, y) \\ &= [\Delta_2 + k^2 n^2(x, y)]u(x, y) = -f(x, y), \end{aligned} \tag{1}$$

$$\begin{aligned} &u(x, y) = O(|\mathbf{r}|^{-1/2}); \\ &(\partial/\partial|\mathbf{r}| - jk)u(x, y) = o(|\mathbf{r}|^{-1/2}); \quad \mathbf{r} = (x, y) \in R^2; \end{aligned} \tag{2}$$

$$\begin{aligned} &n(x, y) \in C^\infty; \quad n(x, y) > 0; \\ &n(x, y) \longrightarrow 1, \quad |\mathbf{r}| \longrightarrow \infty. \end{aligned} \tag{3}$$

The decay rate of the function at infinity for any multiindex α satisfies the condition

$$D_x^\alpha(n(\mathbf{r})) \le c_\alpha(1 + |\mathbf{r}|)^{-|\alpha|-2}, \quad c_\alpha = \text{const}. \tag{3a}$$

The Hamiltonian system generated by Eq. (1) should also comply with the condition that finite motion be absent; i.e., all rays emanating from a point must go to infinity [10].

1063-7710/02/4806-0735$22.00 © 2002 MAIK "Nauka/Interperiodica"

Here, $\Delta_2 = \partial/\partial x^2 + \partial/\partial y^2$ is the Laplacian, $u(x, y)$ is the sound pressure field, k is the wave number, and $f(x, y)$ is the volume density of the source existing in a finite region $D = \mathrm{supp} f$. In general, $f(x, y)$ may be a generalized function; then the solution should be understood as a generalized solution.

If the above conditions are met, a unique solution to problem (1)–(3a) exists and the FAS asymptotically converges to the exact solution [10].

Consider the equation for the fundamental solution to the Helmholtz equation:

$$[\Delta_2 + k^2 n^2(x, y)]G(x, x_0, y, y_0) = \delta(x - x_0)\delta(y - y_0). \quad (4)$$

To find the FAS to Eq. (4), one must construct the Lagrangian manifold associated with the zero value of the Hamiltonian

$$H(\mathbf{r}, \mathbf{p}) = -p_x^2 - p_y^2 + n^2(x, y), \quad (5)$$

which corresponds to the operator $L = \Delta_2 + k^2 n^2(x, y)$ [9, 10]. The Lagrangian manifold is a web of bicharacteristics that are solutions to the Hamiltonian system

$$d\mathbf{r}/dt = \partial H/\partial \mathbf{p}; \quad d\mathbf{p}/dt = -\partial H/\partial \mathbf{r},$$
$$\mathbf{r}|_{t=0} = \mathbf{r}_0 = (x_0, y_0); \quad \mathbf{p}|_{t=0} = \mathbf{p}_0 \quad (6)$$
$$= (p_{0x}, p_{0y}) = (n(x_0, y_0)\cos\varphi, n(x_0, y_0)\sin\varphi).$$

Here, (t, φ) are the coordinates on the Lagrangian manifold, φ is the polar angle on the circle of initial momenta $|\mathbf{p}_0|^2 = n^2(x_0, y_0)$, and $\mathbf{p} = (p_x, p_y)$ is the momentum vector.

Let us make the following assumption. Let a region D^1 contain the region D so that, $\forall \mathbf{r}_0 \in D$ and $\forall \mathbf{r} \in D^1$, the projections of the Lagrangian manifolds onto R^2 are unique and the rays that connect the points $\mathbf{r}_0$ and $\mathbf{r}$ do not intersect; i.e., they lie on a nonsingular map.

It is known [10] that, on a nonsingular map, an FAS to Eq. (4) has the form

$$G_N(\mathbf{r}_0, \mathbf{r}, k) = \frac{-j}{2\sqrt{\pi k}} \times \frac{\exp(j(kS - j\pi/2\gamma(\mathbf{r}_0, \mathbf{r}) - \pi/4))}{|J(\mathbf{r}_0, t, \varphi)|^{1/2}} \sum_{n=0}^{N+2} \frac{\varphi_n(\mathbf{r}, \mathbf{r}_0)}{(jk)^n}. \quad (7)$$

Here, $S(\mathbf{r}_0, \mathbf{r}(t, \varphi))$ is the eikonal on the ray that connects the point $\mathbf{r}_0$ with the point $\mathbf{r}$; φ_n are the transfer amplitudes, where $\varphi_0 = 1$, the others being calculated recursively [10]; $J(\mathbf{r}_0, t, \varphi) = D(x, y, \mathbf{r}_0)/D(t, \varphi)$ is the Jacobian of the change of coordinates from (x, y) to (t, φ); and $\gamma(\mathbf{r}_0, \mathbf{r})$ is the number of zeroes of the Jacobian in the interval $(0, t)$ with allowance for their multiplicity. Since the map is nonsingular, the Jacobian is nonzero everywhere on the ray from $\mathbf{r}_0$ to $\mathbf{r}$, and these points are connected by a single ray. In this case, $\gamma = 0$.

The FAS G_N satisfies the equation

$$LG_N(\mathbf{r}_0, \mathbf{r}) = \delta(x - x_0)\delta(y - y_0) + o(k^{-N-1}).$$

When G_N is known, the solution to Eq. (1) can formally be calculated as the convolution

$$u_N = -\int_D f(\mathbf{r}_0)G_N(\mathbf{r}_0, \mathbf{r})dr_0 = \beta \int_D f(\mathbf{r}_0) \frac{\exp(jkS(\mathbf{r}_0, \mathbf{r}))}{|J(\mathbf{r}_0, t, \varphi)|^{1/2}} \sum_{n=0}^{N} \frac{\varphi_n(\mathbf{r}_0, \mathbf{r})}{(jk)^n} dr_0, \quad (8)$$

where u_N is the FAS to Eq. (1), which satisfies the equation $Lu_N = -f(x, y) + o(k^{-N-1})$, and $\beta = \frac{j}{2\sqrt{\pi k}} \exp(-j\pi/4)$. As follows from Eq. (8), the FAS u_N does not have the form of a geometrooptical series of Eq. (7), which features the following properties [9]: the series has form (7); the eikonal, transfer amplitudes, and Jacobian correspond to the Lagrangian manifold associated with Hamiltonian system (6); and the zero-order transfer amplitude φ_0 remains constant on the ray, the other transfer amplitudes being calculated from φ_0 by a recursive procedure. Therefore, algorithm (8) that calculates the FAS by the Green's function technique is of little use, because, for each point $\mathbf{r}$, it performs the whole of the time-consuming procedure (8) for each point $\mathbf{r}_0 \in D$.

Note that the stationary-phase method does not give a geometrooptical series from FAS in form (8) for the two-dimensional case or in the form of a similar integral in the n-dimensional case, because the eikonal $S(\mathbf{r}_0, \mathbf{r})$ has no stationary-phase point, since $\nabla_{\mathbf{r}_0} S(\mathbf{r}_0, \mathbf{r}) = \mathbf{p}(\mathbf{r}_0, \mathbf{r}) \neq 0$, which follows from conditions (3) and the fact that Hamiltonian (5) is zero. Here, $\mathbf{p}(\mathbf{r}_0, \mathbf{r})$ is the momentum vector at the point $\mathbf{r}_0$ on the ray connecting the points $\mathbf{r}_0$ and $\mathbf{r}$. However, if a stationary point were present, its position would depend on the current point $\mathbf{r}$, which enters the phase function $S(\mathbf{r}_0, \mathbf{r})$ as a parameter.

Let us show that, under the above assumptions, the FAS u_N can nevertheless be represented as a geometrooptical series. To this end, we apply a conformal transformation to Eq. (1) that changes coordinates from (x, y) to (ξ_1, ξ_2). Let $\omega = \omega(z) = \xi_1 + j\xi_2$ be the conformal transformation of the complex variable $z = x + jy$. Then, the Laplacian can be transformed to [12, pp. 334, 474]

$$\Delta_2 = \partial^2/\partial x^2 + \partial^2/\partial y^2 = 4\partial^2/\partial z \partial \bar{z} = (\partial^2/\partial \xi_1^2 + \partial^2/\partial \xi_2^2)|d\omega/dz|^2.$$

In this case, Eq. (1) can be written as

$$\{|d\omega/dz|^2(\partial^2/\partial\xi_1^2 + \partial^2/\partial\xi_2^2) + k^2n^2[x(\xi_1, \xi_2), y(\xi_1, \xi_2)]\}u[x(\xi_1, \xi_2), y(\xi_1, \xi_2)] = -f[x(\xi_1, \xi_2), y(\xi_1, \xi_2)]. \quad (9)$$

According to [12], $|dz/d\omega| = [(\partial x/d\xi_1)^2 + (\partial y/d\xi_1)^2]^{1/2} = [(\partial x/d\xi_2)^2 + (\partial y/d\xi_2)^2]^{1/2} = h_1 = h_2$, where $h_{1,2}$ are the Lamé coefficients, which are equal for the conformal transformation. The following equality is valid [13]: $J_{z\to\omega}(\xi_1, \xi_2) = D(x, y)/D(\xi_1, \xi_2) = h_1h_2$, where $J_{z\to\omega}$ is the Jacobian of the transformation $(x, y) \longrightarrow (\xi_1, \xi_2)$. Therefore, $J_{z\to\omega}(\xi_1, \xi_2) = |dz/d\omega|^2$.

Let such an analytical function $\omega(z)$ exist that the equality

$$|d\omega/dz|^2 = n^2(x, y), \quad (10)$$

is valid in the region D^1 and, hence, $|d\omega/dz|^2 \neq 0$ [see conditions (3)]. Then, Eq. (9) can be transformed as follows (the algorithm for reconstructing an analytical function from its magnitude is given in the Appendix):

$$(\partial^2/\partial\xi_1^2 + \partial^2/\partial\xi_2^2 + k^2)u(x(\xi_1, \xi_2), y(\xi_1, \xi_2)) = -J_{z\to\omega}(\xi_1, \xi_2)\, f(x(\xi_1, \xi_2), y(\xi_1, \xi_2)). \quad (11)$$

As can be seen from Eq. (11), we obtained an inhomogeneous Helmholtz equation with a constant refractive index. Clearly, this transformation turns the rays into straight lines and the wave fronts, which are perpendicular to the rays, into circles when a point source is used.

Consider a point $\mathbf{r}^0 = (x^0, y^0) \in D$. This point can coincide with the geometric center of the antenna or it may be chosen based on other reasons, which will be discussed below. Let us introduce $\rho = [(\xi_1 + \xi_1^0)^0 + (\xi_2 + \xi_2^0)^2]^{1/2}$, where $(\xi_1^0, \xi_2^0) \in \bar{D}$, the point (ξ_1^0, ξ_2^0) on the plane ω corresponds to the point (x^0, y^0) on the plane z, and the region $\bar{D}$ on the plane ω corresponds to the region D^1 on the plane z. If there is no backscatter from the boundary $\partial\bar{D}^1$ between the regions $\bar{D}^1$ and $R^2_\omega\backslash\bar{D}^1$, which can easily be achieved by the smooth continuation of the refractive index to the region $R^2\backslash\bar{D}^1$, the solution to Eq. (11) can be represented as the following geometrooptical series [11]:

$$\bar{u}(\rho, \varphi') \approx \frac{j}{4}\sqrt{\frac{2}{\pi k}}\exp(-j\pi/4)\frac{\exp(jk\rho)}{\rho^{1/2}}\sum_{n=0}^{\infty}\frac{D_n(\varphi')}{(k\rho)^n}. \quad (12)$$

Here, (ρ, φ') are the polar coordinates on the ω plane relative to the point (ξ_1^0, ξ_2^0); $\bar{u}(\rho, \varphi') = u(x(\xi_1, \xi_2), y(\xi_1, \xi_2))$; and the function $D_0(\varphi')$ is defined as

$$D_0(\varphi) = \int_{\bar{D}}\bar{f}(\boldsymbol{\xi})J_{z\to\omega}(\boldsymbol{\xi})\exp(-j\mathbf{k}(\boldsymbol{\xi} - \boldsymbol{\xi}^0))d^2\xi, \quad (13)$$

where $\boldsymbol{\xi} = (\xi_1, \xi_2)$, $\boldsymbol{\xi}^0 = (\xi_1^0, \xi_2^0)$, $\bar{f}(\boldsymbol{\xi}) = f[x(\xi_1, \xi_2), y(\xi_1, \xi_2)]$, and $\mathbf{k} = (k, \varphi)$. The higher order transfer amplitudes are determined by the recurrent formula [11]

$$D_{n+1}(\varphi') = \frac{[\partial^2/\partial\varphi'^2 + n(n+1) + 1/4]}{2j(n+1)}D_n(\varphi'). \quad (14)$$

Now, to obtain a geometrooptical field representation in the original space (x, y), it is necessary to return to this space in expression (12) through the appropriate change of variables. However, it is easier to obtain this representation by comparing the FASs for the fundamental solutions in these two configuration spaces.

Note that, when passing from Eq. (1) to Eqs. (9) and (11), we change the configuration space [for Eq. (1), this is the (x, y) plane; for Eqs. (9) and (11), this is the (ξ_1, ξ_2) plane]. For Eq. (9), original Hamiltonian (5) is simply written in terms of the new variables to become

$$H(\mathbf{p}, \boldsymbol{\xi}) = \left|\frac{d\omega}{dz}\right|^2(-p_{\xi_1}^2 - p_{\xi_2}^2) + n^2(x(\xi_1, \xi_2), y(\xi_1, \xi_2)), \quad \mathbf{p} = (p_{\xi_1}, p_{\xi_2}). \quad (5a)$$

For Eq. (11), the Hamiltonian changes to

$$H_1(\mathbf{p}, \boldsymbol{\xi}) = -p_{\xi_1}^2 - p_{\xi_2}^2 + 1. \quad (15)$$

Therefore, for Eq. (11) and, accordingly, for Hamiltonian (15), the Lagrangian manifold composed of the corresponding bicharacteristics will differ from the Lagrangian manifold associated with Eqs. (1) and (9) and with Hamiltonians (5) and (5a). Note however that, when conditions (3) and (10) are met, solutions to Eqs. (1), (9), and (11) coincide. Therefore, since the change of variables is smooth and the maps are nonsingular, a one-to-one correspondence (diffeomorphism) exists between the points of the bicharacteristics belonging to both Lagrangian manifolds, i.e., to the manifolds associated with Hamiltonians (5), (5a), and (15), and, hence, a one-to-one correspondence exists between the parameters t and t' connected with these manifolds [see system (6)].

The solution to Hamiltonian system (6) for Hamiltonian (15) with the initial condition $\boldsymbol{\xi}|_{t'=0} = \boldsymbol{\xi}^0$ yields $J(\boldsymbol{\xi}^0, t', \varphi') = D(\xi_1, \xi_2, \boldsymbol{\xi}^0)/D(t', \varphi') = 4t'$, $\rho = 2t'$, and $S(\boldsymbol{\xi}^0, \varphi', t') = 2t'$. Here, (φ', t') are the coordinates on the Lagrangian manifold associated with Hamiltonian (15). Since the transformation $(x, y) \longrightarrow (\xi_1, \xi_2)$ is conformal, the angles φ on the initial-momentum circle $p_{0x}^2 + p_{0y}^2 = n^2(x^0, y^0)$ and the angles φ' on the initial-momentum circle $p_{\xi_1^0}^2 + p_{\xi_2^0}^2 = 1$ differ by a constant term α: $\varphi = \varphi' + \alpha$. Assume for simplicity that, after an appropriate shift, the equality $\varphi = \varphi'$ is valid. Then, by virtue of the diffeomorphism described above, a smooth dependence exists between the parameters t and

t' on the respective bicharacteristics. Let us denote the unknown dependence as $t' = \psi(\varphi, t)$ and find it. Let us write an expression for the fundamental solution in the region $\bar{D}^1$ of the ω plane, i.e., with the source function $f(x, y) = -\delta(x - x^0)\delta(y - y^0)$ in Eq. (11). Then, with the equality $\delta(x - x^0)\delta(y - y^0) = \dfrac{\delta(\xi_1 - \xi_1^0)\delta(\xi_2 - \xi_2^0)}{|dz/d\omega|^2}$ [12, p. 769], we obtain the equation

$$(\partial^2/\partial\xi_1^2 + \partial^2/\partial\xi_2^2 + k^2)G(x(\boldsymbol{\xi}), y(\boldsymbol{\xi}), \boldsymbol{\xi}^0, k)$$
$$= \delta(\xi_1 - \xi_1^0)\delta(\xi_2 - \xi_2^0), \quad \boldsymbol{\xi} \in \bar{D}^1, \quad \boldsymbol{\xi}^0 \in \bar{D}$$

for the fundamental solution, which is known from [12]: $G = \dfrac{-j}{4}H_0^{(1)}(k\rho)$. This solution can be represented in the geometrooptical form

$$G \approx \frac{-j}{4}\sqrt{\frac{2}{\pi k}}\exp(-j\pi/4)\frac{\exp(jk\rho)}{\rho^{1/2}}\sum_{n=0}^{\infty}\frac{d_n}{(k\rho)^n} \qquad (16)$$
$$d_0 = 1$$

by using Eqs. (12)–(14). Clearly, expression (16) describes the asymptotics of the Hankel function up to within a constant factor. Next, we substitute $J(\boldsymbol{\xi}^0, t', \varphi') = 4t'$, $\rho = 2t'$, and $S = 2t'$ into Eq. (16) and compare the result with the equivalent expression (7) to obtain

$$t' = |J(\boldsymbol{\xi}^0, t, \varphi)|/4, \quad d_0 = \varphi_0 \equiv 1,$$
$$\varphi_n = d_n\frac{j^n}{(|J(\boldsymbol{\xi}^0, t, \varphi)|/2)^n}. \qquad (17)$$

With Eqs. (17), solution (12) in the original space (x, y) can be written as

$$u(x, y) \approx \frac{j}{2\sqrt{\pi k}}$$
$$\times\frac{\exp\left(j\left(kS(\mathbf{r}^0, \varphi, t) - \dfrac{\pi}{2}\gamma(\mathbf{r}^0, \mathbf{r}) - \pi/4\right)\right)}{|J(\mathbf{r}^0, \varphi, t)|^{1/2}} \qquad (18)$$
$$\times\sum_{n=0}^{\infty}\frac{\Phi_n(\mathbf{r}^0, \varphi, t)}{(jk)^n},$$

where

$$\Phi_0 = D_0 = \int_{\bar{D}}\bar{f}(\boldsymbol{\xi})J_{z\to\omega}(\boldsymbol{\xi})\exp(-j\mathbf{k}(\boldsymbol{\xi} - \boldsymbol{\xi}^0))d^2\xi \qquad (19)$$

and D_n and Φ_n are related due to Eqs. (17) as

$$\Phi_n = D_n\frac{j^n}{(|J(\mathbf{r}^0, t, \varphi)|/2)^n}.$$

The above considerations have shown that the FAS to problem (1) can be represented as a geometrooptical series, for which purpose one must calculate not only the usual source-independent FAS characteristics (the eikonal, the phase paths, and the Jacobian), but also the zero-order transfer amplitude (19), which characterizes the source. Expression (19) must be calculated in the (ξ_1, ξ_2) space through the corresponding conformal transformation, which in some cases may be inconvenient. Consider a technique to overcome this difficulty. To this end, let us find out to which wave in the original space (x, y) the plane wave $\exp(j\mathbf{k}(\boldsymbol{\xi} - \boldsymbol{\xi}^0))$ in the region $\bar{D}^1$ corresponds.

The plane wave front in $\bar{D}^1$ is the limit to which the cylindrical wave front tends as the distance between the points $\boldsymbol{\xi}$ and $\boldsymbol{\xi}^0$ increases without limit. Therefore, the plane wave front in the region $\bar{D}^1$ corresponds to the limiting wave front in the region D^1 when $\mathbf{r}$ goes to infinity. Due to stabilization conditions (3), this limiting front also tends to a plane front when $|\mathbf{r}| \longrightarrow \infty$.

The key circumstance in the further consideration is the fact that, if the refractive index is smoothly varied on the phase path keeping conditions (3) and (4) satisfied, the zero-order transfer amplitude remains constant in contrast to other FAS characteristics. The zero-order transfer amplitude is thus a FAS invariant insensitive to smooth perturbations on the phase path. Therefore, it is possible to vary the refractive index on the phase path so as to obtain the simplest procedure for calculating the zero-order transfer amplitude.

Clearly, this variation is the smooth transition from the current refractive index to its stationary value of $n(x, y) \equiv 1$ outside the region $D_1 = D \cup D_\varepsilon$, $D_1 \subset D^1$, where D_ε is a small neighborhood of D, if the refractive index with its derivatives is smoothly continued to a constant, which is necessary in order to avoid reflections and false caustics. Then, the plane wave $\exp(j\mathbf{k}(\boldsymbol{\xi} - \boldsymbol{\xi}^0))$ in the region $\bar{D}^1$ will correspond to a plane wave refracted by the region D_1 in the (x, y) space deformed as described above. The eikonal $\dfrac{\mathbf{k}}{|\mathbf{k}|}(\boldsymbol{\xi} - \boldsymbol{\xi}^0)$ in the domain ω is thus transformed to the eikonal $\bar{S}(\mathbf{r}^0, \mathbf{r}_0, \varphi) = \bar{S}(\mathbf{r}_0, \varphi) - \bar{S}(\mathbf{r}^0, \varphi)$, where $\mathbf{r}^0, \mathbf{r}_0 \in D_1$. Here, $\bar{S}(\mathbf{r}_0, \varphi)$ is the eikonal at the point $\mathbf{r}_0$ on the front of the refracted wave produced by the plane wave $\exp(j\mathbf{kr})$ incident on the region D_1 from infinity in such a direction that the refracted beam passes through the point $\mathbf{r}^0$ at the angle φ being sought. Then, by returning to variables (x, y) in integral (13), we obtain

$$\Phi_0(\varphi) = D_0(\varphi)$$
$$= \int_D f(\mathbf{r}_0)\exp(-jk\bar{S}(\mathbf{r}^0, \mathbf{r}_0, \varphi))dx_0dy_0.$$

After $\Phi_0(\varphi)$ is found, we can return to the original configuration space (x, y) and use Eq. (18) to calculate the

FAS to Eq. (1). Note that, when the refractive index is constant, $\Phi_0(\varphi)$ is the directional pattern of the antenna.

Consider an example of applying this algorithm. Let the refractive index meet the conditions for the conformal transformation to exist (see Appendix) and be a function of only one variable: $n(x, y) = n(y)$. Take a point $\mathbf{r}^0 \in D$ and find the FAS on the ray leaving $\mathbf{r}^0$ at an angle of $\pi/2$ to the x axis. Clearly, due to the symmetry, this ray will be a straight line parallel to the y axis. This is just the case to which the calculation of the FAS is reduced after the quasi-separation of variables in the x = const cross section of a three-dimensional waveguide whose refractive index and depth depend only on y.

Evidently, the wave front $\bar{S}(\mathbf{r}^0, \mathbf{r}_0) = \text{const}$ will be plane and perpendicular to the chosen ray, and the eikonal will be $\bar{S}(\mathbf{r}^0, \mathbf{r}_0) = \int_{y_0}^{y_0} n(y)dy = \bar{S}(y^0, y_0)$. Here, $\mathbf{r}^0 = (x^0, y^0)$ and $\mathbf{r}_0 = (x_0, y_0)$. The calculations yield $\Phi_0(\mathbf{r}^0, \pi/2) = \int_D f(\mathbf{r}^0)\exp(-jk\int_{y_0}^{y_0} n(y)\,dy)dx_0dy_0$.

Thus, we have shown that the FAS to problem (1) with a distributed source can be represented as a geometrooptical series referred to the point $\mathbf{r}^0$.

The point $\mathbf{r}^0 \in D$ was chosen arbitrarily. However, when choosing this point, one should rely on a certain criterion, e.g., on the condition of minimizing the difference between truncated FAS series (18) and the exact solution to Eq. (1), this problem being beyond the scope of this paper.

The results obtained above can be used to calculate the fields produced by extended sources in real three-dimensional oceanic waveguides, both regular ones with a vertical linear antenna and irregular ones with arbitrary antennas, when the case considered is precisely the one to which a three-dimensional problem is reduced by the quasi-separation of variables [14].

APPENDIX

Let the magnitude $\rho(x, y) = |f(z)|$ of the analytical function $f(z) = d\omega(z)/dz$ be given. It is necessary to reconstruct $f(z)$ and, subsequently, $\omega(z)$. Let us write $f(z)$ in the exponential form as $f(z) = \rho(x, y)\exp(j\theta(x, y))$. Then, its real and imaginary parts, respectively, are

$$\begin{aligned} u(x, y) &= \rho(x, y)\cos[\theta(x, y)]; \\ v(x, y) &= \rho(x, y)\sin[\theta(x, y)]. \end{aligned} \qquad \text{(A.a)}$$

The analysis of the analytical function $\ln f(z)$ shows that $\ln[\rho(x, y)]$ and, hence, $\ln[n(x, y)]$ ([see Eq. (10)] are analytical harmonic functions.

By substituting (A.a) into the Cauchy–Riemann equations, we arrive at

$$\begin{aligned} \frac{\partial\rho}{\partial x}\cos\theta - \rho\frac{\partial\theta}{\partial x}\sin\theta &= \frac{\partial\rho}{\partial y}\sin\theta + \rho\frac{\partial\theta}{\partial y}\cos\theta; \\ \frac{\partial\rho}{\partial y}\cos\theta - \rho\frac{\partial\theta}{\partial y}\sin\theta &= -\frac{\partial\rho}{\partial x}\sin\theta - \rho\frac{\partial\theta}{\partial x}\cos\theta. \end{aligned} \qquad \text{(A.b)}$$

Determining $\tan\theta$ from (A.b), we obtain $\frac{\rho'_x - \rho\theta'_y}{\rho'_y + \rho\theta'_x} = \frac{\rho'_y - \rho\theta'_x}{-(\rho'_x + \rho\theta'_y)}$ or

$$-(\rho'_x - \rho\theta'_y)^2 = (\rho'_y + \rho\theta'_x)^2. \qquad \text{(A.c)}$$

Since Eq. (A.c) contains only real functions, it can only be valid if both its sides are zero, which yields the expressions for θ: $\frac{\partial\theta}{\partial y} = \frac{1}{\rho}\frac{\partial\rho}{\partial x}$ and $\frac{\partial\theta}{\partial x} = -\frac{1}{\rho}\frac{\partial\rho}{\partial y}$. Finally, we obtain

$$\theta = \int\left(\frac{\partial\theta}{\partial x}dx + \frac{\partial\theta}{\partial y}dy\right) = \int\left(-\frac{1}{\rho}\frac{\partial\rho}{\partial y}dx + \frac{1}{\rho}\frac{\partial\rho}{\partial x}dy\right). \qquad \text{(A.d)}$$

Note that the last integral actually contains the derivatives of the real part of $\ln[f(z)]$.

Thus, the original analytical function $f(z) = \rho(x, y)\exp[j\theta(x, y)]$ is reconstructed uniquely. In the reconstruction, we used the assumption that $\ln[n(x, y)]$, where $(x, y) \in D^1$, is a harmonic function. Otherwise, it is necessary to approximate $n(x, y)$ by the magnitude of an analytical function under the condition that the perturbation of the field $u(x, y)$ is small.

The original function $\omega(z)$ can easily be reconstructed from $f(z)$ in the region where it is analytical by the procedure described in [12, pp. 346, 347], the function $\omega(z)$ being also analytical.

Consider an example. Let the refractive index in the region D be $n(x, y) = \rho(x, y) = \exp(\alpha_1 x + \alpha_2 y)$. Then, $\ln[\rho(x, y)] = \alpha_1 x + \alpha_2 y$ is a harmonic function. Formula (A.d) yields $\theta(x, y) = \int -\alpha_2\,dx + \alpha_1 dy = -\alpha_2 x + \alpha_1 y + C$. Then, up to a constant, we have $\ln[f(z)] = (\alpha_1 - j\alpha_2)z$, which yields $f(z) = \exp[(\alpha_1 - j\alpha_2)z]$ and, therefore, $\omega(z) = \frac{1}{\alpha_1 - j\alpha_2}\exp[(\alpha_1 - j\alpha_2)z]$.

REFERENCES

1. A. S. Belogortsev and E. V. Shorkina, Akust. Zh. **40**, 435 (1994) [Acoust. Phys. **40**, 389 (1994)].
2. V. A. Eliseevnin, Akust. Zh. **41**, 427 (1995) [Acoust. Phys. **41**, 375 (1995)].
3. A. N. Stepanov, Akust. Zh. **42**, 291 (1996) [Acoust. Phys. **42**, 257 (1996)].

4. A. N. Stepanov, Akust. Zh. **45**, 278 (1999) [Acoust. Phys. **45**, 242 (1999)].
5. V. M. Kudryashov, Akust. Zh. **46**, 662 (2000) [Acoust. Phys. **46**, 580 (2000)].
6. V. M. Kuz'kin, Akust. Zh. **47**, 678 (2001) [Acoust. Phys. **47**, 591 (2001)].
7. N. V. Zlobina and B. A. Kasatkin, Akust. Zh. **47**, 802 (2001) [Acoust. Phys. **47**, 707 (2001)].
8. N. V. Zlobina and B. A. Kasatkin, Akust. Zh. **48**, 61 (2002) [Acoust. Phys. **48**, 54 (2002)].
9. V. P. Maslov and M. V. Fedoryuk, *Semiclassical Approximation in Quantum Mechanics* (Nauka, Moscow, 1976; Reidel, Dordrecht, 1981).
10. V. V. Kucherenko, Teor. Mat. Fiz. **1** (3), 384 (1969).
11. B. A. Kosyrev and B. P. Sharfarets, Preprint, TOI DVO AN SSSR (Vladivostok, Pacific Oceanological Inst., Far East Division, Russian Academy of Sciences, 1991).
12. P. M. Morse and H. Feshbach, *Methods of Theoretical Physics* (McGraw-Hill, New York, 1953; Inostrannaya Literatura, Moscow, 1958), Vol. 1.
13. G. A. Arfken, *Mathematical Methods for Physicists*, 2nd ed. (Academic, New York, 1970; Atomizdat, Moscow, 1970).
14. B. P. Sharfarets, Akust. Zh. **38**, 345 (1992) [Sov. Phys. Acoust. **38**, 184 (1992)].

Translated by A. Khzmalyan

Acoustical Physics, Vol. 48, No. 6, 2002, pp. 741–743. Translated from Akusticheskiĭ Zhurnal, Vol. 48, No. 6, 2002, pp. 836–838.

SHORT COMMUNICATIONS

Shore Noise in a Calm Sea

M. Yu. Gureev, N. G. Kanev, and E. Yu. Kraĭnov

Andreev Acoustics Institute, Russian Academy of Sciences, ul. Shvernika 4, Moscow, 117036 Russia

e-mail: bvp@akin.ru

Received December 25, 2001

Abstract—Experimental results obtained by measuring the swell-caused underwater shore noise at different distances from a shingly coast are presented. The experiment was carried out on a sea shelf near the waterline. The typical spectrum of the shore noise is shown to have two peaks, one of which, corresponding to lower frequencies, is caused by the filtration of sound in the shallow-water waveguide and the other, corresponding to higher frequencies, is caused by the radiation of the bubble wash foam. The noise fluctuations are found to carry information on the swell period. *© 2002 MAIK "Nauka/Interperiodica".*

Fluctuating shore noise forms an interference of appreciable level for hydroacoustic facilities located near the coast, so knowledge of this noise is important for optimizing the characteristics of sound-receiving systems. In addition, shore noise is informative of shoreline structure, coastal depths, and the period of incoming waves. Only scarce data are available in the recent literature on the experimental and theoretical investigations of shore noise. It seems likely that Kirshov was the first to take an interest in the physics of shore noise in the mid-1960s; some experimental data on shore noise can be found in the paper by Bardyshev *et al.* [1], the review by Urick [2], and some other papers [3, 4] that concern this problem indirectly.

We measured the underwater shore noise near the city of Gelendjik. A hydrophone was sunk to the bottom at three different points that were at distances of 20, 100, and 200 m from the shoreline, and the signal was continuously recorded during this procedure. Figure 1 shows the three corresponding noise spectra averaged over an interval of 10 s. All three spectra are similar in shape and approximately equal in level. The features characteristic of these spectra are the decrease at lower frequencies and the increase at frequencies of 2–5 kHz.

Measurements were carried out in the morning hours, during the period of quiescent weather. The wind velocity from the coast was below 5 m/s, so the sea was

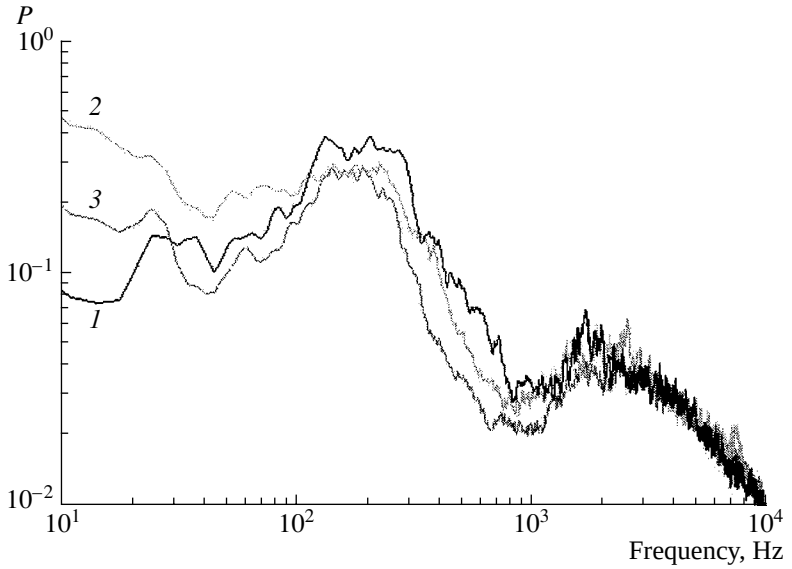

Fig. 1. Spectrum of the noise level for different distances from the shoreline: (*1*) 20, (*2*) 100, and (*3*) 200 m.

1063-7710/02/4806-0741$22.00 © 2002 MAIK "Nauka/Interperiodica"

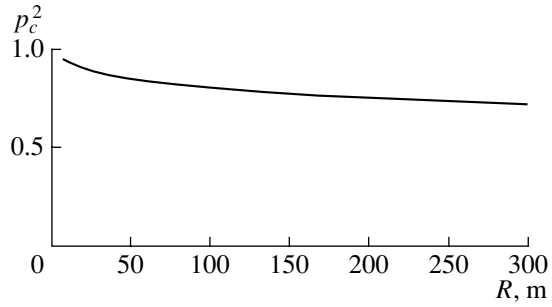

Fig. 2. Coastal noise as a function of distance from the shoreline R.

practically calm. Due to this fact, we can assume that the noise was caused by two sources: the sea (the corresponding noise component is p_s) and the coast (p_c). The coastal noise was caused by the breaking swell whose period measured 3–4 s. This periodicity is characteristic of the total noise pattern, especially for small distances from the shoreline.

Since the sea depth slowly increases with the distance from the shoreline (the slope of the bottom is about 1°), the sea near the coast can be arbitrarily described as a two-dimensional waveguide with soft and hard boundaries. In such a waveguide, the waves propagate without losses when their frequencies exceed the critical frequency: $f > f_k = c/4h$, where c is the sound velocity and h is the waveguide depth. In our case, the critical frequency measured about 100 Hz for all three points 20, 100, and 200 m from the shore. Frequencies below the critical frequency correspond to the decreasing parts of the noise spectra in Fig. 1.

In the waveguide, the energy of a sound wave generated by a point source decreases in inverse proportion to the distance from the shoreline R. The sound field p_c^2 of all sound sources uniformly distributed along the shoreline of length L can be found as a function of the distance R:

$$p_c^2 \propto \int_{-L/2}^{L/2} \frac{dx}{\sqrt{R^2 + x^2}} = \operatorname{arcsinh}\frac{L}{R}.$$

Figure 2 shows this law of power decay with distance. The logarithmic behavior of the noise sound pressure p_c as a function of R makes it possible to assume that the level of the coastal component of shore noise is constant or slowly decays with the distance from the shoreline. It seems likely that the sea component p_s of the shore noise can also be considered as equal for all three distances. Thus, the total noise level $p_n = p_s + p_c$ only slightly varies for the distances used in the experiment, which reflects the fact that the spectra in Fig. 1 nearly coincide.

The wave wash on the coast causes the formation of foam (due to the breaking waves) and the motion of small stones. To describe the coastal component of the noise, we must compare the spectrum averaged over several periods with the spectrum measured during a single wash (Fig. 3). The level of sound measured during a single wave breaking event appears higher at all frequencies. Figure 4 presents the ratio of the spectra shown in Fig. 3. The maximal excess of the level of sound measured during a single wash occurs for higher frequencies. This increase can be explained by an increased number of air bubbles formed in water when

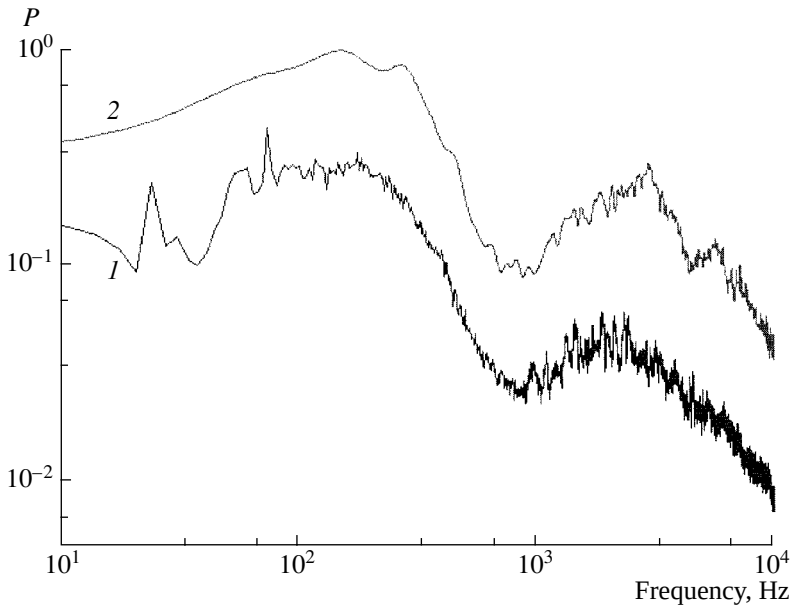

Fig. 3. Average noise spectrum compared with the spectrum of a single wave breaking event for a distance of 100 m from the shoreline: (*1*) spectrum averaged over an interval of 10 s and (*2*) spectrum measured during a single wave wash.

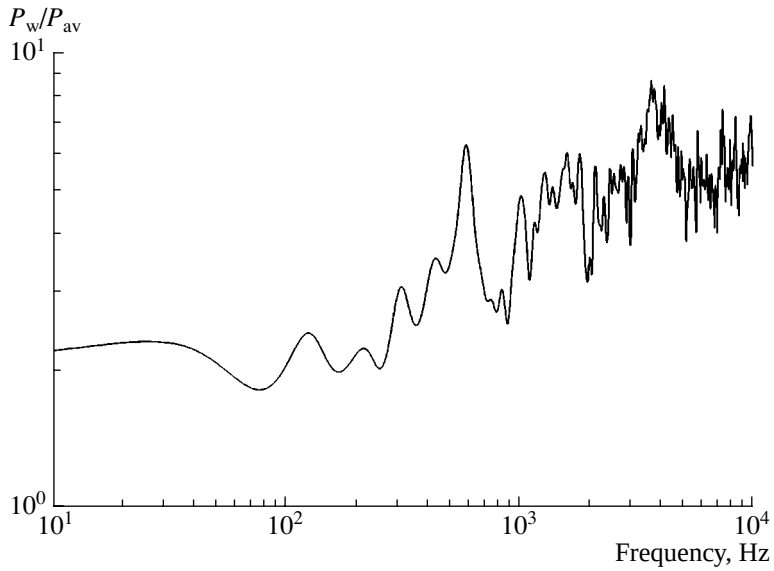

Fig. 4. Ratio of the noise spectrum measured during a single wave wash P_w to the averaged noise spectrum P_{av} at a distance of 20 m from the shoreline.

the wave breaks. The bubbles are excited at resonance frequencies and generate sound due to their cavitation in the wave. Estimating the contribution of the air bubbles to the total noise, we can neglect the interaction between the bubbles. The resonance frequency of monopole oscillations of a gas bubble in a liquid is determined by the well-known formula [5]

$$\omega_0 = \sqrt{\frac{3}{a^2\rho\beta}},$$

where ρ is the density of water, β is the compressibility of air, and a is the radius of the bubble. According to this formula, the peak observed in the spectra at frequencies 2–5 kHz corresponds to bubbles whose size is within 0.5 to 1.5 mm. The Gaussian distribution of the bubble radii $N(r) = N_0 \exp\left[-\frac{(r-r_0)^2}{2\sigma^2}\right]$ with the parameters $r_0 = 1$ mm and $\sigma = 0.5$ mm describes the high-frequency peak. The motion of stones also contributes to the total noise; however, the problem of sound generation by moving stones should be investigated separately.

The qualitative pattern of the shore noise in a calm sea has its distinctive features. The weather and the sea roughness can strongly affect not only the noise level, but also the shape of the noise spectrum. Therefore, it is of interest to carry out experiments for different conditions affecting the shore noise and for regions characterized by different structures and profiles of the bottom in the wave breaking zone.

ACKNOWLEDGMENTS

We thank N.N. Okhrimenko for his assistance in setting up the experiment.

This work was supported by the Russian Foundation for Basic Research, project no. 00-05-64226

REFERENCES

1. V. I. Bardyshev, N. G. Kozhelupova, and V. I. Kryshnyĭ, Akust. Zh. **19**, 129 (1973) [Sov. Phys. Acoust. **19**, 95 (1973)].
2. R. J. Urick, *Ambient Noise in the Sea* (Peninsula, Washington, DC, 1984).
3. J. A. Smith, in *Proceedings of Conference OCEANS-2000* (2000), Vol. 2, p. 781.
4. R. R. Goodman *et al.*, IEEE J. Ocean Eng. **25** (4), 501 (2000).
5. M. A. Isakovich, *General Acoustics* (Nauka, Moscow, 1978).

Translated by A. Vinogradov

Acoustical Physics, Vol. 48, No. 6, 2002, pp. 744–748. Translated from Akusticheskiĭ Zhurnal, Vol. 48, No. 6, 2002, pp. 839–844.

CONFERENCES AND MEETINGS

XI Session of the Russian Acoustical Society

The XI Session of the Russian Acoustical Society was held in Moscow on November 19–23, 2001. The scope of the session covered a wide range of problems of modern acoustics, and the participants of the session included acousticians from almost all regions of Russia. Considerable interest was aroused among the participants by the section "Speech Acoustics and Acoustic Problems of Applied Linguistics." The editorial board of *Acoustical Physics* decided to publish part of the papers presented in this section and devoted to the most topical problems of this promising field of research. The papers were not additionally refereed before publishing.

The Role of Studying the Neural Mechanisms in Designing Hearing Implants and in Speech Discrimination

N. G. Bibikov

Andreev Acoustics Institute, Russian Academy of Sciences, ul. Shvernika 4, Moscow, 117036 Russia
e-mail: bibikov@akin.ru

Abstract—Data on the auditory nerve response to an electric stimulation of the cochlea are presented. Mechanisms of analyzing the temporal fine structure and the amplitude variation of the signal in the cochlear nuclei are described. The studies of the mechanisms underlying the temporal analysis of the envelope and, primarily, of the signal amplitude modulation are of particular importance. The tuning of the auditory system to the level of incident sound in the process of short-term and long-term adaptation is described. Special attention is paid to the levels of internal noise (spontaneous activity) and external noise in the formation of stochastic resonance. All these data can be used in designing conventional and electronic hearing implants, as well as in advanced systems of speech discrimination. A number of these results are analyzed, and recommendations for their possible application are given. *© 2002 MAIK "Nauka/Interperiodica".*

In the last few years, important results concerning the mechanisms of information processing on the periphery of the auditory system and in the individual, sequentially positioned, nuclei of the auditory pathway have been obtained. A better understanding of the active mechanisms of spectral analysis performed mainly by the outer hair cells of the cochlea has been achieved. The neural responses of the auditory nerve of an animal to various sound signals and to an electric stimulation of the cochlea has been analyzed in detail. These data, along with the results of model studies, not only give a better insight into the operation of auditory receptors but also offer possibilities for improving the systems of electrode hearing implants for patients suffering a loss of receptor structures.

ELECTRODE COCHLEAR IMPLANTS

Over a period of several tens of years, electrode cochlear implants have become quite popular in medical practice. This method is the only one that restores the auditory perception to patients with a total hearing loss due to the atrophy of the receptor cells of the cochlea. In many cases, the stimulation of the hearing organs through electrodes placed in the cochlea not only restores auditory perception but also provides a fairly reliable discrimination of fluent speech. However, such a result can be achieved for only a certain number of patients, while for other patients the operation may be useless. Moreover, even in the case of successful operations, the dynamical range of perception and its noise immunity remain rather poor.

In fact, detailed systematic studies of the effects that occur in the internal ear and in the central auditory system in response to an electric stimulation of the cochlea have begun only recently. Most studies have been performed on animals and, primarily, on cats [1–3]. It was found that the spike caused by an electric stimulation can arise at several sites along the auditory nerve fiber, from the basilar membrane to the cochlea outlet. The shortest response occurs in the case of a direct stimulation of the myelinized auditory nerve segment lying even behind the cell body. The delay of this response relative to the electric stimulus is less than half a millisecond. Naturally, the dynamical range of such a response is very small, about 1 dB, and the possibility of transmitting the information on the signal intensity variations is practically absent. On the other hand, the frequency of the signal (at least in the low-frequency

1063-7710/02/4806-0744$22.00

range) can be well transmitted by means of the value of the pulse spacing, because the variance of the instants of the pulse formation is about 10 μs.

When the cochlea is stimulated by signals with somewhat lower intensity, a pulse of the auditory nerve fiber can appear at more peripheral parts of the fiber: in myelinized segments of the auditory nerve before the cell body or even in nonmyelinized segments. The delay of such a response is about 1 ms, the time variance is about 50 μs, and the dynamical range is doubled in this case. Note that, under a strong stimulation, the response in the nonmyelinized segment will be absent because of the refractoriness. Therefore, with increasing intensity, the delay of the response usually changes in a jumplike manner. With a special choice of parameters, it is possible to obtain two separate peaks in the post-stimulus histogram of the response.

Responses with large delays and large dynamical ranges were observed only for the animals that retained viable hair cells. In addition, it has been known for years that the auditory nerve fibers of an impaired cochlea exhibit no spontaneous pulsed activity.

These main results are necessary to understand the sensations experienced by a patient under the electric stimulation of the cochlea and to reveal the basic limitations of this method. Note that an electric pulse propagates along the cochlea with attenuation, and, hence, at different points of the cochlea, different mechanisms of the spike generation are possible with different corresponding delays. As a result, at the subsequent stages of the auditory pathway, where the summation of inputs from many fibers takes place, a desynchronization of the responses is possible. Judging from morphological data, for humans, the scatter in the values of the delay of the auditory nerve fiber excitation can be even greater because of the greater length of the nonmyelinized segment and the absence of myelin around the cell wall [4, 5]. One may assume that precisely this circumstance leads to the absence of the pure tone perception by patients receiving their hearing sensations from electric stimulation.

With hearing implants, the perception of the frequency of sound by the position principle is also difficult because of the limited number of active electrodes. Even the most advanced systems contain no more than 20 electrodes, and not all of them operate perfectly. In addition, because of the electric conductivity of the cochlear liquids, even a bipolar stimulation is not local enough ([6], but see also [7]).

However, the main difficulties in reproducing the normal pattern of the auditory nerve excitation by an electric stimulation are determined by the extremely small dynamic range of each single fiber. In principle, this is evident, because the spike generation is a highly nonlinear threshold process. A normally functioning cochlea has a set of mechanisms providing an extension of the dynamical range. Some of them are: (1) the nonlinearity of the active mechanical–electric–mechanical conversion of the signal by outer hair cells; (2) the combination of the signal with an additional noise component providing, in particular, the spontaneous activity of the fibers; (3) the refractory properties of the auditory nerve fibers; and (4) the adaptation processes in the peripheral and central neurons of the auditory system.

Let us consider each of these mechanisms separately. The transformation of the signal by outer hair cells results in the fact that the vibrations of the basilar membrane become strongly nonlinear with a pronounced saturation at high levels of the external action. This property makes it possible to retain information on the signal variations at high levels. Note that the corresponding operations, which are reduced to a compressional nonlinearity, are easily performed in most existing systems of preliminary signal processing for electronic implants [8].

The positive effect of the noise component on the signal analysis by nonlinear elements has attracted the attention of researchers only recently [9]. The fact that this aspect of information processing in the auditory nerve had been neglected until recent years is presumably explained by the internal origin of the noise signal. However, from some model experiments, it was inferred that precisely the presence of fluctuations made it possible for the whole population of auditory nerve fibers to retain information on time intervals that are much smaller than the time required by the nerve fiber to recover its excitability after a spike generation [10]. Subsequent model experiments clearly demonstrated the role of the noise component in the extension of the dynamical range of the neural responses of the auditory nerve. In addition, it should be noted that the presence of the noise component should increase the variance of the instants of the spike generation under the effect of electric signals, which allows a more adequate reproduction of its shape and, specifically, a suppression of the effect of the aforementioned artificial temporal shifts, which are caused by the discreteness of the sites of spike generation [11]. Some publications directly discuss the possibility of introducing a noise component in the real signals presented to patients with electrode cochlear implants [12, 13]. However, in this case, the problem arises as to how to provide the independence of noise in different fibers of the auditory nerve. In an intact cochlea, the absence of correlation of the spontaneous activity even in adjacent fibers [14] is presumably responsible for the fact that a human does not perceive the spontaneous activity as a real noise signal. To provide this property in the case of electric stimulation seems to be a rather complicated problem, which should be the subject of further studies.

It is well known that all neurons are characterized by refractoriness, which is generally determined as a

reduction of the cell excitability after the spike generation. In the spiral ganglion neurons forming the auditory nerve, at least three stages of refractoriness are present: absolute refractoriness (within fractions of a millisecond), fast relative refractoriness (with a time constant of 1–3 ms), and slow refractoriness (with a time constant of 20–40 ms). There are reasons to believe that the last stage of refractoriness possesses the accumulation property, i.e., the summation of the threshold shifts of successive spikes rapidly following one after another. The effect of the refractory properties of peripheral neurons on the coding of sound signals was analyzed in model experiments, and it was found that even the weakest accumulated refractoriness can determine the experimentally observed decrease in the firing rate of the response of the auditory nerve fiber to tone bursts [15]. Owing to the refractoriness, it is possible to increase the dynamical range of the electric stimulation, if the stimulating pulses are presented at a high rate [3].

The changes that occur in the refractoriness when the synapses of the receptor cells and, possibly, the peripheral outgrowths of spiral ganglion neurons are destroyed remain poorly investigated. There are some data on refractoriness enhancement after the destruction of the cochlea [3]. However, these data concern only fast refractoriness. Accumulated refractoriness, which is essential for the formation of the response to relatively long signals, can appear at the synapse between a hair cell and the fiber and disappear in the case of its impairment.

The mechanism of short-time adaptation in the auditory nerve fibers remains unknown. The choice between the hypotheses based on mediator exhaustion in the synapses of hair cells [16] and on accumulated refractoriness [15] has still not been made. However, judging from the experiments on laboratory animals, in the case of the electric stimulation of an impaired cochlea, the effect of adaptation is drastically reduced, which also affects the ability of the neural network to analyze the signal variations in a wide dynamical range. In an instrumental realization, the adaptation mechanism can be reproduced either by a simple differentiating device or in the form of an accumulated refractoriness element corresponding to one of the units of the peripheral auditory system model used as a preprocessor of the hearing implant. It seems to be quite possible that the recent progress in the understanding of the functioning of the cochlea will allow one to design a preprocessing system for signals presented to the electrodes of the cochlear implants on the basis of an adequate model of all the lost elements of system of signal reception and transformation in the human internal ear.

In closing the section devoted to the prospects of hearing implants, it is appropriate to note the latest trend toward the realization of entirely new possibilities for solving the problem of curing hearing impairment. It has been known long ago that hair cells in the cochlea of birds are able to regenerate. The advances in studying the gene factors of ontogenesis and the growth factors of nerve tissue [17, 18] allow one to hope that a regeneration of human hair cells will be possible in the future.

ANALYSIS OF SIGNALS IN THE CENTRAL AUDITORY SYSTEM

The optimistic predictions concerning the future of cochlear rehabilitation are also supported by the fact that the recent data testify to both the preservation of the neural mechanisms of sound signal processing, even after a long-term absence of auditory inputs to the central nervous system, and the ability of the neural network to undergo plastic changes when the functioning of these inputs is resumed [19]. For example, it has been shown that, in the case of both acute [20] and chronic impairment [21] of the internal ear, an electric stimulation causes the same types of neural responses of the central auditory midbrain as the responses caused by an acoustic stimulation. The thresholds of the response to sound signals prove to be invariable even with the loss of up to 80–90% of the internal hair cells, which should correspond to an approximately equal decrease in the evoked activity of the auditory nerve fibers. In the course of regeneration, the responses of the central auditory system are restored even earlier than the peripheral responses [22].

In this connection, we briefly review the general principles of signal transformation by the neurons of the central auditory system. First of all, it should be noted that, according to the latest concepts, the general principles of signal transformation in the direct auditory pathway (at least, up to the midbrain stage) are much the same for different animals. The idea that the hearing of lower vertebrates is specialized so as to provide the perception of only a narrow range of sounds, e.g., communication sounds or alarm signals, failed to agree with reality. It has become clear that the main function of the auditory system of any vertebrate, from fish to human, is the perception and the analysis of the whole acoustic environment, which, presumably, is necessary for the orientation in the surrounding space [23, 24]. The perception of specialized sounds is presumably performed by special nuclei near the direct auditory pathway [25, 26]. In particular, recently, it was found that a human auditory cortex has an area that is separate from the primary auditory cortex and is selectively excited in response to speech sounds [27].

The general analysis of the acoustic environment is performed on the basis of the information that arrives to the brain from the auditory nerve, all fibers of which

end in the cochlear nuclei. There, the signal is processed by several separate subsystems. The neurons of one of them retain, and even enhance, the temporal features of the signal. The corresponding cells are retained at the next stage of the auditory system, i.e., in the superior olives, where, in particular, the fine analysis of the binaural delays is performed, thus providing sound source localization.

The other system performs the coding of sound intensity variations in each of the frequency channels. In the cochlear nuclei, the coding efficiency for these variations in a wide dynamical range is considerably increased, as compared to the auditory nerve fibers. This occurs because of the summation of the excitations from many auditory nerve fibers with close tuning frequencies. The delayed inhibitory inputs arrive at the same neurons from a somewhat broader region on the basilar membrane. In this situation, even a small increase in the amplitude of an intense signal can cause a spike generation at the neuron output, because the inhibitory input arrives with a certain delay relative to the initiating one [24].

The ability of neurons to reproduce small amplitude variations of relatively loud signals gradually increases with a continuous presentation of the signal. One can assume that the mechanism of such a tuning is related to a gradual increase in the relative contribution of the inhibitory inputs. As a result, the summary level of the input synaptic action proves to be close to the spike generation threshold, so that even a small increase in level causes a synchronous response of the cell. This process, which seems to be universal for the auditory systems of different animals, is sequentially reproduced at the following stages of the auditory system, at least up to the midbrain. In the case of the coding of relatively slow variations of the signal level (up to modulation frequencies of 50–100 Hz), the aforementioned effect is considerably amplified [28] at the midbrain stage and clearly manifests itself already within the first second of the stimulus presentation [29].

Thus, one of the main universal operations of the signal coding in the nervous system is the analysis of the signal amplitude variations by a set of highly nonlinear threshold elements that provide an adaptive tuning of the spike generation threshold to the level of the presented signal. The specific mechanism of this tuning is yet unknown. However, some interesting possibilities have opened up recently in connection with the discovery of the effect of the cell activity on the efficiency of synaptic inputs. According to these data, the efficiency of a synapse increases when the neural spike immediately follows its input, while this efficiency decreases when the input signal appears immediately after the neural spike [30]. Since this process occurs with a certain excess of the weight of inhibitory inputs over that of the initiating ones, the result should be a gradual tuning of the input action to the spike generation threshold of the neuron under study.

An interesting situation occurs when, as a result of the adaptive tuning, the spike generation threshold proves to be higher than the maximal value of the signal amplitude. In this case, conditions for the realization of stochastic resonance are formed in the neuron. The latter does not respond to weak sinusoidal variations of the signal amplitude. If a random noise component is added to the sinusoidal modulating function, a long active response is observed, and this response proves to be synchronized with the weak periodic component of the modulation (Bibikov, to be published). Up to now, stochastic resonance in an intact auditory system was best observed precisely in the case of the coding of weak periodic amplitude variations of intense signals in the adapted regime by the neurons of the higher stages of the auditory system. In the peripheral auditory system, the corresponding effect can be observed only by providing artificial conditions at the levels close to the detection threshold [31, 32]. This is quite natural, because in an intact auditory nerve, noise is actually present, manifesting itself, in particular, as a spontaneous activity.

ACKNOWLEDGMENTS

This work was supported by the Russian Foundation for Basic Research, project no. 02-04-48236.

REFERENCES

1. R. K. Shepherd and E. Javel, Hear. Res. **108**, 112 (1997).
2. R. K. Shepherd and E. Javel, Hear. Res. **130**, 171 (1999).
3. E. Javel and R. K. Shepherd, Hear Res. **140**, 45 (2000).
4. J. Colombo and C. W. Parkins, Hear. Res. **31**, 287 (1987).
5. W. K. Lai and N. Dillier, Audiol. Neuro-Otol. **5**, 333 (2000).
6. A. Kral, R. Hartmann, D. Mortazavi, and R. Klinke, Hear. Res. **121**, 11 (1998).
7. R. P. Morse, G. F. Meyer, and E. F. Evans, Br. J. Audiol. **32**, 111 (1998).
8. J. L. Parkin, L. J. Randolf, and B. D. Parkin, Laryngoscope **103**, 835 (1993).
9. J. Douglass, K. Wilkens, E. Pantazelou, and F. Moss, Nature **365**, 337 (1993).
10. N. G. Bibikov, N. A. Dubrovsky, G. A. Ivanitsky, *et al.*, in *Proceedings of XI International Congress of Phonetic Sciences* (Tallinn, 1987), Vol. 3, p. 67.
11. J. T. Rubinstein, B. S. Wilson, C. C. Finley, and P. J. Abbas, Hear. Res. **127**, 108 (1999).
12. R. Morse, F. Edward, and E. F. Evans, Hear. Res. **133**, 107 (1999).
13. A. J. Matsuoka, P. J. Abbas, J. T. Rubinstein, and C. A. Miller, Hear. Res. **149**, 129 (2000).
14. D. H. Johnson and N. Y. Kiang, Biophys. J. **16**, 719 (1976).

15. N. G. Bibikov and G. A. Ivanitskiĭ, Biofizika **30**, 141 (1985).
16. R. L. Smith and M. L. Brachman, Biol. Cybern. **44**, 107 (1982).
17. C. D'Aldin, J. Ruel, S. Ladrech, *et al.*, Int. J. Dev. Neurosci. **15**, 619 (1997).
18. M. Zine, J. Nyffeler, and F. de Ribaupierre, Hear. Res. **141**, 19 (2000).
19. N. M. Weinberger and D. M. Diamond, Prog. Neurobiol. **29**, 1 (1987).
20. N. G. Bibikov, S. V. Kosterin, and L. I. Tikhomirov, Fiziol Zh. SSSR im. I.M. Sechenova **75**, 868 (1989).
21. R. K. Shepperd, J. H. Baxi, and N. A. Hardie, J. Neurophysiol. **82**, 1363 (1999).
22. Y. Zheng, S. L. McFadden, and D. Henderson, Neuroscience (Oxford) **85**, 579 (1998).
23. A. S. Bregman, *Auditory Scene Analysis: The Perceptual Organization of Sound* (MIT Press, Cambridge, 1990).
24. N. G. Bibikov, in *Neuroinformatic and Neurocomputers* (IEEE Neural Network Council, 1992), Vol. 1, pp. 1–12.
25. N. G. Bibikov, Zh. Evol. Biokhim. Fiziol. **26**, 817 (1990).
26. N. Suga, J. Comp. Physiol. A **174**, 135 (1994).
27. P. Belin, R. J. Ztorre, P. Lafaille, *et al.*, Nature **403**, 309 (2000).
28. N. G. Bibikov, in *Acoustical Signal Processing in the Central Auditory System* (Plenum, New York, 1997), pp. 271–277.
29. N. G. Bibikov and S. V. Nizamov, Hear. Res. **101**, 23 (1996).
30. M. Segal, Prog. Neurobiol. **63**, 61 (2001).
31. K. R. Henry and R. Lewis, Hear. Res. **155**, 91 (2001).
32. K. R. Henry, J. Comp. Physiol. A **184**, 577 (1999).

Translated by E. Golyamina

Acoustical Physics, Vol. 48, No. 6, 2002, pp. 749–751. Translated from Akusticheskiĭ Zhurnal, Vol. 48, No. 6, 2002, pp. 845–848.

CONFERENCES AND MEETINGS

Some Problems of the Acoustic Theory of Speech Production

V. I. Galunov

OOO Oditek, St. Petersburg State University,
ul. Suvorovskaya 7/2-13, Peterhof, St. Petersburg, 198904 Russia
e-mail: auditech@online.ru

Abstract—The classical acoustic theory of speech production has remained basically intact since 1870, when it was first developed by Helmholtz. However, there are some questions that require special consideration, because the answers to them are still unclear. © *2002 MAIK "Nauka/Interperiodica".*

The acoustic theory of speech production in its scientific form was first formulated by Helmholtz in 1870 [1]. The basic ideas of this work remain intact until now and, explicitly or implicitly, are accepted by the majority of specialists in this field of science. Naturally, this theory has acquired a number of mathematical and methodical-technological improvements, which were introduced by different scientists, from the now forgotten publication by Chiba and Kajiama [2] to the classical works by Fant [3] and Ungeheur [4] and, finally, to some recent publications [5, 6].

The Helmholtz model is characterized by two main statements.

(1) The process of speech production consists of two independent components: the excitation of sound itself and the formation of the phonetic quality of sound through the excitation of the resonance frequencies of the articulatory tract (according to Helmholtz) or through filtering (according to recent concepts).

(2) The phonetic quality of sound is determined by the so-called formants, which are determined as the resonance frequencies of the articulatory tract (or the poles of the transfer function of the articulatory filter) or as the spectral maxima of the speech signal [7].

These statements have never been explicitly revised, although they apparently are contrary to fact. This situation occurs, because no one can predict the scientific consequences of such a revision.

Let us first discuss the statement concerning the independence of the sound source and the articulatory filter. Earlier [8], it was found that the phonetic quality of vowels is mainly formed in the larynx without the effect of the articulatory filter. Moreover, from the classical literature, it is well known that the voice source has its own poles and zeros, which directly affects the quality of the speech signal. All this suggests that, if the formants determining the phonetic quality of sound really exist, they are represented by the spectral maxima rather than by the poles of the transfer function that require a deconvolution operation, as is stated by the classical theory.

The second question is whether the processes of speech production and speech perception are symmetric, as the classical theory implies. The fact that using such formants one can obtain a given phonetic quality of sound is evident. (An example is the speech production of birds.) However, is it just these maxima that determine the phonetic quality of speech sounds? This question arose for the first time in the 1930s, after the development of a band vocoder [9]. In the early 1960s, ample experimental data were used to develop the theory of speech intelligibility on the basis of the band representation of a speech signal [10, 11] without considering the formants (it should be noted that, in the Russian version of this theory, the main computational parameter retained the name of "formant intelligibility"). All this suggested the hypothesis (L.A. Varshavskiĭ and I.M. Litvak) that the phonetic quality of sounds is determined by a certain level of the power ratios in the spectral bands while the formants (i.e., the spectral maxima) serve only as a means for the speech production system to obtain the necessary band ratios.

Relying on the aforementioned double set of concepts concerning the formation of the acoustic appearance of speech sounds at the phonetic level, it is natural to assume that there exist several simultaneously operating systems of sound-discriminating features. Precisely the existence of several systems of different types of features provides the stability of speech as a communication system against the effect of a rather wide range of noise and distortions.

The next question concerns the number of the existing formants. The positions of the formants are known for the Russian vowels pronounced separately or in syllables. No noticeable deviations from the results obtained in the classical work by Fant [3] are observed. However, it is known that, in a real speech signal, the formant pattern noticeably changes. It exhibits additional maxima, the splitting of the maxima in the for-

1063-7710/02/4806-0749$22.00

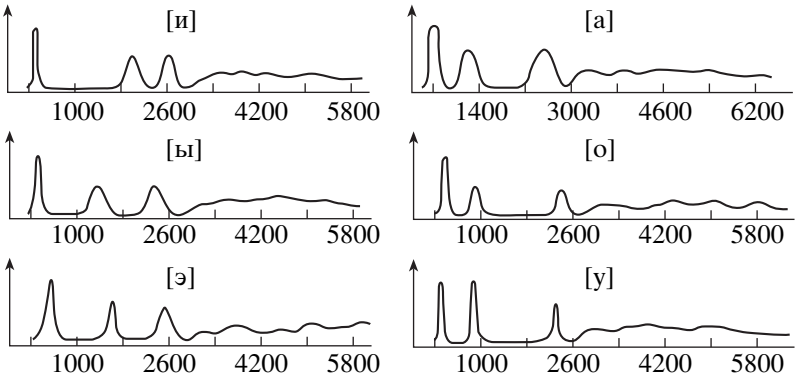

Figure.

mant positions of the ideal version, and the disappearance of the classical formant maxima. These deviations may result from at least the three following factors: the individual features of the speaker, the contextual surroundings, and the situational features (the psychophysical condition of the speaker, the manner of pronouncing in a given audience, etc.).

Suppose we accept the hypothesis that the articulatory system has finite acoustic resonances and filtering abilities while the speaker producing the speech sounds tends to a certain structure of discriminative features, one of which is a specific formant pattern. Then, despite all the aforementioned possible distortions of the "correct" formant structure, the histograms representing the probability distribution of the spectral maxima will exhibit zones where the "correct" formant structures will be observed.

In our previous paper [12], it was shown that, for all vowels, the probability distribution of spectral maxima exhibits three clearly pronounced maxima in the low-frequency part of the spectrum, and these maxima correspond to the first three formants (see figure). In the intervals between them and in the high-frequency region, the probability distribution of maxima is practically uniform and no formant regions can be identified. The aforementioned formant regions coincide with the commonly accepted positions of the three first formants of the Russian vowels. In addition, it should be noted that, in fluent speech, for male voices, an additional spectral maximum is often observed between the second and third formants. For female voices, the disappearance of the second formant is typical (this phenomenon is even more typical of children's voices).

In connection with the problem of the role of formants in speech perception, it is appropriate to mention one more problem that has never been explicitly discussed. It is well known that, in real speech, the main role in the formation of the linguistic image of speech is played by the transitions between sounds. Stationary regions can even exchange places without affecting the perception of the meaning. It is unclear how this correlates with the explicit meaning of stationary regions and with their formant structure in the perception of isolated vowels or syllables.

Now, let us consider the possibilities of a band representation of the speech signal. Evidently, because of purely physical limitations, a speaker cannot control a great number of spectral components in the process of speech production. This follows from the physical limitations of the articulatory tract [13]. If, at a given instant, we can measure a great number of spectral components, with time, they can vary only in a correlated manner. The independent spectral components can be revealed by analyzing the correlation matrices of the temporal envelopes of the spectral components. It is natural to assume that the independent components obtained in this way are precisely the variables that determine the quality of the signal. In our previous study [12], by the factorial analysis of the correlation matrices of spectral components of speech signals, we obtained the following, approximately independent, spectral bands: 80–400, 400–750, 750–1350, 1350–1750, 1750–2200, 2200–2900, and 2900–5000 Hz. The separated components coincide to a fair accuracy with the boundaries of the formant bands (it is interesting that the band 1350–1750 Hz does not correspond to any formants of the Russian vowels but yields the false formant frequently observed for male voices—see above).

Let us return to the conventional scheme. The main assumption is that the informational sound wave is formed in the speech tract as a result of the excitation of natural oscillations of the sound waveguide, which is believed to be the speech tract. These natural oscillations are analyzed by the brain and perceived by a human listener as speech. In principle, such a scheme can exist. Moreover, considerable progress has been achieved with its help. However, there are some points that, in our opinion, are contradictory to fact. First, the real spectra of the same speech signals produced by different speakers are often different, which fundamentally contradicts the conventional scheme. The case of speech production with a considerable change in the speech tract (e.g., with a cigarette in the mouth) is even less understood. Moreover, when a speech signal is

transmitted through a telephone communication channel, its spectrum is considerably distorted, but the meaning of the speech is retained. This fact alone is sufficient to cast some doubt on the conventional model of speech production. There are also some other questions, which, however, can be considered as emotional. Why does nature need such a complex system? Indeed, to form a certain time dependence at the output of the speech tract, it is necessary not only to excite specific modes of the waveguide but also to excite them with certain phase and intensity relationships. In addition, the role of the considerable spatial deformations of the speech tract in the process of speech production is totally unclear.

These questions are eliminated when another model, namely, the modulation model of speech production, is used. In this model, two stages can be distinguished. At the first stage, a sound wave containing no information and playing the role of a carrier is generated. At the second stage, the carrier is modulated, and this modulation contains the whole information about the speech. Here, the role of the speech tract is reduced to the role of a modulator, which makes the considerable spatial deformations of the speech tract quite understandable. The problem of the strict phase and intensity relationships between the natural oscillations is eliminated, because the excited wave can be (and, in our opinion, it is) of a random character. This model explains the noncoincidence of the spectra obtained for the same speech signals, as well as the characteristic features of the transmission through the telephone cables. One of the possible modulation circuits is proposed in our other paper [14].

REFERENCES

1. H. Helmholtz, *Die Lehre von der Tonempfindungen Als Physiologische Graudlage fur Die Theorie der Musik* (Braunschweig, 1870).
2. T. Chiba and M. Kajiama, *The Vowel, Its Nature and Structure* (Tokyo, 1941).
3. G. Fant, *Acoustic Theory of Speech Production* (Mouton, s'Gravenhage, 1960; Nauka, Moscow, 1964).
4. G. Ungeheur, *Elemente Einer Akustischen Theorie der Vokalartikulation* (Springer, Berlin, 1962).
5. *Papers in Speech Communication: Speech Production*, Ed. by R. D. Kent *et al.* (Acoust. Soc. Am., 1991).
6. V. N. Sorokin, *Speech Formation Theory* (Radio i Svyaz', Moscow, 1985).
7. J. L. Flanagan, *Speech Analysis, Synthesis and Perception* (Academic, New York, 1965; Svyaz', Moscow, 1968).
8. V. I. Galunov, B. S. Krylov, S. A. Stankevich, and R. G. Khantemirov, in *Proceedings of III Meeting of Otolaryngologists of the Russian Soviet Federal Socialist Republic* (1972).
9. H. Dudley, *The Vocoder* (Bell Labs., 1939), Record 17, pp. 122–126.
10. K. D. Kryter, J. Acoust. Soc. Am. **34**, 1689 (1962).
11. N. B. Pokrovskiĭ, *Calculation and Measurement of Speech Intelligibility* (Svyaz'izdat, Moscow, 1962).
12. V. I. Galunov and V. I. Garbaruk, in *Proceedings of International Conference: 100 Years of Russian Experimental Phonetics* (St. Petersburg, 2001).
13. V. I. Galunov, Doctoral Dissertation in Physics and Mathematics (1975).
14. V. I. Galunov and V. K. Uvarov, *Once Again on the Voice Formation Mechanism* (n.p, n.d.).

Translated by E. Golyamina

Acoustical Physics, Vol. 48, No. 6, 2002, pp. 752–755. Translated from Akusticheskiĭ Zhurnal, Vol. 48, No. 6, 2002, pp. 849–853.

CONFERENCES AND MEETINGS

Spectral Dynamics and Classification of Russian Vowels

V. B. Kouznetsov

Moscow State Linguistic University, ul. Ostozhenka 38, Moscow, 119034 Russia
e-mail: kvlad@ccas.ru

Abstract—The spectral characteristics of stressed Russian vowels are studied experimentally in relation to the palatalized or nonpalatalized feature of the consonant environment, the local speech tempo, and the speaker effect. The experimental data are used as a basis to discuss the possibility of classifying vowels by their static and dynamic spectral characteristics. The role of individual articulatory strategies and speech tempo is analyzed. © *2002 MAIK "Nauka/Interperiodica".*

The study of the ways vowels function in speech presents one of the most complicated problems, which has not been adequately solved to this day. Resuming the history of speech studies, the well-known phonetician J. Ohala came to the conclusion that there still is no unified understanding of the acoustic–auditory correlates of the phonetic quality of a vowel.

Facing the antinomy of the invariance of phonological units and their frightening realization variability in speech, some linguists fell into phonetic agnosticism by denying the role of articulatory acoustic properties of sound units in their classification (in the phonetic decoding of a speech flow). For example, the authoritative specialist in Russian phonetics L.V. Bondarko drew the conclusion that the properties of the psychological domain of vowel phonemes do not follow from the phonetic (material) properties of their acoustic realizations but are determined, in particular, by such functional properties as the frequency of occurrence in speech or the possibility of alternation in a word (see p. 184 in [1]).

In our opinion, the realization variability of vowels in Russian speech is indeed of an extremely complex but systematic character, which can and must be revealed as a result of a thorough investigation of the ways the sounds function in speech communication.

This paper is focused on the spectral classification of stressed Russian vowels when their variability is caused by such factors as the palatalized (P) or nonpalatalized (NP) feature of the consonant environment, the vowel duration caused not by the speech tempo but by the linguistic variables (sentence length, number of syllables in a word, etc.), and, to some extent, the individual features of the speaker.

The speech material and the speakers taking part in the experiment were as follows. In view of the purpose of the study, three types of speech material were chosen: (1) a monosyllabic pseudoword with a consonant–vowel–consonant (CVC) structure in which the consonants are symmetric and realized as an NP or P fricative [*s*, *s*'] and the vowel is represented by ten corresponding allophones of five vowel phonemes, namely, those between NP consonants (an NP context) [a, e, o, u, ɨ] (NP allophones) and between P consonants (a P context) [ja, je, jo, ju, i] (P allophones). For recording the speech material, a list was compiled in which each of the ten pseudowords was repeated 33 times at random; (2) the aforementioned textual pseudoword was included in a frame sentence "Say … again." As in the previous case, the list for reading consisted of 330 sentences; and (3) the frame sentence "I was informed that the oldest … company has gone bankrupt" contained the pseudoword "bisCVCfurnaya," in which the consonant standing to the left and to the right of the stressed vowel *V* was realized by an NP or a P occlusive [*t*, *t*'] while *V* was represented by the corresponding ten allophones. The list for reading consisted of 110 sentences with the ten initial sentences being repeated 11 times at random.

For the sake of brevity, the first type of speech material will below be called "word-phrase," the second type, "short phrase," and the third type, "long phrase." Subsequent measurements showed [2] that the structure of these phrases made it possible to obtain test vowels of different duration (the mean values were 154, 99, and 76 ms, respectively) when read at a normal speech tempo.

The short-phrase speech material was recorded from four male speakers 25–50 years old, Moscow born, characterized by a normal literary pronunciation, and possessing no speech defects. The rest of the speech material was read by one of these four speakers (speaker *C*).

The spectrum of a vowel was measured at the boundary with the preceding consonant (the transition value) and at the point where the trajectory of the second formant reached its extremum or in the middle of the vowel (the target value). The calculation of the frequencies and amplitudes of the first three formants was usually performed in an automated way; in difficult cases, it was performed by hand with the use of an LPC analysis controlled by the FFT spectrograms. A

1063-7710/02/4806-0752$22.00 © 2002 MAIK "Nauka/Interperiodica"

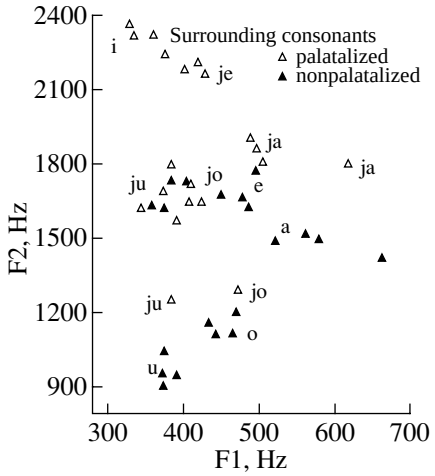

Fig. 1. Mean formant frequencies over four speakers (short phrase).

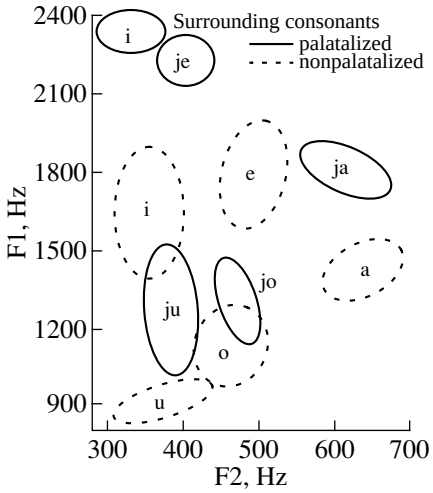

Fig. 2. Mean formant frequencies of speaker *Z* (short phrase).

detailed description of the methodological aspects of the study can be found in [2, 3].

The results of spectral measurements are conventionally presented in the F1–F2 space in the form of dots corresponding to the mean values of parameters (Fig. 1) or in the form of ellipses (the other figures) representing 95% common confidence regions of the parameter values for a given vowel. The orientation of an ellipse is determined by the sign of the correlation coefficient between F1 and F2, and its major axis lies on the straight linear regression of F2 on F1.

Figure 1 shows the mean target frequencies of formants obtained from four speakers. One can see that the same vowels produced by different speakers form a compact group in the F1–F2 plane except for the four vowels produced by speaker *Z*: [ju, jo, ja, a]. These vowels are indicated in Fig. 1. For a more detailed analysis of the results, the data obtained from speaker *Z* and a typical representative of other speakers, namely, speaker *C*, are shown in Figs. 2 and 3, respectively. We begin the analysis with a comparison of the spectral variabilities of allophones of a single phoneme. From Figs. 2 and 3, one can see that the target values of the frequency F1 exhibited by both speakers are higher for low rising P vowels than for the corresponding NP allophones; however, this difference is below the statistical significance level.

As for frequency F2, the difference between its target values for P and NP allophones of the same phoneme lies within 300–700 Hz and, except for one case, is statistically certain for both speakers. The deviation from this rule is related to the intersection of the ellipses of the vowels [o] and [jo] of speaker *Z* (Fig. 2). Note that, for the allophones of the phoneme /u/ of the same speaker, the confidence regions almost touch each other.

Estimating the difference between the NP and P allophones, we come to the conclusion that it cannot be completely ascribed to the effect of coarticulation, when the F structure observed in the context of soft consonants is interpreted as a failure in reaching the acoustic target, which is assumed to be the F structure of the NP allophone. We assume that the realization of a phoneme in the NP and P context is achieved with the use of different articulatory programs. This concept is supported by several arguments. First, the maximal "undershoot" values of F2 recorded in the experiment (see, e.g., the allophones of the phonemes /u/ and /e/ in Fig. 3) evidently exceed the limits usually associated with the coarticulation effect. In our data, an example of vowel variability due to coarticulation can be the allophonic realization of the phoneme /o/ and, to some extent, the phoneme /u/ by speaker *Z* (Fig. 2).

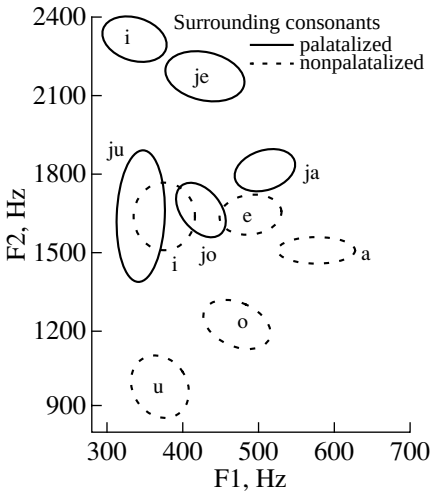

Fig. 3. Mean formant frequencies of speaker *C* (short phrase).

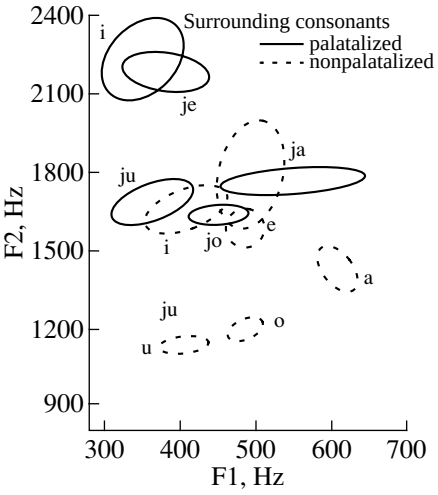

Fig. 4. Mean formant frequencies of speaker *C* (long phrase).

Second, the soft allophones occupy the regions of the F1–F2 plane that are usually ascribed by the International Phonetic Association to the vowels that differ from the basic phoneme version (the NP allophone). According to their formant characteristics measured in the position closest to the target, the vowels [ju] and [jo] of speaker *C* (Fig. 3) can be classified with the front rounded vowels unlike their vis-à-vis, the back rounded ones.

Third, it is believed that the degree of coarticulation is inversely proportional to the time available for the articulation of the sound. However, the formant characteristics of the soft allophones of speaker *C*, when measured in three types of phrases that provide different vowel durations, differ little from each other. This can be seen from Figs. 3 and 4, as well as from the table where the target values of the first three formants are presented for four vowels of speaker *C*. For example, although the mean vowel duration in the long phrase was two times greater than in the short phrase, the difference in the values of F2 did not exceed 150 Hz. It should be also noted that the mean durations of the vowels [jo] and [ju] of speakers *C* and *Z* practically coincide while the formant characteristics of the vowels differ considerably (compare Figs. 2 and 3), which brings up the question as to the identity of the articulatory programs used by these speakers.

Dynamics of formant frequencies for different vowel durations (speaker C, V_i denotes the vowel onset, and V_t is the vowel target)

Vowel	Word-phrase			Short phrase			Long phrase		
	F1	F2	F3	F1	F2	F3	F1	F2	F3
ɨ_i	418	1360	2535	394	1483	2445	420	1654	2555
ɨ_t	403	1504	2503	375	1627	2364	407	1658	2520
E_i	462	1490	2603	451	1575	2542	458	1607	2565
E_t	534	1598	2634	497	1633	2518	474	1633	2614
JO_i	410	1779	2600	385	1855	2621	398	1680	2572
JO_t	479	1570	2522	424	1652	2510	451	1632	2599
JU_i	389	1802	2531	385	1873	2511	385	1715	2525
JU_t	386	1533	2406	346	1624	2391	363	1684	2520

Summarizing the results described above, we can conclude that, in pronouncing NP and P allophones, all the speakers realized different articulatory programs. Speaker *Z* was likely to use the same program for the phonemes /o/ and /u/; in this case, the spectral differences between the NP and P allophones were related to coarticulation.

Now, we proceed to analyzing the relative positions of vowels in the F1–F2 space, regardless of the phonemes to which they belong. From Figs. 1, 2, and 3, one can see that the vowel positions form a triangle whose vertices correspond to the vowels [i, a, u]. This triangle falls into two smaller triangles formed by NP and P allophones. Their vertices correspond to the vowels [ɨ, a, u] and [i, ja, ju], respectively. These triangles have a common side, which lies in the F2 frequency range of 1500–1800 Hz. Note that this does not concern the vowel configuration of speaker *Z*. The common side of triangles is a result of the overlapping of the confidence regions of the vowel [ju] with [ɨ] and [jo] with [ɨ] and [e] (see Fig. 3). For these vowels, the frequencies F2 coincide, and they differ only in the values of F1. This means that the static spectral characteristic of stressed vowels, even when recorded from a single speaker, does not provide their complete discrimination in principle. The ambiguity of the static classification of vowels can be easily eliminated, if we can determine whether a given vowel is pronounced after an NP or a P consonant [4]. It is well known that the type of the preceding consonant can be determined from the formant transition: after a soft consonant, the frequency F2 does not fall below 1700 Hz.

The results of our measurements of the F structure at the boundaries between the test vowels and the preceding consonants are presented in Fig. 5 and in the table for the four aforementioned vowels. One can see that the onset values of the formant transitions obtained for NP and P allophones are widely separated in F2. Thus, combining the data of Figs. 3 and 5 (which allows us to trace the dynamics of the spectral changes that occur on the vowel segment), we obtain a complete differentiation of the test vowels.

In the case of speaker *Z*, the vowel classification is possible within the limits of the static spectral characteristics.

In closing, we consider whether all the aforesaid remains valid in the case of the maximal reduction of the test vowel duration (the long phrase). As for the other two duration ranges, from the point of view of spectral characteristics, we revealed no noticeable dif-

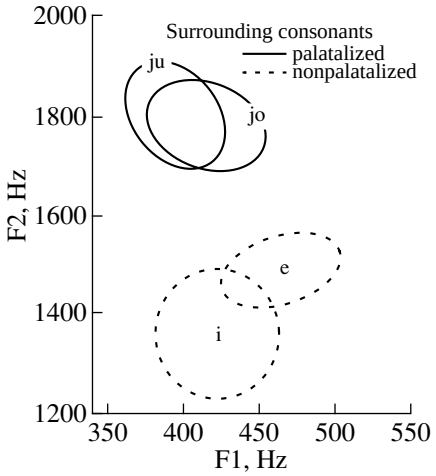

Fig. 5. Frequencies of the onset formant transitions. Speaker *C* (monosyllabic word-phrase).

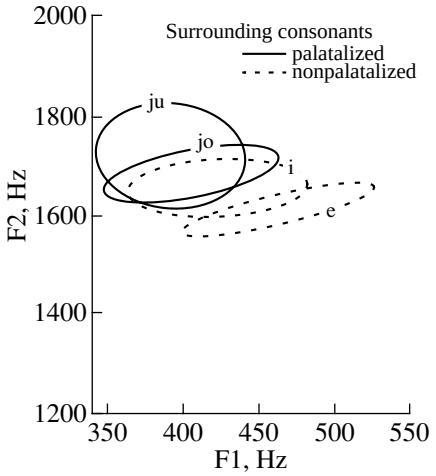

Fig. 6. Frequencies of the onset formant transitions. Speaker *C* (long phrase).

ferences between the vowels taken from a word-phrase and a short phrase.

The analysis of Fig. 4 shows that, compared to the vowels from a short phrase (Fig. 3), the positions of the allophones have become more compact forming three different groups: the clearly distinguished [u, o, a], the closely spaced [ju, ɨ, jo, e] with [ja] approaching them, and the vowels [je] and [i] that are now practically indistinguishable. The majority of ellipses are oriented horizontally, which means a small variability of the frequency F2 of the vowels. As in the case with the vowels from a short phrase, the static spectral information is obviously insufficient for the discrimination of all allophones. The situation has become even worse, because for the vowels [je] and [i], the inclusion of data on the transition values of formants is useless: both vowels are soft allophones. The measurements of the transition values for the vowels [ju, ɨ, jo, e] presented in Fig. 6 show that the differences between the NP and P allophones reach the statistical significance level neither in F1 nor in F2. Only the region of common confidence values for [e] does not overlap with the confidence regions of soft allophones. Thus, the discrimination of the vowels [ju, ɨ, jo, e] on the basis of the spectral information enclosed within the vowel segment proves to be impossible, because the formant transition does not indicate the NP or P feature of the preceding consonant.

Since a human listener does not confuse these vowels (in our previous study [5], we carried out an experiment on the discrimination of the test vowels in a long phrase), one may assume that a human listener first discriminates not individual sounds but greater units like syllables, from which he extracts phonetical units of smaller size. Note that this hypothesis was put forward earlier, but in connection with another problem: it was found that the same fricative noise of a stop consonant is identified in different ways, depending on the phonetic quality of the subsequent vowel [6].

REFERENCES

1. L. V. Bondarko, *Phonetic Description of Language and Phonological Description of Speech* (Leningrad, 1981), p. 198.
2. V. Kouznetsov and A. Ott, in *Estonian Papers in Phonetics (EPP 1984–1985)* (Valgus, Tallinn, 1986), pp. 67–95.
3. V. B. Kouznetsov and A. Ott, in *Proceedings of XI International Congress of Phonetic Sciences* (Tallinn, 1987), Vol. 3, p. 117.
4. V. B. Kouznetsov, in *Transactions of Scientific Works* (MGIIYa im. M. Toreza, Moscow, 1989), No. 329, pp. 38–49.
5. V. B. Kouznetsov and A. Ott, *Automatic Synthesis of Speech. Algorithms of the Letter-to-Sound Conversion and the Control over Speech Segment Duration* (Tallinn, 1989), p. 135.
6. F. S. Cooper *et al.*, J. Acoust. Soc. Am. **24**, 597 (1952).

Translated by E. Golyamina

Acoustical Physics, Vol. 48, No. 6, 2002, pp. 756–757. Translated from Akusticheskiĭ Zhurnal, Vol. 48, No. 6, 2002, pp. 854–855.

LETTER TO THE EDITOR

Allowance for the Interaction between the Potential and Eddy Components of the Velocity Field in Analyzing the Instability of a Shear Flow

S. A. Rybak

Andreev Acoustics Institute, Russian Academy of Sciences, ul. Shvernika 4, Moscow, 117036 Russia

e-mail: rybak@akin.ru

Received December 5, 2001

The interaction between the eddy and potential components of the velocity field due to the boundary conditions at a rigid wall were considered in previous publications [1–3]. This paper analyzes the role of the interaction (coupling) that occurs between the aforementioned components in the liquid itself (rather than at the boundary) in the case of a shear flow. This interaction gives rise to a hydrodynamic instability in a shear flow even in the absence of an inflection point in its profile.

Consider a system of hydrodynamic equations for a two-dimensional model with the (x, y) coordinates, where x is the coordinate along the flow $U(y)$ and y is the coordinate along the flow normal. In the quadratic approximation with respect to the velocity vector $v_i(t, x, y)$, this system of equations has the form

$$\frac{\partial}{\partial t}v_i + \left[(v_k + U\delta_{kx})\frac{\partial}{\partial x_i}(v_i + U\delta_{ix})\right]$$

$$= -\frac{1}{\rho}\frac{\partial p}{\partial x_i} + \eta\Delta v_i + \left(\varsigma + \frac{\eta}{3}\right)\frac{\partial}{\partial x_i}\frac{\partial v_k}{\partial x_k};$$

$$\frac{\partial \rho}{\partial t} + U\frac{\partial \rho}{\partial x} + \frac{\partial}{\partial x_k}(\rho v_k) = 0; \qquad (1)$$

$$\delta\rho = \delta p/c^2 - \frac{\gamma - 1}{2\rho_0 c^4}\delta p^2; \quad v_x = \frac{\partial \varphi}{\partial x} + \frac{\partial \phi}{\partial y};$$

$$v_y = \frac{\partial \varphi}{\partial y} - \frac{\partial \phi}{\partial x}.$$

In the linearized limit, system (1) is reduced as follows:

$$D\Delta\phi - U_{yy}\frac{\partial \phi}{\partial x} + \Delta\varphi U_y + U_{yy}\frac{\partial \varphi}{\partial y} = \eta\Delta^2\phi;$$

$$D\Delta\varphi + \frac{1}{\rho_0}\Delta p = \left(\varsigma + \frac{4}{3}\eta\right)\Delta^2\varphi - 2U_y\frac{\partial}{\partial x}\left(\frac{\partial \varphi}{\partial y} - \frac{\partial \phi}{\partial x}\right); \qquad (2)$$

$$\frac{1}{\rho c^2}Dp + \Delta\varphi = 0; \quad D = \frac{\partial}{\partial t} + U\frac{\partial}{\partial x}.$$

The first equation of system (2) is a modified Orr–Sommerfeld equation [4]. It is this equation that takes into account the relation arising between the eddy component of the velocity field and the potential component because of the presence of the shear flow $U(y)$. The second and third equations are essentially equivalent to the Lighthill equation [5] with the right-hand side linearized against the background of the shear flow. These equations are written with allowance for the Doppler frequency shift that is nonuniform along the Y axis.

The conditions for the appearance of an instability in such a system are not determined by the necessary presence of an inflection point in the profile $U(y)$, as is required by the Rayleigh theorem (see, e.g., [4, 6]) with only the eddy field component taken into account. Let us show that the instability appears even in the simplest case of a linear dependence $U(y)$, which has no inflection points:

$$U(y) = U_0(1 + \varepsilon q y). \qquad (3)$$

Here, q is the projection of the wave vector of a harmonic wave onto the Y axis. We also assume that

$$\varepsilon = \frac{1}{qL} \ll 1, \quad L^{-1} \propto \frac{U_y}{U}. \qquad (4)$$

To analyze the instability, it is necessary to consider the compressibility of the medium, i.e., the finite propagation velocity of a potential (sound) wave coupled with the eddy component according to Eqs. (2). The source of the wave can be, for example, of a noise nature (thermal noise).

This consideration is quite important for explaining the origin of hydrodynamic instability in different situations and, specifically, in the boundary layer where the presence of an inflection point in the profile $U(y)$ is not always evident.

1063-7710/02/4806-0756$22.00

The system of equations (2) with allowance for Eq. (3) has the form (the viscosity is neglected)

$$\begin{aligned} &D\Delta\phi + \Delta\varphi U_y = 0;\\ &D\Delta\varphi + \frac{1}{\rho_0}\Delta p = -2U_y\frac{\partial}{\partial x}\left(\frac{\partial\varphi}{\partial y} - \frac{\partial\phi}{\partial x}\right);\\ &\frac{1}{\rho_0 c^2}Dp + \Delta\varphi = 0. \end{aligned} \tag{5}$$

According to relations (3) and (4), we obtain

$$U_y = \varepsilon q U_0. \tag{6}$$

We solve system (5) to the first order in ε, i.e., assuming that U and U_y are constant. Then, we arrive at the expressions

$$\begin{aligned} \varphi &= c_1\exp[j(-\omega t + kx + qy)],\\ \phi &= c_2\exp[j(-\omega t + kx + qy)]. \end{aligned} \tag{7}$$

We set

$$\omega = \omega_0 + \varepsilon\omega_1. \tag{8}$$

Substituting Eqs. (7) in system (5), we obtain a dispersion relation:

$$\begin{aligned} &(\omega - Uk)^2 - (k^2 + q^2)c^2\\ &= \frac{-2j(\omega - Uk)U_y kq + 2k^2U_y^2}{k^2 + q^2}. \end{aligned} \tag{9}$$

With allowance for Eqs. (3), (4), and (8), we derive

$$\begin{aligned} \omega_0 &= U_0 k + c(k^2 + q^2)^{1/2},\\ \omega_1 &= j\frac{U_0 kq^2}{k^2 + q^2}, \quad j\delta\omega = \varepsilon\omega_1 = j\frac{U_0 kq}{L(k^2 + q^2)}. \end{aligned} \tag{10}$$

In the derivation of these expressions, we used inequality (4) to ignore the last term in the numerator on the right-hand side of Eq. (9).

Hence, even in the simplest case of linear dependence (3) of the shear velocity, the inclusion of the interaction between the potential and eddy components of the wave field leads to a wave instability. It is essential that the compressibility of the medium should be taken into account, because otherwise we obtain a divergence in Eq. (9).

Now, let us consider the development of the instability in the region $y > 0$ on condition that

$$v_y = 0 \text{ on the plane } y = 0 \tag{11}$$

(a rigid wall). The shear flow satisfies the relation

$$U = U_0\frac{y}{L}, \quad 0 < y. \tag{12}$$

The choice of the solution in the form of Eqs. (7) with condition (11) leads to a zero value of the resulting particle velocity component v_y:

$$v_y = \frac{\partial\varphi}{\partial y} - \frac{\partial\phi}{\partial x} = 0, \text{ for all } y > 0. \tag{13}$$

From Eqs. (5), (7), and (13), we obtain

$$q = -j\frac{kU_y}{S}, \quad S = \omega - Uk. \tag{14}$$

It should be emphasized that, for the wave (ϕ, φ) to decay in the direction $y > 0$, it is necessary that condition $\mathrm{Im}\,q > 0$ be satisfied. The latter is valid, in particular, for a wave with $k < 0$.

Now, dispersion relation (9) can be reduced to the form

$$S^4 - c^2k^2(S^2 - U_y^2) = 0. \tag{15}$$

Biquadratic equation (15) has the solution (in particular)

$$\begin{aligned} S = \omega - Uk &= \frac{ck}{\sqrt{2}}\left(1 + j\frac{\varepsilon}{2}\right),\\ \varepsilon &= \left(\frac{4U'^2}{c^2k^2} - 1\right)^{1/2} \end{aligned} \tag{16}$$

with the proviso that $\varepsilon \ll 1$.

In the model under consideration, the instability appears when the condition

$$M^2 = \frac{U^2}{c^2} > \frac{k^2L^2}{4} \tag{17}$$

is satisfied.

The study of the further development of instability evidently requires an analysis of the nonlinear system of equations (1).

ACKNOWLEDGMENTS

This work was supported by the Russian Foundation for Basic Research (grant no. 02-02-17143), the Program for Supporting Scientific Schools (grant no. 00-15-96678), and INTAS (grant no. 99-88).

REFERENCES

1. K. A. Naugol'nykh and S. A. Rybak, Tr. Akust. Inst. Akad. Nauk SSSR, No. 16, 129 (1971).
2. K. A. Naugol'nykh and S. A. Rybak, Akust. Zh. **26**, 890 (1980) [Sov. Phys. Acoust. **26**, 502 (1980)].
3. S. A. Rybak, Akust. Zh. **47**, 717 (2001) [Acoust. Phys. **47**, 629 (2001)].
4. C.-C. Lin, *The Theory of Hydrodynamic Stability* (Cambridge Univ. Press, Cambridge, 1966; Inostrannaya Literatura, Moscow, 1958).
5. M. J. Lighthill, *Waves in Fluids* (Cambridge Univ. Press, Cambridge, 1978; Mir, Moscow, 1981).
6. L. D. Landau and E. M. Lifshitz, *Course of Theoretical Physics*, Vol. 6: *Fluid Mechanics* (Nauka, Moscow, 1986; Pergamon, New York, 1987), Chap 4.

Translated by E. Golyamina

Acoustical Physics, Vol. 48, No. 6, 2002, pp. 758–759. Translated from Akusticheskiĭ Zhurnal, Vol. 48, No. 6, 2002, pp. 856–857.

CHRONICLE

Vadim Alekseevich Golenishchev-Kutuzov (On His 70th Birthday)

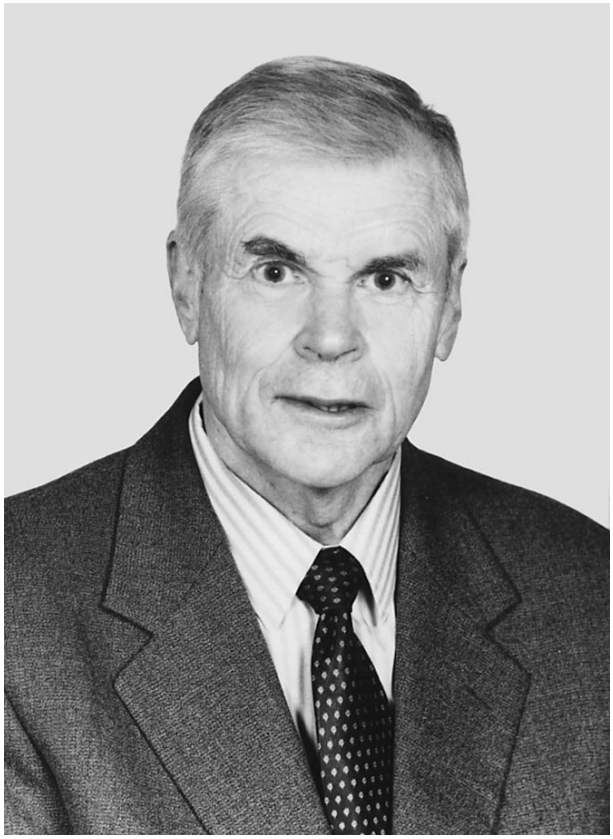

Vadim Alekseevich Golenishchev-Kutuzov was born on July 1, 1932, in Kazan. In 1955, he graduated from Kazan State University, where he specialized in radio-wave physics. During the next seven years, he worked as an assistant professor at this university. Then, he changed his place of work to the Kazan Physicotechnical Institute of the Russian Academy of Sciences, where he advanced from postgraduate student to junior researcher, senior researcher, head of a laboratory (since 1968), and, finally, head of the Department of Quantum Acoustics (since 1973). Since 1979, he combined research with tutorial activity at the Kazan Branch of the Moscow Power Institute (now, Kazan State Power University). From 1984 to 1998, he headed the Department of Industrial Electronics, and in 1994–1996, he was the Dean of the Faculty of Electronic Engineering and Automation. Today, Golenishchev-Kutuzov is a professor in the Department of Industrial Electronics of Kazan State Power University and, simultaneously, a principal researcher at Kazan Physicotechnical Institute of the Russian Academy of Sciences.

In 1964, Golenishchev-Kutuzov defended his candidate's dissertation, and in 1972, his doctoral dissertation, which was entitled "Acoustic Nuclear Magnetic Resonance in Crystals." In 1980, he received the title of Professor.

Golenishchev-Kutuzov belongs to the Kazan scientific school of quantum acoustics, the theoretical foundations of which were laid by the works by S.A. Al'tshuler and U.Kh. Kopvillem. In the late 1950s, Golenishchev-Kutuzov pioneered the study of acoustic paramagnetic resonance, and in 1962, these studies culminated in the discovery of a new effect: the nonresonance absorption of ultrasound by the electron spin system. Together with U.Kh. Kopvillem and N.A. Shamukov, Golenishchev-Kutuzov discovered and studied acoustic electron-nuclear double resonances, which opened the way to a considerable extension of the area of application of acoustic magnetic spectroscopy (a Gold Medal of the Exhibition of Domestic Economic Achievements in 1970). Later, he used the methods of magnetic quantum acoustics in studying the electronic structure of electrically and magnetically ordered crystals. He revealed and investigated such nonlinear acoustic effects as quantum oscillations of nuclear spins in an acoustic wave field (in collaboration with V.F. Tarasov) and a soliton regime of acoustic pulse propagation in a magnet (together with Kh.G. Bogdanova).The results of these studies were generalized in the monographs *Magnetic Quantum Acoustics* written together with V.V. Samartsev, N.K. Solovarov, and B.M. Khabibullin (Nauka, Moscow, 1977) and *Pulsed Optical and Acoustic Coherent Spectroscopy* written together with V.V. Samartsev and B.M. Khabibullin (Nauka, Moscow, 1988).

In the following years, the methods of acoustic electron paramagnetic resonance spectroscopy and photoacoustic spectroscopy were used to develop a complex technique for controlling the quality of crystals in quantum electronics (in collaboration with S.A. Migachev).

Today, Golenishchev-Kutuzov is the leader of the scientific school in studying the electronic structure and nonlinear properties of magnetically and electrically ordered materials, which unites professors and postgraduate students of Kazan State Power University and Kazan Physicotechnical Institute. Over the last ten years, studies in this field have been supported by the Russian Foundation for Basic Research and the Minis-

1063-7710/02/4806-0758$22.00 © 2002 MAIK "Nauka/Interperiodica"

try of Education. More than 20 candidate's and doctoral dissertations were prepared and defended under Golenishchev-Kutuzov's supervision.

Golenishchev-Kutuzov is not only a researcher: since the late 1970s, he delivers lectures to students in electronic engineering and quantum electronics.

Golenishchev-Kutuzov takes active part in the work of scientific councils on acoustics, magnetism, and nondestructive testing of the Russian Academy of Sciences. He is a member of the editorial council of *Acoustical Physics*. He is a full member of the International Academy of Sciences of Universities and a correspondent member of the Academy of Electrotechnical Sciences. Golenishchev-Kutuzov received the titles of Honorary Scientist and Engineer of both Tatarstan (1982) and the Russian Federation (1995). He is a descendant of a well-known noble family of Golenishchev-Kutuzovs.

Colleagues, students, and friends of the brilliant scientist, excellent teacher, and wonderful man Vadim Alekseevich Golenishchev-Kutuzov congratulate him on his 70th birthday and wish that all his new creative ideas and plans come true.

Translated by E. Golyamina

Acoustical Physics, Vol. 48, No. 6, 2002, pp. 760–761. Translated from Akusticheskiĭ Zhurnal, Vol. 48, No. 6, 2002, pp. 858–859.

CHRONICLE

Andreĭ Vladimirovich Rimskiĭ-Korsakov (August 29, 1910–February 9, 2002)

On February 9, 2002, the world-famous Russian scientist Andreĭ Vladimirovich Rimskiĭ-Korsakov—Doctor of Science (Phys.–Math.), professor, and a winner of the USSR State Award—died at the age of 91.

Rimskiĭ-Korsakov, a grandson of the famous Russian composer, lived a long fruitful life filled with creative work. He was born on August 29, 1910, in St. Petersburg, into a family of ancient noble lineage, which gave many prominent statesmen, scientists, and army leaders to Russia. Rimskiĭ-Korsakov received an excellent education: he simultaneously studied at a German general education school and at a music school and then continued and completed his education at the Leningrad Conservatory and the Leningrad Polytechnical Institute.

In 1932, Rimskiĭ-Korsakov began his career at the Research Institute of Musical Industry. His outstanding gifts and combination of musical education and technical knowledge made his work successful from the very beginning. The first Russian electric musical instrument called *Émiriton* was constructed with his participation. The method of studying the frequency characteristics of musical instruments by using pulsed excitation is still in use as a method for determining the noise characteristics of complex vibratory systems. In 1940, after defending his candidate's dissertation, Rimskiĭ-Korsakov changed his place of work and came to the Leningrad Physicotechnical Institute, where he began his studies in hydroacoustics. The experience gained there helped him in designing and testing acoustic mines, which was the work he carried out as a navy officer from 1944. After he was demobilized, Rimskiĭ-Korsakov returned to his studies in musical acoustics and broadcasting.

The great erudition and diversity of interests of Rimskiĭ-Korsakov manifested themselves most impressively at the Acoustics Institute, where he worked since moving to Moscow in 1955 till the last day of his life. There, as the head of the department organized by himself, he conducted extensive studies in aerothermoacoustics, hydroacoustics, and the noise and vibrations of complex mechanical structures. On his initiative, special test benches called "Aeroacoustic tunnel" and "Noise" were built at the Volga research station of the Acoustics Institute. The test benches were designed to study the processes of noise generation by gas jets and flows about obstacles. These studies revealed the mechanism of sound generation by vortices and by rotating fans and blade wheels in air blowers and made it possible to work out recommendations for the design of low-noise turbocompressors and centrifugal ventilators that were later applied in industry. On the basis of the results obtained by studying the self-oscillations of supersonic jets and noise generation by reaction jets, Rimskiĭ-Korsakov and his students developed methods for calculating the noise fields of jet engines and proposed ways for suppressing the self-oscillations of powerful jets of rocket engines. They undertook important studies of noise radiation from gas jets, both cool and heated, and also revealed the origin of the discrete noise components generated by supersonic jets.

The studies of noise and vibrations excited in frame structures by the mechanisms they support were carried out, according to the proposal of Rimskiĭ-Korsakov, both on models at the Volga research station and on real objects in the Black and Baltic seas. Rimskiĭ-Korsakov participated personally in many expeditions, and his knowledge and experience to a considerable degree

1063-7710/02/4806-0760$22.00 © 2002 MAIK "Nauka/Interperiodica"

determined the success of the studies. The results of research expeditions and laboratory studies were regularly discussed at the scientific seminars conducted by Rimskiĭ-Korsakov at his department in an atmosphere of friendly criticism and useful remarks.

A characteristic feature of the scientific activity of Rimskiĭ-Korsakov was his close attention to the most topical issues concerning the needs of industry and the navy. Many scientific developments that found application in industry were conducted by the colleagues of Rimskiĭ-Korsakov under his supervision and with his participation, in cooperation with the leading research institutes of Russia, such as the Zhukovsky Central Aerohydrodynamics Institute, the Krylov Central Research Institute, the Institute of Mechanical Engineering of the Academy of Sciences of the USSR, PO Ékvator (Nikolaev), etc.

Rimskiĭ-Korsakov devoted much time to tutorial activities. His talent for teaching appeared as early as his student years, when he conducted seminars in mathematics at a workers' faculty. In 1946, he began his regular tutorial activity: first, as an associate professor at the Department of Broadcasting and Acoustics of the Leningrad Electrotechnical Institute of Communication, and then, as the head of this department and the dean of the Faculty of Radio Engineering. Due to Rimskiĭ-Korsakov's skilled tutorial activity and wise supervision, the department showed considerable progress. In 1950, Rimskiĭ-Korsakov received his doctoral degree and the title of professor. In 1960, working at the Acoustics Institute, he organized the department of Electroacoustics and Ultrasonics at the Moscow Mining Institute, where he gave lectures on electroacoustics and acoustical measurements. Beginning in 1965, Rimskiĭ-Korsakov taught at the Moscow Institute of Radio Engineering, Electronics, and Automation: he gave lectures on electroacoustics and organized a student's training laboratory. Many of his former students now work at the Acoustics Institute and give lectures themselves, remembering with gratitude the pedagogical talent of Rimskiĭ-Korsakov.

The wide scope of scientific interests of Rimskiĭ-Korsakov is reflected in the great number of his publications. He wrote nine monographs on fundamental problems of acoustics, edited five collections of papers on acoustical aerodynamics, and received more than fifty inventor's certificates. The list of his publications contains more than a hundred papers, both theoretical and experimental, in the fields of electroacoustics, musical acoustics, aerothermoacoustics, hydroacoustics, and noise and vibration in mechanical structures.

Rimskiĭ-Korsakov has given many invited and plenary talks at the All-Union and International scientific conferences (in Moscow, Tokyo, Budapest, Madrid, and London) in Russian, as well as in German, English, and French, having mastered these languages perfectly. From 1965 over a period of 15 years, he represented the USSR in the International Electrotechnical Commission as secretary of the Ultrasound Subcommittee. He was also a member of the International Commission on Acoustics (1968–1974).

The services of Rimskiĭ-Korsakov to Russia were marked by State awards: the USSR State Award, the order of the Red Banner of Labor, the Badge of Honor, and medals.

Rimskiĭ-Korsakov was infinitely devoted to science and worked till the last day of his life. He was always held in high respect and much loved by his colleagues who tried to follow his example. The blessed memory of Andreĭ Vladimirovich Rimskiĭ-Korsakov will always live in the hearts of his numerous students and colleagues.

Translated by A. Kruglov

Acoustical Physics, Vol. 48, No. 6, 2002, pp. 762–763. Translated from Akusticheskiĭ Zhurnal, Vol. 48, No. 6, 2002, pp. 860–861.

INFORMATION

Review of the Monograph *Low-Frequency Ambient Acoustic Noise of the Ocean* by I. F. Kadykov (Editorial URSS, Moscow, 1999)

The monograph is devoted to the studies of low-frequency ambient noise in the ocean. Nowadays, specialists in the remote acoustic sensing of sea basins take an active interest in the passive methods that are based on the use of the ambient noise of a shallow sea and a deep ocean. In this respect, low-frequency noise is most advantageous because of its propagation features: starting from a certain ratio of the elastic wave length to the sea depth, the noise propagates not only in the water layer but also in the structures of the sea floor. This process is accompanied by the partial transformation of the energy of elastic oscillations to surface waves propagating at the interface between the two media. The increase in both the number of propagation channels and the variety of observable elastic waves with different propagation velocities extends the possibilities of the remote acoustic monitoring of natural noise sources and the parameters of the water and bottom propagation channels. In some situations, the use of the signals of natural sources is the only possible way to acoustically monitor a water basin in view of the difficulties encountered in designing artificial low-frequency sound sources.

The problems considered in the book are concerned with the formation, propagation, and measurement of low-frequency noise, from several thousandths of hertz to several hundreds of hertz, and with the analysis of the noise sources.

The book consists of eight chapters. The two initial ones present the main concepts of low-frequency acoustics and the analysis of the latest data on low-frequency noise, its sources, and the main processes responsible for interference in the noise measurements. The author argues that the ambient noise of the ocean is not limited in time and covers a broad frequency band. Therefore, in the experimental studies, it is necessary to separate the noise components of different origin.

The third chapter contains an analysis of the experimental conditions and the techniques used in the low-frequency noise measurements in the ocean. The author presents the estimates of the interfering action of pseudosound caused by the motion of the hydrophone in the water medium, as well as by the turbulence, the pressure fluctuations induced by the surface waves, and the pressure variations caused by the displacements of the bottom. Methods for controlling the interfering effects are proposed.

The fourth and fifth chapters present the experimental data obtained for the low-frequency noise at frequencies from 0.5 Hz to several tens of hertz in different shallow-water regions of the ocean and at frequencies from 0.01 Hz to several hundreds of hertz in deep-ocean regions. It is shown that, in the deep ocean, the maximal noise level is reached at the frequencies 0.15–0.3 Hz, while two local maxima, at 0.1–0.15 and 0.4–0.6 Hz, are observed in shallow seas with depths of several hundreds of meters or less. At frequencies higher than 5 Hz, in the majority of deep-ocean regions, the ambient noise is governed by far ship traffic, the spectrum of this noise being discrete up to 15–20 Hz and nearly independent of the weather conditions up to a frequency of several hundreds of hertz. In seismically active regions, the spectrum of the low-frequency noise can be influenced by earthquakes, the main portion of seismic noise energy lying within the frequency band 0.5–10 Hz. In shallow-water regions that are far from ship traffic, the noise of frequencies higher than 5 Hz is completely determined by the wind at the point of reception. In contrast to deep-water noise, which is formed by nothing but acoustic waves in water, shallow-water noise is not restricted to a single type of elastic waves. At the low-frequency edge of the band, shallow-water noise is governed by the waves on the sea surface and by the zero mode of the elastic waves at the bottom boundary; at frequencies higher than 1–2.5 Hz, this type of noise also includes the first mode of the sound waves propagating in the water layer and the first mode of the surface waves at the sea floor.

In the sixth chapter, the generalized characteristics are given for deep- and shallow-water noise in the ocean. Detailed information is presented on such important noise parameters as its power spectrum and space correlation for different environments: shallow shelf regions and open deep ocean.

The seventh chapter considers the manifestations of different natural sources of elastic waves in the recorded low-frequency noise. Here, for the first time, a detailed analysis is presented for the acoustic and seismic signals of earthquakes, which manifest themselves in the low-frequency ambient noise of the ocean and in the microseismic oscillations on the continent.

1063-7710/02/4806-0762$22.00

In the concluding eighth chapter, the author proposes to use low-frequency ocean noise and the signals of earthquakes to solve some problems of acoustics and oceanography. In particular, the possibility is shown for determining the structure of the sediment bulk in the ocean and sea shelf by measuring the spatial coherence of the ambient noise and for using the water phase of the earthquake-generated signals (the T-phase) to estimate the velocities of elastic waves in the ocean–continent transition zone. A new original mechanism of microseism generation is proposed. It explains the microseism as a result of low-frequency noise transfer from water into the sea floor and its subsequent propagation in the continental area.

The book is based on a large body of original experimental data obtained by the author during the expeditions carried out by the Acoustics Institute in different deep-water regions and shelf zones of the ocean. In the monograph, methodological aspects of in-sea experiments are considered in detail, the state of the art is analyzed, and the prospects for future studies are outlined. The book contains numerous actual data, 118 references, and a qualified analysis of experiments. The monograph is a valuable handbook for specialists whose professional activities are concerned with the exploration of the world ocean.

I. A. Maslov

Translated by E. Kopyl

Acoustical Physics, Vol. 48, No. 6, 2002, pp. 764–766. Translated from Akusticheskiĭ Zhurnal, Vol. 48, No. 6, 2002, pp. 862–864.

INFORMATION

New Books on Acoustics (1998–200)

1998

Ocean Acoustics: Proceedings of Brekhovskikh's Workshop and 7th Session of the Russian Acoustical Society, Shirshov Oceanology Institute, Russian Academy of Sciences, Moscow, 1998 (GEOS, Moscow, 1998), 360 pp.

V. M. Baranov, A. I. Grishchenko, A. M. Karasevich, *et al.*, *Acoustic Diagnostics and Control at the Enterprises of the Fuel-Power Industry* (Nauka, Moscow, 1998), 304 pp.

V. N. Belomestnykh, *Physical-Chemical Acoustics of Crystals* (Tomsk, 1998), 183 pp., with a bibliography of 186 titles.

Study and Exploitation of the World Ocean: Proceedings of the 6th All-Russian Acoustical Conference (with International Participation), December, 1997 (Dal'nauka, Vladivostok, 1998), 249 pp.

N. P. Zagraĭ, *Nonlinear Interactions in Layered and Inhomogeneous Media*, Ed. by V. I. Timoshenko (Taganrog State Radiotechnical University, Taganrog, 1998), 434 pp.

On the History of Russian Hydroacoustics: A Collection of Papers, Essays, and Memoirs, Compiled by Ya. S. Karlik (St. Petersburg, 1998), 691 pp.

V. A. Komarov and V. F. Muzhitskiĭ, and S. Yu. Gurevich, *Acoustic Field*, Vol. 2 of *Theory of Physical Fields* (1998), 300 pp.

Mathematical Problems of the Theory of Wave Propagation, Ed. by V. M. Babich (Moscow, 1998), Issue 27, 340 pp.

Marine Technologies, Ed. by M. D. Ageev, Issue 2 (Dal'nauka, Vladivostok, 1998), 276 pp.

Nonlinear Acoustics of Solids: Proceedings of 8th Session of the Russian Acoustical Society, September 8–10, 1998, Ed. by V. I. Erofeev (Nizhni Novgorod, 1998), 303 pp.

E. F. Orlov and G. A. Sharonov, *Interference of Sound Waves in the Ocean* (Dal'nauka, Vladivostok, 1998), 196 pp.

S. I. Alyab'ev, A. V. Vykhodets, R. Germer, *et al.*, *Radio Broadcasting and Electroacoustics: A Textbook for Communication Universities on Specialty no. 201100 "Radio Communication, Radio Broadcasting, and Television,"* Ed. by Yu. A. Kovalgin (Radio i Svyaz', Moscow, 1998), 791 pp.

I. V. Semchenko and S. A. Khakhomov, *Bulk Acoustic Waves in Crystals in a Rotating Electric Field* (Belorusskaya Nauka, Minsk, 1998), 150 pp.

L. Amundsen and A. Reitan, *Acoustic Surface Scattering from a Wavelet* (Frondheim, 1998), 25 pp.

Y. Ando, *Architectural Acoustics: Blending Sound Sources, Sound Field, and Listeners* (Springer, 1998), 252 pp.

C. Campbell, *Surface Acoustic Waves Devices for Mobile and Wireless Communications* (Academic, New York, 1998), 631 pp.

C. K. Chui, A. K. Chan, and S. Liu, *Wavelet Toolwave* (Academic, New York, 1998), 80 pp.

F. Fahy and J. Walker, *Fundamentals of Noise and Vibration* (E and FN SPON, London, 1998), 500 pp.

P. Filippi, A. Bergassoli, D, Habault, and J. P. Lefebvre, *Acoustics: Basic Physics, Theory, and Method* (Academic, New York, 1998), 336 pp.

H. Groel, J. P. Lefebvre, *et al.*, *Mediacoustic—Teaching Acoustics by Computer* (Villeurbane, France, 1998), CD-ROM.

A. I. Khilko, J. W. Caruthers, and N. A. Sydorovskaia, *Ocean Acoustic Tomography: A Review with Emphasis of the Russian Approach* (Institute of Applied Physics, Russian Academy of Sciences, Nizhni Novgorod, 1998), 195 pp.

S. Kirkup, *The Boundary Element Method in Acoustics* (Integrated Sound Software, 1998), 138 pp. and CD-ROM.

K. Naugolnykh and L. Ostrovsky, *Nonlinear Wave Processes in Acoustics*, Cambridge Texts in Applied Mathematics (Cambridge Univ. Press, Cambridge, 1998), 298 pp., with a bibliography pp. 291–294.

H. Medwin and C. S. Clay, *Fundamentals of Acoustical Oceanography* (Academic, San Diego, 1998), 712 pp.

K. S. Mylvaganam, *Ultrasonic Gas Flowmeters* (1998) 200 pp.

Nonlinear Acoustics, Ed. by M. F. Hamilton and D. T. Blackstock (Academic, San Diego, 1998), 455 pp.

Physical Acoustics, Vol. 25: Subject and Author Cumulative Index Vols. 1–24, Ed. by R. N. Thurston and A. D. Pierce (Academic, New York, 1998), 320 pp.

W. J. Richardson, *et al.*, *Marine Mammals and Noise* (Academic, New York, 1998), 576 pp.

H. Sato and M. C. Fehler, *Seismic Wave Propagation and Scattering in the Heterogeneous Earth*, Modern Acoustics and Signal Processing (Springer, 1998), 308 pp.

The Formation of Acoustic Fields in Oceanic Waveguides: Reconstruction of Inhomogeneities in

1063-7710/02/4806-0764$22.00

Shallow Water (Institute of Applied Physics, Russian Academy of Sciences, Nizhni Novgorod, 1998), Vol. 1, 186 pp.; Vol. 2, pp. 187–355.

M. Tohyama and T. Koike, *Fundamentals of Acoustic Signal Processing* (Academic, New York, 1998), 321 pp.

Ultrasound in Medicine, Ed. by F. A. Duck *et al.* (Institute of Physics, New York, 1998), 314 pp.

Ultrasound Screening for Fetal Anomalies: Is It Worth It? (Academic, New York, 1998), 256 pp.

1999

Aviation Acoustics: Proceedings of the Seminar, Dubna, May 1999 (Central Aerohydrodynamics Institute, Moscow, 1999), 66 pp.

Topical Problems of Aeroacoustics, Hydrodynamics, and Industrial Aerodynamics: Proceedings of the Central Aerohydrodynamics Institute (Central Aerohydrodynamics Institute, Moscow, 1999), No. 2634, 384 pp.

Problems of Fishery Hydroacoustics: Proceedings of the Research Institute of Fish Industry and Oceanography, State Fishery Committee of Russian Federation, Ed. by V. D. Tesler (Institute of Fish Industry and Oceanography, Moscow, 1999), 119 pp.

Hydroacoustic Encyclopedia, Ed. by V. I. Timoshenko (Taganrog State Radiophysical University, Taganrog, 1999), 788 pp.

I. F. Kadykov, *Underwater Low-Frequency Acoustic Noise of the Ocean* (Editorial URSS, Moscow, 1999), 151 pp., with a bibliography pp. 146–151.

Yu. V. Petukhov, *Theory of Hydroacoustic Antennas: A Texbook. Part 1: Additive Aperture Arrays* (Nizhni Novgorod State University, Nizhni Novgorod, 1999), 144 pp.

Problems of Measuring the Parameters of Hydroacoustic Fields and Signal Processing: Proceedings of the VNIIFTRI State Enterprise (Moscow, 1999), 136 pp.

Seismoacoustics of Transition Zones: Abstracts of Papers of All-Russian Symposium on Seismoacoustics Devoted to the 275th Anniversary of the Russian Academy of Sciences, Vladivostok, September 20–26, 1999 (Pacific Oceanological Institute, Far-East Division, Russian Academy of Sciences, Valdivostok, 1999), 82 pp.

Modern Speech Technologies: Proceedings of 9th Session of the Russian Acoustical Society, Acoustics Institute, Moscow, 1999 (GEOS, Moscow, 1999), 166 pp.

O. B. Khavroshkin, *Some Problems of Nonlinear Seismology: A Monograph* (United Institute of Earth Physics, Russian Academy of Sciences, Moscow, 1999), 286 pp.

Acoustic Cavitation and Sonoluminescence, Ed. by J. R. Blake, Philos. Trans. R. Soc. (London), Ser. A, **357** (1999), No. 1751, pp. 199–369.

R. T. Beyer, *Sound of Our Times: Two Hundred Years of Acoustics* (Springer, New York, 1999), 444 pp.; Reviewed by D. S. Raichel in J. Acoust. Soc. Am., **106** (1) 15 (1999).

W. J. Cavanaugh and J. A. Wilkes, *Architectural Acoustics: Principles and Practice* (Wiley, New York, 1999), 332 pp.; Reviewed by J. C. Jaffe in J. Acoust. Soc. Am. **105** (5) 2548 (1999).

A. Doicu, Y. A. Eremin, and T. Wriedt, *Acoustic and Electromagnetic Scattering Analysis Using Discrete Sources* (Academic, London, 1999), 280 pp.

S. Mallat, *A Wavelet Four of Signals Processing*, 2nd Edition (Academic, New York, 1999), 664 pp.

M. R. Schroeder, *Computer Speech: Recognition, Compression, Synthesis*, Springer Series in Information Sciences (Springer, 1999), Vol. 35, 313 pp.

Ultrasonic Instruments and Devices: Reference for Modern Instrumentation, Techniques, and Technology, Ed. by E. P. Papadakis (Academic, San Diego, 1999), 809 pp.

E. G. Williams, *Fourier Acoustics. Sound Radiation and Nearfield Acoustical Holography* (Academic, 1999), 272 pp.

E. Zwicker and H. Fostl, *Psychoacoustics: Facts and Models*, 2nd Edition (Springer, Berlin, 1999), 416 pp.

2000

O. V. Abramov, *Effect of Intense Ultrasound on Liquid and Solid Metals* (Nauka, Moscow, 2000), 312 pp.

Acoustics of Inhomogeneous Media: Proceedings of Prof. S.A. Rybak's Seminar. Yearbook 2000 of the Russian Acoustical Society, Ed. by S. A. Rybak (Moscow, 2000), 185 pp.

Ocean Acoustics: Proceedings of 8th Workshop of Academician L.M. Brekhovskikh (GEOS, Moscow, 2000), 211 pp.

Acoustic Measurements and Standardization. Ultrasound and Ultrasonic Technologies. Geoacoustics. Speech Acoustics. Medical and Biological Acoustics. Atmospheric Acoustics: Proceedings of 10th Session of the Russian Acoustical Society, May 29–June 2, 2000 (Moscow, 2000), Vol. 2, 230 pp.

Vibroacoustics in Medicine: Proceedings of I All-Russian Scientific-Practical Conference, St. Petersburg, June 8–9, 2000, Ed. by O. I. Efanov (Vita Nova, St. Petersburg, 2000), 153 pp.

Hydroacoustics: Collection of Papers on Science and Engineering, Ed. by Yu. A. Koryakin (Morfizpribor Central Research Institute, St. Petersburg, 2000), 95 pp.

B. A. Kasatkin and N. V. Zlobina, *Nonclassical Solution of the Classical Problems of Acoustics* (Dal'nauka, Vladivostok, 2000), 162 pp.

A. G. Leĭko, Yu. E. Shchamarin, and V. P. Tkachenko, *Underwater Acoustic Antennas: Methods of Sound Field Calculations*, Acoustician's Library:

Underwater Electroacoustic Equipment and Devices (Kiev, 2000), Vol. 1, 320 pp.

Laser Photoacoustic Spectroscopy of Intermolecular Interactions in Gases, by Yu. N. Ponomarev *et al.*, Ed. by L. N. Sinitsa (RASKO, Tomsk, 2000), 199 pp.

Applied Technologies of Hydroacoustics and Hydrophysics: Proceedings of 5th International Conference, St. Petersburg, June 6–9, 2000, Hydroacoustic Equipment (St. Petersburg, 2000), 336 pp.

Ultrasonic Technological Processes—2000: Abstracts of Papers of International Conference, Arkhangel'sk, September 27–30, 2000 (Severodvinsk, 2000), 220 pp.

A. N. Akansu and R. A. Haddad, *Multiresolution Signal Decomposition* (Academic, New York, 2000), 480 pp.

E. H. Berger, L. H. Royster, J. D. Royster, D. P. Friscoll, and M. Layne, *The Noise Manual* (S. Hirzel–EAA, 2000), 796 pp.; Reviewed by C. Nocke in Acustica **87** (4) 521 (2001).

S. Elliott, *Signal Processing for Active Control* (Academic, London, 2000), 544 pp.

F. G. Fahy, *Foundations of Engineering Acoustics* (Academic, New York, 2000), 443 pp.

Handbook of Elastic Properties of Solids, Liquids, and Gases, Ed. by M. Levy *et al.* (Academic, London, 2000), Vols. 1–4. Vol. 1: *Dynamic Methods for Measuring the Elastic Properties of Solids*; Vol. 2: *Elastic Properties of Solids: Theory, Elements and Compounds, Novel Materials, Technological Materials, Alloys, Building Materials*; Vol. 3: *Elastic Properties of Solids: Biological and Organic Materials, Earth and Marine Sciences*; Vol. 4: *Elastic Properties of Fluids: Liquids and Gases.*

K.-Y. Hashimoto, *Surface Acoustic Wave Devices in Telecommunications* (Springer, 2000), 334 pp.

L. E. Kinsler, A. R. Frey, A. B. Coppens, and J. V. Sanders, *Fundamentals of Acoustics* (Wiley, 2000), 560 pp.

C. Morfey, *Dictionary of Acoustics* (Academic, New York, 2000), 200 pp.

E. P. Papadakis, *Ultrasonic Instruments and Devices* (Academic, New York, 2000).

D. R. Raichel, *The Science and Applications of Acoustics* (Springer, 2000), 450 pp.

S. D. Snyder, *Active Noise Control Primer* (Springer, 2000), 190 pp.

Underwater Acoustics: Proceedings of 5th European Conference ECUA-2000, Lyon, July 10–13, 2000, Ed. by M. E. Zakharia (Lyon, 2000), Vol. 1, 746 pp.; Vol. 2, 749 pp.

W. A. Yost, *Fundamentals of Hearing: An Introduction*, 4th Edition (Academic, 2000), 375 pp.

Compiled by N. E. Shmakova